

VOLUME 9

NUMBER 2

2018

ISSN 2218-7987  
eISSN 2409-5508

International Journal of  
**Mathematics**  
and **Physics**



Al-Farabi Kazakh National University

---

The International Journal of Mathematics and Physics is a peer-reviewed international journal covering all branches of mathematics and physics. The Journal welcomes papers on modern problems of mathematics and physics, in particular, Applied Mathematics, Algebra, Mathematical Analysis, Differential Equations, Mechanics, Informatics, Mathematical Modeling, Applied Physics, Radio Physics, Thermophysics, Nuclear Physics, Nanotechnology, and etc.

---

International Journal of Mathematics and Physics is published twice a year by al-Farabi Kazakh National University, 71 al-Farabi ave., 050040, Almaty, Kazakhstan  
website: <http://ijmph.kaznu.kz/>

Any inquiry for subscriptions should be send to:  
Prof. Tlekkabul Ramazanov, al-Farabi Kazakh National University  
71 al-Farabi ave., 050040, Almaty, Kazakhstan  
e-mail: [Tlekkabul.Ramazanov@kaznu.kz](mailto:Tlekkabul.Ramazanov@kaznu.kz)

## **EDITORIAL**

The most significant scientific achievements are attained through joint efforts of different sciences, mathematics and physics are among them. Therefore publication of the Journal, which shows results of current investigations in the field of mathematics and physics, will allow wider exhibition of scientific problems, tasks and discoveries.

One of the basic goals of the Journal is to promote extensive exchange of information between scientists from all over the world. We propose publishing service for original papers and materials of Mathematical and Physical Conferences (by selection) held in different countries and in the Republic of Kazakhstan.

Creation of the special International Journal of Mathematics and Physics is of great importance because a vast amount of scientists are willing to publish their articles and it will help to widen the geography of future dissemination. We will also be glad to publish papers of scientists from all the continents.

The Journal will publish experimental and theoretical investigations on Mathematics, Physical Technology and Physics. Among the subject emphasized are modern problems of Applied Mathematics, Algebra, Mathematical Analysis, Differential Equations, Mechanics, Informatics, Mathematical Modeling, Astronomy, Space Research, Theoretical Physics, Plasma Physics, Chemical Physics, Radio Physics, Thermophysics, Nuclear Physics, Nanotechnology, and etc.

The Journal is issued on the base of al-Farabi Kazakh National University. Leading scientists from different countries of the world agreed to join the Editorial Board of the Journal.

The Journal is published twice a year by al-Farabi Kazakh National University. We hope to receive papers from many laboratories which are interested in applications of the scientific principles of mathematics and physics and are carrying out researches on such subjects as production of new materials or technological problems.

IRSTI 27.41.41

B. Mukanova, T. Mirgalikyzy, M. Turarova

L.N. Gumilyov Eurasian National University, Astana, Kazakhstan,  
e-mail: mbsha01@gmail.com, m\_t85@mail.ru, marzhan\_08@mail.ru

### **Numerical aspects of the adaptive computational grid in solving the problems of electrical prospecting with direct current**

**Abstract.** This paper is devoted to the numerical aspects of the adaptive computational grid in solving the problems of electrical prospecting with direct current. The purpose of this work is to determine the acceptable parameters of various algorithms for constructing a computational grid for computing electrical tomography curves associated with the ground surface relief. Optimal algorithms for constructing a computational grid in problems of calculating of apparent resistivity curves, associated with the ground surface relief, can improve the accuracy in computation and cost-effectiveness in using computational resources. A mathematical model for calculating the field and of apparent resistivity curves, based on the theory of potentials, and the discretization of the surface of the calculated boundary are described. The problem is reduced to solving an integral equation.

We described here results of that method applied to the relief of simple 2D forms. Our calculations show that use of grid with triangulation gives the same results as a grid constructed with a refinement at the vicinity of the source electrode. However, due to the refinement at the vicinity of the source electrode and measuring line, the grid with triangulation is more efficient and allows one to calculate the function of apparent resistivity with relatively small number of nodes – approximately above 2000.

The data obtained in numerical experiments are basis for further research and for definition of the influence of relief forms on the distortion of apparent resistivity curves.

**Key words:** Method of integral equations, EIT, ground surface relief, apparent resistivity curves, computational grid.

#### **Introduction**

Progress in computing technologies has led to significant changes in software and hardware for geophysical methods of sounding of non-homogeneous media. Portable multi-channel systems for computerized geophysical equipments have evolved, which have changed the traditional method of field work. One of the leading methods of geoelectric research, used worldwide is the Vertical Electrical Sounding (VES) method in the modification of the electrical impedance tomography (EIT). The works that had the most influence on the development of the electrical tomography method in geophysics are the following: Edwards L.S. (1977); Barker R.D. (1981, 1992); Griffiths D.H. and Turnbull J. (1985); Zohdy A.A.R.

(1989); Dahlin T. (1993, 1996); Loke M.H. and Barker R.D. (1996); Bobachev A.A., Modin I.N. and others (1995, 1996, 2006, 2008) [1-10].

In the problems of VES the study of the influence of experimental conditions on apparent resistivity curves is of major importance, in particular, that is the impact of a relief of the sounding medium. The review of the main researches concerning the influence of the ground surface relief is reported in the article [11]. As it is shown in works [11, 12], an efficient and accurate way to calculate the influence of a shape of a ground surface relief on sounding data is the Integral Equations Method (IEM). The method is based on representation of the potential of the stationary electric field via potentials of simple layers distributed on a surface of the medium and internal contact boundaries.

In practice, construction of a geoelectric section of the medium is carried out on the basis of measurements of apparent resistivity and using of 2D and 3D inversion programs. These programs solve the inverse problem of EIT (for instance, Res2DInv, the author is M.H. Loke, 2000; and ZondRes2D of A.E. Kaminsky, last updated 26.06.10). In most cases the solution is smooth with blurred boundaries that do not always correspond to real geological situation. The sharp geoelectric borders become diffused, and the distortions of curves of apparent resistivity related with a surface relief generate pseudo anomalies. From the best of our knowledge there are no programs which accurately calculate the influence of distortions, related with a ground surface relief.

### Mathematical model and discretization of the surface

As it is shown in [11], the problem of the numerical computation of a direct current field in the homogeneous medium with a ground surface relief can be reduced to the solution of the Fredholm integral equation of the second kind with a weak singularity:

$$q(P) = \iint_{\Gamma} q(M) \frac{\cos \psi_{PM}}{|PM|^2} d\Gamma(M) + F_0(P) \quad (1)$$

Here  $M, P$  are points of the boundary  $\Gamma$  of the medium on which the integral is taken,  $q(P)$  is the density of a simple layer on boundary  $\Gamma$  which allows to calculate the potential of the field,  $\psi_{PM}$  is a corner between a normal vector at the point  $P$  and the vector  $PM$ ,  $F_0(P)$  is the given function. Actually,  $F_0(P)$  is expressed via the potential of the source electrode.

In [11] the method of integral equations is realized numerically on the grid refined near the source electrode, where large gradients of the field exist. The relief is mapped on the plane surface and the calculated grid is constructed in polar coordinates. The source electrode is located at the origin point. The measuring line passes along the radius. Then the grid is adapted to the relief surface and to the position of the source electrode by the inverse mapping it to the relief surface (Figures 1, 2). Due to the integration error for coarse grid the calculated values of apparent resistivity show nonphysical oscillations when the distance from the origin of the coordinates (Figure 3, an asterisk indicates the position of the current source electrode) increases.

To avoid these oscillations in the numerical solution, we have to make a significant refinement of the mesh and a local refinement of grid cells near the measurement line. It complicates the algorithm and breaks uniformity of the calculations.

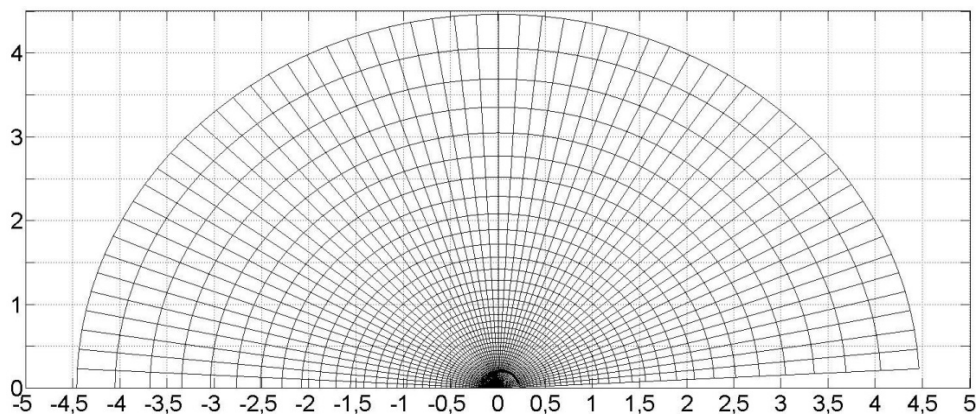


Figure 1 – Computational grid in the polar coordinate system mapped to the plane

Other source of errors is the replacement of the infinite domain of integration by a finite domain; it means that we neglect induced charges outside of the calculated area. For decrease of this error it is necessary to reach compromise between expansion of calculated domain and the number of grid nodes. The solution is the use of a coarse grid far from current sources and the measurement line, since in these

areas the potential of the field decreases inversely proportional to radius.

To avoid mentioned above nonphysical oscillation and exclude excessive refinement of the grid, an alternate computational grid is constructed. This grid is based on the triangulation and is adapted not only to the position of the source electrode, but also is condensed near measuring line. In that

algorithm the calculated area is set by some oval, its size is sufficient in order that it has been possible to neglect the field far from the source (Figures 4, 5).

Acceptable size of the grid is determined via series of numerical experiments for each considered relief form.

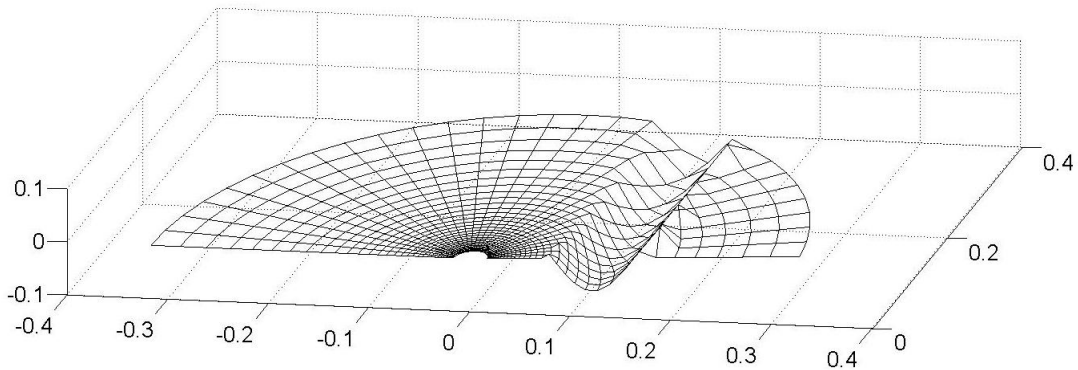


Figure 2 – Computational grid in the Cartesian coordinate system with the surface topography

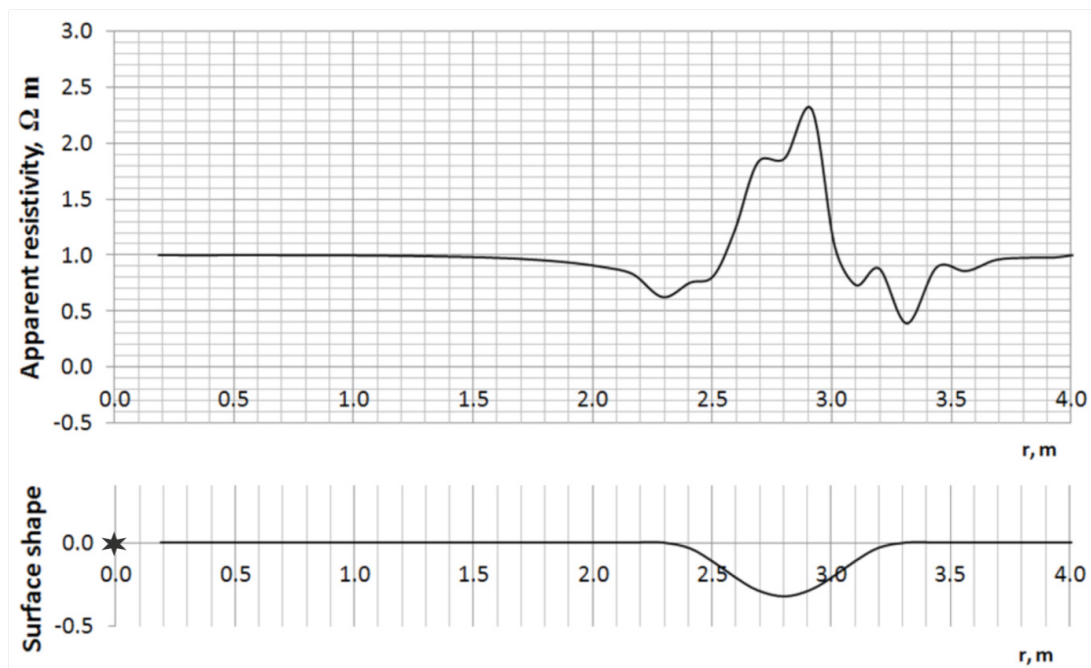


Figure 3 – The calculation of the apparent resistivity far from the current source electrode and the corresponding relief for the grid with number of layers  $N = 20$

The grid construction problem is reduced to the following steps: map a relief surface of the medium on 2D domain of an oval shape on the plane. This oval is composed of two semicircles and one rectangle. Then we divide that oval into triangles with a condensation to the line connecting the centers of the semicircles. This line lies on a larger axis of an oval and corresponds to the measuring line. Due to the symmetry for 2D examples described below, only

nodes of one half of the oval are used for calculations.

Note that in the article [13] several tests of the described method are successfully performed for two-layered model of the medium

*Brief description of the construction algorithm of a grid nodes.* The user sets quantity of layers  $N$ , i.e. the oval is divided into  $N$  layers by the rule of concentric semi-ovals of radius  $r_i = \exp(i * h_s -$

$l)/\alpha$ , where  $i$  is the number of a concentric semi-oval,  $hs = \ln(1 + a * \alpha) / N$  is a grid step on radius in the logarithmic coordinates,  $\alpha$  is the coefficient of irregularity of the grid. Then thickness of the  $i$ -th layer will be  $r_i - r_{i-1}$ . Then the massif of nodes placed on for each layer is defined. By the triangulation method the set of triangles satisfying Delaunay condition is formed for the given set of nodes. This condition allows to generate a set of

triangles which are whenever possibly close to the set of equilateral triangles. Though in mathematical packages the functions realizing Delaunay's triangulation are described, we elaborated the algorithm which is much simpler than the common algorithm, because we takes into account features of our grid, namely, its layered structure and logarithmic expansion with distance from the axis of the calculated area.

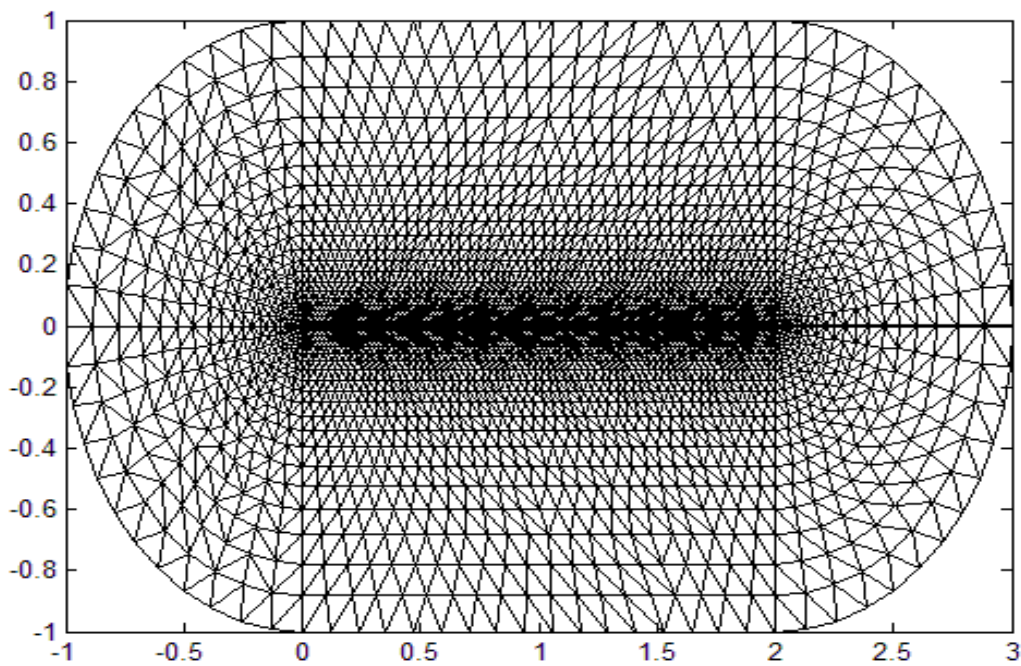


**Figure 4** – The triangulation of the calculated area refined near the measuring line

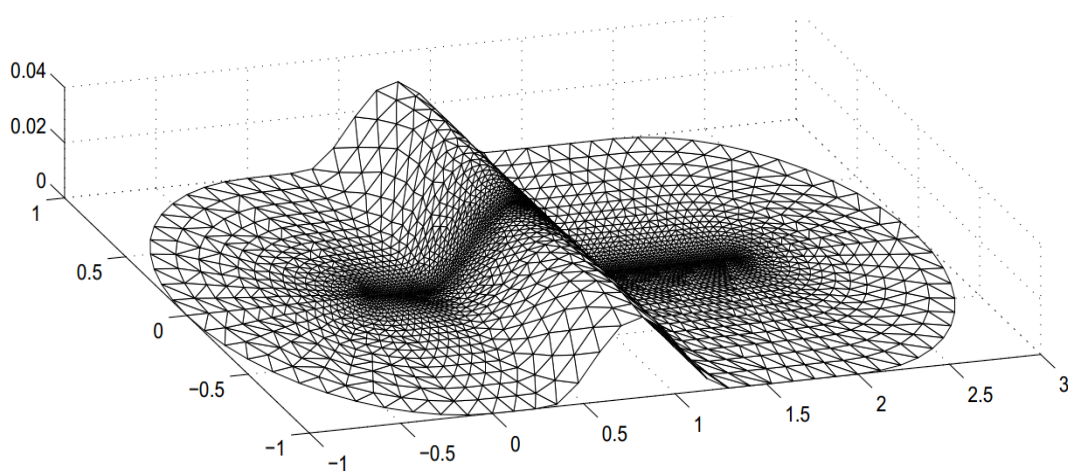


**Figure 5** – Triangulation of the relief surface

Calculated parameters of the algorithm are as follows:  $L$  is the distance between center of side semicircles of an oval;  $a$  is the maximal radius of semicircles of an oval;  $N$  is a quantity of layers of the grid;  $\alpha$  is a coefficient of irregularity of the grid. The higher the coefficient of irregularity is, the more is a difference between the size of internal and external triangles. The program generates a set of nodes and triangles which further are used to solve an integral equation.

### Numerical results

Series of numerical experiments have been made to define acceptable parameters of the grid (Figures 6, 7, 8), and comparison of the results for two algorithms of grid's construction are provided (Figures 9, 10).

Impact on the triangulation of the irregularity parameter  $\alpha$ , number of layers  $N$ , the radius of semicircles of an oval  $a$  and length  $L$  have been analyzed. Number of nodes and triangles depend on these parameters and are determined after triangulation. Calculations are made with parameters  $\alpha$  in the range 1.0÷16.0,  $N$  changes in the range 10÷100, parameters of  $a$  and  $L$  are assigned as  $a$  in 0.5÷2.0,  $L = 2 \cdot a$ .

Numerical experiments are executed for models with the negative and positive relief shapes, with sharp and smooth slope angles, also for a wavy shape of a relief. Source electrode is located in the origin of the coordinates. In Figure 9 curves of apparent resistivity are constructed for a ground surface relief in the shape of hemispherical convexity with smooth slope angles for different calculation parameters. An asterisk indicates the position of the current source electrode.

Numerical experiments show that the most acceptable parameters of calculations provide a sufficient condensation of the grid at the proximity of the measuring line, and the sufficient length of this line: at  $L=2 \cdot a$ . The most admissible values are the following:  $\alpha$  – not less than 8.0;  $N$  – not less than 20. At the same time the 20-layer grid is formed of triangles, with number of nodes is equal to 1834 and number of triangles is equal to 3416. Then the computational domain has been made wider by increasing parameter  $a$  in the interval [1, 2.]. It turns out that changes of curves of apparent resistivity are within 0.6%. However, for every value of relief slope angles it is recommended to determine admissible parameters anew by making refinements of the grid and comparing the results.

Calculated curves of apparent resistivity for models of a ground surface relief for the negative and positive shapes in the form of hemispherical (semicircular) concavity and convexity for different slope angles  $\alpha = 30, 45, 60^\circ$  are given in Figures 10, 11, an asterisk indicates the position of the current source electrode. It follows from numerical experiments that values of maxima (minima) of the apparent resistivity curve considerably increases (decreases) with increase of a slope angle.

Numerical results obtained for the same relief form for two type of grids has been compared with number of nodes close each other. For the grid with triangulation on relief with sinusoidal shape and slope angle  $60^\circ$  we use values of parameters  $L=5$ ,  $a = 2.5$ ,  $\alpha = 8.0$ ,  $N=20$ . In those parameters 20-layer grid has 2170 nodes.

The main parameters for the grid refinement only in the vicinity of the source electrode are the number of divisions along the radius and the angle [11]. Calculations on this grid are made on 20-layered grid with 2000 nodes.

Calculated apparent resistivity curves for two grid types are compared in Figures (12, 13). An asterisk indicates the position of the current source electrode. It is seen that for the grid refined only near source electrode non-physical oscillations appear, which are related with coarse grid away from the source electrode. Satisfactory results for this grid were found only with number of nodes equal to 8640. So, this kind of grid leads to the consumption of large machine resources. At the same time, results which are taken by mentioned above triangulation algorithm gives physical reliable curves of sounding with number of nodes above 2000.

Then we have made numerical simulations to check influence of other parameters. When the parameter  $a$  changes in the interval from 1 to 2, the relative change of apparent resistivity is not more than 0.6%. At the same time, maximal relative difference between apparent resistivity calculated for  $N = 30$  and  $N = 90$  is 2.5%. Changes of  $N$  between 90 and 100 is followed by changes of apparent resistivity not more than 0.5%. Changes of  $\alpha$  between 8 and 16 yield to relative difference of apparent resistivity not more than 0.2%. These mean, that for this relief form and length of measurement line with slope angle  $\leq 20^\circ$  admissible calculation parameters are:  $a = 1$ ,  $\alpha=8$ ,  $N = 30$ .

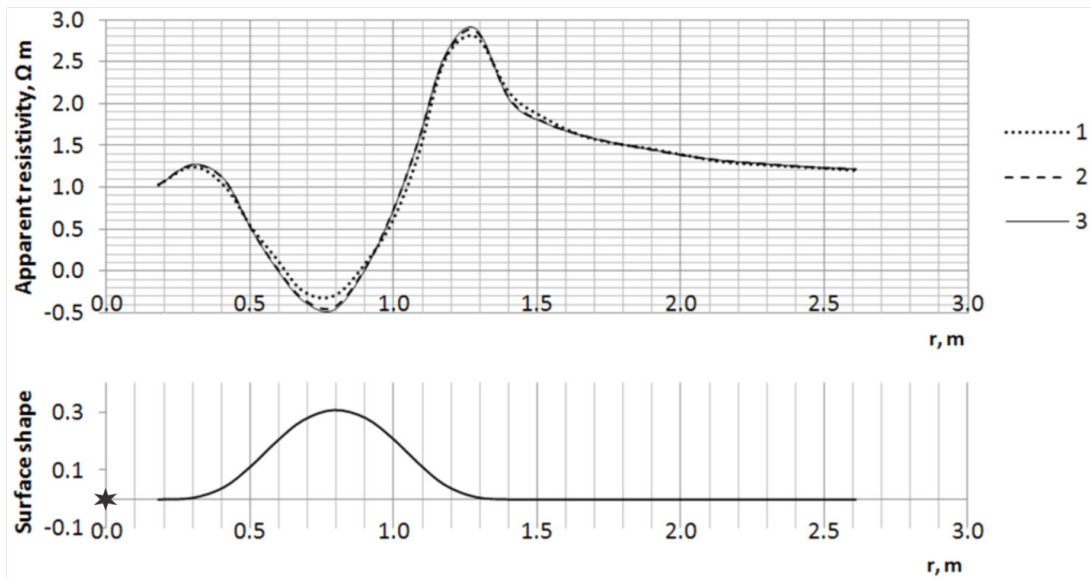
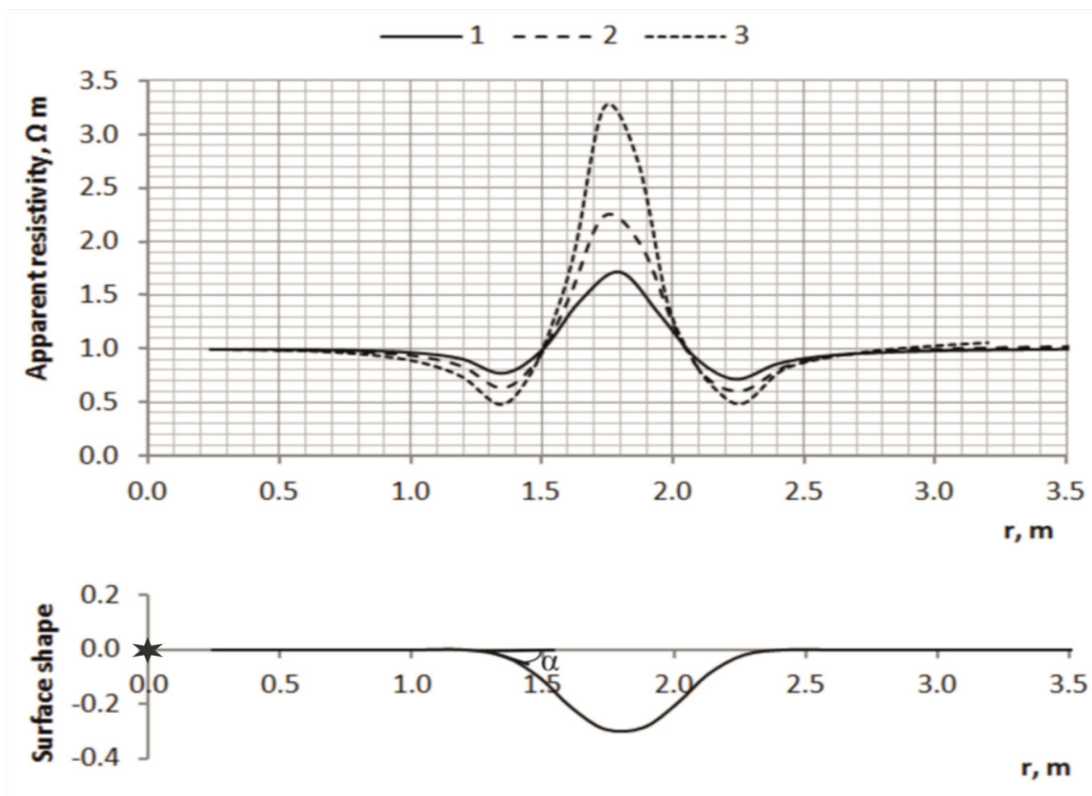


**Figure 6** – The shape of the ground surface relief and curves of apparent resistivity:  
 1 – the solution obtained for parameters  $N=10, \alpha=1.0, f=372, k=660$ ;  
 2 – the solution obtained for parameters  $N=20, \alpha=8.0, f=1834, k=3416$ ;  
 3 – the solution obtained for parameters  $N=40, \alpha=16.0, f=8716, k=16718$



1 – slope angle  $\alpha = 30^\circ$ ; 2 – slope angle  $\alpha = 45^\circ$ ; 3 – slope angle  $\alpha = 60^\circ$

**Figure 7** – Curves of apparent resistivity for the model of the surface with negative shape

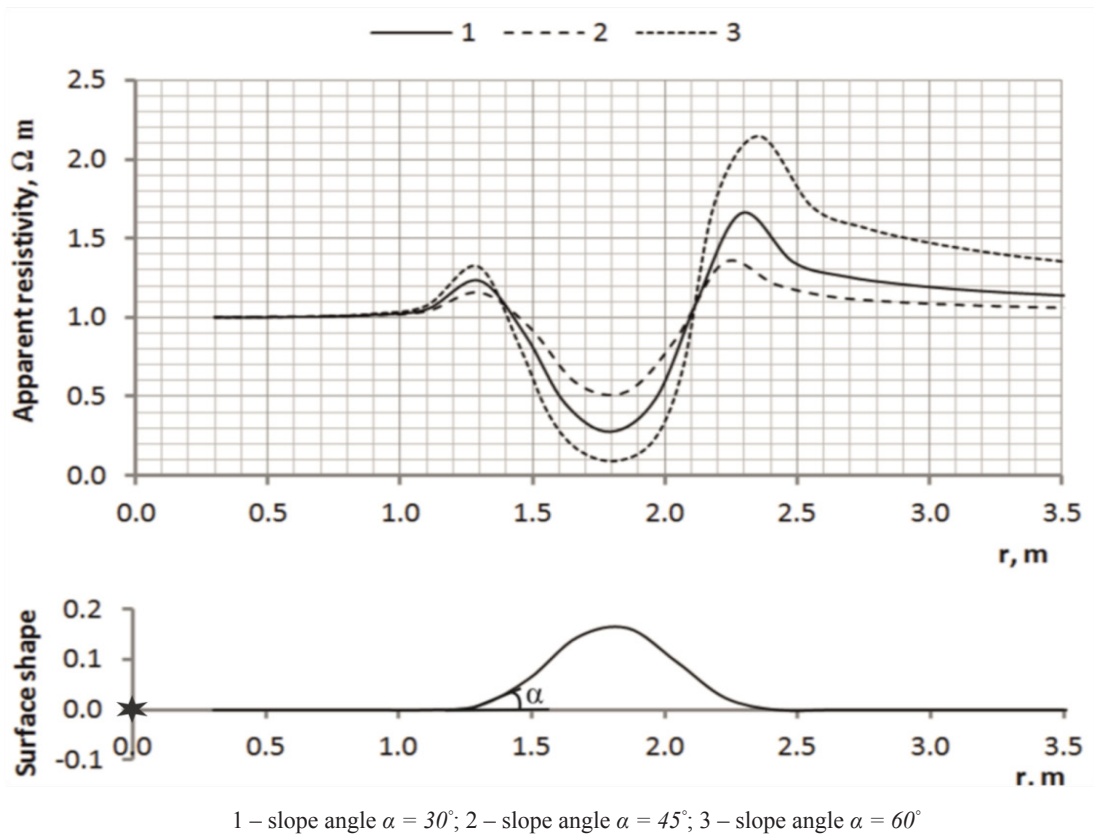


Figure 8 – Curves of apparent resistivity for the model of the surface with positive shape

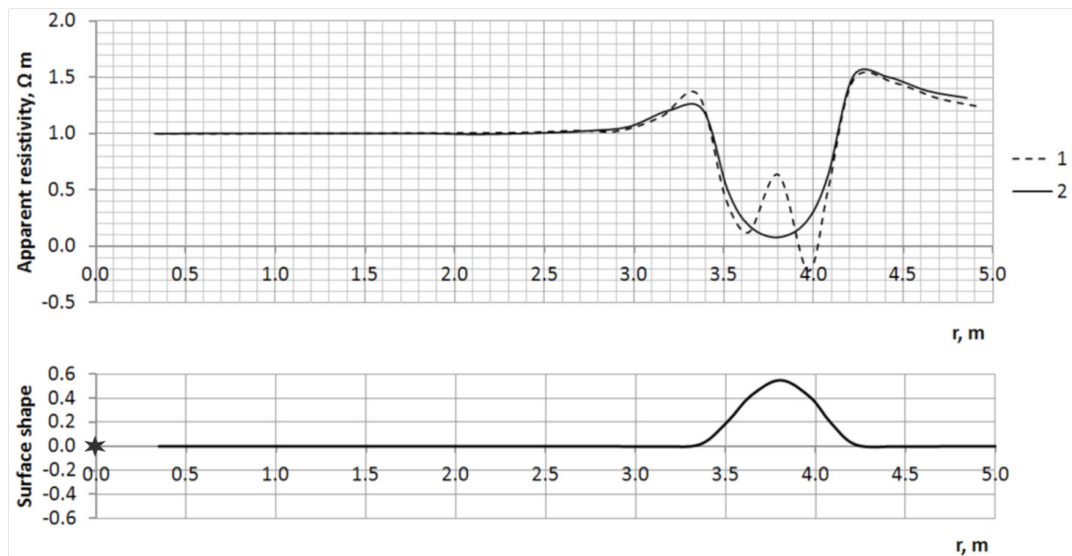
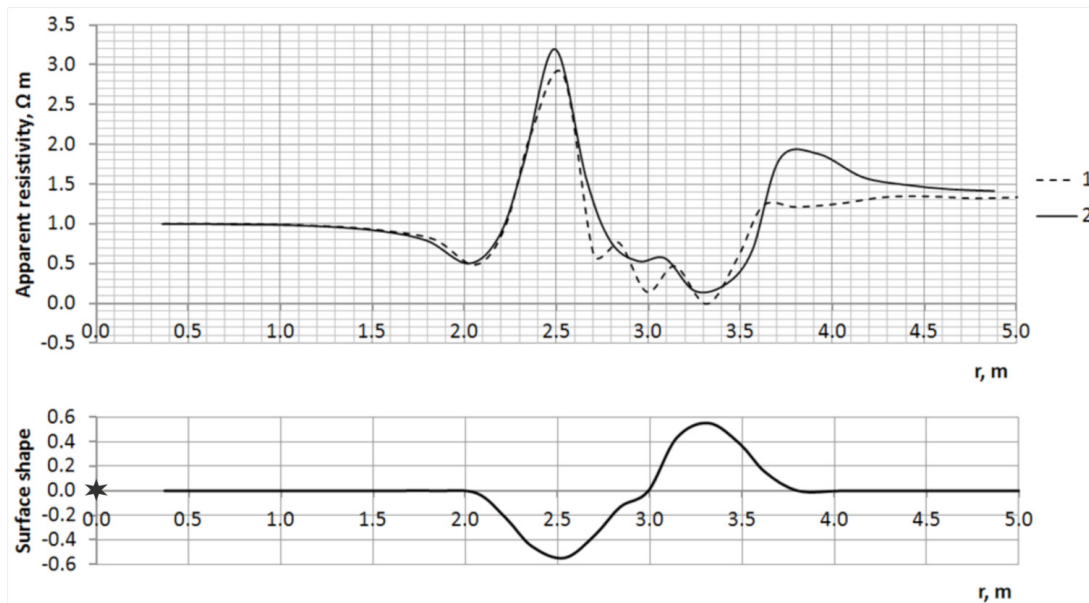


Figure 9 – The shape of the simulated ground surface and curves of apparent resistivity which are taken with different algorithms of grid's construction:  
1 – by grid adapted to source electrode, 2 – by grid with triangulation adapted to measuring line



**Figure 10** – The shape of the simulated ground surface and curves of apparent resistivity are taken with different algorithms of grid's construction:

1 – by grid adapted to source electrode, 2 – by grid with triangulation adapted to measuring line

Calculations are made for surfaces with given analytical form. Such method of assigning a function of the relief is very comfortable for simulations. However, in practice, the relief parameters are determined by field experiments. In electrical tomography method the relief is determined by the profiling step (distance between electrodes) and heights of measuring electrodes which are placed along sounding area. This definition of the relief allows creating a table of values of the height function. The heights correspond to the values of the function  $-z_j$  ( $j=1..k$ ), and the corresponding values of the argument  $-x_j$ , can be calculated through the values of the step along the profile. For approximation of that tabulated function the interpolation methods are applied.

For construction of computational grid on the arbitrary relief we considered two methods of interpolation of the relief surface: based on spline functions and on radial basis functions (RBF) [14]. Calculations are performed for different parameters of grid (number of nodes has been equal to 4147, 5222, 7155, 8044). The big advantage of RBF interpolation method is its computational efficiency compared with the spline interpolation method. For example, simulation on the grid with number of nodes  $f=7155$  on a computer with processor Intel Core i7-4700, frequency 2.40 GHz, 16 GB RAM, takes 900-1000 seconds for spline interpolated functions, while calculations with RBF method take 120-140

seconds. Note that the calculation time depends on relief form also.

### Conclusion

Interpretation of EIT data without taking into account influence of the relief form can give pseudo anomalies. We described here numerical method to compute the field and curves of apparent resistivity for a homogeneous medium with relief boundary based on the potential theory. Problem is reduced to the solution of an integral equation. The main feature of the method is its high accuracy and efficiency in calculations of the field for three-dimensional geometry of the relief and for medium with several inner contact boundaries [15]. We described here results of that method applied to the relief of simple 2D forms. Our calculations show that use of grid with triangulation gives the same results as a grid constructed with a refinement at the vicinity of the source electrode. However, due to the refinement at the vicinity of the source electrode and measuring line, the grid with triangulation is more efficient and allows one to calculate the function of apparent resistivity with relatively small number of nodes – approximately above 2000.

The data obtained in numerical experiments are basis for further research and for definition of the influence of relief forms on the distortion of apparent resistivity curves.

## References

1. Edwards L.S. "A modified pseudo-section for resistivity and induced polarization." *Geophysics* 42, no. 5 (1977): 1020-1036.
2. Barker R. D. "The offset system of electrical resistivity sounding and its use with a multicore cable." *Geophysical Prospecting* 29, no. 1 (1981): 128-143.
3. Barker R.D. "A simple algorithm for electrical imaging of the subsurface." *First Break* 10, no. 2 (1992): 53-62.
4. Griffiths D.H. and Turnbull J. "A multi-electrode array for resistivity surveying." *First Break* 3, no. 7 (1985): 16-20.
5. Zohdy A.A.R. "A new method for the automatic interpretation of Schlumberger and Wenner sounding curves." *Geophysics* 54, no. 2 (1989): 245-253.
6. Dahlin T. "On the Automation of 2D Resistivity Surveying for Engineering and Environmental Applications." (PhD diss., Lund University, 1993): 187.
7. Dahlin T. "2D resistivity surveying for environmental and engineering applications." *First Break* 14, no. 7 (1996): 275-283.
8. Loke M.H., Barker R.D. "Rapid least-squares inversion of apparent resistivity pseudo sections using a quasi-Newton method." *Geophysical Prospecting* 44, no. 1 (1996): 131-152
9. Bobachev A., Modin I., Pervago E., Shevnin V. "Mnogoelectrodnye electicheskie zondirovaniya v usloviyah gorizontalno-neodnorodnyh sred [Multi-electrode electrical sounding in a horizontally inhomogeneous media]." *Exploration Geophysics. Overview. JSC Geoinformmark* 2 (1996): 50.
10. Modin I., Bobachev A. "Electrotomografiya so standartnymi electrorazvedochnymi kompleksami [Electron tomography with standard electro complexes]." *Exploration and protection of mineral resource* no. 1 (2008): 43-47.
11. Mirgalikyzy T., Mukanova B., Modin I. "Method of Integral Equations for the Problem of Electrical Tomography in a Medium with Ground Surface Relief." *Journal of Applied Mathematic* (2015).
12. Orunkhanov M., Mukanova B. "The integral equations method in problems of electrical sounding." *Advances in High Performance Computing and Computational Sciences, Springer-Berlin-Heidelberg* (2006): 15-21.
13. Mukanova B., Mirgalikyzy T., Modin I. "Testing the results of numerical simulation of problems of electrical prospecting with direct current." *Bulletin of the National Academy of Sciences of the Republic of Kazakhstan* no. 4 (2015): 19-26.
14. Grady B. Wright. "Radial Basis Function Interpolation: Numerical and Analytical Developments." (PhD diss., University of Colorado at Boulder Boulder, CO, USA 2003): 155.
15. Mukanova B., Mirgalikyzy T. "Modeling the impact of relief boundaries in solving the direct problem of direct current electrical sounding *Communications in Computer and Information Science.*" *Mathematical Modeling of Technological Processes: International Conference, CITech-2015* (2015): 117-123.

IRSTI 27.41.41

<sup>1</sup>S. Aisagaliev, <sup>1</sup>Zh. Zhunussova, <sup>2</sup>H. Akca

<sup>1</sup>Al-Farabi Kazakh National University, Almaty, Kazakhstan  
e-mail: Serikbai.Aisagaliev@kaznu.kz

<sup>2</sup>Abu-Dhabi University, Abu-Dhabi, UAE  
e-mail: Haydar.Akca@adu.ac.ae

### Immersion principle for a variation calculus problem with boundary conditions

**Abstract.** The immersion principle is based on the investigation of the Fredholm integral equation of the first kind. For the Fredholm integral equation of the first kind, the existence theorem for the solution as well as the theorem on its general solution are proved. The basis of the proposed method for solving the variation problem is the immersion principle. The essence of the immersion principle is that the original variation problem with the boundary conditions with phase and integral constraints is replaced by equivalent optimal control problem with a free right end of the trajectory. This approach is made possible by finding the general solution of a class of Fredholm integral equations of the first order. In this work a method for solving the Lagrange problem with phase restrictions for processes described by ordinary differential equations without involvement of the Lagrange principle is supposed. Necessary and sufficient conditions for existence of a solution of the variation problem are obtained, feasible control is found and optimal solution is constructed by narrowing the field of feasible controls. In contrast to the well-known method for solving the problem of the variation calculus on the basis of the Lagrange principle, an entirely new approach an "immersion principle" is proposed.

**Key words:** immersion principle, feasible control, integral equations, optimal control, optimal solution, minimizing sequence.

#### Problem statement

We consider the following problem: minimize the functional

$$J(u(\cdot), x_0, x_1) = \int_{t_0}^{t_1} F_0(x(t), u(t), x_0, x_1, t) dt \rightarrow \inf \quad (1.1)$$

at conditions

$$\dot{x} = A(t)x + B(t)f(x, u, t), \quad t \in I = [t_0, t_1] \quad (1.2)$$

with boundary conditions

$$(x(t_0)) = x_0, x(t_1) = x_1 \in S_0 \times S_1 = S \subset R^{2n} \quad (1.3)$$

in the presence of phase constraints

$$x(t) \in G(t) : G(t) = \{x \in R^n / \omega(t) \leq F(x, t) \leq \phi(t), \quad t \in I\},$$

and integral constraints

$$g_j(u(\cdot), x_0, x_1) \leq 0, \quad j = \overline{1, m_1}; \quad g_j(u(\cdot), x_0, x_1) = 0, \quad j = \overline{m_1 + 1, m_2}, \quad (1.4)$$

$$g_j(u(\cdot), x_0, x_1) =$$

$$\int_{t_0}^{t_1} f_{0j}(x(t), u(t), x_0, x_1, t) dt, \quad j = \overline{1, m_2}, \quad (1.5)$$

where the control

$$u(\cdot) \in L_2(I, R^m). \tag{1.6}$$

Here  $A(t)$ ,  $B(t)$  are matrices with piecewise-continuous elements of orders  $n \times n$ ,  $n \times r$ , respectively, a vector function  $f(x, u, t) = (f_1(x, u, t), \dots, f_r(x, u, t))$  is continuous with respect to the variables  $(x, u, t) \in R^n \times R^m \times I$ , satisfies the Lipschitz condition by  $x$ , i.e.

$$|f(x, u, t) - f(y, u, t)| \leq l(t) |x - y|, \tag{1.7}$$

$$\forall (x, u, t), (y, u, t) \in R^n \times R^m \times I$$

and the condition

$$|f(x, u, t)| \leq c_0(|x| + |u|^2) + c_1(t), \tag{1.8}$$

$$\forall (x, u, t),$$

where  $l(t) \geq 0$ ,  $l(t) \in L_1(I, R^1)$ ,  $c_0 = const > 0$ ,  $c_1(t) \geq 0$ ,  $c_1(t) \in L_1(I, R^1)$ .

The vector function  $F(x, t) = (F_1(x, t), \dots, F_s(x, t))$  is continuous with respect to the variables  $(x, t) \in R^n \times I$ . Function  $f_0(x, u, x_0, x_1, t) = (f_{01}(x, u, x_0, x_1, t), \dots, f_{0m_2}(x, u, x_0, x_1, t))$  satisfies the condition

$$|f_0(x, u, x_0, x_1, t)| \leq c_2(|x| + |u|^2 + |x_0| + |x_1|) + c_3(t),$$

$$\forall (x, u, x_0, x_1, t), (y, u, x_0, x_1, t) \in R^n \times R^m \times R^n \times R^n \times I,$$

$$c_2 = const \geq 0, c_3(t) \geq 0, c_3(t) \in L_1(I, R^1).$$

Scalar function  $F_0(x, u, x_0, x_1, t)$  is defined and continuous with respect to the variables together with partial derivatives by variables  $(x, u, x_0, x_1)$ ,  $\omega(t)$ ,  $\varphi(t)$ ,  $t \in I$  are given  $s$  – dimensional functions.  $S$  is given bounded convex closed set of  $R^{2n}$ , the time moments  $t_0, t_1$  are fixed.

In particular, the set  $S = \{(x_0, x_1) \in R^{2n} / H_j(x_0, x_1) \leq 0, j = \overline{1, p_1}; < a_j, (x_0, x_1) > = 0, j = \overline{p_1 + 1, p_2}\}$ , where  $H_j(x_0, x_1)$ ,  $j = \overline{1, p_1}$  are convex functions,  $a_j \in R^{2n}$ ,  $j = \overline{p_1 + 1, p_2}$  are given vectors.

Note, that if the conditions (1.7), (1.8) are satisfied for any control  $u(\cdot) \in L_2(I, R^m)$  and the initial condition  $x(t_0) = x_0$  of the differential equation (1.2) has a unique solution  $x(t)$ ,  $t \in I$ . This solution has derivative  $\dot{x} \in L_2(I, R^n)$  and satisfies equation (1.2) for almost all  $t \in I$ .

It should be noted that integral constraints

$$g_j(u(\cdot), x_0, x_1) = \int_{t_0}^{t_1} f_{0j}(x(t), u(t), x_0, x_1, t) dt \leq 0, \tag{1.9}$$

$$j = \overline{1, m_1},$$

by introducing additional variables  $d_j \geq 0$ ,  $j = \overline{1, m_1}$ , can be written in the form

$$g_j(u(\cdot), x_0, x_1) = -d_j, j = \overline{1, m_1}.$$

Let the vector be  $\bar{c} = (-d_1, \dots, -d_{m_1}, 0, 0, \dots, 0) \in R^{m_2}$ , where  $d_j \geq 0$ ,  $j = \overline{1, m_1}$ . Let a set be  $Q = \{\bar{c} \in R^{m_2} / d_j \geq 0, j = \overline{1, m_1}\}$ , where  $d_j \geq 0$ ,  $j = \overline{1, m_1}$  are unknown numbers.

**Definition 1.1.** The triple  $(u_*(t), x_0^*, x_1^*) \in U \times S_0 \times S_1$  is called by admissible control for the problem (1.1) – (1.6), if the boundary problem (1.2) – (1.6) has a solution. A set of all admissible controls is denoted by  $\Sigma$ ,  $\Sigma \subset U \times S_0 \times S_1$ .

From this definition it follows that for each element of the set  $\Sigma$  the following properties are satisfied: 1) the solutions  $x_*(t)$ ,  $t \in I$  of the differential equation (1.2), issuing from the point  $x_0^* \in S_0$ , satisfy the condition  $x_*(t_1) = x_1^* \in S_1$ , and

also  $(x_0^*, x_1^*) \in S_0 \times S_1 = S$ ; 2) the inclusion  $x_*(t) \in G(t)$ ,  $t \in I$  holds; 3) for each element of the set  $\Sigma$  we have the equality  $g(u(\cdot), x_0, x_1) = \bar{c}$ , where

$$g(u_*(\cdot), x_0^*, x_1^*) = (g_1(u_*(\cdot), x_0^*, x_1^*), \dots, g_{m_2}(u_*(\cdot), x_0^*, x_1^*)).$$

The following problems are set:

**Problem 1.2.** Find the necessary and sufficient conditions for the existence of a solution of the boundary value problem (1.2) – (1.6).

Note, that the optimal control problem (1.1) – (1.6) has a solution if and only if the boundary value problem (1.2) – (1.6) has a solution.

**Problem 1.3.** Find an admissible control  $(u_*(t), x_0^*, x_1^*) \in \Sigma \subset U \times S_0 \times S_1$ .

If problem 1 has a solution, then there exists an admissible control.

**Problem 1.4.** Find the optimal control  $\bar{u}_*(t) \in U(t)$ , the point  $(\bar{x}_0^*, \bar{x}_1^*) \in S_0 \times S_1 = S$  and the optimal trajectory  $\bar{x}_*(t; t_0, \bar{x}_0^*)$ ,  $t \in I$ ,

where  $\bar{x}_*(t) \in G(t)$ ,  $t \in I$ ,  $\bar{x}_*(t_1) = \bar{x}_1^* \in S_1$ ,

$$g_j(\bar{u}_*(\cdot), \bar{x}_0^*, \bar{x}_1^*) \leq 0, \quad j = \overline{1, m_1},$$

$$g_j(\bar{u}_*(\cdot), \bar{x}_0^*, \bar{x}_1^*) = 0, \quad j = \overline{m_1 + 1, m_2},$$

$$J(\bar{u}_*(\cdot), \bar{x}_0^*, \bar{x}_1^*) = \inf J(\bar{u}(\cdot), \bar{x}_0^*, \bar{x}_1^*),$$

$$\forall (\bar{u}(\cdot), \bar{x}_0^*, \bar{x}_1^*) \in L_2(I, R^m) \times S_0 \times S_1.$$

One of the methods for solving the problem of variation calculus is the Lagrange principle. The Lagrange principle allows to reduce the solution of the original problem to the search for an extremum of the Lagrange functional obtained by introducing auxiliary variables (Lagrange multipliers).

In the classical variation calculus, it is assumed that the solution of the differential equation (1.2) belongs to the space  $C^1(I, R^n)$  and the control  $u(t)$ ,  $t \in I$  of the space  $C(I, R^m)$  in the optimal control problems [5], the solution  $x \in KC^1(I, R^n)$  and control  $u(t) \in KC^1(I, R^m)$ . In this paper, the control  $u(t)$ ,  $t \in I$  is chosen from  $L_2(I, R^m)$ , and the solution  $x(t)$ ,  $t \in I$  is an absolutely continuous function on the interval  $I = [t_0, t_1]$ . For this case, the existence and uniqueness of the solutions of the initial problem for equation (1.2) are presented in the references [4, 6, 7, 8].

The purpose of this paper is to create a method for solving the problem of the variation calculus for processes described by ordinary differential

equations with phase and integral constraints that differ from the known methods based on the Lagrange principle. It is a continuation of the scientific research presented in [9, 10].

### The immersion principle

Let the vector function be  $f_0(x, u, x_0, x_1, t) = (f_{01}(x, u, x_0, x_1, t), \dots, f_{0m_2}(x, u, x_0, x_1, t))$ . We introduce the vector function  $\eta(t) = (\eta_1(t), \dots, \eta_{m_2}(t))$ ,

$$t \in I \text{ as } \eta(t) = \int_{t_0}^t f_0(x(\tau), u(\tau), x_0, x_1, \tau) d\tau, \quad t \in I.$$

It follows that

$$\dot{\eta}(t) = f_0(x(t), u(t), x_0, x_1, t),$$

$$\begin{aligned} \eta(t_0) &= 0, \quad \eta(t_1) = \\ &= \bar{c} \in Q, \quad (x_0, x_1) \in S, \quad u(t) \in L_2(I, R^m), \\ &\quad x(t) \in G(t). \end{aligned}$$

Now the optimal control problem (1.1) – (1.6) is written in the form: minimize the functional

$$\begin{aligned} J(u(\cdot), x_0, x_1) = \\ = \int_{t_0}^{t_1} F_0(x(t), u(t), x_0, x_1, t) dt \rightarrow \inf \end{aligned} \quad (2.1)$$

at conditions

$$\dot{x} = A(t)x + B(t)f(x, u, t), \quad t \in I, \quad (2.2)$$

$$\dot{\eta}(t) = f_0(x(t), u(t), x_0, x_1, t), \quad t \in I, \quad (2.3)$$

$$\begin{aligned} (x_0, x_1) &\in S = S_0 \times S_1, \\ \eta(t_0) &= 0, \quad \eta(t_1) = \bar{c} \in Q, \end{aligned} \quad (2.4)$$

$$x(t) \in G(t), \quad u(\cdot) \in L_2(I, R^m), \quad t \in I. \quad (2.5)$$

Note, that the problems (1.1) – (1.6) and (2.1) – (2.5) are equivalent. We introduce the following vectors and matrices

$$\xi = \begin{pmatrix} x \\ \eta \end{pmatrix}, \quad A_1(t) = \begin{pmatrix} A(t) & O_{n, m_2} \\ O_{m_2, n} & O_{m_2, m_2} \end{pmatrix},$$

$$B_1(t) = \begin{pmatrix} B(t) \\ O_{m_2, r} \end{pmatrix}, \quad B_2 = \begin{pmatrix} O_{n, m_2} \\ I_{m_2} \end{pmatrix},$$

$$\xi(t_0) = \begin{pmatrix} x(t_0) = x_0 \\ \eta(t_0) = 0 \end{pmatrix} = \xi_0, \quad \xi(t_1) = \begin{pmatrix} x(t_1) = x_1 \\ \eta(t_1) = \bar{c} \end{pmatrix},$$

$$P_1 = (I_n, O_{n, m_2}),$$

where  $O_{k,q}$  is a rectangular matrix of order  $k \times q$  with zero elements,  $I_n$  is the unit matrix of order  $n \times n$ .

Then the optimal control problem (2.1) – (2.5) has the form: minimize the functional

$$J(u(\cdot), x_0, x_1) = \int_{t_0}^{t_1} F_0(P_1 \xi(t), u(t), x_0, x_1, t) dt \rightarrow \inf \quad (2.6)$$

at conditions

$$\dot{\xi} = A_1(t)\xi + B_1(t)f(P_1 \xi, u, t) + B_2 f_0(P_1 \xi, u, x_0, x_1, t), \quad (2.7)$$

$$\xi(t_0) = \xi_0 \in S_0 \times O_{m_2, 1}, \quad \xi(t_1) = \xi_1 \in S_1 \times Q, \quad (2.8)$$

$$P_1 \xi(t) \in G(t), \quad u(\cdot) \in L_2(I, R^m), \quad \bar{c} \in Q. \quad (2.9)$$

Let a set be

$$\Gamma = \{d \in R^m / d \geq 0\}. \quad (2.10)$$

We consider a linear controllable system

$$\dot{y} = A_1(t)y + B_1(t)w_1(t) + B_2 w_2(t), \quad t \in I, \quad (2.11)$$

$$w_1(\cdot) \in L_2(I, R^r), \quad w_2(\cdot) \in L_2(I, R^{m_2}), \quad (2.12)$$

$$y(t_0) = \xi(t_0) = \xi_0 \in S_0 \times O_{m_2, 1},$$

$$y(t_1) = \xi(t_1) = \xi_1 \in S_1 \times Q. \quad (2.13)$$

The bases of the immersion principle are the following theorems on the properties of the solution of the Fredholm integral equation of the first kind

$$Ku = \int_{t_0}^{t_1} K(t_0, t)u(t)dt = a, \quad (2.14)$$

where  $K : L_2(I, R^k) \rightarrow R^{n_1}$ ,  $K(t_0, t)$  is a given matrix of order  $n_1 \times k$  with piecewise-continuous elements by  $t$  for each fixed  $t_0$ ,  $t_0 \in \Delta_0 \subset R^1$ ,  $t_1 \in \Delta_1 \subset R^1$ ,  $\Delta_0 \cap \Delta_1 = \emptyset$ ,  $\emptyset$  is an empty set,  $a \in R^{n_1}$  is any given vector,  $u(\cdot) \in L_2(I, R^k)$  is the origin function.

**Theorem 2.1.** *The integral equation (2.14) for any fixed  $a \in R^{n_1}$  has a solution if and only if the matrix*

$$C(t_0, t_1) = \int_{t_0}^{t_1} K(t_0, t)K^*(t_0, t)dt, \quad (2.15)$$

*of order  $n_1 \times n_1$  is positive definite, where (\*) is a transposition sign.*

**Theorem 2.2.** *Let the matrix  $C(t_0, t_1)$  be positive definite. Then the general solution of the integral equation (2.14) has the form*

$$u(t) = K^*(t_0, t)C^{-1}(t_0, t_1)a + v(t) - K^*(t_0, t)C^{-1}(t_0, t_1) \int_{t_0}^{t_1} K(t_0, t)v(t)dt, \quad t \in I, \quad (2.16)$$

where  $v(\cdot) \in L_2(I, R^k)$  is an arbitrary function,  $a \in R^{n_1}$  is any vector.

The proofs of Theorems 2.1. and 2.2. are given in [9, 10].

Let the matrix  $B_3(t) = (B_1(t), B_2)$  of order  $(n + m_2) \times (m_2 + r)$ , and a vector function  $w(t) = (w_1(t), w_2(t)) \in L_2(I, R^{r+m_2})$ . It is easy to verify that the control  $w(\cdot) \in L_2(I, R^{r+m_2})$ , which takes the trajectory of the system (2.9) from any initial state  $\xi_0$  to any desired final state  $\xi_1$ , is a solution of the integral equation

$$\int_{t_0}^{t_1} \Phi(t_0, t)B_3(t)w(t)dt = a, \quad (2.17)$$

where  $\Phi(t, \tau) = \lambda(t)\lambda^{-1}(\tau)$ ,  $\lambda(t)$  is a fundamental matrix of solutions of linear homogeneous system  $\dot{\rho} = A_1(t)\rho$ , the vector

$$a = a(\xi_0, \xi_1) = \Phi(t_0, t_1)\xi_1 - \xi_0. \quad (2.18)$$

As follows from (2.14), (2.17), the matrix  $K(t_0, t) = \Phi(t_0, t)B_3(t)$ , at  $n_1 = n + m_2$ ,  $k = r + m_2$ . For the integral equation (2.15) the statements of Theorems 2.1. and 2.2. are applicable. From the initial data of the system (2.11) – (2.13) we define the following matrices and vectors

$$\begin{aligned} T(t_0, t_1) &= \int_{t_0}^{t_1} \Phi(t_0, t)B_3(t)B_3^*(t)\Phi^*(t_0, t)dt = \\ &= \int_{t_0}^{t_1} K(t_0, t)K^*(t_0, t)dt = C(t_0, t_1), \end{aligned}$$

$$\begin{aligned} \Lambda_1(t, \xi_0, \xi_1) &= B_3^*\Phi^*(t_0, t)T^{-1}(t_0, t_1)a = \\ &= K^*(t_0, t_1)C^{-1}(t_0, t_1)a = \\ &= \begin{pmatrix} B_1^*(t)\Phi^*(t_0, t)T^{-1}(t_0, t_1)a \\ B_2^*\Phi^*(t_0, t)T^{-1}(t_0, t_1)a \end{pmatrix}, \end{aligned}$$

$$\begin{aligned} N_1(t) &= -B_3^*(t)\Phi^*(t_0, t)T^{-1}(t_0, t_1)\Phi(t_0, t_1) = \\ &= -K^*(t_0, t)C(t_0, t_1)\Phi(t_0, t_1) = \\ &= \begin{pmatrix} -B_1^*(t)\Phi^*(t_0, t)T^{-1}(t_0, t_1)\Phi(t_0, t_1) \\ -B_2^*\Phi^*(t_0, t)T^{-1}(t_0, t_1)\Phi(t_0, t_1) \end{pmatrix} = \begin{pmatrix} N_{11}(t) \\ N_{12}(t) \end{pmatrix}, \end{aligned}$$

$$\begin{aligned} \Lambda_2(t, \xi_0, \xi_1) &= \Phi(t, t_0)T(t, t_1)T^{-1}(t_0, t_1)\xi_0 + \\ &+ \Phi(t, t_0)T(t_0, t)T^{-1}(t_0, t_1)\Phi(t_0, t_1)\xi_1, \end{aligned}$$

$$\begin{aligned} N_2(t) &= -\Phi(t, t_0)T(t_0, t)T^{-1}(t_0, t_1)\Phi(t_0, t_1), \\ &t \in T, \end{aligned}$$

$$\begin{aligned} T(t, t_1) &= \int_t^{t_1} \Phi(t_0, \tau)B_3(\tau)B_3^*(\tau)\Phi^*(t_0, \tau)d\tau, \\ T(t_0, t) &= T(t_0, t_1) - T(t, t_1), \quad t \in I, \end{aligned}$$

where the vector  $a$  is defined by formula (2.16).

**Theorem 2.3.** Let the matrix be  $T(t_0, t_1) > 0$ .

Then the control

$w(\cdot) = (w_1(\cdot), w_2(\cdot)) \in L_2(I, R^{r+m_2})$  transforms the trajectory of the system (2.11) – (2.13) from the initial point  $\xi_0 \in S_0 \times O_{m_2,1}$  to the final state  $\xi_1 \in S_1 \times Q$  if and only if

$$\begin{aligned} w_1(t) \in W_1 &= \{w_1(\cdot) \in L_2(I, R^r) / w_1(t) = \\ &= v_1(t) + B_1^*(t)\Phi^*(t_0, t)T^{-1}(t_0, t_1)a + \\ &+ N_{11}(t)z(t_1, v), \end{aligned} \quad (2.19)$$

$$t \in I, \quad \forall v_1(\cdot), \quad v_1(\cdot) \in L_2(I, R^r)\},$$

$$\begin{aligned} w_2(t) \in W_2 &= \{w_2(\cdot) \in L_2(I, R^{m_2}) / w_2(t) = \\ &= v_2(t) + B_2^*\Phi^*(t_0, t)T^{-1}(t_0, t_1)a + \\ &+ N_{12}(t)z(t_1, v), \end{aligned} \quad (2.20)$$

$$t \in I, \quad \forall v_2(\cdot), \quad v_2(\cdot) \in L_2(I, R^{m_2})\},$$

where  $v(t) = (v_1(t), v_2(t))$ ,  $v_1(\cdot) \in L_2(I, R^r)$ ,  $v_2(\cdot) \in L_2(I, R^{m_2})$  are arbitrary functions. The function  $z(t, v) = z(t, v_1, v_2)$ ,  $t \in I$  is the solution of the differential equation

$$\begin{aligned} \dot{z} &= A_1z + B_1(t)v_1(t) + B_2v_2(t), \\ z(t_0) &= 0, \quad t \in I, \end{aligned} \quad (2.21)$$

$$v_1(\cdot) \in L_2(I, R^r), \quad v_2(\cdot) \in L_2(I, R^{m_2}). \quad (2.22)$$

The solution of the differential equation (2.11) corresponding to the control (2.19), (2.20) has the form

$$\begin{aligned} y(t) &= z(t) + \Lambda_2(t, \xi_0, \xi_1) + N_2(t)z(t_1, v), \\ &t \in I, \end{aligned} \quad (2.23)$$

where  $z(t) = z(t_1, v)$ ,  $t \in I$ .

**Proof.** The proof of the theorem follows from Theorems 2.1. and 2.2. As follows from the above, the solution of the boundary value problem (2.11) – (2.13) reduces to finding the general solution of the integral equation (2.17). The integral equation (2.17) is a particular case of (2.14), where  $K(t_0, t) = \Phi(t_0, t)B_3(t)$ . Further, by replacing  $K(t_0, t)$  on  $\Phi(t_0, t)B_3(t)$  we get  $C(t_0, t_1) = T(t_0, t_1)$  (see (2.15)). From (2.16) follows (2.19), (2.20). The differential equation (2.21) with control (2.22) and relation (2.23) follows directly from formulas

$$z(t, v) = \int_{t_0}^t \Phi(t, \tau) B_3(\tau) v(\tau) d\tau,$$

$$z(t_1, v) = \Phi(t_1, t_0) \int_{t_0}^{t_1} \Phi(t_0, t) B_3(t) v(t) dt.$$

It is easy to see, that  $y(t_0) = \xi_0$ ,  $y(t_1) = \xi_1$ . The theorem is proved.

Note, that: 1) the sets  $W_1 = W_1(t) \subset L_2(I, R^r)$ ,  $W_2 = W_2(t) \subset L_2(I, R^{m_2})$  contain all sets of the functions  $w_1(t)$ ,  $w_2(t)$ ,  $t \in I$ , for which the boundary value problem (2.11) – (2.13) has a solution; 2)  $w_1(t) \in W_1$ ,  $w_2(t) \in W_2$ , then the solution of the system (2.11) – (2.13) is defined by formula (2.23); 3) outside sets  $W_1$ ,  $W_2$  there are no controls for which the boundary value problem (2.11) – (2.13) has a solution; 4) Theorem 2.3. allows to replace the boundary value problem (2.11) – (2.13) by the initial problem (2.21) – (2.23).

**Lemma 2.4.** Let the matrix be  $T(t_0, t_1) > 0$ . Then the boundary problem (2.7) – (2.10) is equivalent to the following problem

$$w_1(t) \in W_1, w_1(t) = f(P_1 y(t), u(t), x_0, x_1, t),$$

$$t \in I, \quad (2.24)$$

$$w_2(t) \in W_2, w_2(t) = f_0(P_1 y(t), u(t), x_0, x_1, t),$$

$$t \in I, \quad (2.25)$$

$$p(t) = F(P_1 y(t), t) \in V = V(t) = \{p(\cdot) \in L_2(I, R^s) / \omega(t) \leq p(t) \leq \phi(t), t \in I\}, \quad (2.26)$$

$$\dot{z} = A_1(t)z + B_1(t)v_1(t) + B_2 v_2(t), z(t_0) = 0, t \in I, \quad (2.27)$$

$$v_1(\cdot) \in L_2(I, R^r), v_2(\cdot) \in L_2(I, R^{m_2}), \quad (2.28)$$

$$(x_0, x_1) \in S_0 \times S_1 = S \subset R^{2n},$$

$$u(\cdot) \in L_2(I, R^m), d \in \Gamma, \quad (2.29)$$

where the function  $y(t)$ ,  $t \in I$  is defined by the formula (2.23).

**Proof.** Lemma 2.4. states, that the boundary value problem (2.7) – (2.10) has a solution if and only if the relations (2.24) – (2.29) are satisfied.

In fact, if the relations (2.24) – (2.29) are held, then  $y(t) = \xi(t)$ ,  $t \in I$ , moreover  $y(t_0) = \xi(t_0) = \xi_0$ ,  $y(t_1) = \xi(t_1) = \xi_1$  and the inclusions (2.9), (2.10) are satisfied.

We suppose, that the boundary value problem (2.7) – (2.10) has a solution. It is possible if and only if  $f(P_1 \xi(t), u(t), t) \in W_1$ ,  $f_0(P_1 \xi(t), u(t), x_0, x_1, t) \in W_2$  by Theorem 2.3. These inclusions are equivalent to equalities (2.24), (2.25), where  $z(t)$ ,  $t \in I$  – is a solution of the differential equation (2.27) with controls (2.28). The inclusion  $P_1 \xi(t) \in G(t)$ ,  $t \in I$  has the form (2.26), and the relations (2.9), (2.10) are written in the form (2.29). The lemma is proved.

**Lemma 2.5.** Let the matrix be  $T(t_0, t_1) > 0$ . Then the boundary value problem of optimal control with constraints (1.1) – (1.6) is equivalent to the following problem: minimize the functional

$$I(u(\cdot), p(\cdot), v_1(\cdot), v_2(\cdot), x_0, x_1, d) =$$

$$= \int_{t_0}^{t_1} F_0(P_1 y(t), u(t), x_0, x_1, t) dt \rightarrow \inf \quad (2.30)$$

at conditions

$$\begin{aligned}
I_1(u(\cdot), p(\cdot), v_1(\cdot), v_2(\cdot), x_0, x_1, d) = \\
= \int_{t_0}^{t_1} F_1(q(t), t) dt = \int_{t_0}^{t_1} [|w_1(t) - \\
-f(P_1 y(t), u(t), t)|^2 + |w_2(t) - \\
-f_0(P_1 y(t), u(t), x_0, x_1, t)|^2 + \\
+ |p(t) - F(P_1 y(t), t)|^2] dt = 0,
\end{aligned} \quad (2.31)$$

$$\begin{aligned}
\dot{z} = A_1(t)z + B_1(t)v_1(t) + B_2 v_2(t), \\
z(t_0) = 0, t \in I,
\end{aligned} \quad (2.32)$$

$$v_1(\cdot) \in L_2(I, R^r), v_2(\cdot) \in L_2(I, R^{m_2}), \quad (2.33)$$

$$\begin{aligned}
(x_0, x_1) \in S_0 \times S_1 = S \subset R^{2n}, \\
p(t) \in V(t), u(\cdot) \in L_2(I, R^m), d \in \Gamma,
\end{aligned} \quad (2.34)$$

where  $w_1(t) \in W_1$ ,  $w_2(t) \in W_2$ , the function  $y(t)$ ,  $t \in I$  is defined by the formula (2.23).

**Proof.** The proof follows from Lemma 2.4. The value of the functional  $I_1 \geq 0$ . The functional  $I_1 = 0$  if and only if the equalities (2.24) – (2.26) are satisfied, relations (2.27) – (2.29) coincide with (2.31) – (2.33). The functional (1.1) can be written in the form (2.30). The lemma is proved.

The function

$$\begin{aligned}
F_1(q(t), t) = \\
= |w_1(t) - f(P_1 y(t), u(t), x_0, x_1, t)|^2 + \\
+ |w_2(t) - f_0(P_1 y(t), u(t), x_0, x_1, t)|^2 + \\
+ |p(t) - F(P_1 y(t), t)|^2,
\end{aligned}$$

where  $w_1(t) \in W_1$ ,  $w_2(t) \in W_2$ ,

$$y(t) = z(t, v) + \Lambda_2(t, \xi_0, \xi_1) + N_2(t)z(t_1, v), t \in I,$$

$$q(t) = (z(t, v), z(t_1, v), u(t), p(t), v_1(t), v_2(t), x_0, x_1, d)$$

Note, that:

1) Since the initial problem (1.1) – (1.6) is equivalent to (2.30) – (2.33), that the problem (1.1) – (1.6) has a solution if and only if the relations (2.30) – (2.33) are satisfied;

2) Since the value  $I_1 \geq 0$ , that for the existence of a solution of the boundary value problem (1.2) – (1.6) it is necessary and sufficient that  $\inf I_1(u, p, v_1, v_2, x_0, x_1, d) = 0$  under the conditions (2.27) – (2.29).

3) The transition from the original boundary value problem (1.2) – (1.6) to the initial optimal control problem  $I_1(u, p, v_1, v_2, x_0, x_1, d) \rightarrow \inf$  under the conditions (2.27) – (2.29) is called the immersion principle.

### Conclusion

The Lagrange problem of the variation calculus is investigated in the presence of phase and integral constraints for processes described by ordinary differential equations. The particular cases of which are the simplest problem, the Bolz problem, the isoperimetric problem, the conditional extremum problem.

The main scientific results are:

- reduction of the boundary value problem connected to the conditions in the Lagrange problem to the initial optimal control problem with a specific functional;
- necessary and sufficient conditions for the existence of the admissible control;
- method of constructing an admissible control on the limit point of the minimizing sequence;

The scientific novelty of the results is that: there is no need to introduce additional variables in the form of Lagrange multipliers; proof of the existence of a saddle point of the Lagrange functional.

### References

1. Bliss Dzh. “Lectures on variation calculus.” (M.: IL, 1950), 348.
2. Lavrentev M.A., Lyusternik L.A. “Basics of variation calculus.” ONTI 1 (1935): 148-400.
3. Yang L. “Lectures on variation calculus and optimal control theory.” Mir (1974): 488.
4. Alekseev V.M., Tihomirov V.M., Fomin S.V. “Optimal control.” Nauka (1979): 430.
5. Pontryagin L.S., Boltyanskiy V.G., Gamkrelidze R.V., Mischenko E.F. “Mathematical theory of optimal processes.” Nauka (1969): 384.

6. Varga Dzh. "Optimal control by differential and functional equations." Nauka (1977): 624.
7. Gamkrelidze R.V. "Basics of optimal control." (Tbilisi: Izd-vo Tbilisskogo n-ta, 1977), 253.
8. Li Ya.B., Markus L. "Basics of the optimal control theory." Nauka (1972): 574.
9. Aysagaliev S.A., Sevryugin I.V. "Controlability and speed of the process described by linear system of ordinary differential equations." Mathematical journal 13, no. 2(4) (2013): 5–30.
10. Aysagaliev S.A., Kabidoldanova A.A. "Optimal control by dynamic systems." Palmarium Academic Publishing (Verlag, Germany, 2012): 288.

IRSTI 27.29.23

A. Bountis

Nazarbayev University, Department of Mathematics,  
School of Science and Technology,  
Astana, Kazakhstan, e-mail: anastasios.bountis@nu.edu.kz

### Complex Dynamics and Statistics in Hamiltonian 1-Dimensional Lattices

**Abstract.** In this paper I review in a brief and introductory way some important developments in the analysis of the dynamics and statistics of  $N$  – dimensional Hamiltonian systems, in which my research team and I have played an important role over the last two decades. The results I describe here have helped us understand the surprising importance of simple periodic orbits and their local stability properties in revealing crucial dynamical and statistical properties of the systems as a whole. This has led us to introduce the concepts of “strong” and “weak” chaos that are expected to play a significant role in better understanding the complexity of these multi-dimensional systems, which have important applications in solid state, field theory, superconductivity and more recently nonlinear optics.

**Key words:**  $N$  – dimensional Hamiltonian systems, superconductivity, nonlinear optics.

#### Introduction

Let us consider the 2- degree of freedom Hamiltonian system:

$$H = H_0 + \varepsilon H_1 = \frac{1}{2}(p_x^2 + p_y^2) + \frac{1}{4}(x^4 + y^4) + \varepsilon x^2 y^2 \quad (1)$$

Its solutions for  $\varepsilon = 0$  (the uncoupled case), plotted as intersection points on a Poincare surface of section of the 4 – dimensional space, are shown as a family of smooth closed curves in the graph on Figure 1.

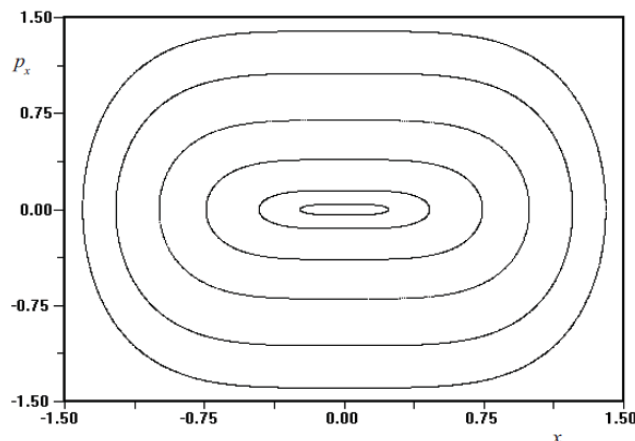


**Figure 1** – A surface of section plot on the plane  $x(t_k), p_x(t_k)$ , (every time  $y(t_k)=0$ ). All orbits are obtained for the same constant value of the Hamiltonian,  $H=E$

It is important to note that in this integrable (separable) case, all solutions correspond to periodic and quasiperiodic orbits with two frequencies  $\omega_1$  and  $\omega_2$  belonging to the two uncoupled oscillators in (1). Thus, if  $\omega_1$  and  $\omega_2$  are rationally related, i.e.  $\omega_1 / \omega_2 = m/n$  ( $m, n$  positive integers) the corresponding closed curves in Figure 1 are filled with periodic orbits, while if  $\omega_1 / \omega_2 =$  irrational, the curves are filled by a single initial condition by an orbit that never closes and is called a quasiperiodic solution.

Let us now make  $\varepsilon > 0$ , e.g.  $\varepsilon=0.02$ . What we discover is remarkable: While many smooth closed curves corresponding to  $\omega_1 / \omega_2 =$  irrational survive, those that correspond to  $\omega_1 / \omega_2 =$  rational have disappeared giving their place to chains of islands having a stable periodic orbit at their center and a chain of “saddle – like” regions where two pointed regions meet at an unstable periodic orbit of the same period, see Figure 2 below. Now if we magnify the region close to one of those unstable

periodic points shown in Figure 2(a) by an arrow, an amazingly complex network of islands, as well as small scale chaotic region that we will later identify with “weak chaos”, are revealed in Figure 2(b) below [1].

If we now further increase the value of  $\varepsilon$  to  $\varepsilon = 0.2$ , we observe in Figure 3, that the small scale chaotic regimes observed near unstable periodic orbits (saddle points) of Figure 2 have now grown considerably into domains that we will refer to as domains of “strong chaos” later in this paper. Although we don’t show it here, as one can imagine, increasing further the value of  $\varepsilon$ , the islands of stable periodic motion will diminish in size, while the strongly chaotic regimes will further increase, showing a tendency to occupy most of the available phase space. The same effect will occur, if we fix the value of  $\varepsilon > 0$  and start increasing the total energy  $E$  at which the surfaces of section are computed.

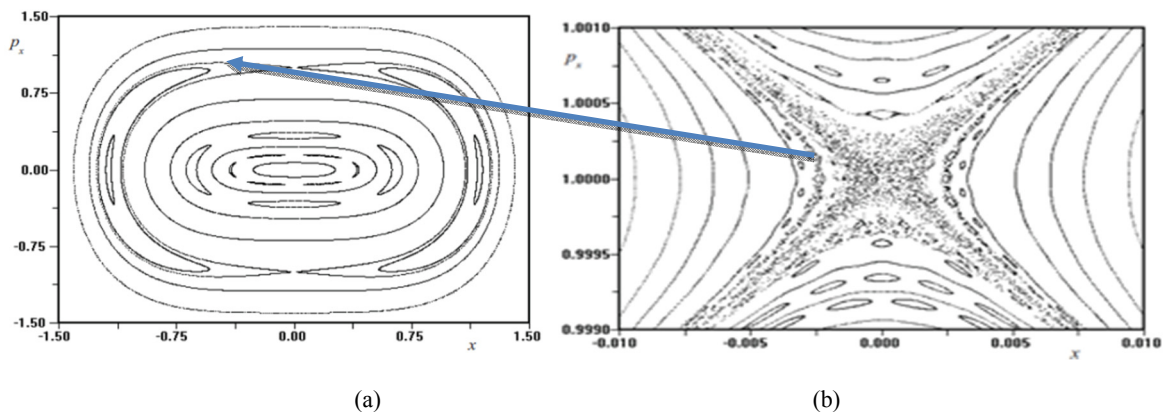


**Figure 2** (a) – The surface of section of Figure 1 showing orbit intersections in the plane  $x(t_k), p_x(t_k)$ , for  $\varepsilon=0.02$ . (b) A magnification of the region shown by the arrow in (a), where, besides the chains of small islands having stable periodic orbits at their center, one observes a region of randomly scattered points which constitute a “weakly chaotic” domain.

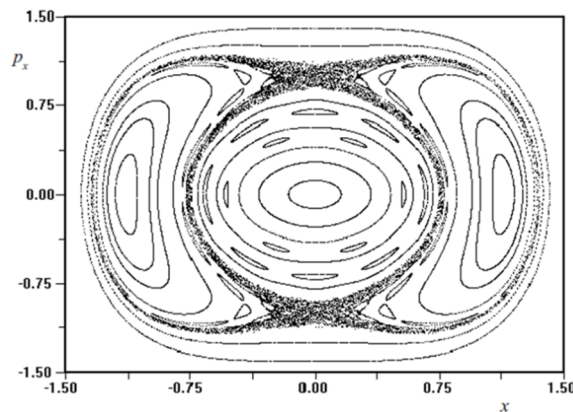


**Figure 3** – The surface of section of the orbits for  $\varepsilon=0.2$  and the same energy value  $E$  as in Figure 2. Note how the weakly chaotic domains of Figure 2 have grown to a much greater size forming regions that we will later

**Simple periodic orbits, weak and strong chaos**

We study Hamiltonian dynamical systems of  $N$  degrees of freedom (dof), in an  $2N$ -dimensional phase space of position and momentum coordinates, whose equations of motion are written in the form

$$\frac{dq_k}{dt} = \frac{\partial H}{\partial p_k}, \frac{dp_k}{dt} = -\frac{\partial H}{\partial q_k}, k = 1, 2, \dots, N, \quad (2)$$

where  $H$  is the Hamiltonian function. For more details on the results that follow in the present paper the reader is invited to consult [2].

If  $H$  does not explicitly depend on the time  $t$ , it represents a first integral, whose value gives the total energy of the system  $E$ . We will assume that the Hamiltonian can be expanded in *power series as a sum of homogeneous polynomials* of degree  $m \geq 2$ , so that the origin is a stable equilibrium point of the system:

$$H = H_2(q_1, \dots, q_N, p_1, \dots, p_N) + H_3(q_1, \dots, q_N) + \dots = E. \quad (3)$$

We now assume that  $H_m = 0$  for all  $m > 2$  and that the linear equations resulting from (2) and (3), yield a matrix, whose eigenvalues all occur in conjugate imaginary pairs,  $\pm i\omega_q$ , and thus provide the frequencies of the so-called normal mode oscillations of the linearized system.

$$H_2 = \sum_{q=1}^N E_q = E, E_q = \frac{1}{2} (P_q^2 + \omega_q^2 Q_q^2), \quad q = 1, 2, \dots, N, \quad (4)$$

where  $P_q, Q_q$  are the normal mode coordinates.

Then, according to a famous theorem by Lyapunov, if none of the ratios of these eigenvalues,  $\omega_j/\omega_k$  is rational, for any  $j, k = 1, 2, \dots, N, j \neq k$ , all linear normal modes continue to exist as periodic solutions of the nonlinear system.

If the frequencies for  $H_m \neq 0$  are close to those of the linear modes, the continuation of the linear modes are examples of simple periodic orbits (SPOs) of the nonlinear system, where all variables

oscillate with the same frequency. We shall mention below the spectrum of Lyapunov exponents, and will discuss how its properties are connected to the emergence of strongly (large scale) chaotic behavior in the solutions.

We will also describe the method of the Generalized Alignment Indices  $GALI_k, k=1, 2, \dots, 2N$ , which efficiently identify domains of chaos and order in  $N$  dof Hamiltonian systems and  $2N$ -dimensional ( $2N$ -D) symplectic maps.

**Indicators of regular and chaotic dynamics**

One of the most important questions in Hamiltonian dynamics concerns the connection between the local (linear) stability properties of simple periodic solutions of Hamiltonian systems, with the more “global” dynamics. We will examine this question using the one-dimensional lattice (or chain) of coupled oscillators called the Fermi Pasta Ulam  $\beta$ -model described by the  $N$  dof Hamiltonian

$$H = \frac{1}{2} \sum_{j=1}^N p_j^2 + \sum_{j=1}^N \frac{1}{2} (x_{j+1} - x_j)^2 + \frac{\beta}{4} \sum_{j=1}^N (x_{j+1} - x_j)^4 = E, \quad (5)$$

where  $x_j$  are the displacements of the particles from their equilibrium positions, and  $p_j = dx_j/dt$  are the momenta,  $\beta$  is a positive real constant and  $E$  is the total energy. Let us now consider some examples of simple periodic solutions (SPOs), which have well-defined symmetries and are known in closed form:

(I) the out of phase (pi-mode)

$$\hat{x}_j(t) = -\hat{x}_{j+1}(t) = \hat{x}(t), j = 1, 2, \dots, N \quad (6)$$

where  $N$  is even, under periodic boundary conditions;

(II) the SPO1 mode, where every 2 particles one is stationary and those on its either side move out of phase;

(III) the SPO2 mode, where every 3 particles one is stationary and the two on either side move out of phase both under fixed boundary conditions (fbc).

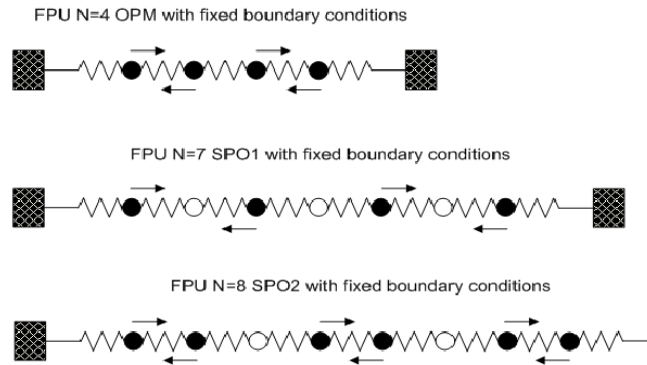


**Figure 4** – Examples of SPOs that we have called the Out of Phase (or pi-) Mode (above), the SPO1 orbit (middle) and the SPO2 orbit (below)

Applying Lyapunov's Theorem to the FPU system we can prove the existence of SPOs as continuations of the linear normal modes of the system, whose energies and frequencies are

$$E_q = \frac{1}{2} (P_q^2 + \omega_q^2 Q_q^2),$$

$$\omega_q = 2 \sin\left(\frac{\pi q}{2(N+1)}\right), \quad q = 1, 2, \dots, N \quad (7)$$

It is thus easy to verify that SPO1 and SPO2 orbits, as NNMs, are identified by the indices  $q = (N+1)/2$  and  $q = 2(N+1)/3$  respectively.

In fact, it is possible to formulate a semi-analytical criterion for “weak” chaos:

We have verified numerically that the above NNMs first destabilize at energy densities of the form

$$E_c/N \sim 1/N^\alpha, \quad \alpha=1,2, \text{ as } N \rightarrow \infty. \quad (8)$$

In agreement with an analytical criterion by Flach and co-workers [3],  $E_c/N \sim \pi^2/6\beta N^2$ , we find that for  $\alpha = 2$  orbits (like SPO2) instability implies “weak” chaos and the breakup of FPU recurrences. On the other hand, if  $\alpha = 1$ , for which the SPO1 mode destabilizes we find what we shall later call “strong” chaos. Indeed, we believe that (8) may be true for other NNM solutions as well, but so far no proof of this statement is available.

### Lyapunov exponents and “strong” chaos

Chaotic behavior is usually studied by evaluating the spectrum of Lyapunov exponents,  $L_i, i=1, \dots, 2N$ , (LEs)  $L_1=L_{max}>L_2>\dots>L_{2N}$ , defined as follows:

$$K_t^i = \frac{1}{t} \ln \frac{|w_i(t)|}{|w_i(0)|}, \quad i.e.$$

$$L_i = \lim_{t \rightarrow \infty} K_t^i, \quad i = 1, 2, \dots, 2N \quad (9)$$

where  $K_t^i$  represent rates of separation from the reference orbit of small deviations  $w_i(t)$  along the  $2N$  directions in phase space. If the maximum of these exponents  $L_{max} > 0$ , the orbit is chaotic, while if  $L_{max} = 0$  the orbit is stable. In the thermodynamic limit, where  $E \rightarrow \infty$  and  $N \rightarrow \infty$  (with  $E/N$  fixed), the Lyapunov spectrum near unstable NNMs tends to a smooth curve, see Figure 5(a) above [2].

For our two orbits SPO1 and SPO2, at low energies when they are unstable, we find that their Lyapunov spectra are distinct see Figure 5(b). Raising the energy, however, we observe in Figure 5(c) that the Lyapunov spectra converge to the same exponentially decreasing function  $L_i(N) \sim \exp(-ai/N), i=1,2,\dots,N$ , thus providing evidence that the orbits explore the same chaotic region.

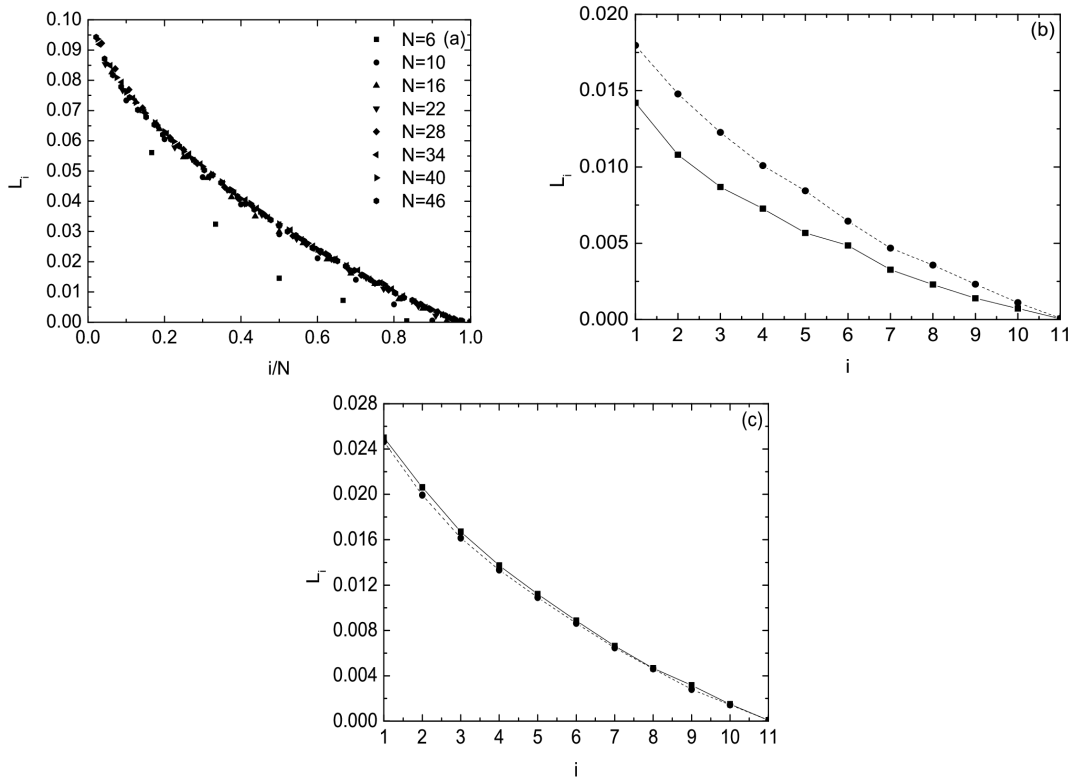


**Figure 5** – (a) The spectrum of Lyapunov exponents near an out of phase orbit of the  $\beta$  – FPU model as E and N grow ( $E/N=3/4$ ). In (b) and (c) the Lyapunov spectra of solutions starting near unstable SPO1 and SPO2 orbits converge, as the energy grows from  $E= 2.1$  in (b) to  $E=2.6$  for (c), indicating that the chaotic regions about these orbits have merged

**Beyond Lyapunov exponents: The Generalized Alignment Indices (GALI)**

As mentioned above, the Lyapunov exponents are always computed with respect to a *single deviation vector* from the reference orbit. More than a decade ago, however, several researchers [4, 5] introduced an alternative approach by defining as *the GALI indicators* quantities which take into account simultaneously 2, 3 or more deviations from the reference orbit, obtaining thus more comprehensive results, enabling us to: (a) detect the chaotic nature of the orbits more rapidly than other methods and, (b) identify quasiperiodic motion providing also the dimension of the torus.

The  $GALI_k$ ,  $k = 2, 3, \dots, N$  indicators are defined, through the evolution of  $k$  initially linearly independent deviation vectors  $w_i(0)$ , as the volume

of a  $k$ -parallelepiped given by the wedge product

$$GALI_k = \|\hat{w}_1(t) \wedge \hat{w}_2(t) \dots \wedge \hat{w}_k(t)\|, \quad i = 1, 2, \dots, k \tag{10}$$

whose  $k$  edges are the unitary deviations  $\hat{w}_i(t) = w_i(t)/\|w_i(t)\|$ . Thus, it is evident that if at least two of the deviation vectors become linearly dependent, the volume of the  $k$  – parallelepiped represented by the wedge product in (10) becomes zero, and the  $GALI_k$  vanishes. Thus, as expected, for chaotic orbits, deviation vectors tend to become linearly dependent in the direction defined by the maximal Lyapunov exponent. As an example of this effect, we show schematically in Figure 6 below how this happens in the case of the  $GALI_2$  indicator

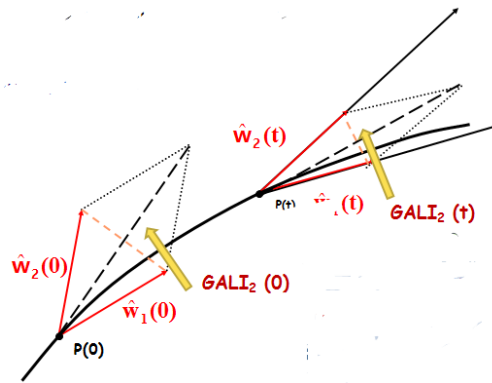


Figure 6 – Behavior of GALI<sub>2</sub> for chaotic motion

In fact, one can show analytically that in the case of chaotic orbits, all GALI<sub>k</sub> tend to zero exponentially for large t, following a detailed asymptotic argument analyzing the quantities (10) in determinants and keeping the most dominant terms as  $t \rightarrow \infty$  [2]. To see the main idea of how this is done, we show in the next subsection that  $GALI_2(t) \sim \exp[-(\sigma_1 - \sigma_2)t] \rightarrow 0$ ,  $\sigma_1 > \sigma_2$ , being approximations of the two largest Lyapunov exponents  $L_1 > L_2$ .

**Asymptotic analysis of the GALI<sub>2</sub> for chaotic motion**

The evolution of one deviation vector from a chaotic orbit can be approximated by the expression:

$$v_1(t) = \sum_{i=1}^{2n} c_i^{(1)} e^{\sigma_i t} \hat{e}_i \approx c_1^{(1)} e^{\sigma_1 t} \hat{e}_1 + c_2^{(1)} e^{\sigma_2 t} \hat{e}_2 + \dots \tag{9}$$

where  $\sigma_1 > \sigma_2 > \dots$  are approximate values of the Lyapunov exponents up to the time t of integration.

Thus, dividing this deviation by its magnitude we derive a leading order estimate for  $w_1(t)$ :

$$w_1 = \frac{v_1(t)}{|v_1(t)|} = \frac{c_1^{(1)} e^{\sigma_1 t} \hat{e}_1 + c_2^{(1)} e^{\sigma_2 t} \hat{e}_2}{|c_1^{(1)}| e^{\sigma_1 t}} = \pm \hat{e}_1 + \frac{c_2^{(1)}}{|c_1^{(1)}|} e^{-(\sigma_1 - \sigma_2)t} \hat{e}_2, \tag{10}$$

and an analogous expression for  $w_2(t)$ :

$$w_2 = \frac{v_2(t)}{|v_2(t)|} = \frac{c_1^{(2)} e^{\sigma_1 t} \hat{e}_1 + c_2^{(2)} e^{\sigma_2 t} \hat{e}_2}{|c_1^{(2)}| e^{\sigma_1 t}} = \pm \hat{e}_1 + \frac{c_2^{(2)}}{|c_1^{(2)}|} e^{-(\sigma_1 - \sigma_2)t} \hat{e}_2, \tag{11}$$

Taking their cross product gives the following result:

$$GALI_2 = |w_1(t) \wedge w_2(t)| \approx \left| \frac{c_2^{(1)}}{c_1^{(1)}} \pm \frac{c_2^{(2)}}{c_1^{(2)}} \right| e^{-(\sigma_1 - \sigma_2)t}, \tag{12}$$

which clearly demonstrates what we referred to above as exponential decrease of the GALIs to zero as t goes to infinity.

**Behavior of GALI<sub>2</sub> for regular motion**

It is also of great importance to analyze how GALIs will behave in time if they represent deviations of “ordered” or “regular” orbits, which have zero Lyapunov exponents and lie on tori of N – dimensional quasiperiodic motion in N dof Hamiltonian systems. Remarkably enough, all deviation vectors in that case become tangent to the torus, and, for a k -dimensional torus, the GALI of the associated k linearly independent vectors *will not go to zero* since the volume of the corresponding parallelepiped will *not vanish* (see a pictorial representation of this in Figure 7 below in the case of a 2 – dimensional torus).

We now make the following *very important observation*: As we just explained, in the case of regular orbits lying on s-dimensional tori, all

deviation vectors tend to fall on the tangent space of the torus. As a result, if we start with  $k \leq s$ , the deviation vectors will remain linearly independent on the tangent space of the torus and the  $GALI_k$  will be approximately constant, different from zero. Hence, for quasiperiodic motion, we find  $GALI_2(t) \approx \text{const. for all } t > 0$ .

Now, what is interesting is that if we start with  $k > s$  deviation vectors, since only  $s$  of them will in the end be linearly independent, the  $GALI$  will again go to zero, but this *time following a power law!* Clearly, this will be of great help in **identifying the actual dimension** of the torus, for which no other such criteria are available.

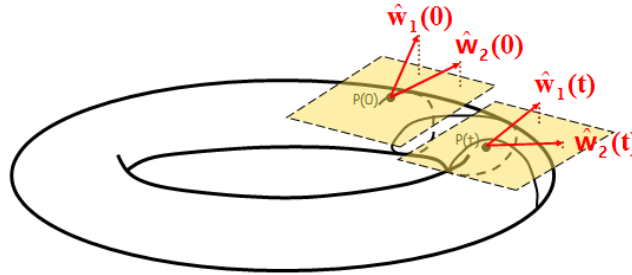


Figure 7 – Behavior of  $GALI_2$  for regular motion occurring on a 2-dimensional torus.

Summarizing, we have shown by asymptotic analysis that: (a) for a chaotic orbit, all deviation vectors tend to align in the direction of  $L_1$ , and all  $GALI_k$  tend to zero exponentially following the law

$$GALI_k \propto \exp(-(L_1 - L_2 + L_1 - L_3 + \dots + L_1 - L_k)t) \quad (13)$$

where  $L_i$  are the  $k$  largest LEs. (b) On the other hand, for  $k > s$ , all  $GALI_k$  approach 0 as  $t \rightarrow \infty$  following power laws,

$$GALI_k \propto \frac{1}{t^{k-s}}, s < k \leq 2N - s,$$

$$GALI_k \propto \frac{1}{t^{2(k-N)}}, 2N - s < k \leq 2N, \quad (14)$$

since some deviation vectors will eventually become linearly dependent. In Figure 8 below we display some applications of the above theory to the study of tori in a 2 dof and a 3 dof Hamiltonian system. In the former case the tori are 2 – dimensional and for this reason  $GALI_2$  tends to a constant while higher  $GALI$ s decay by power laws given by (14), while in the latter the tori are 3 – dimensional and, therefore, not only  $GALI_2$ , but also  $GALI_3$  go to zero following the power laws (14) presented above.

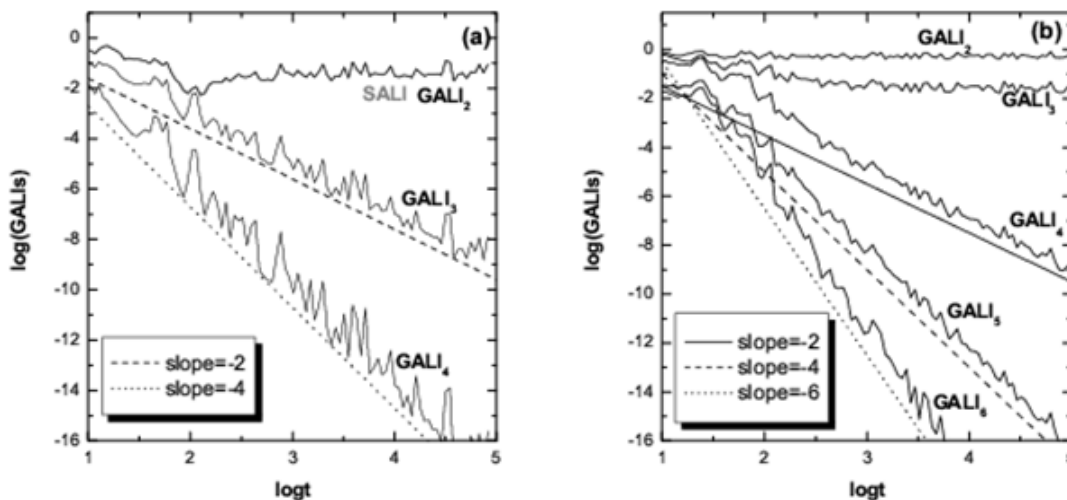


Figure 8 – The  $GALI$  indices for a Hamiltonian system of (a) 2 degrees of freedom and (b) 3 degrees of freedom. In case (a), since only  $GALI_2$  is constant the motion lies on a 2-dimensional torus, while in (b), where both  $GALI_2$  and  $GALI_3$  are constant, the torus is 3-dimensional

## Localization in 1-dimensional lattices

### Localization in Fourier space

In 1955, by E. Fermi, J. Pasta and S. Ulam (FPU) used the computers available at the Los Alamos National Laboratory to integrate a chain of 31 nonlinear oscillators, coupled to their nearest neighbors, and investigate how energy was shared by all normal modes of the system. Starting with

initial conditions placed on the  $q=1$  linear normal mode, they discovered, for small energies, a near-recurrence to their initial state after relatively short times exciting very few other modes, see Figure 9 (a) (for more explanations, the reader is again invited to consult the relevant chapters of [2]).

This remarkable observation ran contrary to the expectation of energy sharing among all modes predicted by equilibrium statistical mechanics and was termed the “paradox” of FPU recurrences.

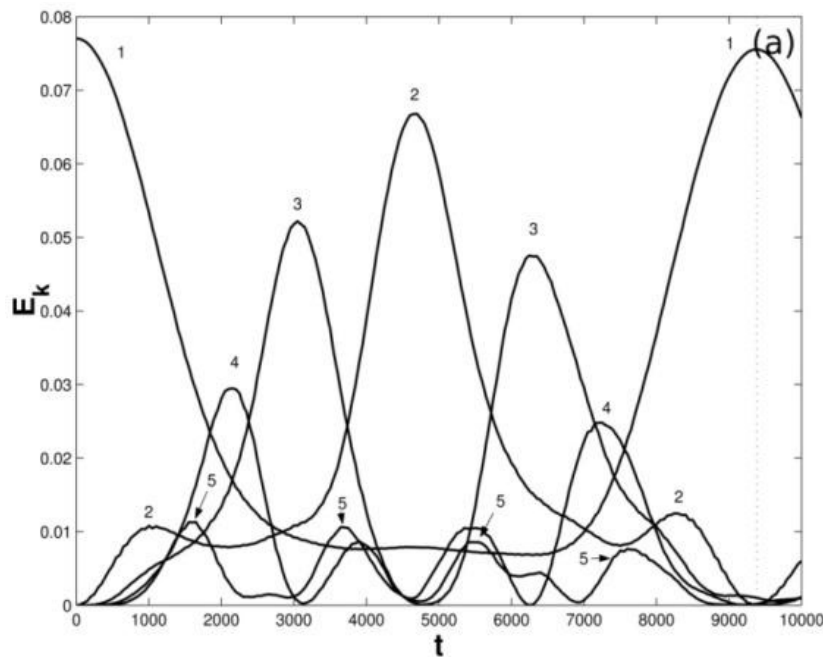


**Figure 9** – (a) Localization in modal space in the form of FPU recurrences, discovered by Fermi Pasta and Ulam, for a lattice of 31 particles

“Energy localization” here implies localization in Fourier  $q$ -modal space, as the FPU recurrences were observed when all the energy was placed in the  $q=1$  mode.

Flach and his co-workers, in 2005 [3] introduced the concept of  $q$ -breathers, as exact periodic solutions of the problem. They showed that if we excite a single low  $q$ -breather mode the total energy remains localized only within a few of these low frequency modes, also called metastable states or natural packets.

A more complete interpretation of the FPU paradox was provided by our group [6], where we introduced the concept of  $q$ -tori, reconciling

$q$ -breathers with the metastable packets of low-frequency modes. Now we shall use the GALI indices to study the stability of these  $q$ -tori and the breakdown of the associated FPU recurrences.

More specifically, in Figure 10 below we show that it is indeed possible in an  $N = 8$  dof case to study a torus of dimension 2 by selecting initial conditions exciting a continuation of 2 linear modes (see Figure 10(a)). Then, because this torus is stable, its dimensionality for long times is verified by only the  $GALI_2$  being constant while the higher order GALIs decay by algebraic power laws given by (14) (see Figure 10(b)).

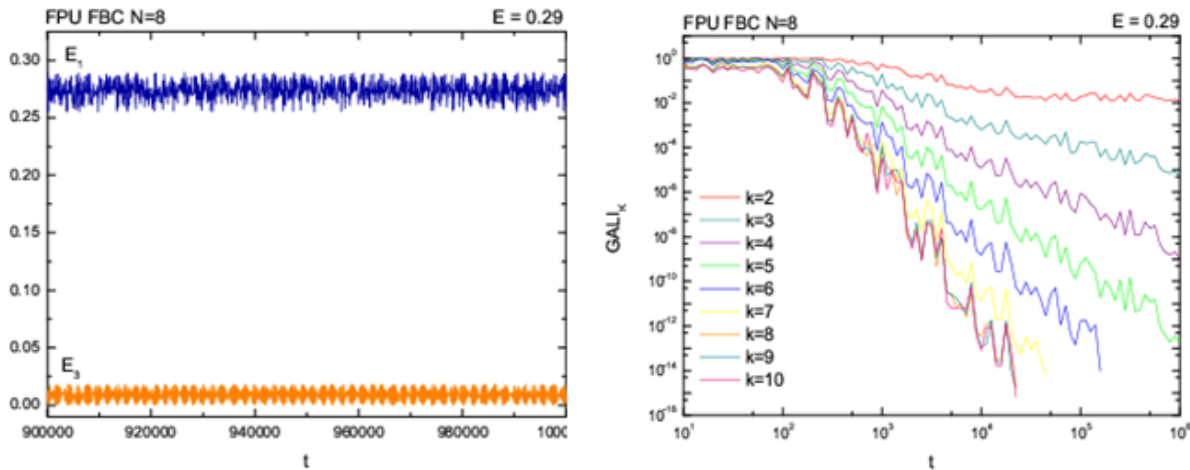


**Figure 10** – FPU with 8 particles: (a) Only the  $E_1$  and  $E_3$  modes are excited. Observe that the associated  $q$ -torus is 2-dimensional, since (b) only  $GALI_2 = \text{const.}$  and all other  $GALI_k$  decay by power laws

On the other hand, if the torus is unstable, and initial conditions nearby are going to wander in the weakly chaotic region that surrounds it, the GALIs are going to show it by falling exponentially to zero. In Figure 11(a) below we exemplify this by showing the behavior of  $GALI_2$ , while all higher order

GALIs (not shown here) also fall to zero exponentially according to the laws (13). Note that, if one wanted to study this phenomenon by tracking the energies of the two excited modes, he would discover it much later in time through the excitation of other modes, s shown in Figure 11 (b)

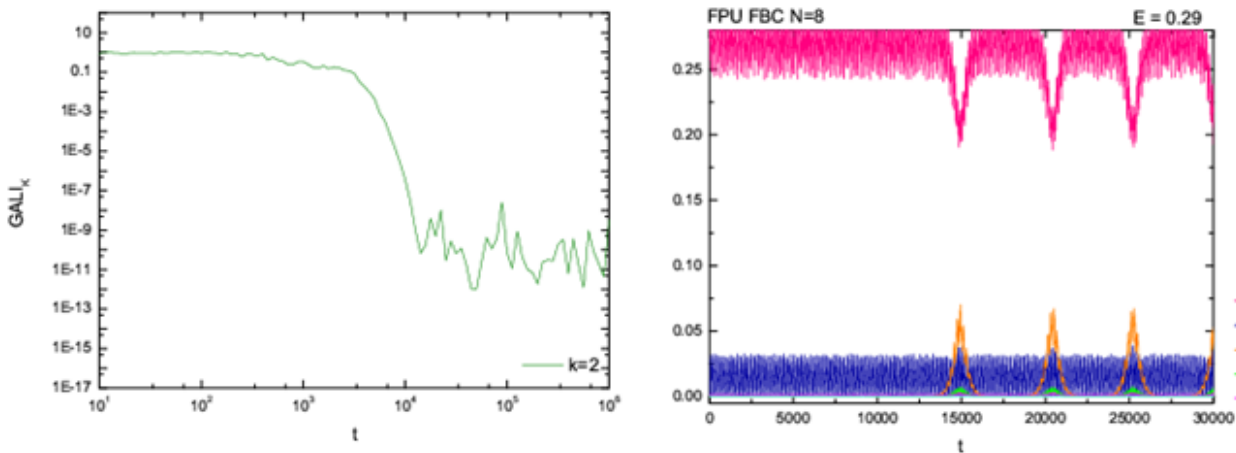


**Figure 11** – FPU with 8 particles and initial conditions near a  $q=2$  torus: (a) The evolution of  $GALI_2$  shows already at  $t \approx 1000$  that the orbit diffuses away from the torus weakly chaotically. (b) This becomes visible, as the FPU recurrences break down at  $t \approx 14000$  through the excitation of different modes

**Localization in configuration space**

It is also very interesting to apply the above approach to the localization of spatial coordinates in nonlinear lattices, through the occurrence of a fascinating type of exponentially localized periodic oscillations, called discrete breathers [7, 8]. These solutions have been verified analytically and

numerically on a variety of lattices, like the Klein-Gordon (KG) chain

$$x_n'' = -V'(x_n) + \alpha(x_{n+1} - 2x_n + x_{n-1}),$$

$$V(x) = \frac{1}{2}Kx^2 + \frac{1}{4}x^4 \tag{15}$$

$-\infty < n < \infty$ , where  $V(x)$  is an on-site potential and  $\alpha > 0$  is a coupling parameter. One example of such a breather solution is shown here in Figure 12 below. Expanding in Fourier series, one finds that

discrete breathers are directly related to homoclinic orbits of invertible maps, through which one can prescribe a numerical procedure for constructing them to arbitrarily high accuracy [7, 8].

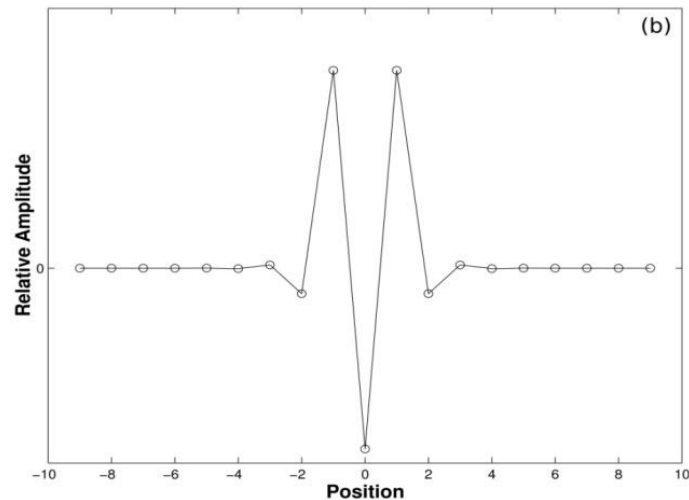


**Figure 12** – Localization in configuration space in the form of a discrete breather of a harmonic nearest neighbor chain with on site nonlinear potential of the Klein Gordon type

Indeed, keeping only the leading term  $x_n(t) = A_n \cos(\omega_b t)$  in such an expansion we obtain the map

$$A_{n+1} = -A_{n-1} + CA_n + \alpha^{-1}A_n^3, \quad (16)$$

$$C = -2 + (K - \omega_b^2)/\alpha,$$

which provides a very good approximation for the amplitudes  $A_n$ , as homoclinic orbits lying at the intersections of the invariant manifolds of the saddle point at the origin of (16), at  $|C| > 2$ .

Discrete breathers constitute one more example of what we call Simple Periodic Orbits, with all particles oscillating with frequency  $\omega_b$  outside the phonon band of NNMs.

An interesting question here would be to identify whether discrete breathers are surrounded by low-dimensional tori when they are stable. If so,

it would be pertinent to study the dimensionality of these tori and their stability using our GALI indices to determine if these localized solutions will eventually break down as time evolves.

As we observe in Figure 13 below, in the case of a 31 particle lattice where a stable breather is followed for very long times, the oscillations of the central particle (larger band in Figure 13(a)), its two adjacent particles (middle size band) and the very small oscillations of all the others (small size band) remain practically constant up to  $t = 1.4 \times 10^6$  time units. Using the GALIs, however, one does not need to integrate over such extended time intervals. As is already evident in Figure 13(b), for times as short as  $t = 10^4$  time units, the stability and dimensionality of the breather are detected by the constancy of  $GALI_2$ , and the fact that all other higher order GALIs decay by power laws.

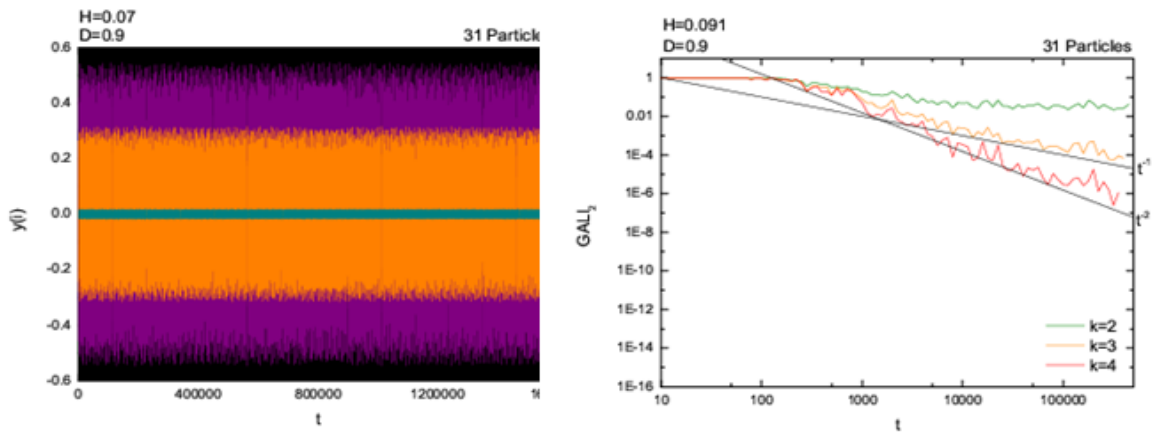


**Figure 13** – (Stable torus): (a) The oscillations of the central three particles of a KG chain of  $N=31$  particles do not break down, forming a quasiperiodic breather. (b) The torus is 2-dimensional, since only  $GAL_2$  remains constant, while all other  $GAL_k$  decrease by power laws

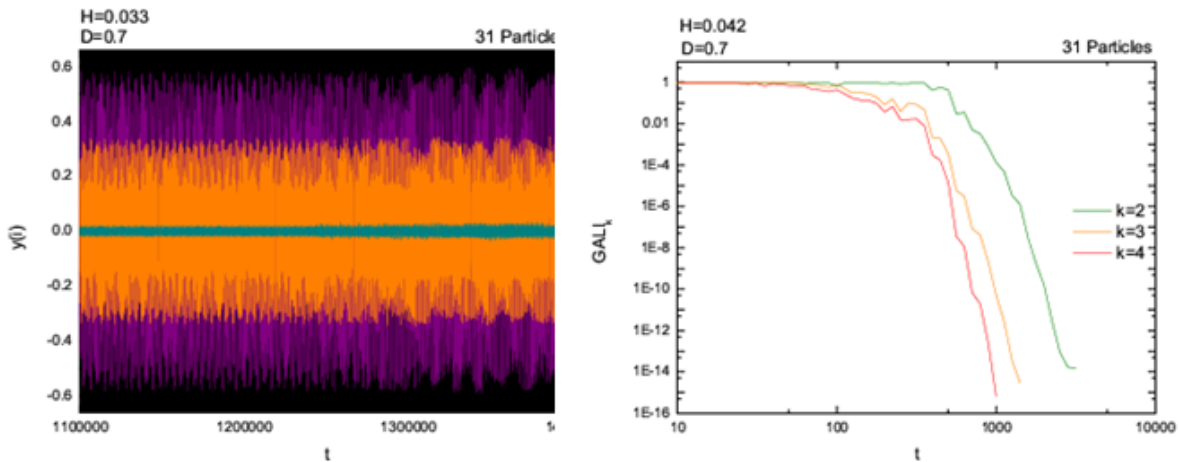


**Figure 14** – (Unstable torus): (a) The oscillations of the central 3 particles, starting further from the breather, appear quasiperiodic for very long times. (b) The solution, however, is chaotic and the “torus” eventually breaks down since the  $GAL_k$  decay exponentially

On the other hand, when we increase the energy of the system somewhat, the breather oscillations become irregular (see Figure 14 (a)) and the breather collapses after  $t=1.4 \times 10^6$  time units, while the  $GAL_k$ s fall exponentially much sooner (see Figure 14 (b)), declaring after only a few thousand time units that this solution is dynamically unstable and will eventually break down!

**Complex statistics of chaotic dynamics**

To study and understand the statistical properties of chaotic behavior in Hamiltonian systems, it is important to recall first some basic facts of equilibrium thermodynamics also reviewed in [9]. As is well-known, in Boltzmann – Gibbs statistics, if a system can be at any one of  $i=1,2,\dots,W$

states with probability  $p_i$ , its entropy is given by the famous formula

$$S_{BG} = -k \sum_{i=1}^W p_i \ln p_i,$$

under the constraint

$$\sum_{i=1}^W p_i = 1, \tag{17}$$

where  $k$  is the Boltzmann's constant. The BG entropy satisfies the property of additivity, i.e. if  $A$  and  $B$  are two independent systems, their union entropy is  $S_{BG}(A+B) = S_{BG}(A)+S_{BG}(B)$ . At thermal equilibrium, and for a continuum set of states depending on one variable,  $x$ , the probability density that optimizes the BG entropy subject to the constraints (17), zero mean and variance  $V$  is, of course, the well-known Gaussian

$$p(x) = e^{-x^2/2V} / \sqrt{2V}. \quad (18)$$

Another important property of the BG entropy is that it is *extensive*, i.e. that  $S_{BG}/N$  is finite in the limit  $N \rightarrow \infty$ . But, many physically important systems governed by long range interactions are neither additive nor extensive, like self-gravitating systems of finitely many mass points and ferromagnetic spin models. For such systems the so-called Tsallis entropy has been proposed [9]

$$S_q = k \frac{1 - \sum_{i=1}^W p_i^q}{1-q},$$

under the constraint

$$\sum_{i=1}^W p_i = 1, \quad (19)$$

depending on an index  $q$ . For a continuum set of states  $x$ , the Tsallis entropy is optimized by the  $q$ -Gaussian pdf

$$p_q(x) = a e^{-\beta x^2} = a(1 - (1 - q)\beta x^2)^{1/(1-q)}, \quad (20)$$

where  $\beta=1/kT$  is a free parameter and  $a > 0$  a normalization constant. Expression (20) tends to a Gaussian, as  $q \rightarrow 1$   $e_q \rightarrow e$ . The Tsallis entropy is not additive, and, in general, non-extensive. It offers us the possibility of studying problems whose correlations decay *not exponentially* but by power laws, thus implying that the interactions within such systems are of the long range type.

### The case of multi-degree-of freedom Hamiltonian systems

In the realm of multi – dimensional Hamiltonian systems analyzed in this paper, there are many situations where the dynamics is weakly chaotic and may, therefore, possess Tsallis statistics of the type described above.

For example, we have found that, in the  $\beta$ -FPU model, near an unstable SPO1 orbit of a 5-particle chain, orbits that remain “trapped” for very long times in a thin chaotic region (see Figures 15, 16) and are described by pdfs of the  $q$ -Gaussian type with  $q \approx 2.8$  [11].

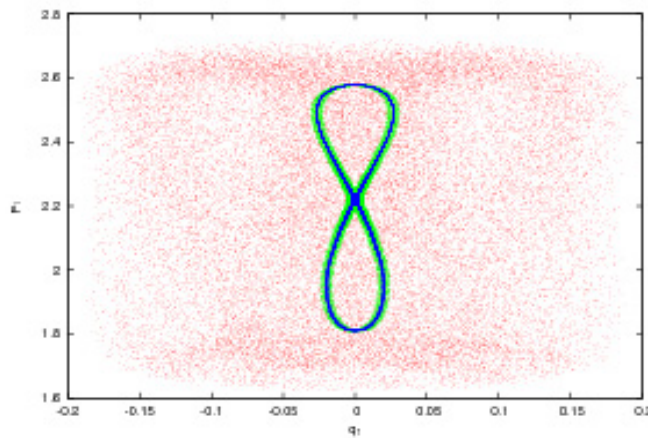


**Figure 15** – Three different orbits with initial conditions very close to an unstable SPO1 orbit of the 5 particle FPU- $\beta$  chain: The black “figure eight” in the middle starts from a distance of  $10^{-7}$ , the green one starts within 0.0001 and the red one extending over a much larger region, starts within 0.01 from the saddle point

These are what we call quasi-stationary states (QSS) of the dynamics. Following these states for long times, one typically finds that their pdfs pass through QSS described by  $q$ -Gaussians of  $q > 1$ , see

Figure 16 (a,b,d,c), until they finally converge to Gaussians with  $q = 1$ , when the orbits escape to a much larger domain of strong chaos, see Figure 16 (c,e).

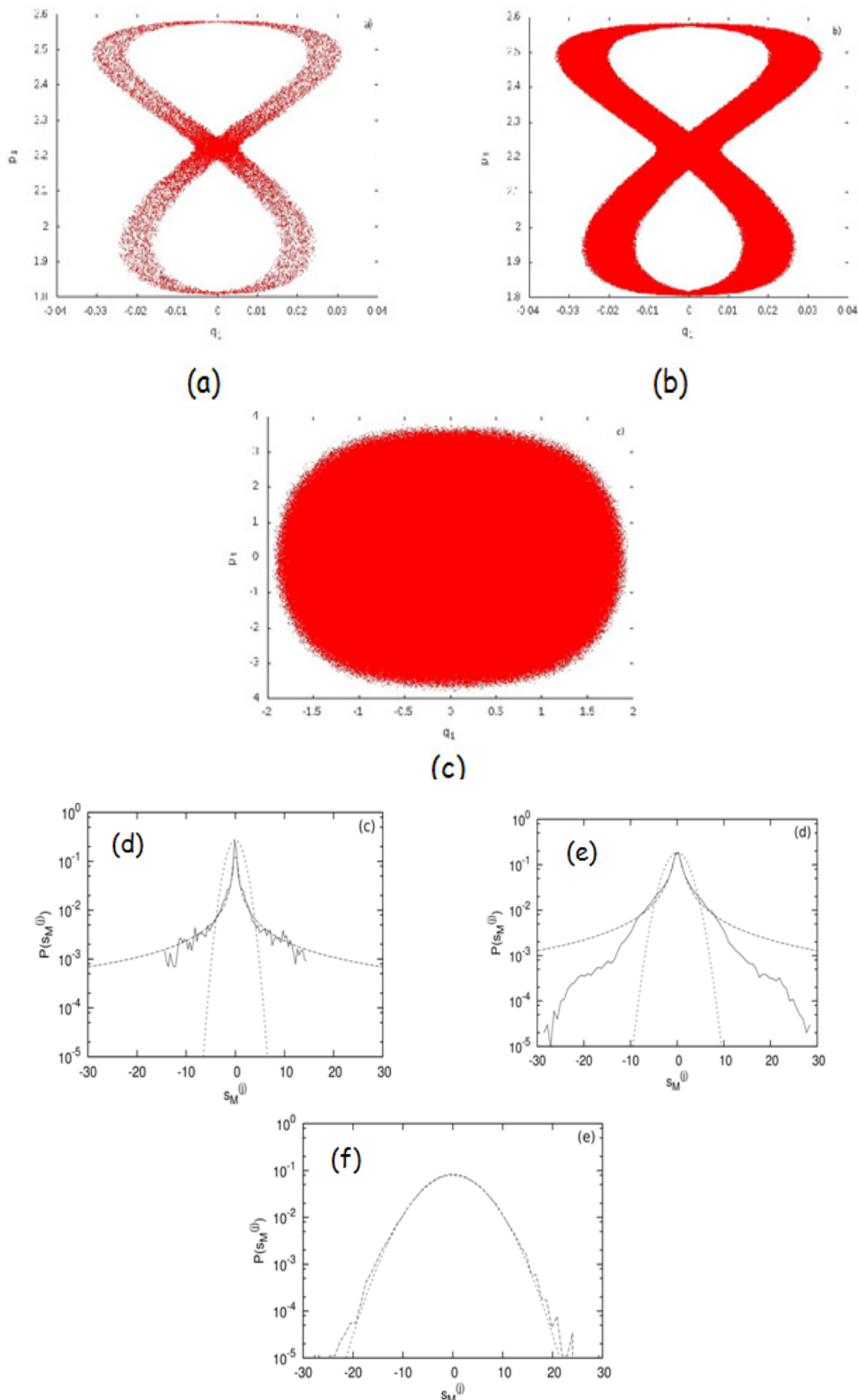


**Figure 16** – Orbits starting at a distance of  $1.0 \cdot 10^{-7}$  from the unstable SPO1 orbit, integrated for: (a)  $t=10^5$ , (b)  $t=10^7$ , until they eventually escape in the large chaotic sea (c)  $t=10^8$  (d – f): Plots of pdfs of position variables for a 5- particle FPU chain and initial conditions close to an unstable SPO1 orbit. The QSS observed here are well described by q-Gaussians with (d)  $q = 2.78$ , then (e)  $q = 2.48$ , until the orbit drifts away to a wide chaotic sea and the pdfs converge to (f) Gaussians with  $q=1.05$

Another example of a weakly chaotic orbit located near an SPO2 orbit of a multi – dimensional  $\beta$  – FPU Hamiltonian system has been

found to “stick” on a low – dimensional torus and remain for extremely long times near a type of quasiperiodic motion is shown in Figure 17 below

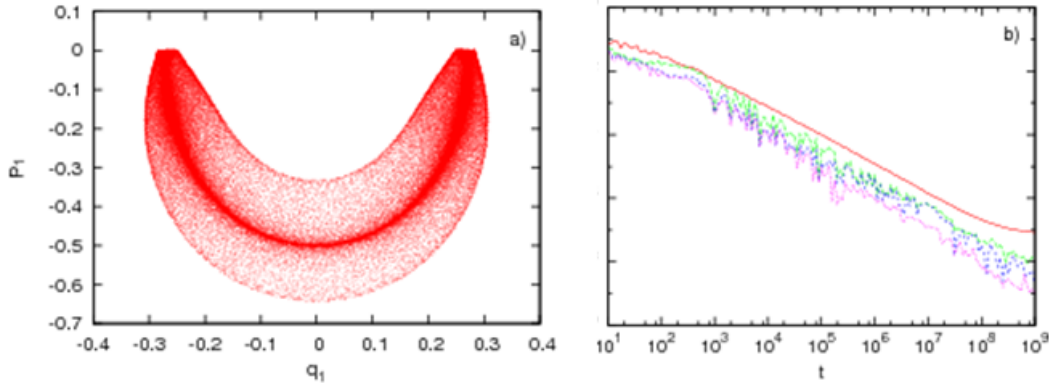


**Figure 17** – (a) The dynamics near an SPO2 orbit “sticks” to a quasiperiodic torus, at least up to  $t=10^8$ . The weakly chaotic nature of the motion is shown in (b), where we have plotted the 4 largest Lyapunov exponents up to  $t=10^9$ . Although they all decrease towards zero, at about  $t > 10^9$ , the largest exponent shows a tendency to converge to a positive value, indicating that the orbit is chaotic

As Figure 17 demonstrates this orbit is dynamically very “stable”, as it remains for very long times near a regular quasiperiodic torus. Its chaotic nature, however, is clearly exemplified by the fact that after nearly  $t=10^8$  time units its largest Lyapunov exponents stops decreasing towards zero and starts to converge to a positive value! This is clear evidence that this orbit is not regular and can

therefore be characterized as weakly chaotic, according to the terminology used in this paper.

The interesting question that arises, therefore, is whether a statistical analysis of this orbit also shows that this orbit can also be characterized as weakly chaotic, by plotting the probability distributions of averaged sums of its coordinates, as was done above for the orbit shown in Figure 16.

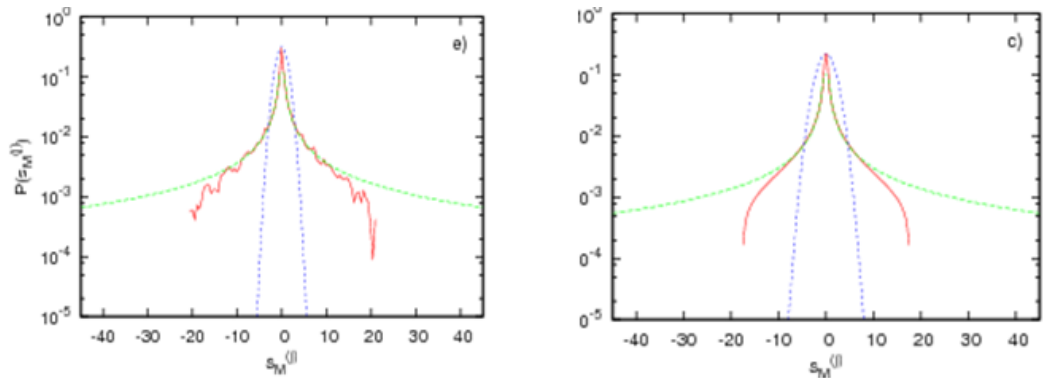


**Figure 18** – Left: The distribution of the normalized sum pdf of the orbit starting near SPO2, for a total integration time  $t=10^6$ . Right: Final integration time  $t=10^{10}$ . The pdf has converged to an almost analytical shape that is close to a q-Gaussian with  $q \approx 2.769$  near the center, and seems to have analytical form

Indeed, as is clearly seen in Figure 18, the probability density functions (pdfs) associated with this orbit are not Gaussian but are well described by q- Gaussian distributions of the form (20). The

remarkable observation we make here is that, after  $10^{10}$  time units, the pdfs appear to converge to a smooth distribution, that departs from a q- Gaussian type at large distances away from its mean value.

This type of complexity provides one further justification for the title of this paper.

### Weak chaos in 2-dimensional area – preserving maps

It is instructive to illustrate some of the phenomena we have described in this paper on a 2-dimensional area – preserving map, which represents a simple model of a Hamiltonian systems of 2 – degrees of freedom. The question we wish to address here is whether what we have called strong and weak chaos can be observed in systems of low dimensions as well. For this reason, we shall examine the behavior of a model called the McMillan map expressed by the following equations mapping the  $x_n, y_n$  plane to itself [11]:

$$\begin{aligned}x_{n+1} &= y_n, \\y_{n+1} &= -x_n + \frac{2\mu y_n}{y_n^2 + 1} + \varepsilon y_n, \\n &= 0, 1, 2, 3, \dots\end{aligned}\quad (21)$$

For  $\varepsilon = 0$  this system is integrable as it possesses a constant of the motion of the form  $x^2 + y^2 + x^2 y^2 - 2\mu xy = \text{const}$ . It is also easy to see that it also possesses a saddle point at the origin for  $\mu > 1$ . When  $\varepsilon > 0$  and small (21) becomes non – integrable and chaotic orbits are expected to appear near its origin forming “figure eight” domains of the type shown in Figure 15. What we would like to investigate here is whether these orbits also display strongly and weakly chaotic properties similar to what we found earlier when we were discussing multi – dimensional systems.

The results we obtained in [11] we indeed quite interesting: We first noted that for several  $\mu, \varepsilon$  values the chaotic orbits wandering around the saddle point at (0,0) formed indeed a “figure eight” similar to the one of Figure 15 in a generally

strongly chaotic fashion [11]. In other words, when followed for as many as  $2^{20}$  iterations (time units) the pdfs produced by averaged sums of the coordinates appeared to converge to Gaussian distributions. In other words, the orbits wandered around a “figure eight” domain chaotic domain and their pdfs passed through a sequence of q-Gaussian states, with  $q > 1$ , until they become true Gaussians, with  $q = 1$ .

However, for certain choices of parameter values, the orbits exhibited a remarkable “diffusive” behavior, as they began after a certain time to escape from the “figure eight” and wander about in the plane along a chaotic boundary surrounding chains of islands that encircled the central “figure eight” region! This produced a complex pattern of chaotic domains in which the orbits wandered about, “sticking” often as it were in the vicinity of “thinner” chaotic regions surrounding higher order saddle points of the map extending over island chains of stable periodic orbits of (21) that also encircle the origin. It was precisely in these cases where we discovered that the pdfs of our chaotic orbits began to converge to a true q (>1)-Gaussian, for  $n \rightarrow \infty$ , as shown in Figure 19 and Figure 20 below, thus demonstrating their weakly chaotic nature.

### The role of Long Range Interactions

As was mentioned earlier, all the results described above appear to suggest that the statistical properties of chaotic motions in Hamiltonian systems must depend on the *type of interactions* characterizing these motions. More specifically, we postulated that if these interactions are “short” (e.g. exponential) this might account for the strong chaos characterizing states that are described by Gaussian pdfs. On the other hand, if the interactions are long ranged (e.g. decaying by power laws) this would entail that the pdfs obtained after sufficiently long times would be of the q – Gaussian type.

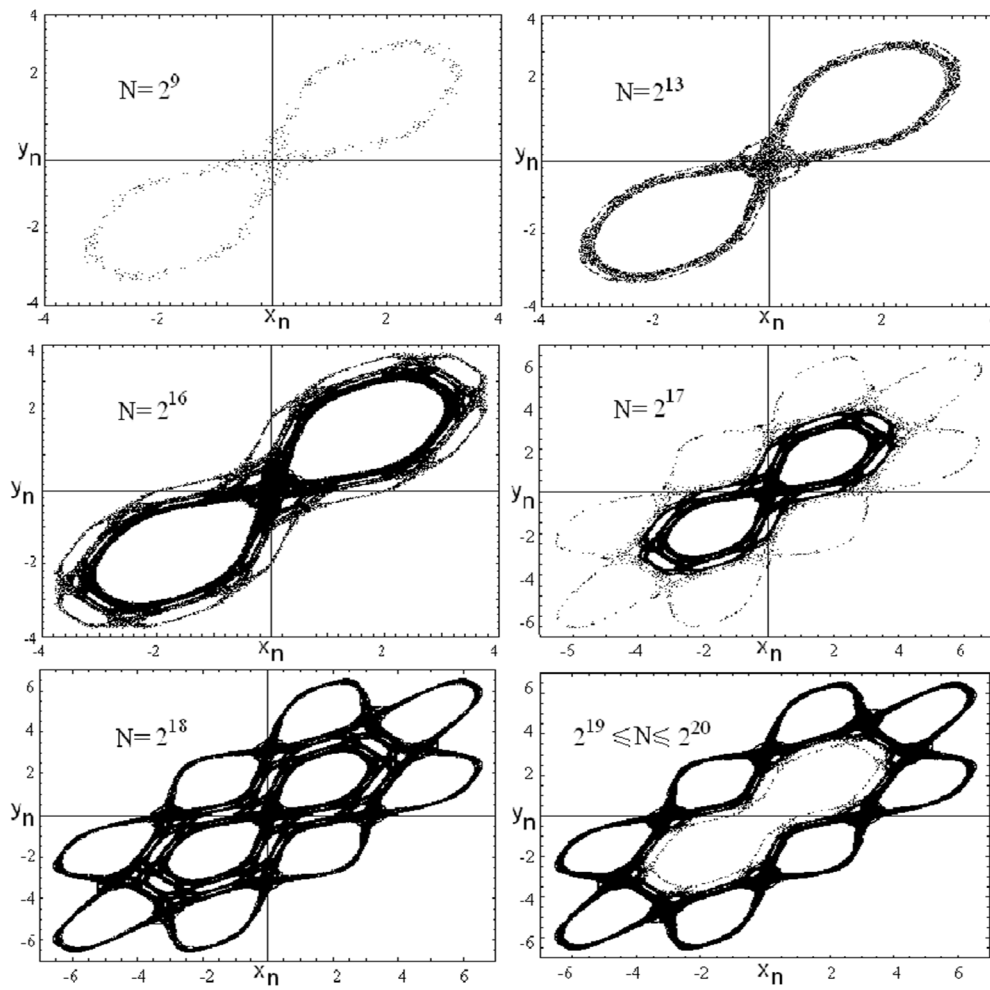


Figure 19 – Upper: Diffusive motion of orbits in a thin chaotic layer of the 2-d area – preserving map (21), starting near the unstable fixed point at the origin, and evolving to  $N=2^{20}$  iterations

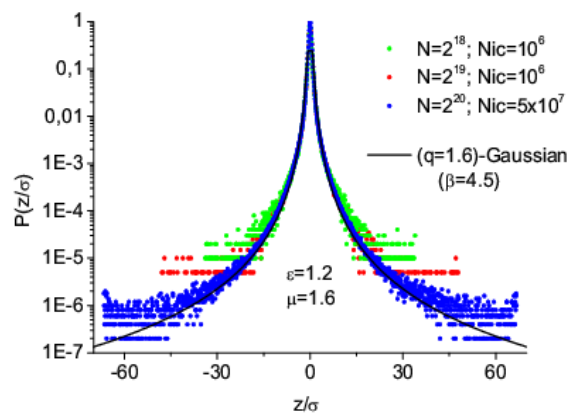


Figure 20 – The pdfs representing the normalized sum of averages of the  $x_n$  coordinate of the map, for the chaotic orbit of Figure 18 are seen to converge after  $2^{20}$  iterations to the  $q$ -Gaussian shown here, with  $q=1.6$

Thus, to test the validity of the above the above conjecture we decided to extend our studies and consider a class of  $N$  – dimensional Hamiltonians that involve Long Range Interactions (LRI) of the kind exemplified by the following class of FPU models:

$$H = \frac{1}{2} \sum_{n=1}^N p_n^2 + \frac{1}{2} \sum_{n=0}^N (x_{n+1} - x_n)^2 + \frac{b}{\underline{N}(N,\alpha)} \sum_{n=0}^N \sum_{m=n+1}^N \frac{(x_n - x_m)^4}{|n-m|^\alpha} = U(N), \quad (22)$$

where  $b > 0$  and  $\alpha \geq 0$  is an important parameter introduced to “measure” the length of the interactions [12.13]. Note that to keep all energy terms in the Hamiltonian extensive, i.e. proportional to  $N$ , we have introduced before the quartic part of the potential the factor

$$\begin{aligned} \underline{N}(N,\alpha) &= \frac{1}{N} \sum_{i=0}^N \sum_{j=i+1}^N \frac{1}{(j-i)^\alpha} = \\ &= \frac{1}{N} \sum_{i=0}^N \frac{N+1-i}{(i+1)^\alpha}, \end{aligned} \quad (23)$$

What we found was indeed very interesting: Noting first that  $\alpha = \infty$  represents the shortest type of (nearest neighbor) interactions considered already in sections 3 and 4 of this paper, we studied the full range of  $\alpha$  values all the way down to  $0 \leq \alpha \leq 1$  representing the regime of the longest type of LRI possible. As Figure 21 and Figure 22 below demonstrate, as  $\alpha$  became smaller than  $\alpha = 1$ , a surprising phenomenon of “regularization” of the dynamics was observed (see Figure 21): The maximum Lyapunov exponent  $\lambda > 0$  was seen to decrease to values that seem to tend to zero! In other words, a kind of *weakly chaotic* behavior was discovered, showing that LRI has a “stabilizing” effect on the dynamics.

To see whether this “regularization” effect extends also to the statistical properties of the motion we studied the pdfs of sums of averaged momenta of our chaotic orbits and discovered that these also tended to become closely approximated by  $q$  – Gaussian distributions in the LRI regime  $0 \leq \alpha \leq 1$  (see Figure 22). On the other hand, in the regime  $\alpha > 1$  where the interactions may be characterized of “shorter” type, the same pdfs quickly converged to  $q$  – Gaussians, demonstrating that the nature of the dynamics is characterized by a stronger form of chaos (see Figure 22)!

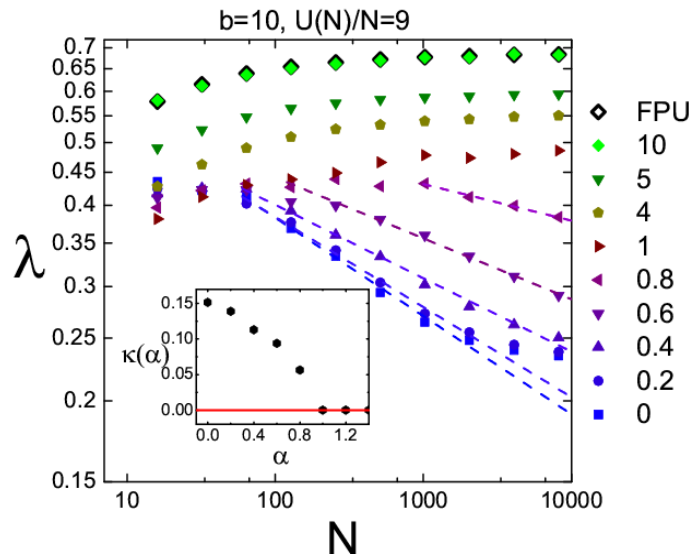


**Figure 21** – LRI restores order out of chaos: For  $0 < \alpha < 1$  the maximal Lyapunov exponent  $\lambda$  starts to decay to zero as  $N$  increases and  $\alpha$  “weaker” form of chaos is expected

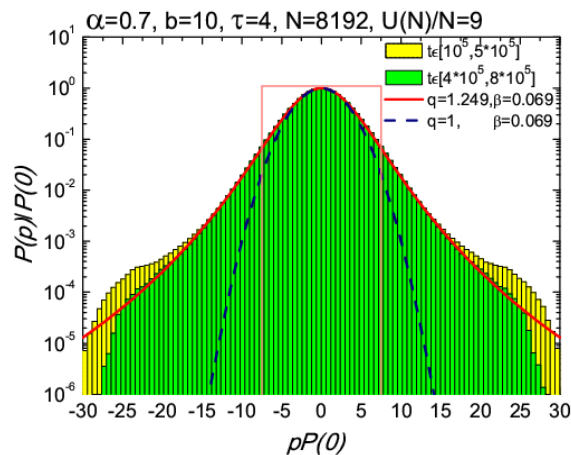


**Figure 22** – The momentum probability density function (pdf) for Long Range Interactions,  $\alpha = 0.7$ , converges to a  $q$ -Gaussian with  $q=1.249$  indicating a “weaker” form of chaos as time increases

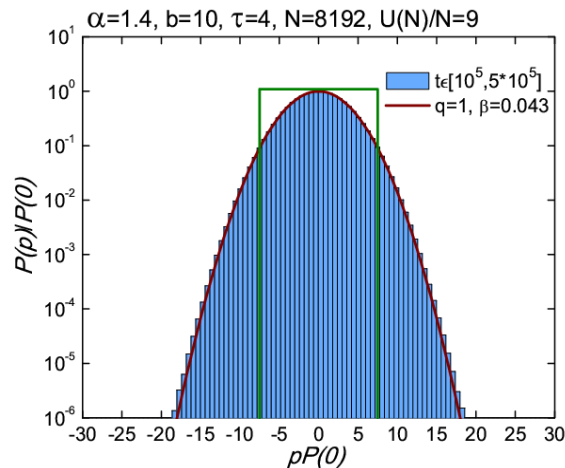


**Figure 23** – On the contrary, the pdfs of the momenta for shorter ranges of interactions with  $\alpha > 1$  (in the above example  $\alpha = 1.4$ ), are seen to quickly converge to a pure Gaussian, indicating “strong” chaos

To test these ideas further, we proceeded to carry additional studies to see e.g. how the  $q$  index of the pdfs behaves in these very interesting LRI regimes and obtained results of the kind shown in Figure 23.

We also observed, however, that in all cases we studied, if the time interval of our integrations increased, a critical time  $t_c$  was always reached where the  $q$  values started to decrease, exhibiting a tendency to go back to  $q=1$  where strong chaos and real Gaussians prevail.

Another important effect was also observed in the LRI regime, when the number of particles  $N$  was increased (see Figure 25(b)): The  $q$  index of the pdfs

was also seen to increase as  $N$  becomes larger and larger, suggesting that weakly chaotic dynamics may also be found in the thermodynamic limit where  $N$  and the total energy  $E$  become larger and larger while  $E/N$  is kept constant.

Thus, scaling our parameter  $b$  by the critical time  $t_c$  and plotting the pdfs at each  $t_c$  vs. the value of  $1/N$  we discovered a remarkable “phase diagram”, see Figure 25 below, dividing the parameter plane in two regimes: One characterized by Gaussians, strong chaos and BG statistics and one where pdfs are  $q$  – Gaussians and the weakly chaotic motion and Tsallis thermostatistics reign!

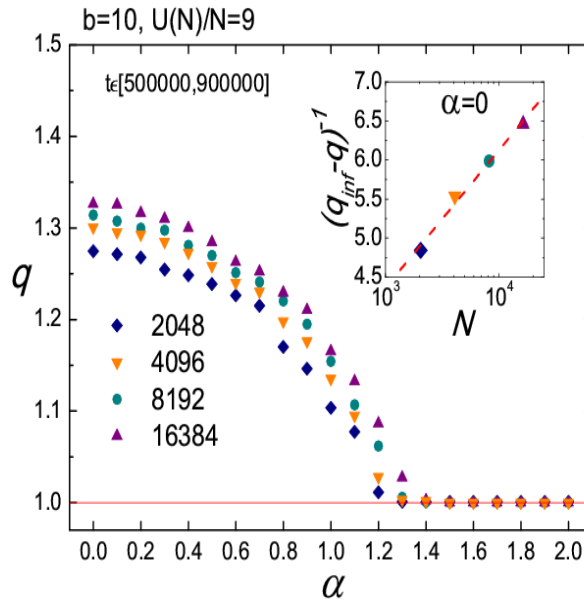


**Figure 24** – The pdf index  $q$  decreases to 1 over the regime of Long Range Interactions, from  $\alpha = 0$  to just above  $\alpha = 1$ , where shorter range interactions take over

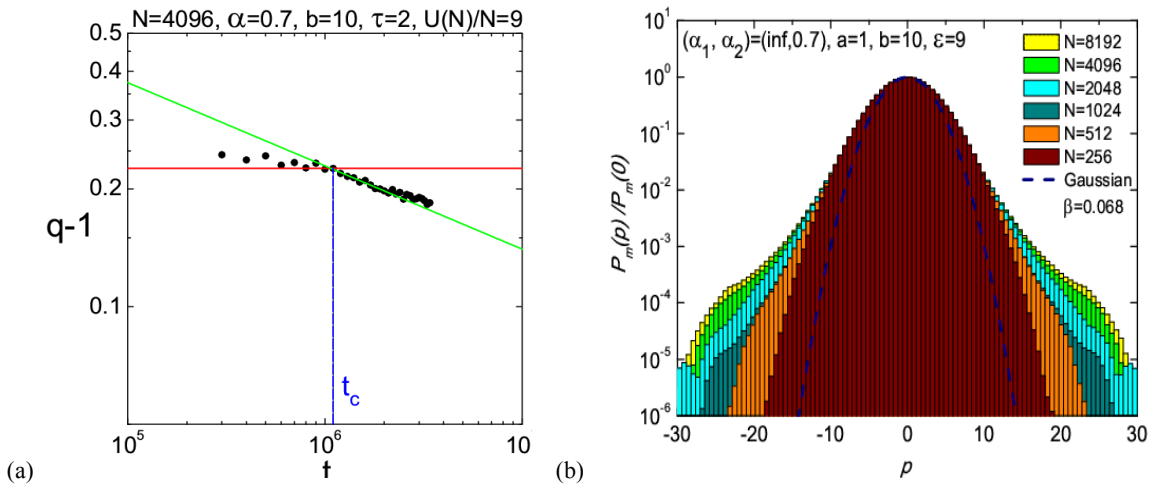


**Figure 25** – (a): For LRI,  $\alpha=0.7$ , the index  $q$ , starts to decrease towards 1 after a time threshold  $t_c \approx 10^6$ , for these parameter values. (b): Momentum distributions for the system with  $b = 10$ ,  $\epsilon = 9$ ,  $\alpha = 0.7$  for increasing  $N$  values.

Note that as  $N$  grows the pdfs are described by a  $q$ -Gaussian whose index  $q$  increases from 1.17 for  $N = 512$  until 1.25 for  $N = 8192$

Finally, we completed our study by plotting the  $q$  parameter as a function of  $1/\log(N)$  as  $N$  grows to higher and higher values. Based in the results plotted in Figure 27 we thus proposed the following formula

$$q(N, \alpha) = q_\infty(\alpha) - \frac{c(\alpha)}{\log N}. \quad (24)$$

demonstrating the dependence of  $q$  on  $N$  in the LRI regime. As a result, we can use this formula to estimate the asymptotic behavior of  $q \rightarrow q_\infty$  in the limit  $N \rightarrow \infty$ . Note that as  $N$  becomes larger and larger, the above formula allows us to determine the values  $q_\infty(\alpha)$  that the  $q$ -Gaussian pdfs will have in that limit.

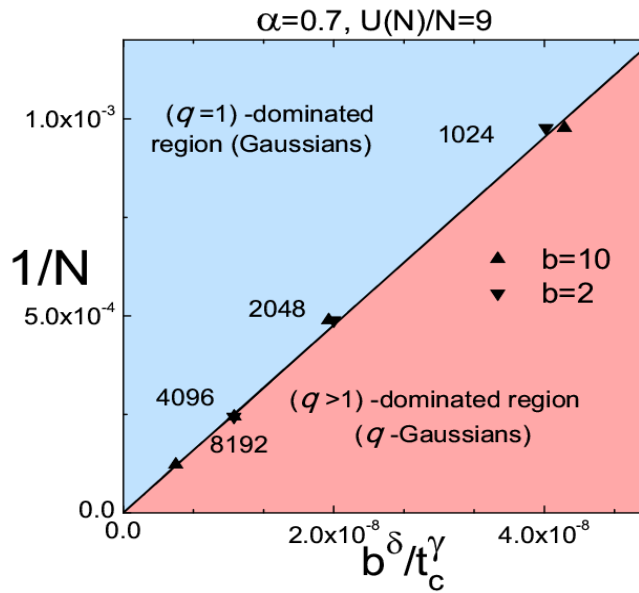


**Figure 26** – A “phase transition diagram” is obtained, separating BG from Tsallis thermostatics, in which the limits  $t \rightarrow \infty$  and  $N \rightarrow \infty$  do not commute

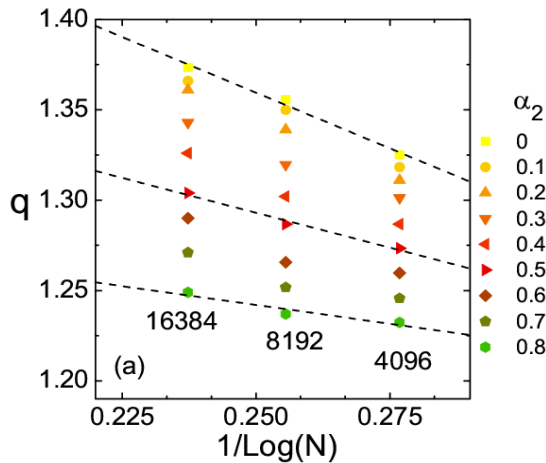


**Figure 27** – The index  $q$  depends linearly on  $1/\log N$  for  $N=4096, 8192, 16384$ , as  $\alpha$  changes, according the formula (24)

Next, in our more recent work [13], we extended the above results to study of  $N$  – dimensional Hamiltonian systems in which the “length” of the linear interactions (represented by quadratic terms in the potential of the Hamiltonian function) are characterized by a different  $\alpha$  index than those of the nonlinear interactions, represented by quartic terms in the potential. We also considered the effect of LRI in  $N$  – dimensional Hamiltonian lattices, where besides the interparticle interactions each particle possesses an on site potential of its own [14].

It is not the place here, however, to also describe these results, as they are of a more advanced and

specialized character. We thus prefer to encourage the interested reader to consult the corresponding references [13, 14] and limit ourselves to summarizing these findings in the Conclusion section that follows.

### Conclusions

In this work, we have reviewed a number of results of our research team in the broader field of study that may be called following Complex Dynamics and Statistics of Hamiltonian systems. Although the work presented here has focused

primarily on 1-D lattices of the so called  $\beta$  – FPU models involving quartic and quadratic interactions, we believe that they are much more general and can be found also be bound in similar systems with other type of nonlinearities. Indeed, weakly and strongly chaotic motions appear in conservative systems of low dimensionality, even 2 – dimensional area preserving maps like the McMillan model analyzed in section 5.2.

Our main conclusions can, therefore, be summarized as follows:

1. We have demonstrated the importance of Nonlinear Normal Modes in exploring “weak” and “strong” chaos, depending on the energy density  $E/N > 0$  at which they first become unstable. At energies where they have just destabilized it is possible to find in their vicinity weakly chaotic motions that “stick” to the associated saddle points for very long times.

2. We mentioned the significance of Lyapunov spectra in quantifying strong chaos, and introduced the  $GALI_k$  spectrum of indices  $k=2,3,4,\dots$ , which are best suited for identifying chaos, when they vanish exponentially. We also stressed the fact that in the case of quasiperiodic motion, where the GALIs decay as power laws, they offer the most convenient strategy known to date by which the dimensionality of the torus can be determined.

3. The GALI indices can also be used to study the breakdown of localization in 1-dimensional lattices: (i) In modal space connected to FPU recurrences and (ii) in position space, occurring in the form of discrete breathers, for which we can predict their breakdown long before it can be detected by other methods.

4. When Long Range Interactions are imposed (LRI) on the nonlinear forces (quartic terms in the potential of our FPU models) – for any range of linear interactions – we obtain weakly chaotic motion characterized by q-Gaussian pdfs with  $q > 1$  (Tsallis thermostatics).

5. More specifically, in the LRI regime, we find a new “phase transition diagram”, separating BG from Tsallis thermostatics, in which the limits  $t \rightarrow \infty$  and  $N \rightarrow \infty$  do not commute.

6. When we introduce LRI *only on the linear forces* (quadratic part of the potential) we obtain strongly chaotic motion demonstrated by pure Gaussian pdfs with  $q = 1$  (Boltzmann Gibbs thermodynamics).

7. When LRI are imposed on the nonlinear forces, we find for long times limiting values  $q_\infty > 1$  as  $N \rightarrow \infty$ , showing that the system remains weakly

chaotic (with Tsallis and not Boltzmann Gibbs thermostatics) in the thermodynamic limit.

8. Finally, when we include in our potentials, besides the interparticle interactions, terms associated with local potentials at the site of each separate particle, LRI again yields evidence of highly regular dynamics, as single-site excitations lead to special low-dimensional solutions, that may be well described by a 2 – degree of freedom Duffing oscillator. On the other hand, the behavior of the maximal Lyapunov exponent, suggests in that case an approach to “quasi integrable” behavior in the thermodynamic limit, characterized by non-Gaussian momentum distributions.

## References

1. M. Lieberman, A. Lichtenberg. “Regular and Chaotic Dynamics.” Springer Verlag, New York (1986).
2. Bountis T. and Skokos H. “Complex Hamiltonian Dynamics.” Springer Synergetics series, Springer, Berlin (2012).
3. S. Flach, M.V. Ivanchenko and O.I. Kanakov “q-Breathers and the Fermi-Pasta-Ulam Problem.” Phys. Rev. Lett. 95, 064102 (2005).
4. Skokos, Ch., Bountis, T., Antonopoulos, C. “Geometrical properties of local dynamics in Hamiltonian systems: The generalized alignment index (GALI) method.” Physica D231, (2007): 30-54.
5. Skokos Ch., Bountis T., Antonopoulos C. “Detecting chaos, determining the dimensions of tori and predicting slow diffusion in Fermi Pasta-Ulam lattices by the generalized alignment index method.” Eur. Phys. J. Sp. Top. 165, (2008): 5-14.
6. Christodoulidi H., Efthymiopoulos C., Bountis T. “Energy localization on q-tori, long-term stability, and the interpretation of Fermi-Pasta-Ulam recurrences.” Phys. Rev. E 81, 016210 (2010).
7. J. Bergamin, T. Bountis and C. Jung “A Method for Locating Symmetric Homoclinic Orbits Using Symbolic Dynamics.” J. Phys. A: Math. Gen. 33, (2000): 8059-8070.
8. J. Bergamin, T. Bountis and M. Vrahatis, “Homoclinic Orbits of Invertible Maps.” Nonlinearity 15, (2002): 1603–1619.
9. C. Tsallis “Introduction to Nonextensive Statistical Mechanics – Approaching a Complex World.” (Springer, New York, 2009).
10. Antonopoulos C., Bountis T., Basios V. “Quasi-stationary chaotic states of multidimensional

Hamiltonian systems.” *Physica A* 390, (2011): 3290-3307.

11. Ruiz Lopez G., Bountis T. and Tsallis C. “Time – Evolving Statistics of Chaotic Orbits in Conservative Maps in the Context of the Central Limit Theorem.” *Intern. J. Bifurc. Chaos* 22 (9), (2012): 12502.

12. Christodoulidi H., Tsallis C., Bountis T. “Fermi-Pasta-Ulam model with long-range interactions: Dynamics and thermostatics.” *EPJ Letters* 108, 40006 (2014).

13. Christodoulidi H. Bountis T., Tsallis C., Drossos L. “Chaotic Behavior of the Fermi-Pasta-Ulam Model with Different Ranges of Particle interactions.” *J. Stat. Mech.* 12 (12), 123206 (2016).

14. Christodoulidi H., A. Bountis A., Drossos L. “The Effect of Long-Range Interactions on the Dynamics and Statistics of 1-D Hamiltonian Lattices with On-Site Potential.” *EPJST* 227 (5, 6), (2018): 563.

IRSTI 27.31.21

<sup>1,2</sup>M. Borikhanov, <sup>1,2\*</sup>B.T. Torebek<sup>1</sup>Al-Farabi Kazakh National University, Almaty, Kazakhstan<sup>2</sup>Institute of Mathematics and Mathematical Modeling, Almaty, Kazakhstan

\*e-mail: torebek@math.kz

### Critical exponents of Fujita type for certain time-fractional diffusion equations

**Abstract.** Solutions of initial value problems for non-linear parabolic partial differential equations may not exist for all time. In other words, these solutions may blow up in some sense or other. Recently in connection with problems for some class of non-linear parabolic equations, Kaplan [1], Ito [2] and Friedman [3] gave certain sufficient conditions under which the solutions blow up in a finite time. Although their results are not identical, we can say according to them that the solutions are apt to blow up when the initial values are sufficiently large. The data at which solutions can blow up is called critical exponents of Fujita.

The present paper is devoted to research critical exponents of Fujita type for certain non-linear time-fractional diffusion equations with the nonnegative initial condition. The Riemann-Liouville derivative is used as a fractional derivative. To prove the blow up, we use the known test function method developed in papers by Mitidieri and Pohozaev [16].

**Key words:** blow-up, global weak solution, critical exponents of Fujita, time-fractional diffusion equation.

#### Introduction

In the paper [4], Fujita considered the initial value problem:

$$\begin{cases} u_t = \Delta u + u^p, & \text{for } (x, t) \in R^N \times (0, \infty), \\ u(x, 0) = a(x) \geq 0, & \text{for } x \in R^N, \end{cases} \quad (1)$$

where  $p$  is positive number,  $a(x) \in L^1(R^N)$  is nonnegative and positive on some subset of  $R^N$  of positive measure and  $\Delta$  denotes the Laplacian in  $N$  variables.

More precisely, he considered this problem on  $R^N \times [0, T)$  for some  $T \leq +\infty$ . A (classical or weak solution) of equation on  $R^N \times [0, T)$  for some  $T < +\infty$  is called a local (in time) solution. The supremum of all such  $T$ 's for which a solution exists

is called the maximal time of existence,  $T_{max}$ . When  $T_{max} = +\infty$  we say the solution is global. When  $T_{max} < +\infty$ , we say the solution of equation is not global (or the solution "blows up in finite time").

Let  $p_c = 2/N$ . Fujita proved the following assertions:

- (i) if  $0 < p < p_c$  and  $a(x) > 0$  for some  $x_0$ , then the solution of problem (1) grows infinitely at some finite instant of time;
- (ii) if  $p > p_c$ , then problem has a positive solution for every  $t > 0$ .

More exactly, for each  $k > 0$ , there exists a  $\delta > 0$  such that problem (1) has a global solution whenever  $0 \leq a(x) \leq \delta e^{-k|x|^2}$ . The number  $p_c$  is referred to as the *critical exponent*. In the critical case, this problem was solved in [5] for  $N = 1, 2$  and in [6] for arbitrary  $N$ . It was shown that

if  $p = p_c$  and then there is no nonnegative global solution for any nontrivial initial data. The proof was simplified by Weissler [7].

Later, Fujita [8] extended his own results to the more general case in which  $f(u)$  (the term describing the reaction) is convex and satisfies appropriate conditions (the main of which is the Osgood condition). The results obtained for problem (1) were generalized in [9] to the case of an initial-boundary value problem in a cone with the term  $|x|^\sigma u^{p+1}$  instead of  $u^{p+1}$ ; it was proved that, in this case, the critical exponent is equal to  $(2 + \sigma) / N$ .

It was shown in [10] that the critical exponent for the porous medium equation is equal to  $m - 1 + 2 / N$ , where  $m > (N - 2) + / N$ .

The equation

$$u_t = \Delta u^m + |x|^\sigma t^s u^{1+p}, \quad t > 0, \quad x \in R^N,$$

with nonnegative initial data was considered in [11]. It was shown that the critical exponent for this problem is equal to  $(m - 1)(s - 1) + (2 + 2s + \sigma) / N > 0$ .

The following parabolic equation with the fractional power  $(-\Delta)^{\beta/2}, 0 < \beta < 2$ , of the Laplace operator was studied in [12]:

$$u_t + (-\Delta)^{\beta/2} u = u^{1+p}, \quad (t, x) \in R^+ \times R^N.$$

Using Fujita's method [4], the authors [13] discussed nonnegative solutions of the equation

$$u_t + (-\Delta)^{\beta/2} u = h(t) u^{1+p}, \quad (t, x) \in R^+ \times R^N. \quad (2)$$

where  $h(t)$  behaves as at  $\sigma > -1, 0 < pN\beta \leq \beta(1 + \sigma)$ . The proof given in [13] is based on the reduction of Eq. (2) to an ordinary differential equation for the mean value of  $u$  with the use of the fundamental solution [say,  $P_\beta(x, t)$ ] of  $L_\beta := \partial / \partial t + (-\Delta)^{\beta/2}$ . Apparently, the approach of [13] cannot be used for systems of two differential equations with distinct diffusion terms unless, for example,  $P_\beta(x, t)$  can be compared with  $P_\gamma(x, t)$  for  $\beta < \gamma$ .

The following spatio-temporal fractional equation

$$\begin{cases} D_{0+}^\alpha u + (-\Delta)^{\beta/2} (u) = h(x, t) u^{1+p}, & \text{for } (x, t) \in R^N \times R^+, \\ u(x, 0) = u_0(x) \geq 0, & \text{for } x \in R^N, \end{cases}$$

where  $D_{0+}^\alpha, \alpha \in (0, 1)$  is the fractional derivative in the sense of Caputo,  $\beta \in [1, 2]$  with nonnegative initial data was considered in [14]. The critical exponent for this problem is equal to

$$1 < p < p_c = 1 + \frac{\alpha(\beta + \alpha) + \beta\rho}{\alpha N + \beta(1 - \alpha)}.$$

The main goal of the present research is to obtain results on critical exponents for time - fractional diffusion equation of the form

$$u_t = \frac{\partial^2}{\partial x^2} D_{+t}^{1-\alpha} u + u^p, \quad (x, t) \in R \times (0, T) = \Omega \quad (3)$$

with the initial condition

$$u(x, 0) = u_0(x) \geq 0 \quad (4)$$

where  $D_{+t}^{1-\alpha}$  denotes the time-derivative of arbitrary order  $(0, 1)$  in the sense of Riemann-Liouville.

In the case,  $\alpha = 1$  the time-fractional diffusion equation (3) reduces to the usual heat equation, which is well documented in [4].

**Some definitions and properties of fractional operators**

**Definition 1.** [15]The left and right Riemann-Liouville fractional integrals  $I_{a+}^\alpha$  and  $I_{b-}^\alpha$  of order  $\alpha \in R, (\alpha > 0)$  are given by

$$I_{a+}^\alpha f(t) = \frac{1}{\Gamma(\alpha)} \int_a^t (t-s)^{\alpha-1} f(s) ds, \quad t \in (a, b],$$

and

$$I_{b-}^\alpha f(t) = \frac{1}{\Gamma(\alpha)} \int_t^b (s-t)^{\alpha-1} f(s) ds, \quad t \in [a, b),$$

respectively. Here  $\Gamma(\alpha)$  denotes the Euler gamma function.

**Definition 2.** [15] The left Riemann-Liouville fractional derivative  $D_{a+}^\alpha$  of order  $\alpha \in R$ , ( $0 < \alpha < 1$ ) is defined by

$$D_{a+}^\alpha f(t) = \frac{d}{dt} I_{a+}^{1-\alpha} f(t) = \frac{1}{\Gamma(1-\alpha)} \int_a^t (t-s)^{-\alpha} f(s) ds, \quad t \in (a, b],$$

Similarly, the right Riemann-Liouville fractional derivative  $D_{b-}^\alpha$  of order  $\alpha \in R$ , ( $0 < \alpha < 1$ ) is defined by

$$D_{b-}^\alpha f(t) = \frac{d}{dt} I_{b-}^{1-\alpha} f(t) = \frac{1}{\Gamma(1-\alpha)} \int_t^b (s-t)^{-\alpha} f(s) ds, \quad t \in [a, b).$$

**Definition 3.** [15] The left and the right Caputo fractional derivatives of order  $\alpha \in R$ , ( $0 < \alpha < 1$ ) is defined, respectively, by

$$D_{a+}^\alpha f(t) = I_{a+}^{1-\alpha} \frac{d}{dt} f(t) = \frac{1}{\Gamma(1-\alpha)} \int_a^t (t-s)^{-\alpha} f'(s) ds, \quad t \in (a, b],$$

and

$$D_{b-}^\alpha f(t) = -I_{b-}^{1-\alpha} \frac{d}{dt} f(t) = -\frac{1}{\Gamma(1-\alpha)} \int_t^b (s-t)^{-\alpha} f'(s) ds, \quad t \in [a, b).$$

requires  $f'(s) \in L^1(0, T)$ .

**Definition 4.** A function  $u \in L^1_{loc}(\Omega_T)$ , ( $\Omega_T := (x, t) \in R \times (0, T)$ ) is a local weak solution to time-fractional diffusion equation on  $\Omega_T$  such that

$$L(u, \varphi) = \int_{\Omega_T} u(x, t) D_{T-}^{1-\alpha} \varphi_{xx}(x, t) dx dt + \int_{\Omega_T} u(x, t) \varphi_t(x, t) dx dt + \int_{\Omega_T} u^p(x, t) \varphi(x, t) dx dt$$

where

$$L(u, \varphi) = \int_0^T D_{t+}^{1-\alpha} u(x, t) \varphi_x(x, t) \Big|_R dt - \int_0^T \frac{\partial}{\partial x} D_{t+}^{1-\alpha} u(x, t) \varphi(x, t) \Big|_R dt - \int_R u_0(x) \varphi(x, 0) dx,$$

for any test function  $\varphi(x, t) \in C^{2,1}_{x,t}(\Omega_T)$  defined on the domain  $\Omega_T$  with  $\varphi(x, T) = 0$ .

**Property 5.** Integrating fractional integral by parts

$$\int_{\Omega_T} I_{t+}^\alpha u(x, t) f(x, t) dx dt = \int_{\Omega_T} u(x, t) I_{T-}^{1-\alpha} f(x, t) dx dt.$$

**Main results**

Multiply the time-fractional diffusion equation (1) by a test function  $\varphi(x, t)$ , we have

$$\int_0^T \int_R u_t(x, t) \varphi(x, t) dx dt = \int_0^T \int_R \frac{\partial^2}{\partial x^2} D_{t+}^{1-\alpha} u(x, t) \varphi(x, t) dx dt + \int_0^T \int_R u^p(x, t) \varphi(x, t) dx dt.$$

Integrating by parts the equation (3) and note that  $\varphi(x, T) = 0$  we get

$$\int_0^T \int_R u_t(x, t) \varphi(x, t) dx dt = - \int_R u_0(x) \varphi(x, 0) dx + \int_0^T \int_R u(x, t) \varphi_t(x, t) dx dt, \tag{5}$$

and

$$\begin{aligned} & \int_0^T \int_R \frac{\partial^2}{\partial x^2} D_{t+}^{1-\alpha} u(x,t) \varphi(x,t) dxdt = \\ & = \int_0^T \frac{\partial}{\partial x} D_{t+}^{1-\alpha} u(x,t) \varphi(x,t) \Big|_R dt - \\ & \quad - \int_0^T D_{t+}^{1-\alpha} u(x,t) \varphi_x(x,t) \Big|_R dt + \\ & \quad + \int_0^T \int_R D_{t+}^{1-\alpha} u(x,t) \varphi_{xx}(x,t) dxdt \end{aligned} \tag{6}$$

By Property 5 the last part of the (6), can be written as

$$\begin{aligned} & \int_0^T \int_R D_{t+}^{1-\alpha} u(x,t) \varphi_{xx}(x,t) dxdt = \\ & = \int_0^T \int_R u(x,t) D_{T-}^{1-\alpha} \varphi_{xx}(x,t) dxdt \end{aligned}$$

Obviously, we can write the equation (3)-(4) in the following form

$$\begin{aligned} L(u, \varphi) &= \int_{\Omega_T} u(x,t) D_{T-}^{1-\alpha} \varphi_{xx}(x,t) dxdt + \\ & + \int_{\Omega_T} u(x,t) \varphi_t(x,t) dxdt + \\ & + \int_{\Omega_T} u^p(x,t) \varphi(x,t) dxdt \end{aligned} \tag{7}$$

where

$$\begin{aligned} L(u, \varphi) &= \int_0^T D_{t+}^{1-\alpha} u(x,t) \varphi_x(x,t) \Big|_R dt - \\ & - \int_0^T \frac{\partial}{\partial x} D_{t+}^{1-\alpha} u(x,t) \varphi(x,t) \Big|_R dt - \int_R u_0(x) \varphi(x,0) dx, \end{aligned}$$

$$\begin{aligned} & \int_{\Omega_{TR^{2/\theta}}} u(x,t) [D_{TR^{2/\theta}-}^{1-\alpha} \varphi_{xx}(x,t)] \varphi(x,t) dxdt \leq \\ & \leq \varepsilon \int_{\Omega_{TR^{2/\theta}}} |u(x,t)|^p \varphi(x,t) dxdt + C(\varepsilon) \int_{\Omega_{TR^{2/\theta}}} |D_{TR^{2/\theta}-}^{1-\alpha} \varphi_{xx}(x,t)|^{p'} \varphi^{-p'/p}(x,t) dxdt. \end{aligned}$$

**Theorem 1.** Let  $p > 1$ . If

$$1 < p \leq p_c = 1 + \frac{2}{\alpha},$$

then problem (3) admits no global weak nonnegative solutions other than the trivial one.

Proof. The proof proceeds by contradiction. Suppose that  $u$  is a nontrivial nonnegative solution which exists globally in time. That is  $u$  exists in  $(0, T^*)$  for any arbitrary  $T^* > 0$ . Let  $T, R$  and  $\theta$  be positive real numbers such that  $0 < TR^{2/\theta} < T^*$ .

Let  $\Phi(z)$  be a smooth nonincreasing function such that

$$\Phi(z) = \begin{cases} 1 & \text{if } z \leq 1 \\ 0 & \text{if } z \geq 2 \end{cases}$$

and  $0 \leq \Phi(z) \leq 1$ .

The test function  $\varphi(x,t)$  is chosen so that

$$\begin{aligned} & \int_{\Omega_T} |D_{TR^{2/\theta}-}^{1-\alpha} \varphi_{xx}(x,t)|^{p'} \varphi^{-p'/p}(x,t) dxdt < \\ & < \infty, \int_{\Omega_T} |\varphi_t(x,t)|^{p'} \varphi^{-p'/p}(x,t) dxdt < \infty. \end{aligned} \tag{8}$$

To estimate the right-hand side of the Definition 4 on  $\Omega_{TR^{2/\theta}}$ , we write

$$\begin{aligned} & \int_{\Omega_{TR^{2/\theta}}} u(x,t) [D_{TR^{2/\theta}-}^{1-\alpha} \varphi_{xx}(x,t)] dxdt = \\ & = \int_{\Omega_{TR^{2/\theta}}} u(x,t) \varphi^{1/p}(x,t) [D_{TR^{2/\theta}-}^{1-\alpha} \varphi_{xx}(x,t)] \varphi^{-1/p}(x,t) dxdt \end{aligned}$$

Therefore, by using the  $\varepsilon$ -Young equality we have

Similarly,

$$\int_{\Omega_{TR^{2/\theta}}} u(x,t)\varphi_t(x,t) dxdt \leq \varepsilon \int_{\Omega_{TR^{2/\theta}}} |u(x,t)|^p \varphi(x,t) dxdt + C(\varepsilon) \int_{\Omega_{TR^{2/\theta}}} |\varphi_t(x,t)|^{p'} \varphi^{-p'/p}(x,t) dxdt.$$

Now, taking  $\varepsilon$  small enough, we obtain the estimate

$$\int_{\Omega_{TR^{2/\theta}}} |u(x,t)|^p \varphi(x,t) dxdt \leq C(\varepsilon) \int_{\Omega_{TR^{2/\theta}}} \left\{ |D_{TR^{2/\theta}}^{1-\alpha} \varphi_{xx}(x,t)|^{p'} + |\varphi_t(x,t)|^{p'} \right\} \varphi^{-p'/p}(x,t) dxdt. \tag{9}$$

We set

$$\Omega := \left\{ (y, \tau) \in R \times (0, T / R^{2/\theta}), y^2 + \tau^\theta < 2 \right\},$$

$$\varphi(x,t) = \Phi \left( \frac{x^2 + t^\theta}{R^2} \right),$$

$$\mu(y, \tau) = y^2 + \tau^\theta.$$

where  $R, \theta \in \mathbb{Z}^+$ .

Let us perform the change of variables  $t = \tau R^{2/\theta}$ ,  $x = yR$  and set

Now, we choose  $\theta$  such that the right-hand sides of

$$\begin{aligned} \int_{\Omega_{TR^{2/\theta}}} |D_{TR^{2/\theta}}^{1-\alpha} \varphi_{xx}(x,t)|^{p'} \varphi^{-p'/p}(x,t) dxdt &= \int_{\Omega_{TR^{2/\theta}}} \left| -\frac{1}{\Gamma(\alpha)} \int_{\tau R^{2/\theta}}^{TR^{2/\theta}} (s-t)^{\alpha-1} \varphi_{xxx}(x,s) ds \right|^{p'} \varphi^{-p'/p}(x,t) dxdt = \\ &= \int_{\Omega_{TR^{2/\theta}}} \left| -\frac{1}{\Gamma(\alpha)} \int_{\tau}^T (R^{2/\theta} \xi - R^{2/\theta} \tau)^{\alpha-1} \frac{1}{R^2 R^{2/\theta}} (\Phi_{\xi yy} \circ \mu) R^{2/\theta} d\xi \right|^{p'} (\Phi \circ \mu)^{-p'/p} R dy R^{2/\theta} d\tau \leq \\ &\leq R^{2/\theta(\alpha-1)p'-2p'+2/\theta+1} \int_{\Omega_{TR^{2/\theta}}} \left| -\frac{1}{\Gamma(\alpha)} \int_{\tau}^T (\xi - \tau)^{\alpha-1} (\Phi_{\xi yy} \circ \mu) d\xi \right|^{p'} (\Phi \circ \mu)^{-p'/p} dy d\tau \leq \\ &\leq R^{2/\theta(\alpha-1)p'-2p'+2/\theta+1} \int_{\Omega_{TR^{2/\theta}}} |D_{T-}^{1-\alpha} (\Phi_{\tau yy} \circ \mu)|^{p'} (\Phi \circ \mu)^{-p'/p} dy d\tau \end{aligned}$$

and

$$\int_{\Omega_{TR^{2/\theta}}} |\varphi_t(x,t)|^{p'} \varphi^{-p'/p}(x,t) dxdt \leq R^{-2/\theta p'+2/\theta+1} \int_{\Omega_{TR^{2/\theta}}} |(\Phi_\tau \circ \mu)|^{p'} (\Phi \circ \mu)^{-p'/p} dy d\tau$$

are of the same order in  $R$ . In doing so we find  $\theta = \alpha$ .

Then have the estimate

$$\int_{\Omega_{TR^{2/\alpha}}} |u(x,t)|^{p'} \varphi(x,t) dxdt \leq CR^\lambda, \tag{10}$$

where

$$\lambda = \frac{2}{\theta}(\alpha - 1)p' - 2p' + \frac{2}{\theta} + 1$$

and

$$C = C(\varepsilon) \int_{\Omega_{TR^{2/\theta}}} \left( \left| D_{T^-}^{1-\alpha} (\Phi_{\tau yy} \circ \mu) \right|^{p'} + \left| (\Phi_{\tau} \circ \mu) \right|^{-p'} \right) \left| (\Phi \circ \mu) \right|^{-p'/p} dyd\tau.$$

If we choose  $\lambda < 0$ , (i.e. is  $p < p_c$ ) and let  $R \rightarrow \infty$  in (10), we obtain

$$\int_{\Omega} u^p(x, t) dxdt \leq 0. \tag{11}$$

This implies that  $u = 0$  a.e., which is a contradiction.

In case  $\lambda = 0$ , (i.e. is  $p = p_c$ ) observe that the convergence of the integral in (10) if

$$\Omega_R = \{(x, t) \in R \times (0, T) : R^2 < x^2 + t^\alpha \leq 2R^2\}$$

then

$$\lim_{R \rightarrow \infty} \int_{\Omega_R} |u(x, t)|^p \varphi(x, t) dxdt = 0 \tag{12}$$

If instead of using the  $\varepsilon$ -Young equality, we rather use the Hölder inequality, then instead of estimate (9), we get

$$\int_{\Omega_{TR^{2/\alpha}}} |u(x, t)|^p \varphi(x, t) dxdt \leq L \left( \int_{\Omega_R} |u(x, t)|^p \varphi(y, \tau) dyd\tau \right)^{1/p} \tag{13}$$

where

$$L := \left( \int_{\Omega_1} \left| D_{T^-}^{1-\alpha} (\Phi_{\tau yy} \circ \mu) \right|^{p'} (\Phi \circ \mu)^{-p'/p} dyd\tau \right)^{p'} + \left( \int_{\Omega_1} \left| (\Phi_{\tau} \circ \mu) \right|^{p'} (\Phi \circ \mu)^{-p'/p} dyd\tau \right)^{1/p'}$$

and

$$\Omega_1 = \{(y, \tau) \in R \times (0, T / R^{2/\alpha}) : 1 < y^2 + \tau^\alpha \leq 2\}.$$

Using (13), we obtain via (12), after passing to the limit as  $R \rightarrow \infty$ ,

$$\int_{\Omega} |u(x, t)|^p dxdt = 0$$

This leads to  $u = 0$  a.e. and completes the proof.

**Conclusion**

In this paper were studied Fujita-type critical exponents for certain time-fractional diffusion equations with the nonnegative initial condition. As a result, using the test function method, the critical

exponents of Fujita were determined in the following form  $1 < p \leq p_c = 1 + \frac{2}{\alpha}$ .

Consequently, by using the Fujita-type critical exponents we proved that, the problem (3) admits no global weak nonnegative solutions other than the trivial one.

**Acknowledgments**

This research is financially supported by a grant No. AP05131756 from the Ministry of Science and Education of the Republic of Kazakhstan.

**References**

1. Kaplan S. "On the growth of solutions quasi-linear parabolic equations." *Comm. Pure Appl. Math.* 16 (1963): 305-330.

2. Ito S. "On the blowing up of solutions quasi-linear parabolic equations." *Bulletin of the Mathematical Society of Japan*. 18, no. 1 (1966): 44-47.
3. Friedman A. "Remarks on non-linear parabolic equations." *Proc. of Symposia in Appl. Math.* 17 (1965): 3-23.
4. Fujita H. "On the blowing up of solutions of the Cauchy problem for  $u_t = \Delta u + u^{1+\alpha}$ ." *J. Fac. Sci. Univ. Tokyo Sect. 13* (1966): 109-124.
5. Hayakawa. "On Nonexistence of Global Solutions of Some Semilinear Parabolic Differential Equations." *Proc. Japan Acad.* 49, no. 7 (1973).
6. Kobayashi K., Sirao T. and Tanaka H. "On the growing up problem for semilinear heat equations." *J. Math. Soc. Japan*. 29, no. 3 (1977).
7. Weissler F.B. "Existence and non-existence of global solutions for a semilinear heat equation." *Israel J. Math.* 38, no. 1-2 (1981).
8. Fujita H. "On some nonexistence and nonuniqueness theorems for nonlinear parabolic equations." *Proc. Symp. Pure Math.* 18, part I (1968): 138-161.
9. Bandle C. and Levine. "On the existence and nonexistence of global solutions of reaction-diffusion equations in sectorial domains." *Trans. Amer. Math. Soc.* 316, no. 2 (1989): 595-622.
10. Samarskii A., Galaktionov V., Kurdyumov, S., and Mikhailov A. "Blow-up in quasilinear parabolic equations." *Bulletin (New Series) of the American Mathematical Society* 33, no. 4 (1996).
11. Qi Y.W. "The critical exponents of parabolic equations and blow-up in  $R^N$ ." *Proc. Roy. Soc. Edinburgh Sect. A*. 128, no. 1(1998): 123-136.
12. Sugitani S. "On nonexistence of global solutions for some nonlinear integral equations." *Osaka J. Math.* 12 (1975): 29-40.
13. Guedda M. and Kirane, M. "A note on nonexistence of global solutions to a nonlinear integral equation." *Bull. of the Belgian Math. Soc.* 6 (1999): 491-497.
14. Kirane M., Laskri Y., Tatar N., "Critical exponents of Fujita type for certain evolution equations and systems with spatio-temporal fractional derivatives." *J. Math. Anal. Appl.* 312 (2005): 488-501.
15. Kilbas A. A., Srivastava H. M. and Trujillo J. J.. *Theory and Applications of Fractional Differential Equations*. North-Holland Mathematics Studies. (2006) 69-90.
16. Pohozaev S.I. and Mitidieri E.L. "A priori estimates and blow-up of solutions to nonlinear partial differential equations and inequalities." *Tr. Mat. Inst. Steklova*. 269 (2010): 110-119.

IRSTI 27.29.23

<sup>1</sup>B. Bekbolat, <sup>2</sup>N. Tokmagambetov

<sup>1</sup>Al-Farabi Kazakh National University, Almaty, Kazakhstan  
<sup>2</sup>Institute of Mathematics and Mathematical Modeling, Almaty, Kazakhstan  
 e-mail: tokmagambetov@math.kz

### On a boundedness result of non-toroidal pseudo-differential operators

**Abstract.** In this article, we prove boundedness results for  $\theta$ -toroidal pseudo-differential operators generated by a differentiation operator with a non-periodic boundary condition.  $\theta$ -toroidal pseudo-differential operators are a natural generalization of a toroidal one. As in the classical case, this class of operators act on a suitable test function space by weighting the Fourier transform “very well”. Standard operations as adjoints, products and commutators with  $\theta$ -toroidal pseudo-differential operators can be characterized by their  $\theta$ -toroidal symbols. For pseudo-differential operators on  $\mathbb{R}^n$ , the symbol analysis is well developed. Here, we provide more complicated properties of the  $\theta$ -toroidal pseudo calculus. Namely, we introduce a Holder space induced by a differentiation operator with a non-periodic boundary condition. Finally, for the elements of this space we prove theorems on boundedness of the operators acting on the specified functional spaces. Indeed, in this paper we continue a development of the so called “non-harmonic analysis” introduced in the recent papers of the authors.

**Key words:**  $\theta$ -toroidal pseudo-differential operator,  $\theta$ -toroidal Holder space,  $\theta$ -Fourier transform,  $\theta$ -symbol, bounded operator.

#### Introduction

In [3], it was introduced an analysis generated by the differential operator

$$Ly(x) = -i \frac{dy(x)}{dx}, \quad 0 < x < 1 \quad (1)$$

acting on  $L_2(0; 1)$  with the boundary condition

$$\theta y(0) - y(1) = 0, \quad (2)$$

where  $\theta \geq 1$ .

Spectrum of the operator  $L$  is

$$\lambda_\xi = -i \ln \theta + 2\xi\pi, \quad \xi \in \mathbb{Z} \quad (3)$$

System of eigenfunctions of the operator  $L$  is

$$u_\xi(x) = \theta^x e^{i2\xi\pi x}, \quad \xi \in \mathbb{Z}. \quad (4)$$

and the biorthogonal system to  $u_\xi(x)$  in  $L_2(0; 1)$  is

$$v_\xi(x) = \theta^{-x} e^{i2\xi\pi x}, \quad \xi \in \mathbb{Z}. \quad (5)$$

For the following spectral properties of the operator  $L$  we refer to [3] and [7].

1. The system of eigenfunctions of the operator  $L$  is a Riesz basis in  $L_2(0; 1)$ ;
2. If function  $f$  belongs to the domain of operator  $L$ , then  $f(x)$  expands to a uniformly convergent series of eigenfunctions of the operator  $L$ ;
3. The resolvent of the operator  $L$  is

$$(L - \lambda I)^{-1}f(x) = i \frac{e^{i\lambda(x+1)}}{\Delta(\lambda)} \int_0^1 e^{-i\lambda t} f(t) dt + ie^{i\lambda x} \int_0^x e^{-i\lambda t} f(t) dt,$$

Where  $\Delta(\lambda) = \theta - e^{i\lambda}$ .

$$|\Delta_\xi^\alpha \partial_x^\beta a(x, \xi)| \leq C_{\alpha\beta m} \langle \xi \rangle^{m-\rho\alpha+\delta\beta} \tag{10}$$

**$\theta$ -toroidal pseudo-differential operators**

$\theta$ -Fourier transform and  $\theta$ -toroidal Hölder spaces. Here we give a definition of  $\theta$ -Fourier transform [3].  $\theta$ -Fourier transform  $(f \mapsto \hat{f}): C_0^\infty[0,1] \rightarrow S(Z)$  is given by

$$\hat{f}(\xi) := \int_0^1 f(x) \overline{v_\xi(x)} dx \tag{6}$$

and its inverse  $\hat{f}(\xi)^{-1}$  is given by

$$f(x) = \sum_{\xi \in Z} \hat{f}(\xi) u_\xi(x). \tag{7}$$

*Remark 1* The functional space  $C_0^\infty[0,1]$  is called the space of test functions and  $S(Z)$  is space of rapidly decaying functions [3].

In what follows, we will use the following spaces from [5].

We define  $\theta$ -toroidal Hölder spaces

$$\Lambda^s([0,1], \theta) = \left\{ f: [0,1] \rightarrow \mathbb{C}: |f|_{\Lambda^s} = \sup_{x,h \in [0,1]} \frac{|f(x+h)-f(x)|}{|h|^s} < \infty \right\} \tag{8}$$

$$\Lambda_0^s([0,1], \theta) = \{f \in \Lambda^s([0,1], \theta): f(0) = 0\} \tag{9}$$

for each  $0 < s \leq 1$ . These spaces are Banach.

$\theta$ -toroidal symbol class. Suppose that  $m \in \mathbb{R}, 0 \leq \delta, \rho \leq 1$ . Then the  $\theta$ -toroidal symbol class  $S_{\delta, \rho}^m([0,1] \times Z)$  consists of those function  $a(x, \xi)$  which are smooth in  $x$  for all  $\xi \in Z$ , and which satisfy

for every  $\xi \in Z, x \in [0,1], \alpha, \beta \in Z_+$ , where

$$\langle \xi \rangle := 1 + |\xi|.$$

We call  $a(x, \xi)$  a symbol [3]. The operator  $\Delta_\xi$  is the difference operator

$$\Delta_\xi \hat{\sigma}(\xi) := \widehat{\epsilon \sigma}(\xi),$$

where  $\hat{\sigma}(\xi): Z \rightarrow \mathbb{C}$ .

We denote the  $\theta$ -toroidal pseudo-differential operator by

$$a(X, D)f(x) = \sum_{\xi \in Z} u_\xi(x) a(x, \xi) \hat{f}(\xi) \tag{11}$$

where  $a(x, \xi)$  is a symbol of a  $\theta$ -toroidal pseudo-differential operator [5].

We can write for  $h \in T$ ,

$$a(X, D)f(x+h) = \sum_{\xi \in Z} u_\xi(x) a(x+h, \xi) \int_0^1 f(y+h) \overline{v_\xi(x)} dy.$$

**Theorem 1. (Bernstein).** Assume that  $f \in \Lambda_0^s([0,1], \theta)$ , for  $s > \frac{1}{2}$ . Then we have  $|\hat{f}|_{L^1(Z)} \leq C_s \|f\|_{\Lambda^s}$ .

**Proof.** We prove this statement by recalling a definition of the norm

$$\begin{aligned} |\hat{f}|_{L^1(Z)} &= \sum_{\xi \in Z} |\hat{f}(\xi)| = \sum_{\xi \in Z} \left| \int_0^1 f(x) \overline{v_\xi(x)} dx \right| \leq \sum_{\xi \in Z} \int_0^1 |f(x)| dx = \\ &= \sum_{\xi \in Z} \int_0^1 \frac{|f(x) - f(0)|}{|x|^s} |x|^s dx \leq \sum_{\xi \in Z} \int_0^1 \sup_{x \in [0,1]} \frac{|f(x) - f(0)|}{|x|^s} |x|^s dx \\ &\leq \sum_{\xi \in Z} |f|_{\Lambda^s} \int_0^1 x^s dx \leq \sum_{\xi \in Z} \frac{1}{s+1} |f|_{\Lambda^s} \leq \sum_{\xi \in Z} \frac{1}{s+1} \left( |f|_{\Lambda^s} + \sup_{x \in [0,1]} |f(x)| \right) = \left( \sum_{\xi \in Z} \frac{1}{s+1} \right) \|f\|_{\Lambda^s} \leq C_s \|f\|_{\Lambda^s}. \end{aligned}$$

Finally, we proved the theorem.

### Boundedness for $\theta$ -toroidal pseudo-differential operator

Here we prove similar theorems as in [5].

**Theorem 2.** Let  $a(X, D) = a(D)$  be a pseudo-differential operator with symbol  $a(\xi)$  depending only on the discrete variable  $\xi$ . If  $a(\xi) \in L^1(\mathbb{Z})$ , then

$$|a(D)f|_{\Lambda^s} \leq \|a\|_{L^1(\mathbb{Z})} \|f\|_{\Lambda^s},$$

for  $0 < s \leq 1$ .

**Proof.** By the formula, we have

$$\begin{aligned} & a(X, D)f(x+h) - a(X, D)f(x) = \\ & = \sum_{\xi \in \mathbb{Z}} u_{\xi}(x) a(\xi) \int_0^1 (f(y+h) - f(y)) \overline{v_{\xi}(y)} dy. \end{aligned}$$

Thus, we obtain

$$\begin{aligned} & \frac{|a(X, D)f(x+h) - a(X, D)f(x)|}{|h|^s} \leq \\ & \leq \sum_{\xi \in \mathbb{Z}} \left( |a(\xi)| \int_0^1 \frac{|f(y+h) - f(y)|}{|h|^s} dy \right). \end{aligned}$$

$$\begin{aligned} & \frac{|a(X, D)f(x+h) - a(X, D)f(x)|}{|h|^s} \leq \sum_{\xi \in \mathbb{Z}} |h|^{1-s} |a(x_h, \xi) \ln \theta + i2\pi \xi a(x_h, \xi) + a'(x_h, \xi)| |\hat{f}(\xi)| \leq \\ & \leq \sum_{\xi \in \mathbb{Z}} C_1 (|\ln \theta| |a(x_h, \xi)| + 2\pi |\xi| |a(x_h, \xi)| + |a'(x_h, \xi)|) |\hat{f}(\xi)| \leq \sum_{\xi \in \mathbb{Z}} C_1 (C\langle \xi \rangle^m + |\xi| C\langle \xi \rangle^m + C\langle \xi \rangle^{m+\delta}) |\hat{f}(\xi)| \leq \\ & \leq \sum_{\xi \in \mathbb{Z}} C_1 (C\langle \xi \rangle^m + C\langle \xi \rangle^{m+1} + C\langle \xi \rangle^{m+\delta}) |\hat{f}(\xi)| \leq \sum_{\xi \in \mathbb{Z}} 3CC_1 |\hat{f}(\xi)| \leq 3CC_1 C_s \|f\|_{\Lambda^s}. \end{aligned}$$

Thus,

$$|a(X, D)f|_{\Lambda^s} \leq M \|f\|_{\Lambda^s}.$$

The next theorem gives a single sufficient condition on the symbol  $a(x, \xi)$  for the corresponding pseudo-differential operator

$$a(X, D): \Lambda_0^s([0, 1], \theta) \rightarrow \Lambda^s([0, 1], \theta)$$

Finally, we get

$$|a(D)f|_{\Lambda^s} \leq \left( \sum_{\xi \in \mathbb{Z}} |a(\xi)| \right) \|f\|_{\Lambda^s}.$$

**Theorem 3.** Let  $\frac{1}{2} < s < 1$  and  $a \in S_{\delta, \rho}^{-m}([0, 1] \times \mathbb{Z})$ ,  $m \geq 1$ . Then there exists  $M > 0$  such that

$$|a(X, D)f|_{\Lambda^s} \leq M \|f\|_{\Lambda^s}.$$

**Proof.** By the mean value theorem, there exists  $x_h \in [0, 1]$  such that

$$\begin{aligned} & u_{\xi}(x+h)a(x+h, \xi) - u_{\xi}(x)a(x, \xi) = \\ & = hu_{\xi}(x_h)(a(x_h, \xi) \ln \theta + i2\pi \xi a(x_h, \xi) + a'(x_h, \xi)). \end{aligned}$$

By the Bernstein's theorem, we have

to be bounded for  $0 < s < 1$ .

**Theorem 4.** Let  $0 < s < 1$ ,  $0 \leq \delta < \rho \leq 1$  and  $m > 1 + \delta$ . If  $a \in S_{\delta, \rho}^{-m}$  then, the operator

$$a(X, D): \Lambda_0^s([0, 1], \theta) \rightarrow \Lambda^s([0, 1], \theta)$$

is bounded.

**Proof.** Suppose  $f \in \Lambda_0^s([0, 1], \theta)$ , we get

$$\begin{aligned}
 & a(X, D)f(x + h) - a(X, D)f(x) = \\
 & = \sum_{\xi \in Z} u_{\xi}(x) \left( a(x + h, \xi) \int_0^1 f(y + h) \overline{v_{\xi}(y)} dy - a(x, \xi) \int_0^1 f(y) \overline{v_{\xi}(y)} dy \right) = \\
 & = \sum_{\xi \in Z} u_{\xi}(x) \left( a(x + h, \xi) \int_0^1 (f(y + h) - f(y)) \overline{v_{\xi}(y)} dy \right) + \\
 & + \sum_{\xi \in Z} u_{\xi}(x) \left( (a(x + h, \xi) - a(x, \xi)) \int_0^1 f(y) \overline{v_{\xi}(y)} dy \right).
 \end{aligned}$$

Therefore, using the value mean theorem, we obtain

$$\begin{aligned}
 & \frac{|a(X, D)f(x + h) - a(X, D)f(x)|}{|h|^s} \\
 & \leq \sum_{\xi \in Z} \left( |a(x + h, \xi)| \int_0^1 \frac{|f(y + h) - f(y)|}{|h|^s} dy + \frac{|a(x + h, \xi) - a(x, \xi)|}{|h|^s} \int_0^1 |f(y)| dy \right) \\
 & \leq \sum_{\xi \in Z} \left( |a(x + h, \xi)| \int_0^1 \frac{|f(y + h) - f(y)|}{|h|^s} dy + \frac{|h| |a'(x_h, \xi)|}{|h|^s} \int_0^1 |f(y)| dy \right) \\
 & \leq \sum_{\xi \in Z} \left( C\langle \xi \rangle^{-m} |f|_{\Lambda_0^s} + |h|^{1-s} C\langle \xi \rangle^{-m+\delta} \int_0^1 |f(y)| dy \right) \leq \sum_{\xi \in Z} \left( C\langle \xi \rangle^{-m} |f|_{\Lambda_0^s} + |h|^{1-s} C \int_0^1 \frac{|f(y) - f(0)|}{|y|^s} |y|^s dy \right) \\
 & \leq |f|_{\Lambda_0^s} (\sum_{\xi \in Z} C\langle \xi \rangle^{-m+\delta}) \left( \langle \xi \rangle^{-\delta} + \frac{1}{s+1} \right) \leq |f|_{\Lambda_0^s} (\sum_{\xi \in Z} C\langle \xi \rangle^{-m+\delta}) \left( 1 + \frac{1}{s+1} \right).
 \end{aligned}$$

Finally, we obtain

$$|a(X, D)f|_{\Lambda^s} \leq |f|_{\Lambda_0^s} \left( \sum_{\xi \in Z} C\langle \xi \rangle^{-m+\delta} \right) \left( 1 + \frac{1}{s+1} \right).$$

*Remark.* It follows from the proof of Theorem 4 that

$$|a(X, D)f|_{\Lambda^s} \leq |f|_{\Lambda_0^s} \sum_{\xi \in Z} \left( C\langle \xi \rangle^{-m+\delta} + \frac{|a(\cdot, \xi)|_{\Lambda_0^s}}{s+1} \right).$$

So, if  $|a(\cdot, \xi)|_{\Lambda_0^s} \in L^1(Z)$ , then  $|a(X, D)f|_{\Lambda^s} \leq M|f|_{\Lambda_0^s}$ , with  $M = \sum_{\xi \in Z} C_1 \left( C\langle \xi \rangle^{-m+\delta} + \frac{|p(\cdot, \xi)|_{\Lambda_0^s}}{s+1} \right) < \infty$ . In conclusion, the operator  $a(X, D)$  will be bounded from  $\Lambda_0^s([0, 1], \theta)$  into  $\Lambda^s([0, 1], \theta)$ . So we obtain the next result:

**Theorem 5.** Let  $s \neq 1$ ,  $m > 1$  and  $|a(\cdot, \xi)|_{\Lambda_0^s} \in L^1(Z)$ . If  $a \in S_{\delta, \rho}^{-m}$  then  $a(X, D): \Lambda_0^s([0, 1], \theta) \rightarrow \Lambda^s([0, 1], \theta)$  is a bounded operator.

**Theorem 6.** Let  $0 < \varepsilon < 1$  and  $k \in \mathbb{N}$  with  $k > \frac{n}{2}$ , let  $a$  be a symbol such that  $|\Delta_{\xi}^{\alpha} a(x, \xi)| \leq C_{\alpha} \langle \xi \rangle^{-\frac{n}{2} \varepsilon - (1-\varepsilon)|\alpha|}$ ,  $|\partial_x^{\beta} \xi a(x, \xi)| \leq C_{\beta} \langle \xi \rangle^{-\frac{n}{2}}$ , for  $|\alpha|, |\beta| \leq k$ . Then,  $a(X, D)$  is a bounded operator from  $L^p(\mathbb{T})$  into  $L^p(\mathbb{T})$  for  $2 \leq p < \infty$ .

In the following theorems, we obtain Hölder boundedness using the Morrey inequality [6]: if  $1 < p < \infty$  and  $s_p = 1 - \frac{1}{p}$ , then for  $x, y \in \mathbb{R}$  we have

$$\frac{|u(x+h) - u(x)|}{|h|^{s_p}} \leq |u'(x)|_{L^p(\mathbb{R})}.$$

$$\begin{aligned} \frac{|a(X, D)f(x+h) - a(X, D)f(x)|}{|h|^{s_p}} &\leq C \left| \frac{d}{dx} a(X, D)u \right|_{L^2} \leq C \left\| \frac{d}{dx} a(X, D) \right\|_{(L^2, L^2)} |u|_{L^2} \\ &= C \left\| \frac{d}{dx} a(X, D) \right\|_{(L^2, L^2)} \left( \int_0^1 \frac{|u(x) - u(0)|}{|x|^{2(\frac{1}{2})}} |x|^{2(\frac{1}{2})} dx \right)^{\frac{1}{2}} \leq C \left\| \frac{d}{dx} a(X, D) \right\|_{(L^2, L^2)} \left(\frac{1}{2}\right)^{\frac{1}{2}} |u|_{\Lambda_0^{\frac{1}{2}}} \end{aligned}$$

Finally,

$$\|a(X, D)f\|_{\Lambda_0^{\frac{1}{2}}([0,1], \theta)} \leq \max \left\{ \sup_{x \in [0,1]} |a(x, \cdot)|_{L^1(\mathbb{Z})}, C \left\| \frac{d}{dx} a(X, D) \right\|_{(L^2, L^2)} \left(\frac{1}{2}\right)^{\frac{1}{2}} \right\} \|f\|_{\Lambda_0^{\frac{1}{2}}([0,1], \theta)}$$

**Theorem 8.** Let  $0 < \varepsilon < 1$  and  $a(x, \xi)$  be a symbol such that  $|\Delta_{\xi}^{\alpha} a(x, \xi)| \leq C_{\alpha} \langle \xi \rangle^{-\frac{\varepsilon}{2} - (1-\varepsilon)|\alpha|}$ ,  $|\partial_x^{\beta} \xi a(x, \xi)| \leq C_{\beta} \langle \xi \rangle^{-\frac{\varepsilon}{2}}$ , for  $0 \leq |\alpha|, |\beta| \leq 1$ . If  $\frac{1}{2} < s < 1$ , then  $a(X, D): \Lambda_0^s([0,1], \theta) \rightarrow \Lambda^s([0,1], \theta)$  is a bounded linear operator.

$$\begin{aligned} \frac{|a(X, D)u(x+h) - a(X, D)u(x)|}{|h|^s} &\leq C \left| \frac{d}{dx} a(X, D)u \right|_{L^p} \leq C \left\| \frac{d}{dx} a(X, D) \right\|_{(L^p, L^p)} |u|_{L^p} \\ &= C \left\| \frac{d}{dx} a(X, D) \right\|_{(L^p, L^p)} \left( \int_0^1 \frac{|u(x) - u(0)|}{|x|^{p^s}} |x|^{p^s} dx \right)^{\frac{1}{2}} \leq C \left\| \frac{d}{dx} a(X, D) \right\|_{(L^p, L^p)} \left(\frac{1}{p}\right)^{\frac{1}{p}} |u|_{\Lambda_0^s}. \end{aligned}$$

Function on the torus may be thought as those functions on  $\mathbb{R}$  that are 1-periodic, under these assumptions, we can use a toroidal version of Morrey inequality on  $L^p(\mathbb{T})$ .

**Theorem 7.** Let  $0 \leq \delta < \rho \leq 1$  and  $m > 1$ . If  $a \in S_{\delta, \rho}^{-m}$ , then  $a(X, D): \Lambda_0^{\frac{1}{2}}([0,1], \theta) \rightarrow \Lambda^{\frac{1}{2}}([0,1], \theta)$  is a bounded operator.

**Proof.** The composition of the pseudo-differential operators  $\frac{d}{dx}$  and  $a(X, D)$  is the pseudo-differential operator  $\frac{d}{dx} a(X, D)$  of degree  $-m + 1 < 0$ , so,  $T = \frac{d}{dx} a(X, D): L^2(0,1) \rightarrow L^2(0,1)$ . If  $u \in \Lambda_0^{\frac{1}{2}}([0,1], \theta)$ , then

**Proof.** If  $\frac{1}{2} \leq s < 1$ , there exists  $2 \leq p < \infty$  such that  $s = 1 - \frac{1}{p}$ . Applying Theorem 6 to the symbol  $i2\pi\xi a(x, \xi)$  we obtain  $L^p(0,1)$ - boundedness for the operator  $\frac{d}{dx} a(X, D)$ . If  $u \in \Lambda_0^s([0,1], \theta)$ , then

Hence,

$$|a(X, D)u|_{\Lambda^s} \leq C \left\| \frac{d}{dx} a(X, D) \right\|_{(L^p, L^p)} \left( \frac{1}{p} \right)^{\frac{1}{p}} |u|_{\Lambda_0^s}$$

Now, since  $|\xi a(x, \xi)| \leq C \langle \xi \rangle^{-\frac{\varepsilon}{2}}$ , we get

$$|a(x, \xi)| \leq C \langle \xi \rangle^{-\frac{\varepsilon}{2}} |\xi|^{-1}, \xi \neq 0.$$

Hence, we obtain

$$M = \sup_{x \in [0,1]} |a(x, \cdot)|_{L^1(\mathbb{Z})} < \infty$$

Therefore

$$\|a(X, D)f\|_{\Lambda_0^s([0,1], \theta)} \leq \max \left\{ M, C \left\| \frac{d}{dx} p(X, D) \right\|_{(L^p, L^p)} \left( \frac{1}{p} \right)^{\frac{1}{p}} \right\} \|f\|_{\Lambda_0^s([0,1], \theta)}.$$

**Acknowledgement.** The authors were supported by the Ministry of Education and Science of the Republic of Kazakhstan, MESRK Grant AP05130994.

## References

1. Agranovich M.S. "Spectral properties of elliptic pseudo-differential operators on a closed curve." *Func. Anal. Appl.* 13 (1979): 279-281.
2. Agranovich M.S. "On elliptic pseudo-differential operators on a closed curve." *Trans. Moscow Math. Soc.* 47 (1985): 23-74.
3. Kanguzhin B.E., Tokmagambetov N. and Tulenov K. "Pseudo-differential operators generated by a non-local boundary value problem." *Complex Variables and Elliptic Equations* 60, no. 1 (2015): 107-117.
4. Brézis, H. "Analyse fonctionnelle: théorie et applications." (Paris: Éditions Dunod, 1999), 427.
5. Cardona D. "Holder estimates for pseudo-differential operators on  $T^1$ ." *J. Pseudo-Differ. Oper. Appl.* 5 (2014): 517-525.
6. Delgado, J. "L<sup>p</sup> bounds for pseudo-differential operators on the torus." *Oper. Theory Adv. Appl.* 231, (2012): 103-116.
7. Kanguzhin B.E, Sadybekov M.A. "Differential operators on a segment. Distributions of the eigenvalues." (Almaty: Gylym, 1996), 312.
8. Ruzhansky M, Turunen V. "Pseudo-differential operators and symmetries." (Basel: Birkhauser, 2010), 697.
9. Ruzhansky M, Turunen V. "Quantization of pseudo-differential operators on the torus." *J. Fourier Anal. Appl.* 16 (2010): 943-982.
10. Ruzhansky M, Turunen V. "On the Fourier analysis of operators on the torus. Modern trends in pseudo-differential operators." *Operator theory advances and applications* 172 (2007): 87-105.
11. Ruzhansky M, Turunen V. "Global quantization of pseudo-differential operators on compact Lie groups, SU(2) and 3-sphere." *Int. Math. Res. Not.* 11 (2013): 2439-2496.
12. Ruzhansky M, Turunen V. "Sharp garding inequality on compact Lie groups." *J. Funct. Anal.* 260 (2011): 2881-2901.
13. Ruzhansky M, Wirth J. "On multipliers on compact Lie groups." *Funct. Anal. Appl.* 47 (2013): 72-75.
14. Taylor M. "Pseudo-differential operators and nonlinear PDE." (Boston (MA): Birkhauser, 1991), 202.
15. Taylor M. "Pseudo-differential operators." (Princeton (NJ): Princeton University Press, 1981), 468.

IRSTI 27.35.17

D.B. Zhakebayev, \*K.K. Karzhaubayev, E.S. Moisseyeva, N.V. Tsoy

National Engineering Academy, Almaty, Kazakhstan

\*e-mail: kairzhan.k@gmail.com

### **Simulation of thermal flows by lattice Boltzmann method on the CUDA computational platform**

**Abstract.** Originating from lattice gas automata theory, the lattice Boltzmann method (LBM) is an interesting alternative to the solving of Navier-Stokes equations. In contrast to isothermal simulations, for a while thermal flow simulations were challenging for LBM. Thermal flow simulations are important task in various fields of research. Despite a large amount of work and research the dynamics of thermally induced flows are still highly demanded. Motivation of this work is development of computational tool for simulation of the dynamics of thermal flows. To this purpose, we developed LES-LBM solver accelerated by the Graphics Processing Unit (GPU) on the CUDA computational platform, integrating LBM with Large Eddy Simulation (LES). Simplicity of coding is usually an appealing feature of the LBM. Conventional implementations of LBM suffer from high memory consumption and poor computational performance. The main advantage of the solvers based on GPU is their ability to perform significantly more floating point operations per unit time (FLOPS) than a Central Processing Unit (CPU) and a good scalability of explicit parallel algorithms. LES-LBM code was tested on the NVIDIA GeForce GTX 1050 ti and NVIDIA TESLA K80 GPUs.

**Key words:** The lattice Boltzmann method, CUDA, thermal flow.

#### **Introduction**

In June 2007 NVIDIA released a new framework named CUDA for general parallel processing applications. This framework enables developers to implement GPU parallel programs in C, C++ languages and allows direct access to the GPU computing power without complicated graphics API. Special tools which are included in an official software development kit (SDK) allows to debug GPU programs in runtime. Since 2007 a lot of numerical libraries presented. They allow to create efficient programs with less effort, and cover such numerical algorithms like linear algebra operations, sparse matrix computations, Fourier transforms, image algorithms etc.

In a market NVIDIA has several separate products, GeForce is for gaming, Quadro is for professional OpenGL based rendering and Tesla for high performance computations. Tesla compute

accelerators get strong positions in a such high performance areas as financial analysis and scientific computations. A lot of supercomputer providers use NVIDIA GPUs to create energy efficient computing clusters. One of the secret of the high popularity among users is the support of most popular proprietary (CUDA) and open standards (OpenCL, DirectCompute) for GPU programming.

Effort to use GPU as a massively parallel processor computational fluid dynamics (CFD) started in the beginning of 2000. One of the first publications was a chapter in the GPU Gems Books by M. J. Harris [1]. In the Chapter 38 he described realization of simple fluid dynamics solver based on Stam's stable fluids [2]. Later several authors published results of implementing Marker and Cell method on a GPU [3].

The smoothed particle hydrodynamics (SPH) is another approach for simulation of the fluid dynamics, without direct use of the Navier Stokes

equations. Originally developed in [4] SPH is a meshfree Lagrangian method which tracks position and movement of many fluid particles, which allows direct mass conservation. One drawback over grid-based techniques is the need for large numbers of particles to produce simulations of equivalent resolution. Explicit nature of the method allows it to run effectively on massive parallel processors as GPU [5-7].

The lattice Boltzmann method (LBM) is a relatively novel approach in computational fluid dynamics (CFD), which, unlike most other CFD methods, does not rely in directly solving the Navier-Stokes equations by a numerical algorithm.

One of the most interesting feature of LBM is that numerical procedure has the data locality property. Such a property is very well suited to be implemented in a massively parallel processors, like GPUs [8-11]. In [12] LBM Large Eddy Simulations for high Reynolds numbers were performed. Developed numerical implementation was able to run on four Fermi class GPUs simultaneously. Large GPU memory (24GB) allowed to perform simulations with relatively high spatial resolution (max grid size 10240x10240) with active double precision mode. However, authors mentioned that four GPUs were located on the same machine, and there is strong hardware limitation for further improvement of spatial resolution. To overcome this fact, authors recommended to extend their implementation to multinode GPU clusters.

On the other hand, while for describing hydrodynamic turbulence models based on the Navier-Stokes equations have been used almost exclusively for almost two centuries, a significant increase in interest in LBM methods has recently been explained by their computational efficiency. These methods, based on the Boltzmann equation, make it possible to predict the macroscopic magnitudes of continuum mechanics, such as velocity and pressure. Although it was proven several years ago that hydrodynamic turbulence can be accurately described using these methods, the development of LES within LBM is still at a very early stage [13]. For example, the LES-LBM methods are used in [14-19].

**Lattice Boltzmann Method**

The basic quantity of the LBM is the discrete velocity distribution function  $f_i(\vec{x}, t)$  which is also called particle populations. Particle populations

represents the density of particles with velocity  $\vec{c}_i = (c_{ix}, c_{iy}, c_{iz})$  at position-time  $(\vec{x}, t), \vec{x} = \{x, y, z\}$ . The discrete velocities are chosen such as to link each lattice site to some of its neighbors. Fig. 1 shows the D3Q27 stencil, where each node is connected to 26 of its nearest neighbors, and position 0 assigned to resting particles.

$$\rho(\vec{x}, t) = \sum_i f_i(\vec{x}, t) \tag{1}$$

$$\rho u(\vec{x}, t) = \sum_i c_i f_i(\vec{x}, t) \tag{2}$$

By discretising the Boltzmann equation in velocity space, physical space, and time, we find the *lattice Boltzmann equation*:

$$f_i(\vec{x} + \vec{c}_i \Delta t, t + \Delta t) = f_i(\vec{x}, t) + \Omega_i(\vec{x}, t) + S_i \tag{3}$$

Where  $\Omega$  is collision operator and  $S_i$  is force. One of simplest models for collision is Bhatnagar-Gros-Krook [20], which relaxes the populations towards an equilibrium  $f^{eq}$  at a rate determined by the relaxation time  $\tau$ :

$$\Omega_i(f) = -\frac{f_i - f_i^{eq}}{\tau} \Delta t \tag{4}$$

$$f_i^{eq}(\vec{x}, t) = w_i \rho \left( 1 + \frac{u \cdot c_i}{c_s^2} + \frac{(u \cdot c_i)^2}{2c_s^4} - \frac{u \cdot u}{2c_s^2} \right) \tag{5}$$

Relation between physical kinematic viscosity and lattice relaxation time is given by [10], where  $c_s$  is the lattice speed of sound:

$$\nu = c_s^2 \left( \tau - \frac{\Delta t}{2} \right) \tag{6}$$

Numerical algorithm for LBM consists of collision (7) and streaming (8) steps. During streaming particles propagate to neighbor nodes fig. 2a-b.

$$f_i^*(\vec{x}, t) = f_i(\vec{x}, t) - \frac{\Delta t}{\tau} (f_i(\vec{x}, t) - f_i^{eq}(\vec{x}, t)) \tag{7}$$

$$f_i(\vec{x} + \vec{c}_i \Delta t, t + \Delta t) = f_i^*(\vec{x}, t) \tag{8}$$

$$S_i = \left( 1 - \frac{\Delta t}{2\tau} \right) w_i \left( \frac{c_{i\alpha}}{c_s^2} + \frac{(c_{i\alpha} c_{i\beta} - c_s^2 \delta_{\alpha\beta}) u_\beta}{c_s^4} \right) F_\alpha \tag{9}$$

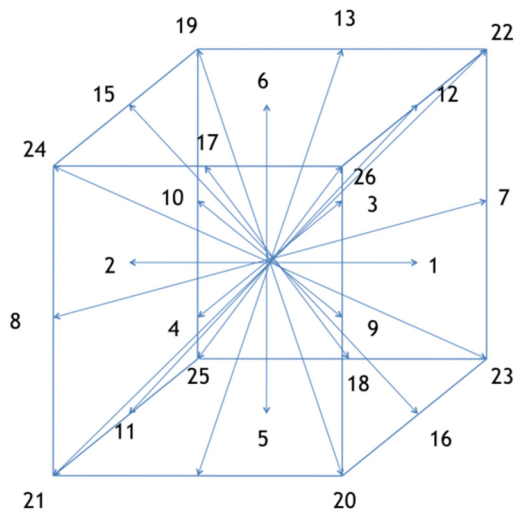


Figure 1 - D3Q27 lattice model used in the simulations

In many situations, the work from viscous dissipation and compression is so small that it does not significantly contribute to the heat balance. It is then sufficient to consider an advection-diffusion

equation for temperature without heat source terms, together with the incompressible Navier-Stokes eq. For such simulations often two population model is applied, in which there is separate distribution function for temperature -  $g_i$  is introduced. For temperature distribution function same equations are applied for collision and streaming process (7-8).

Buoyancy is modeled through force density  $\mathbf{F}$ . If density variations due temperature is small Boussinesq approximation could be used [10-11].

Numerical algorithm for LBM reads as:

---

```

for each time step  $t$  do
  compute macroscopic velocity, temperature and density
  compute equilibrium distribution for  $g$ 
  perform one step of collision for  $g$ 
  apply boundary conditions for temperature
  perform propagation step
  compute equilibrium distribution for  $f$ 
  perform one step of collision for  $f$ 
  apply boundary conditions for velocity
  perform propagation step
endfor

```

---

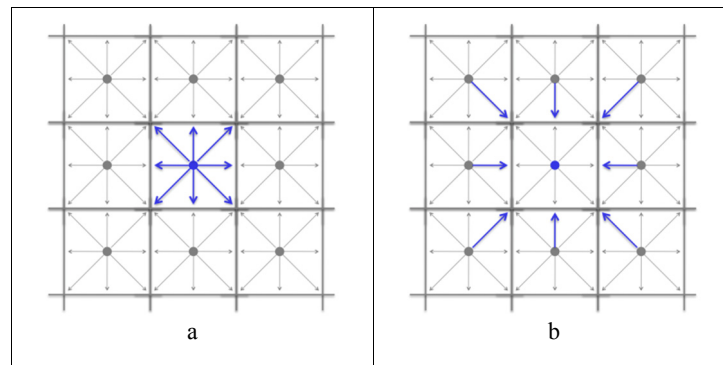
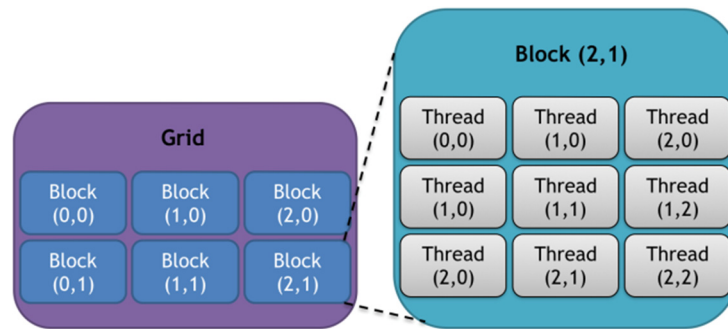


Figure 2 – Streaming from central node (a) and streaming into central node (b)

### CUDA implementation

CUDA enabled simulation code is implemented in the CUDA C language which is an extension to the C language. Functions in a CUDA C are marked as host functions, device functions and kernels. Host functions are simple C functions which executed by host processor. Device functions are special functions which should be launched on a GPU. Kernel functions are used to launch GPU functions from the host code.

Kernel function runs in parallel on the GPU. During launch of the kernel a lot of kernel copies executed in parallel by GPU. The execution pattern is identified by a grid. The grid is the special configuration of the parallel threads, which are grouped into blocks. Grid and block layout could be one, two and three dimensional. Fig. 3 show example of the grid which has 6 blocks and two dimensional layout. Each block in fig. 3 also has two dimensional layout with 9 threads, total number of threads 54.



**Figure 3** – CUDA execution model

Each thread is executed by Streaming multiprocessor (SM). SM has several scalar processors (SP) which actually runs code. Special scheduling algorithms and chips make use of large amount of SP on a GPU.

For convenience, “threadIdx” is a 3-component vector, so threads can be identified using a one-dimensional, two-dimensional, or three-dimensional thread index, forming a one-dimensional, two-dimensional, or three-dimensional block of threads. This provides a natural way to invoke calculations for elements in a domain, such as a vector, matrix, or volume.

The index of a threads and its identifier are directly related to each other: they are the same for a one-dimensional block; for a two-dimensional block of size (Dx, Dy), the thread ID of index(x, y) is (x +

y Dx); for a three-dimensional block of size (Dx, Dy, Dz), the thread ID of index(x, y, z) is (x + y Dx + z Dx Dy).

There is a limit on the number of threads in a block, since it is expected that all threads of a block will be on the same processor core and must share the limited memory resources of this core. On modern GPUs, a block of threads can contain up to 1024 threads.

However, the kernel can be executed by several blocks of threads of the same shape, so that the total number of threads is equal to the number of threads in the block multiplied by the number of blocks.

Listing 1 provides example of GPU kernel function for streaming stage in LBM simulations. Variables i, j, k are used to assign memory location for each thread.

**Listing 1** – GPU kernel function

```

__global__ void stream(float *f_dst, float *f_src)
{
    unsigned int i = threadIdx.x + blockIdx.x * blockDim.x;
    unsigned int j = threadIdx.y + blockIdx.y * blockDim.y;
    unsigned int k = threadIdx.z + blockIdx.z * blockDim.z;

    for (unsigned int l=0; l<NDIR; l++) {
        unsigned int i2 = (NX + i - dirx[l]) % NX;
        unsigned int j2 = (NY + j - diry[l]) % NY;
        unsigned int k2 = (NZ + k - dirz[l]) % NZ;

        f_dst[voffset(i, j, k, l)] = f_src[voffset(i2, j2, k2, l)];
    }
}

```

CUDA programming model introduces concept of memory types. CUDA enabled GPU has device, shared, texture, constant cache and register memory. Register memory is very fast memory, with on-chip implementation. Size of register memory may vary between GPU’s, but it is usually small, and cannot

store arrays. Shared memory is special memory which is shared between threads of the same block. Proper use of shared memory may decrease load to global GPU memory. Global GPU memory or device memory is large memory, which is slow comparably to other types of memory, but has

advantage of big size, often several gigabytes. There is also special caches to store constant values and one-two-three dimensional textures. Use of texture cache may increase simulation speed if there exist special pattern while accessing data in cache.

To archive high performance CUDA implies that programmer uses right type of memory for various data. Results of the simulation should be uploaded to CPU or host memory using special CUDA API calls.

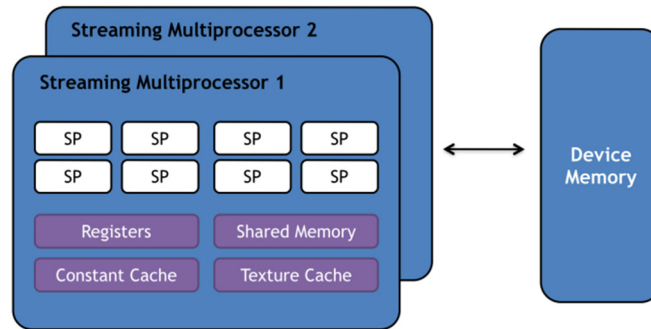


Figure 4 - CUDA hardware model

## Results

The CUDA LBM solver implemented on the GPU is used to study the differentially heated cubic cavity outlined in Fig. 5. Two opposite vertical walls have imposed temperatures  $-T_0$  and  $+T_0$ , whereas the remaining walls are adiabatic. This configuration has been extensively studied in the two-dimensional configuration and various benchmark solution are available.

All simulation parameters were the same as in the benchmark solution [11]. In order to perform validation, the flow in the differentially heated

cavity is computed for Rayleigh numbers equal to  $10^4$ ,  $10^5$ ,  $10^6$  and  $10^7$ . The results are compared with available data. Table 1 gives the obtained Nusselt numbers as well as the values published in [11]. GPU simulations shows good results which are in accordance with the reference values.

Simulations were performed in a single precision mode on a NVIDIA 1050 and Tesla K80 GPUs. Their characteristics are presented in the table 2. Mesh size is  $128 \times 128 \times 64$ . Additional comparison was made with multicore workstation with 64 available cores and 256 threads. Results of performance comparison is presented in fig. 6.

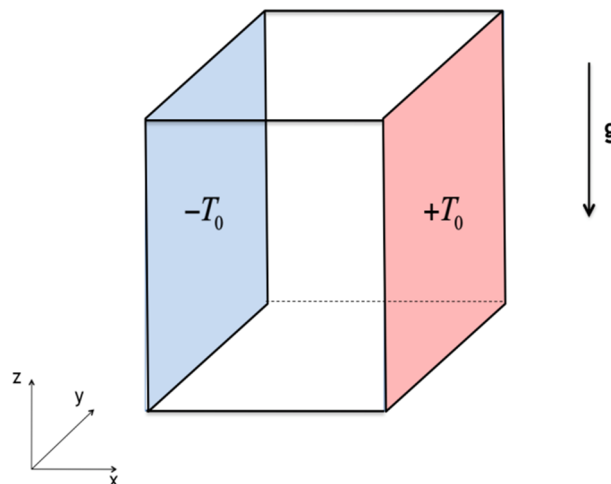
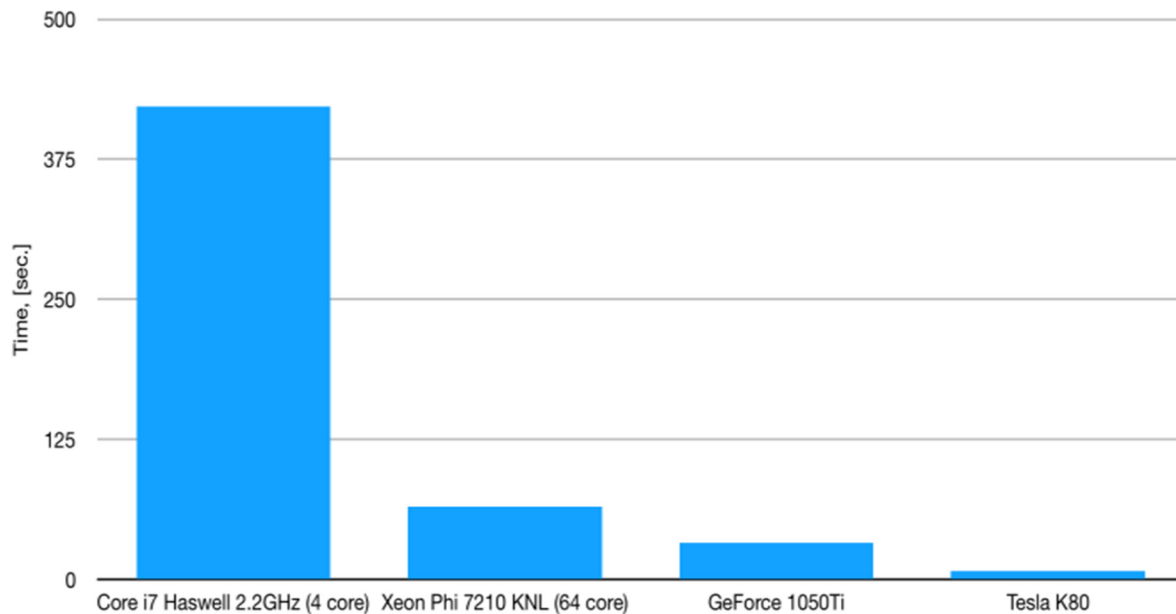


Figure 5 – Natural convection scheme

**Table 1** – Comparison of Nusselt numbers

Rayleight number	$10^4$	$10^5$	$10^6$	$10^7$
Present	2.031	4.3302	8.6468	16.4193
Obrecht [11]	2.056	4.3382	8.6457	16.4202

**Figure 6** – Performance comparison**Table 2** – GPU parameters

Parameter/GPU	1050 Ti	Tesla K80
CUDA cores	768	4992
GPU Clock	1392 MHz	875 MHz
SP performance	2.1 TFlops	8.73 TFlops
DP performance	1/32 of SP	2.91 TFlops
Memory	4 GB GDDR5	24 GB GDDR5
Bandwidth	112 GB/s	480 GB/s
ECC support	No	Yes

## Conclusion

In this paper, we presented in-house thermal LBM solver for CUDA enabled GPU workstations. Validity of the numerical algorithm was tested on a benchmark Natural convection problem. The code uses separate populations for velocity and temperature. According to the timings GPU based LBM gets higher performance in comparison with the single CPU code. Code runtime also compared with the results of OpenMP version of the code, which is executed on Xeon Phi KNL workstation with 64 available cores. Promising results shows

that GPU accelerated LBM is a good alternative to CPU versions. Drawback of the CUDA code is the dependence on the CUDA platform and decisions made by Nvidia company. Also, most of the CUDA libraries are closed source, or proprietary standards, which is opposite to the role of the OpenMP.

Still a plenty of improvements are possible to the code. One is the extension of the algorithm to multi GPU and multi node configurations and more aggressive optimization for memory bandwidth.

Developed code could be used in various thermal fluid flow simulations for which Boussinesq approximation for density fluctuations is valid.

## Acknowledgements

This work was supported by the MES Republic of Kazakhstan (grant number AP05132121).

## References

1. Fernando R. “GPU gems: programming techniques, tips and tricks for real-time graphics.” (Pearson Higher Education, 2004).
2. Stam J. “Stable fluids.” *Proceedings of the 26th annual conference on Computer graphics and interactive techniques. – ACM Press/Addison-Wesley Publishing Co.* (1999): 121-128.
3. L. M. Itu, C. Suci, F. Moldoveanu, A. Postelnicu and C. Suci “Optimized GPU based simulation of the incompressible Navier-Stokes equations on a MAC grid.” *RoEduNet International Conference 10th Edition: Networking in Education and Research, Iasi* (2011): 1-4.
4. R.A. Gingold, J.J. Monaghan “Smoothed particle hydrodynamics: theory and application to non-spherical stars.” *Mon. Not. R. Astron. Soc.* 181 (1977): 375–89.
5. Alexis Héroult, Annamaria Vicari, and Ciro Del Negro “A SPH thermal model for the cooling of a lava lake.” *Proceedings of the 3th SPHERIC Workshop* (Lausanne, 2008).
6. Robert A. Dalrymple and Alexis Héroult “Levee breaching with GPU-SPHysics code.” *Proceedings of the 4th SPHERIC Workshop* (Nantes, 2009).
7. Robert A. Dalrymple, Annamaria Vicari, Ciro Del Negro, and Robert A. Dalrymple, “Modeling water waves in the surf zone with GPU-SPHysics.” *Proceedings of the 4th SPHERIC Workshop* (Nantes, 2009).
8. Christian Obrecht, Frédéric Kuznik, Bernard Tourancheau, Jean-Jacques Roux “Scalable lattice Boltzmann solvers for CUDA GPU clusters.” *Parallel Computing* 139, no. 6-7 (2013): <https://doi.org/10.1016/j.parco.2013.04.001>.
9. Parmigiani A., Huber C., Chopard B. et al. *Eur. Phys. J. Spec. Top.* 171 (2009): 37. <https://doi.org/10.1140/epjst/e2009-01009-7>.
10. Krüger T., Kusumaatmaja H., Kuzmin A., Shardt O., Silva G., Viggen E. M. “The Lattice Boltzmann Method.” *Springer* (2017).
11. Lars Moastuen “Real-time simulation of the incompressible Navier-Stokes equations on the GPU.” (PhD diss., Oslo University, July 2007).
12. Li C., Maa J.P.Y., Kang H. *Sci. China Phys. Mech. Astron.* 55 (2012): 1894. <https://doi.org/10.1007/s11433-012-4856-9>.
13. Xu H., Malaspinas O., Sagaut P. “Sensitivity Analysis and Optimal Strategies of MRT-LBM for CAA-Determination of free relaxation parameters in MRT-LBM.” *Eighth International Conference for Mesoscopic Methods in Engineering and Science* (2010).
14. Stiebler M. et al. “Lattice Boltzmann large eddy simulation of subcritical flows around a sphere on non-uniform grids.” *Computers & Mathematics with Applications* 61, no. 12 (2011): 3475-3484.
15. Jacob J., Malaspinas O., Sagaut P. “A new hybrid recursive regularised Bhatnagar–Gross–Krook collision model for Lattice Boltzmann method-based large eddy simulation.” *Journal of Turbulence* (2018): 1-26.
16. Pradhan A., Yadav S. “Large Eddy Simulation using Lattice Boltzmann Method based on Sigma Model.” *Procedia Engineering* 127 (2015): 177-184.
17. Liou T. M., Wang C. S. “Large eddy simulation of rotating turbulent flows and heat transfer by the lattice Boltzmann method.” *Physics of Fluids* 30, no. 1 (2018): 015106.
18. Hamane D., Guerri O., Larbi S. “Investigation of flow around a circular cylinder in laminar and turbulent flow using the Lattice Boltzmann method.” *AIP Conference Proceedings* 1648, no. 1 (2015): 850094.
19. Cui X. et al. “A 2D DEM–LBM study on soil behaviour due to locally injected fluid.” *Particuology* 10, no. 2 (2012): 242-252.
20. Z. Guo, C. Zheng, B. Shi “Discrete lattice effects on the forcing term in the lattice Boltzmann method.” *Phys. Rev. E* 65 (4) (2002) 046308.
21. S.K. Kang, Y.A. Hassan “A direct-forcing immersed boundary method for the thermal lattice Boltzmann method.” *Comput. Fluids* 49 (1) (2011): 36–45.
22. Obrecht C. et al. “The TheLMA project: A thermal lattice Boltzmann solver for the GPU.” *Computers & Fluids* 54 (2012): 118-126

IRSTI 27.35.17

S.D. Maussumbekova, K. Khan

Faculty of Mechanic-Mathematical, Al-Farabi Kazakh National University,  
Almaty, Kazakhstan, e-mail: saulemaussumbekova@gmail.com

### **Computational study of temperature stratification effect on harmful gases expansion in the atmosphere**

**Abstract.** To date, the study of atmospheric pollution is of great interest. Assessment, monitoring and calculation of concentrations of harmful impurities in the atmosphere with their source is based on theoretical studies, and it is possible to make short-term forecasts used to control emissions from industrial enterprises. Disposal of waste by industrial enterprises, often consisting not only of light impurities, but also of heavy elements, does not always control what constitutes a danger to living creatures and flora in the affected area. Computational model is constructed for determination of harmful impurities expansion in atmosphere, which is most serious environmental problems in many industrial cities in the world. Numerical calculations are obtained by program complex ANSYS. There is given analysis and results of calculations determining the distribution of harmful impurities concentrations in different temperature gradient. Calculations are conducted for different pollutant-emission rate from point source. There is studied the influence of temperature in ground layer on the dynamics of harmful impurities concentration from point source. Obtained results allow to predict of distribution contour of impurities and its extent.

**Key words:** atmospheric boundary layer, numerical modeling, ANSYS software system, spread of polluting substances.

#### **Introduction**

Dispersion of pollution represents an important environmental problem with respect to human health. In urban areas, several sources of pollution (e.g. wind-blown dust, vehicle exhaust, toxic and odorous emissions) may be unpleasant and dangerous. Among them, pollutant emissions from rooftop stacks is a factor that can seriously affect the quality of fresh-air at intakes of the emitting and/or surrounding buildings, and potentially compromising the well-being of these buildings' occupants. Additionally, inside cities – where the building density increases – the stack emissions can be accumulated between buildings, thus inducing an increase of the contaminant concentration because reduced airflow passes through the zone's boundaries as compared to free-stream flow.

The problem of environmental protection and restoration is becoming one of the most important tasks of science, the development of which is stimulated by the ever-increasing pace of technological progress in all countries of the world.

The rapid development of industry contributed to the emergence of an acute problem for humanity – the preservation of ecological systems that historically formed on our planet. In recent decades, environmental systems have experienced a significant impact of natural, especially anthropogenic factors, changing in an undesirable direction for nature. The increased concentration of pollutants is observed in the atmosphere of almost every industrial city, so there is a need to solve the problem of assessing and modeling the spread of pollutants in the atmosphere from local stationary sources to prevent or reduce their impact on the ecosystem. A wide range of environmental protection tasks is being solved using mathematical modeling methods. This approach allows testing multiple options for work, to predict various scenarios for the development of the process while varying the initial data. A lot of articles have been published in which studies of atmospheric pollution from different directions and taking into account various factors are presented [1-6].

Numerical simulations with CFD offer some advantages compared to other methods; they are

relatively less expensive, they provide results of flow features at every point in space simultaneously [7]) and they do not suffer from potentially incompatible similarity because simulations can be conducted at full scale [8]. In addition, at the micro-scale, the CFD technique is the preferred way of investigation and very suitable for parametric studies for various physical flow and dispersion processes [9]. Due to the rapid development in computer hardware and numerical modelling, CFD has been increasingly used and adopted to simulate the flow development and pollutant dispersion [10]. Many studies have shown that the approach is capable of reproducing the qualitative features of airflow and pollutant distributions [11]. However, the accuracy and reliability of CFD are of concern, thus solution verification and validation studies are imperative [12]. Since experience has already shown that numerical results do not compare among themselves [13], experimental tests (i.e. field and reduced-scale measurements) appear unquestionably necessary for fulfilling the requirements of assessing the quality of CFD simulation [14]. In addition, one of the objectives of laboratory studies has frequently been to aid the development of dispersion algorithms that can be used in dispersion modelling packages to predict behaviour near and around buildings [15].

In this paper, we consider the effect of temperature stratification on the distribution of concentrations of harmful substances in the atmosphere emitted by industrial enterprises through local sources (pipes). The mathematical model of the problem is a system of Navier-Stokes equations, energy equations and equations for the  $k$ - $\epsilon$  model of turbulence. This system of equations is solved with using of FLUENT package [17].

### Physical statement of problem

One of the conditions affecting the dynamics of the distribution of harmful substances is the stratification of temperature in height, due to the ability of the earth's surface to absorb or radiate heat [1].

The paper deals with the problem of spreading the concentration of harmful substances in the atmosphere emitted by industrial enterprises through point sources (pipes), taking into account of temperatures variation with vertical. Computational domain is the rectangle with width – 60 m and height – 30 m. The point source (pipe) is located at 4 meters apart from left boundary. Diameter of source's mouth is 1.2 m, height of source is 7 m. Figure 1 schematically shows computational domain.

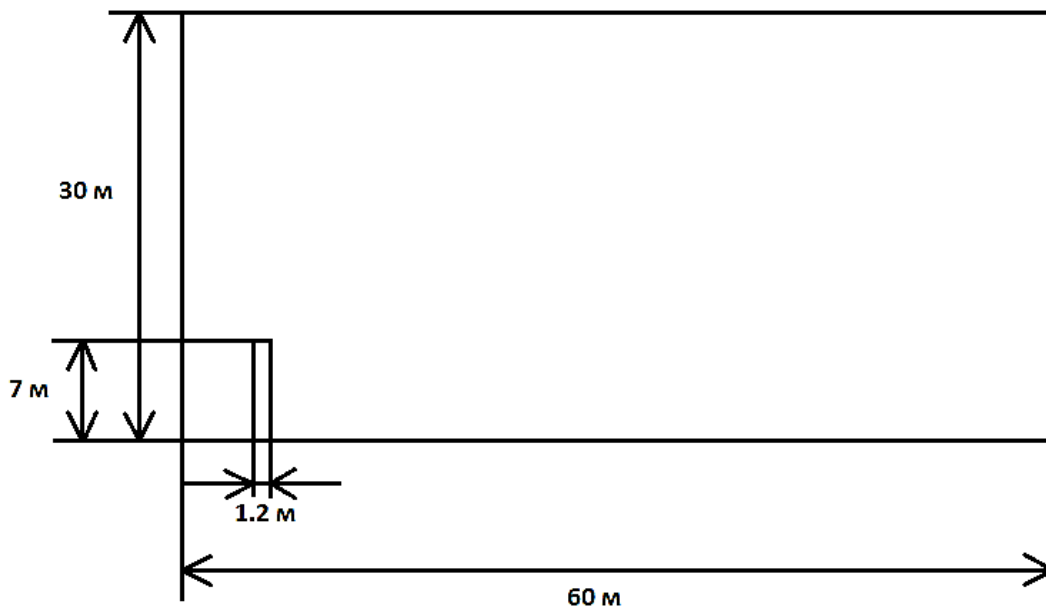


Figure 1 – Scheme of computational domain

### Solution method

ANSYS software was used for solving of problem. At first stage, geometry of object was created with the help of built-in DesignModeler editor. Mesh editor allows sampling computational domain. Transition to Setup editor allows setting initial and boundary conditions of task, and choose solution method. In General we set Type – Pressure-Based, Time – Transient, VelocityFormulation – Absolute, 2DSpace – Planar. Below we put a tick in front of Gravity and assign value along vertical axis  $-9.8 \text{ m/s}^2$ . In Models, we add energy equation, We change Viscous to Standard  $k-\epsilon$ , Species to SpeciesTransport, here we choose MixtureMaterial – methane-air, Reactions – Volumetric and Turbulence – Chemistry Interaction – Eddy-Dissipation. Here, we use UDF to set temperature gradient. We create \*.c file, where we set temperature profile. To use it in the project, we call menu Define -> DefineFunctions -> Interpret ..., select created file. After that, in settings of Cell Zone Conditions, we put a tick in front of FixedValues and change Temperature from none to udf\_y\_temperature. Specifying values on boundaries of domain is done in Boundary Conditions tab. Values of incoming flow velocity to domain in air\_inlet, emission rate

of methane from pipe in gas\_inlet are specified. Oxygen mass fraction in air\_inlet is 0.23, and methane mass fraction in gas\_inlet is 1. In air\_inlet, temperature is changed from none to udf\_y\_temperature.

As solution method, the method SIMPLE (Semi-Implicit Method for Pressure Linked Equations) was chosen, put it otherwise – splitting method by physical parameters. Then calculation is initialized.

### Analysis of results

Calculations were carried out in different variations of temperature gradient and rate of harmful impurities emission from mouth of source. Results were obtained at pollutant-emission rates: 2.5 m/s, 4 m/s, 10 m/s. Air flow from the left moves at velocity of 0.5 m/s. This airflow velocity according to the Beaufort scale corresponds to determination of wind strength – quiet [9]. That is, in this case, direction of wind can be seen through smoke, but not over weathervane, leaves of trees remain motionless. Presented figures determine the state of plume on the thirtieth second. Iteration step in time is 0.1 s.

Figure 2 shows methane ( $\text{CH}_4$ ) concentration distribution in case of temperature decrease with altitude.

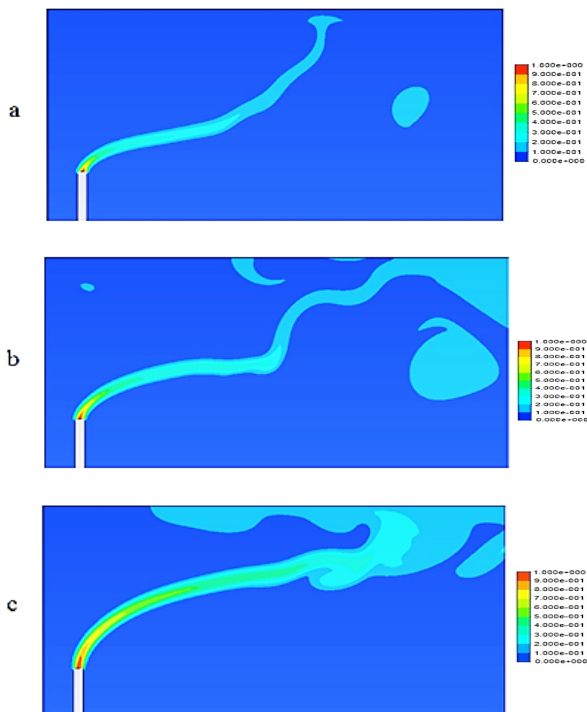


Figure 2 – Methane ( $\text{CH}_4$ ) concentration distribution in case of temperature decrease with altitude

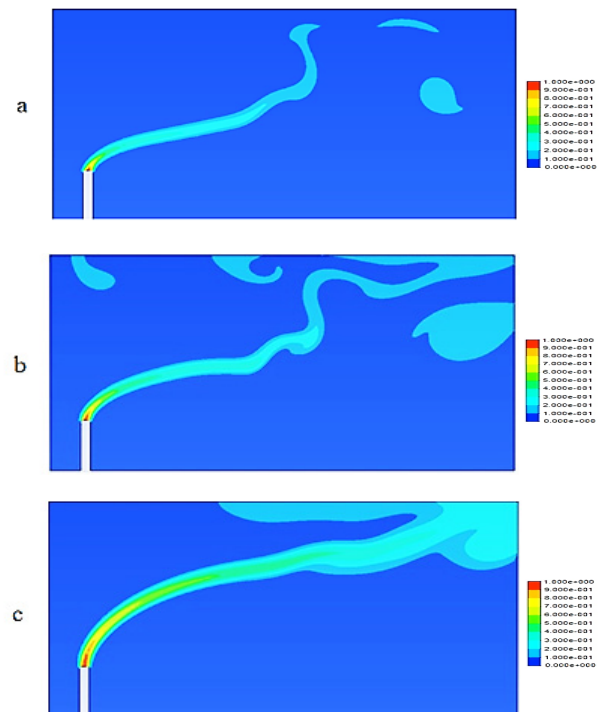


Figure 3 – Methane ( $\text{CH}_4$ ) concentration distribution in the case of inversion (increase in temperature with altitude)

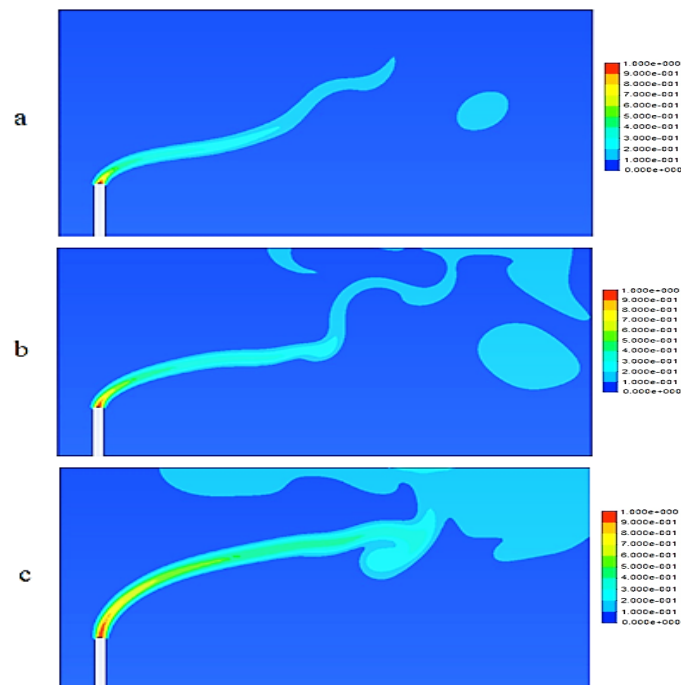
Figure 3 shows methane ( $CH_4$ ) concentration distribution in case of inversion. In comparison with Figure 2, which presents the case of methane concentration distribution at negative temperature gradient, most of impurities is transported on considerable distance in direction of wind motion before it reaches considerable concentration in earth's surface. This is due to dominance of small-scale mechanical turbulence arising at low temperature gradients [9]. In comparison with figure 2, which presents the case of methane concentration distribution at positive temperature gradient, it can be seen that contaminants are removed over long distances, so low concentrations of harmful substances reach ground level and weak mechanical turbulence arises [7].

Figure 4 is picture of methane concentration distribution emitted into atmosphere by point source, in case when the source mouth is located above the upper boundary of inversion layer.

Inversion layer, located below level of source mouth, is natural barrier to lowering pollutants to earth's surface. Figure 5. describe of methane concentration distribution which emitted into

atmosphere by local source, in case when the source mouth is located below the lower boundary of inversion layer. It can be noted that significant parts of concentration are separated from source by considerable distance. Dispersion also occurs at considerable distance from source. This is due to the fact that above mouth of source is powerful inversion layer, which prevents dispersion of harmful substances released into the atmosphere. Significant concentrations of harmful substances remain closer to earth's surface. Inversion layer located above the level of source's mouth is obstacle to dispersion of harmful substances, and therefore impurities concentration in surface layer can be higher than calculated one in several times.

Figure 6 describes of methane concentration distribution at pollutant-emission rate of 2.5 m/s. Four cases are considered, each of which corresponds to given temperature gradient. 6 (a) is characteristic for the case when temperature decreases with altitude; 6 (b) – for the case of inversion; 6 (c) – for the case when mouth of source is located above the upper boundary of inversion layer; 6 (d) – for case when the source mouth is located below the lower boundary of inversion layer.



**Figure 4** – Methane ( $CH_4$ ) concentration distribution in case when the source mouth is located above the upper boundary of inversion layer

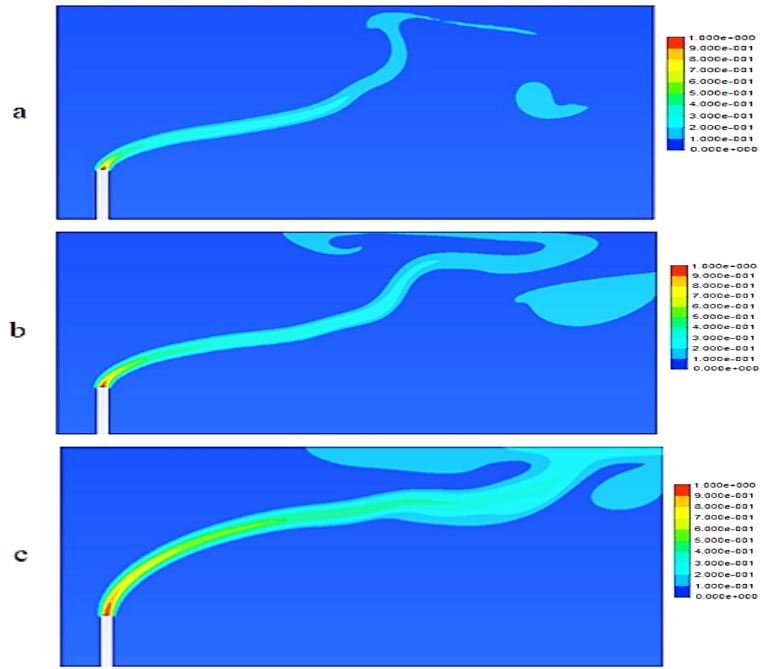


Figure 5 – Methane ( $CH_4$ ) concentration distribution in case when the source mouth is located below the lower boundary of inversion layer

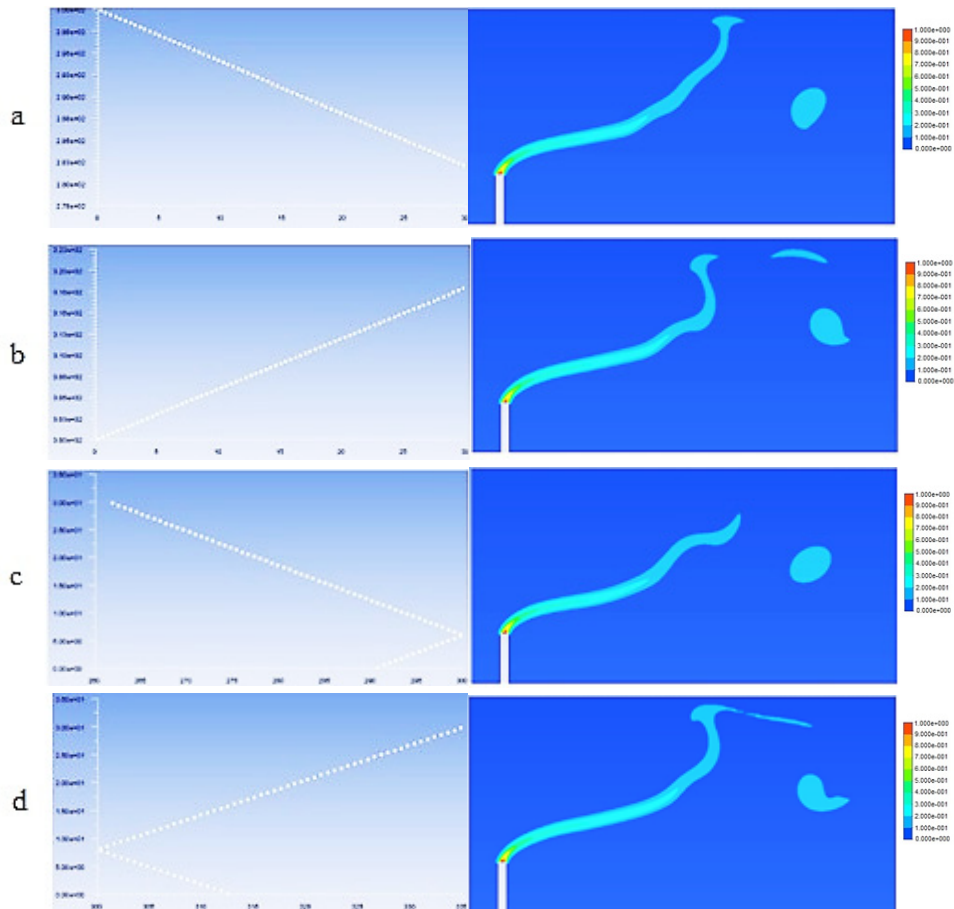


Figure 6 – Methane ( $CH_4$ ) concentration distribution for various initial temperature profiles in case when pollutant-emission rate is 2.5 m/s

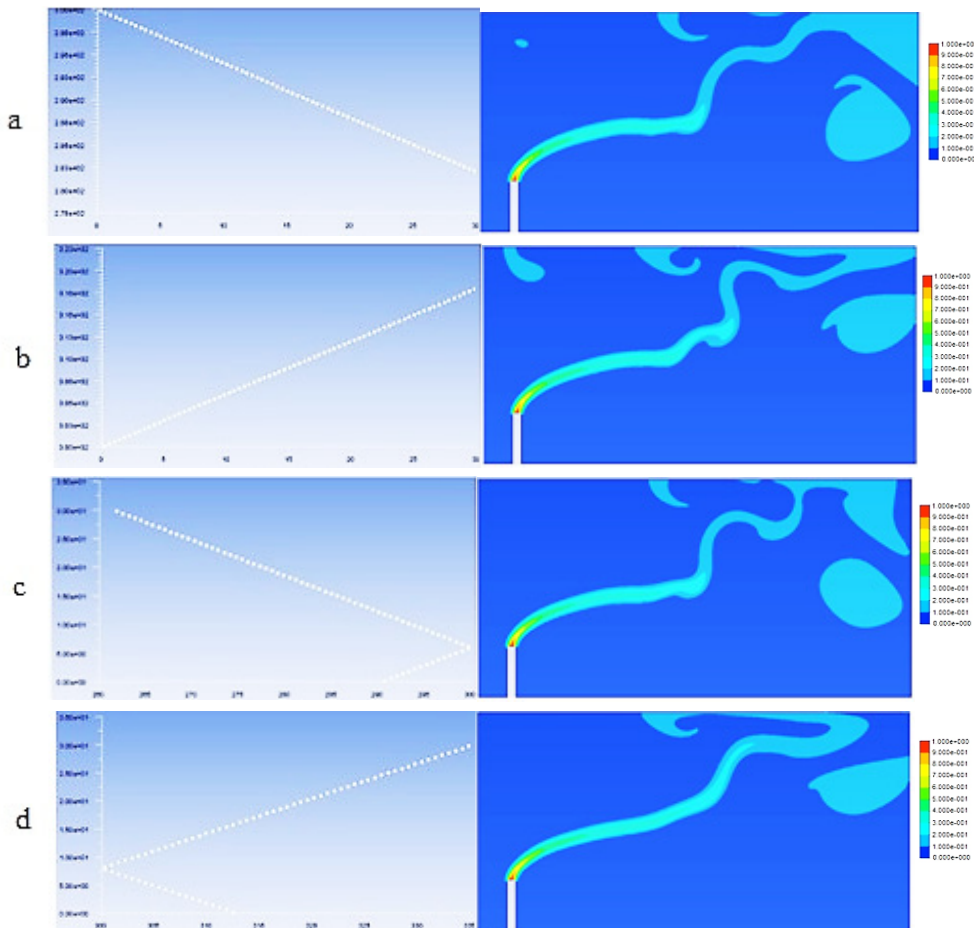
In Figure 7 were presented the methane concentration distribution at pollutant-emission rate of 4 m/s. Four cases are considered, each of which corresponds to given temperature gradient. 7 (a) is characteristic for the case when temperature decreases with altitude; 7 (b) – for the case of inversion; 7 (c) – for the case when mouth of source is located above the upper boundary of inversion layer; 7 (d) – for case when the source mouth is located below the lower boundary of inversion layer.

The computational experiment was done for the speed 10 m/s. Four cases are considered, each of which corresponds to given temperature gradient. 8 (a) is characteristic for the case when temperature decreases with altitude; 8 (b) – for the case of inversion; 8 (c) – for the case when mouth of source is located above the upper boundary of inversion layer; 8 (d) – for the case when the source mouth is located below the lower boundary of inversion layer.

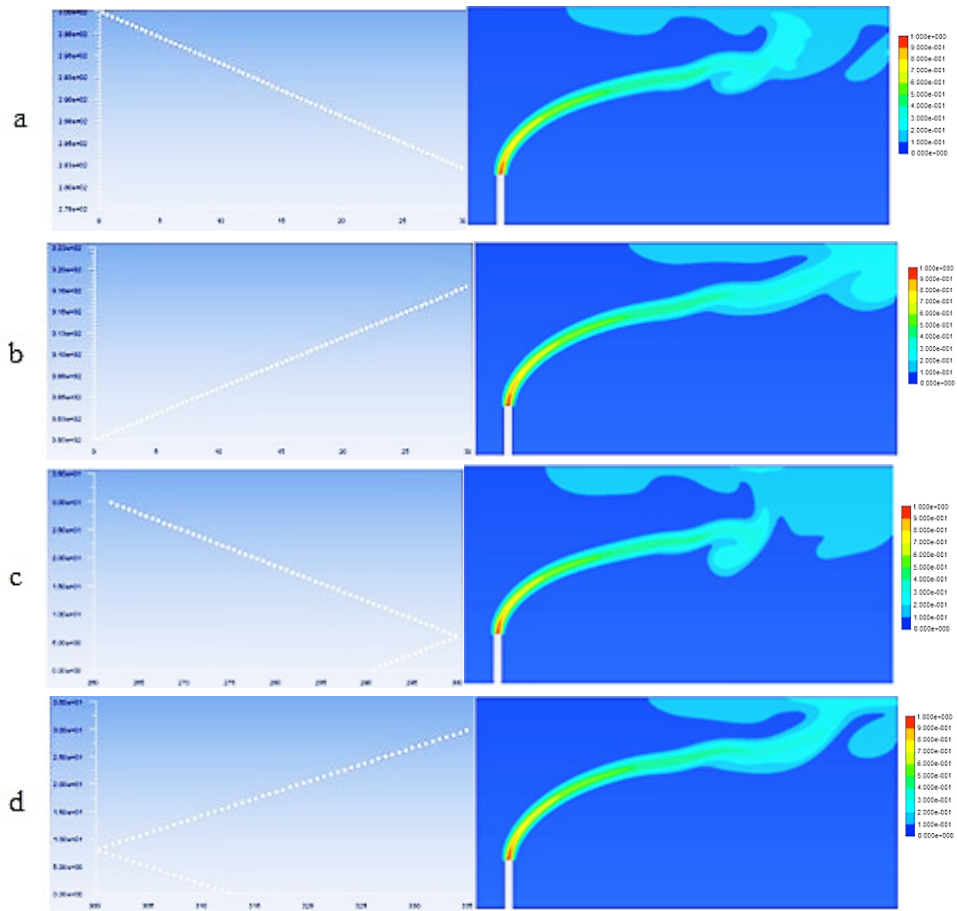
Thus, represented results allow to note wind influence importance to harmful substances distribution in atmosphere which are thrown out by point source of industrial enterprise.

Figure 9 corresponds to methane concentration distribution of at  $t = 10$  sec (10 (a)),  $t = 30$  sec (10 (b)),  $t = 60$  sec (10 (c)). As can be seen, at first stage, significant concentrations remain near mouth of source, scattering is noticeably observed. In second stage, significant concentrations are transferred to more remote distance from source, followed by dispersion. Third stage shows the most pronounced form of plume. Significant concentrations are transported a considerable distance from source in direction of wind propagation, followed by dispersion.

Opposed to case when mouth of source is located below the lower boundary of inversion layer, which is shown in Figure 10, significant concentrations are transferred on shorter distance from source.



**Figure 7** – Methane ( $CH_4$ ) concentration distribution for various initial temperature profiles in case when pollutant-emission rate is 4 m/s



**Figure 8** – Methane ( $CH_4$ ) concentration distribution for various initial temperature profiles in case when pollutant-emission rate is 4 m/s

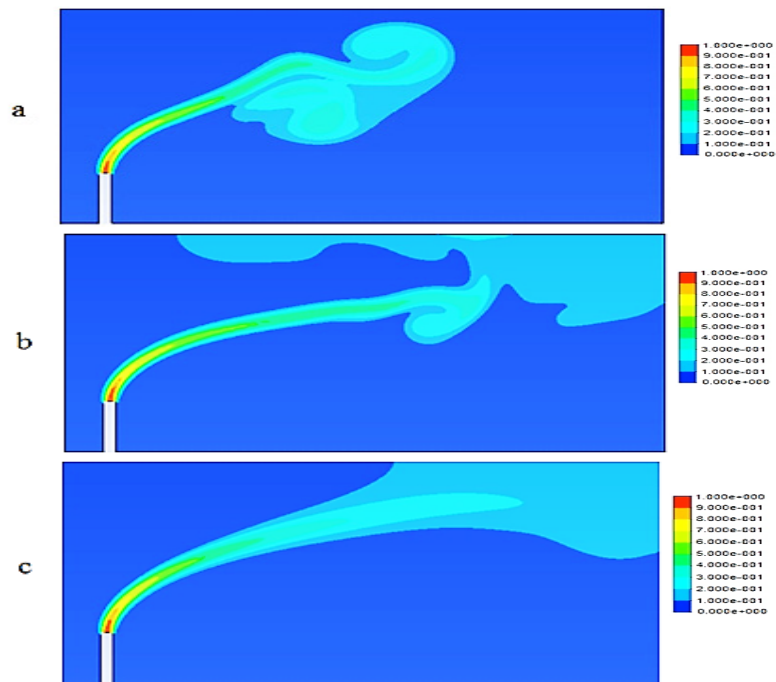


**Figure 9** – Temporal distribution of methane ( $CH_4$ ) concentration in case when the upper boundary of inversion is located below mouth of source

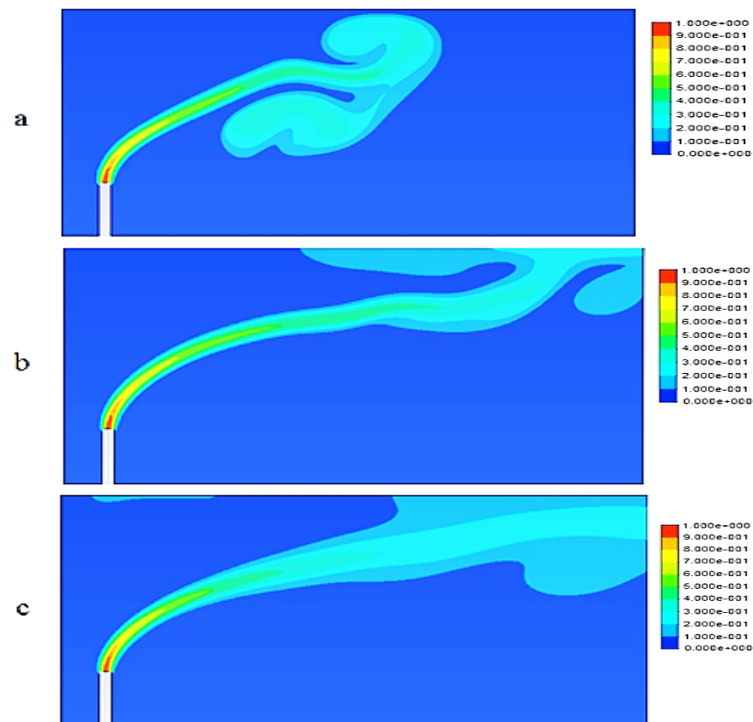


**Figure 9** – Temporal distribution of methane ( $CH_4$ ) concentration in case when the lower boundary of inversion is located above mouth of source

It can be seen how plume acquires more pronounced cone shape over time. In comparison with Figure 10, it can be noted that dispersion of harmful substances is greater, which is due to fact that plume enters the atmosphere layer, where temperature gradient is positive. It can also be noted that in case when inversion layer is below mouth of source, significant concentrations of harmful substances are observed at higher altitude than when inversion layer is located above mouth of source.

Figure 10 shows methane concentration distribution emitted by point source at velocity of 10 m/s over time ( $t = 10$  s (10 (a)),  $t = 30$  s (10 (b)),  $t = 60$  s (10 (s))), taking into account that mouth of source is located below the lower boundary of inversion layer. In contrast to the case when mouth of source is located above the upper boundary of inversion layer, which is shown in Figure 9, significant concentrations are transferred to a larger distance from source. It can also be noted that dispersion of harmful substances is less, which is due to fact that plume enters to inversion layer, which prevents diffusion. In case when inversion layer is below mouth of source, significant concentrations of harmful substances are observed at lower altitude

than when inversion layer is located above mouth of source.

According to this, it can be argued that the case where inversion layer is located below mouth of source is safer for ecology of ground layer.

### Conclusion

Thus, the computational model is constructed to determine expansion of harmful impurities in ground layer in different temperature stratification based on ANSYS software. Numerical experiments are conducted for different pollutant-emission rate from point source, for different temperature stratifications with altitude, which makes it possible to predict flame contour and its extent.

Obtained results can be used to predict distribution of concentration in ground layer, quality of air composition, that has a significant effect on state of environment ecology. Analyzing the obtained results makes possible to note the necessity of creating similar models for predicting the distribution of harmful substances concentration in ground layer, which will affect the state of environment ecology in general, and of atmosphere in particular.

## References

1. Kader B. "Temperature and Concentration Profiles." *Journal of Heat and Mass Transfer* no. 24(9) (1981): 1541–1544.
2. Kader B. A. "Heat and Mass Transfer in Pressure-Gradient Boundary Layers." *Int. J. Heat Mass Transfer* 34 (1991): 2837–2857.
3. Khaikine I.N., Kuznetsova I.N., Kadygrov E.N., Miller A.A. "Investigation of temporal-spatial parameters of an urban heat island on the basis of passive micro-wave remote sensing." *Theor. Appl. Climatol* 84, no. 1 (2006): 161–169.
4. Wei T., Fife P., Klewicki J., and McMurtry P. "Properties of the Mean Momentum Balance in Turbulent Boundary Layer, Pipe and Channel Flows." *J. Fluid Mech.* 522 (2005): 303–327.
5. Le P. M., and Papavassiliou D. V. "On Temperature Prediction at Low Re Turbulent Flows Using the Churchill Turbulent Heat Flux Correlation." *Int.J. Heat Mass Transfer* 49 (2006): 3681–3690.
6. Xia Wang, Luciano Castillo, Guillermo Araya. "Temperature Scalings and Profiles in Forced Convection Turbulent Boundary Layers." *Journal of Heat Transfer* 130(2) (2008). DOI: 10.1115/1.2813781.
7. Berlyand, M.E. "Prediction and regulation of air pollution." L.: Gidrometeoizdat 136 (1991): 121.
8. Ji Xing, Zhenyi Liu, Ping Huang, Changgen Feng, Yi Zhou, Deping Zhang, Feng Wang. "Experimental and numerical study of the dispersion of carbon dioxide plume." *Journal of Hazardous Materials* 256–257 (2013): 40-48.
9. P. Moonen, T. Defraeye, V. Dorer, B. Blocken, J. Carmeliet "Urban physics: effect of the micro-climate on comfort, health and energy demand." *Frontiers of Architectural Research* 1 (3) (2012): 197-228.
10. H. Montazeri, B. Blocken "CFD simulation of wind-induced pressure coefficients on buildings with and without balconies: validation and sensitivity analysis." *Building and Environment* 60 (2013): 137-149.
11. P. Gousseau, B. Blocken, T. Stathopoulos, G.J.F. Van-Heijst. "CFD simulation of near-field pollutant dispersion on a high-resolution grid: a case study by LES and RANS for a building group in downtown Montreal." *Atmospheric Environment* 45 (2) (2011): 428-438.
12. P. Wang, H. Mu. "Numerical simulation of pollutant flow and dispersion in different street layouts." *International Journal Environment Study* 67 (2) (2010): 155-167.
13. Y. Huang, X. Hu, N. Zeng. "Impact of wedge-shaped roofs on airflow and pollutant dispersion inside urban street canyons." *Building and Environment* 44 (2009): 2335-2347.
14. T. Stathopoulos. "Computational wind engineering: past achievements and future challenges." *Journal of Wind Engineering and Industrial Aerodynamics* 67–68 (1997): 509-532.
15. I. Abohela, N. Hamza, S. Dudek "Effect of roof shape, wind direction, building height and urban configuration on the energy yield and positioning of roof mounted wind turbines." *Renewable Energy* 50 (2013): 1106-1118.
16. Valger S.A., Danilov M.N., Zakharova Yu.V., Fedorova N.N. "Basics of PC ANSYS 16.0: tutorial." Novosibirsk: NSABU (2015): 240.

IRSTI 27.35.17

<sup>1</sup>A. Beketayeva, <sup>2</sup>A.Zadauly

<sup>1</sup>Institute of Mathematics and Mathematical Modeling  
of Ministry of Education and Science of Republic of Kazakhstan, Almaty, Kazakhstan  
e-mail: azimaras10@gmail.com

<sup>2</sup>Institute of Mechanics and Engineering Science  
of Ministry of Education and Science of Republic of Kazakhstan, Almaty, Kazakhstan  
e-mail: akerkeh\_333@mail.ru

### **Influence of slit sizes on the interaction structure of supersonic turbulent air flow with a multi-component injection jet in a channel**

**Abstract.** The supersonic air flow in a flat channel with transverse injection of a turbulent hydrogen jet through a slit in the bottom wall is numerically simulated. The solution of the initial Favre-averaged Navier-Stokes equations closed by the  $k-\omega$  turbulence model is performed using an algorithm built on the basis of the WENO scheme. The interaction of a shock-wave structure with boundary layers on the lower and upper walls under conditions of an internal turbulent flow is investigated, namely, the effect of the width of the jet slit is studied. It is found that, in addition to the known shock-wave structures arising from the interaction of the incident flow with the transverse jet and the interaction of the main shock wave with the boundary layers near the walls, there is an additional system of shock waves and separation of the flow on the bottom wall at some distance from the jet downwards flow. Comparison with experimental data showed satisfactory agreement.

**Key words:** supersonic flow, perfect gas, boundary layer, the Navier-Stokes equations.

#### **Introduction**

Most published theoretical studies of the interaction of the jet and the oncoming flow in the channel mainly consider the jet injection region and generally the boundary conditions of symmetry or free flow are realized at the upper boundary [1-3], which greatly simplifies the solution of an assigned task. For example, in [1] the processes of mixing and chemical reactions during the transverse injection of a sound jet of hydrogen into a supersonic air stream with the parameters of  $M_\infty = 4$ ,  $T = 1000K$   $p = 4atm$  were calculated. Some features of the emerging flow were identified, including establishing the existence of the reverse current zones in front of the injector and behind it and obtaining the distributions of concentrations of the mixture of components. Studies in [2] dealt with

the transverse injection of gaseous fuel at an angle into a low elongated supersonic combustion channel. It is shown numerically that the fuel injection at an angle leads to an increase in the efficiency of mixing of fuel with air. The authors of [3] considered the flow of a multicomponent gas mixture with the injection of a helium jet through a circular opening at different angles of inclination ( $30^\circ$ ,  $90^\circ$  and  $150^\circ$ ). The influence of the angle of inclination of the injecting jet on a supersonic gas mixing was studied. It was found that the larger the angle, the greater the overall coefficient of pressure loss in the jet.

The mechanism of formation of the shock-wave structure of the aforementioned flow is well described in the literature [1-7]. A schematic picture of the flow in the injection region is shown in Figure 1, where 1 is the head shock wave resulting from the

deceleration of the oncoming flow in front of the jet, 2 and 3 are oblique and closing shock waves, respectively. The intersection of the head, oblique and closing shock waves at one point is the  $\lambda$ -shaped structure. The diagram depicts vortices in front of the jet formed as a result of the primary and secondary separation of the flow from the wall. In this case, the vortex, located closer to the jet, moves

counterclockwise and the vortex located at a greater distance from it, moves clockwise [4-6]. The figure also shows the detachable area behind the jet which occurs due to the discharge zone. In addition, the flow diagram (Figure 1) shows a weak shock, which is formed behind the injection nozzle when a stream of airflow that has passed around the blown jet flows onto the wall.

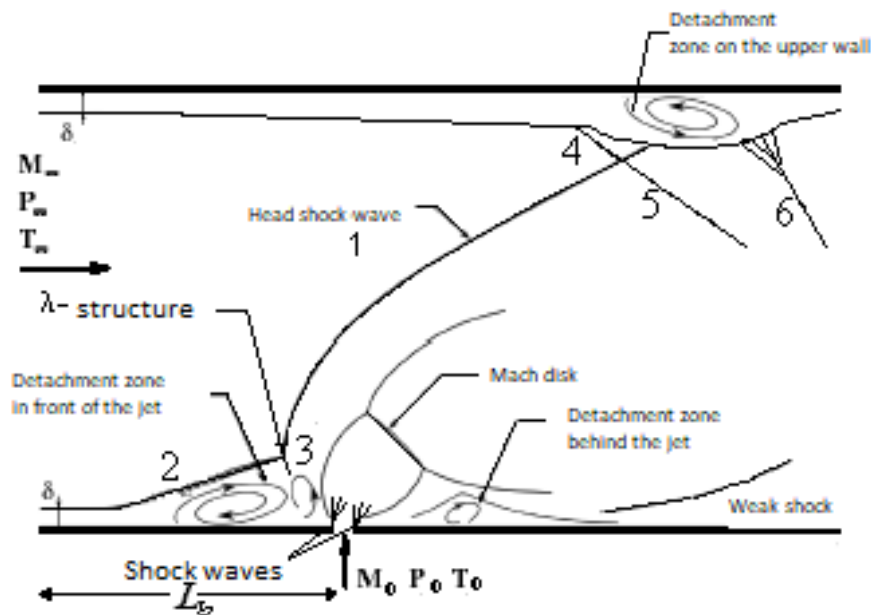


Figure 1 – The flow diagram

In some papers, the interaction of a transverse jet blown from the bottom wall and a shock wave falling from the upper wall of the channel was considered which also somewhat simplifies the formulation of the problem and allows a detailed study of their interaction. Thus in [8], the interaction of a falling shock wave and a transverse jet in a supersonic flow was numerically studied. The influence of the size and location of the shock wave generator falling from the top wall on the pressure profiles on the bottom wall in the region of the jet injection was studied. The inclination angle of the generator ranged from  $15,784^\circ$  to  $35,974^\circ$ . The authors showed that not only the inclination angle, but also the size of the generator significantly increases the interaction area both in front of the jet and behind it. In [9] the results of a study of the influence of shock waves on supersonic burning of a hydrogen jet were given, and the main attention was on the growth of the mixing layer. The effect of the

falling shock wave on the turbulent boundary layer was numerically investigated in [10] where the intensity of the shock wave was changed by adjusting the angle of the shock wave generator. Such models of turbulence as the  $k-\varepsilon$ ,  $k-\varepsilon / k-\omega$  hybrid model and the model with one equation for turbulent viscosity were studied in the work.

Experimental and theoretical papers studied the interaction of the falling shock wave but with the boundary layer [11–12]. There are almost no studies devoted to the interaction of a shock wave with a boundary layer under conditions of an internal turbulent flow. A schematic picture of the interaction of the shock wave with the boundary layer on the upper wall is also shown in Figure 1. Here 1 is the head shock wave falling on the upper wall, 4 is the shock wave separating the detachment region on the upper wall from the supersonic oncoming stream, 5 is the reflected shock wave and 6 is the compression wave arising at the point of

attachment of the detached flow. Thus, in [11] the results of calculations obtained by the method of large eddies are presented. The focus is on studying the structure of the flow, the size of the detachment zone, as well as the dynamic and thermal loads that occur during this interaction. The conditions under which the angle of inclination and the intensity of the shock wave lead to the separation of the boundary layer were investigated in [12].

The practical interest of supersonic flow with injection of jets in a channel is associated with the arising loads on both the upper and lower walls of the channel. The structure of the interaction will depend on the parameters of the injection jet, as well as on the height of the channel itself. As mentioned above, the problems of interaction of a shock wave with the injection jet and with boundary layers are mainly considered separately, not only because of the complexity of the numerical implementation of the nature of the flow and of the gas under consideration, but also with the presence of the upper wall, which requires reliable numerical calculation methods.

The difficulties encountered in the numerical solution of the problems described above do not allow a full study of the structure of both the interaction of the jet with the transverse flow and the interaction of the shock wave with the boundary layers on the lower and upper walls. The main problem of numerical simulation is well reflected in the literature [13-16]. At present, quasi-monotone

conservative schemes of a higher approximation order, such as TVD (Total Variation Diminishing Schemes), ENO (Essentially Nonoscillatory Schemes), WENO (Weighted ENO) schemes [18-19], are widely used to solve such complex problems. In [16] the authors developed the ENO scheme based on the Godunov method and showed the applicability of the scheme in solving the problem of supersonic flow of a multicomponent gas in a flat channel with injection of perpendicular jets.

The purpose of this paper is the numerical simulation of supersonic flow in a flat channel with transverse injection of a multicomponent jet and the study of the interaction of a shock wave arising in front of the injection jet with a boundary layer on both the lower and upper walls. Also included is the numerical study of the conditions of detachment of the boundary layer on the walls, as well as the influence of the jet width on the occurrence of detachment.

### Problem definition

A supersonic flow of air with a transverse jet injection from the bottom wall of a rectangular channel is shown in Figure 1. The system of two-dimensional Favre-averaged Navier-Stokes equations for a multicomponent gas mixture with respect to Cartesian coordinates in a conservative form is represented in the form:

$$\frac{\partial \vec{U}}{\partial t} + \frac{\partial (\vec{E} \vec{E}_v)}{\partial x} + \frac{\partial (\vec{F} \vec{F}_v)}{\partial z} = 0 \quad (1.1)$$

$$\vec{U} = (\rho, \rho u, \rho w, E_t, \rho Y_k)^T,$$

$$\vec{E} = (\rho u, \rho u^2 + P, \rho u w, (E_t + P)u, \rho u Y_k)^T, \quad \vec{F} = (\rho w, \rho u w, \rho w^2 + P, (E_t + P)w, \rho w Y_k)^T,$$

$$\vec{E}_v = (0, \tau_{xx}, \tau_{xz}, u\tau_{xx} + w\tau_{xz} - q_x, J_{kx})^T, \quad \vec{F}_v = (0, \tau_{xz}, \tau_{zz}, u\tau_{xz} + w\tau_{zz} - q_z, J_{kz})^T,$$

$$P = \frac{\rho T}{\gamma_\infty M_\infty^2 W}, \quad W = \left( \sum_{k=1}^{N_p} \frac{Y_k}{W_k} \right)^{-1}, \quad \sum_{k=1}^{N_p} Y_k = 1 \quad (1.2)$$

$$E_t = \frac{\rho}{\gamma_\infty M_\infty^2} h - P + \frac{1}{2} \rho (u^2 + w^2), \quad h = \sum_{k=1}^{N_p} Y_k h_k, \quad h_k = h_k^0 + \int_{T_0}^T c_{pk} dT, \quad c_{pk} = C_{pk} / W_k \quad (1.3)$$

$$\tau_{xx} = \frac{\mu}{Re} \left( 2u_x - \frac{2}{3}(u_x + w_z) \right), \quad \tau_{zz} = \frac{\mu}{Re} \left( 2w_z - \frac{2}{3}(u_x + w_z) \right), \quad \tau_{xz} = \tau_{zx} = \frac{\mu}{Re} (u_z + w_x),$$

$$q_x = \left( \frac{\mu}{PrRe} \right) \frac{\partial T}{\partial x} + \frac{1}{\gamma_\infty M_\infty^2} \sum_{k=1}^{N_p} h_k J_{xk}, \quad q_z = \left( \frac{\mu}{PrRe} \right) \frac{\partial T}{\partial z} + \frac{1}{\gamma_\infty M_\infty^2} \sum_{k=1}^{N_p} h_k J_{zk}.$$

$$J_{kx} = \frac{\mu}{ScRe} \frac{\partial Y_k}{\partial x}, \quad J_{kz} = \frac{\mu}{ScRe} \frac{\partial Y_k}{\partial z}$$

The equations (1.1) are written in a dimensionless form in the generally accepted notation; the flow parameters ( $u_\infty, \rho_\infty, T_\infty$ ) are accepted as determining ones; the pressure (P) and total energy ( $E_t$ ) are related to the value  $u_\infty^2 \rho_\infty$ ; specific enthalpy ( $h_k$ ) is related to the value  $RT_\infty/W_\infty$ ; the molar specific heats ( $C_{pk}$ ) are related to  $R$ ; the characteristic length parameter is the slit width.  $Y_k$  is the mass concentration of  $k$  component; the mass concentration index  $k=1$  is related to  $O_2$ ;  $k=2-H_2$  (or  $k=2-He$ ),  $k=3-N_2$ , and  $N_p = 3$  are the numbers of the gas mixture.  $W_k$  is the molecular weight of  $k$  component;  $Re, Pr, Sc$  are the Reynolds, Prandtl and Schmidt numbers, respectively;  $\tau_{xx}, \tau_{zz}, \tau_{xz}, \tau_{zx}$  are viscous stress tensors;  $q_x, d_x, J_{xk}, J_{zk}$  are thermal and diffusion flows (diffusion flows are calculated according to Fick's law); and  $\mu = \mu_l + \mu_t$  are coefficients of laminar and turbulent viscosity. To determine  $\mu_t$ , the  $k-\omega$  turbulence model is used.

**Boundary conditions**

At the input:

$$W_k = W_{k\infty}, \quad P = P_\infty, \quad T = T_\infty, \quad u = M_\infty \sqrt{\frac{\gamma_\infty R_0 T_\infty}{W_\infty}},$$

$$w = 0, \quad Y_k = Y_{k\infty}, \quad x = 0, \quad 0 \leq z \leq H;$$

in the input section near the channel walls, the boundary layer is specified, and the longitudinal velocity is approximated by a power law; at the slit:

$$W_k = W_{k0}, \quad P = nP_\infty, \quad T = T_0, \quad w = M_0 \sqrt{\frac{\gamma_0 R_0 T_0}{W_0}},$$

$$u = 0, \quad Y_k = Y_{k0}, \quad z = 0, \quad L_b \leq x \leq L_b + h;$$

( $n = P_0/P_\infty$  is the pressure ratio degree;  $P_0, P_\infty$  are the pressures in the jet and in the flow, respectively;  $M_0, M_\infty$  are the Mach numbers in the jet and in the flow, respectively; indexes of 0 and  $\infty$  are related to the parameters of the jet and the flow);

on the lower and upper walls the condition of adhesion and insulation is settled; on the output boundary, nonreflection conditions are specified [17].

**Method of solution**

On the lower and upper walls in the boundary layer, as well as at the level of the slit, thickening of the grid is introduced for a more accurate numerical solution. Then the equations (1.1) in the transformed coordinate system are written in the form:

$$\frac{\partial \tilde{U}}{\partial t} + \frac{\partial \tilde{E}}{\partial \xi} + \frac{\partial \tilde{F}}{\partial \eta} = \frac{\partial \tilde{E}_{v2}}{\partial \xi} + \frac{\partial \tilde{E}_{vm}}{\partial \xi} + \frac{\partial \tilde{F}_{v2}}{\partial \eta} + \frac{\partial \tilde{F}_{vm}}{\partial \eta} \quad (3.1)$$

$$\tilde{U} = \bar{U}/J, \quad \tilde{E} = \xi_x \bar{E}/J, \quad \tilde{F} = \eta_z \bar{F}/J,$$

$$\tilde{E}_{v2} = \xi_x \bar{E}_{v2}/J, \quad \tilde{E}_{vm} = \xi_x \bar{E}_{vm}/J,$$

$$\tilde{F}_{v2} = \eta_z \bar{F}_{v2}/J, \quad \tilde{F}_{vm} = \eta_z \bar{F}_{vm}/J.$$

$J = \partial(\xi, \eta) / \partial(x, z)$  - the Jacobian of transformation.

The coordinate transformation parameters are described in detail in [16, 18].

In this paper convective terms are approximated using the WENO scheme, which is based on the ENO scheme and described in detail in [18]. In the proposed WENO scheme when interpolating a piecewise constant polynomial function, the Newton third-order polynomials are used. Instead of

choosing one interpolation polynomial a convex combination is used with the weighting coefficients of all represented polynomials. This achieves a substantially non-oscillating property of the scheme which increases the order of approximation of the scheme. In accordance with [18], a one-step finite-difference scheme for integrating the system (3.1) over time is represented by:

$$\Delta \tilde{U}^{n+1} + \Delta t \left[ (\hat{A}^+ + \hat{A}^-) \frac{\partial \tilde{E}^m}{\partial \xi} + (\hat{B}^+ + \hat{B}^-) \frac{\partial \tilde{F}^m}{\partial \eta} - \left[ \frac{\partial (\tilde{E}_{v2}^{n+1} + \tilde{E}_{vm}^n)}{\partial \xi} - \frac{\partial (\tilde{F}_{v2}^{n+1} + \tilde{F}_{vm}^n)}{\partial \eta} \right] \right] = O\left(\frac{1}{2} \Delta t^2\right) \tag{3.2}$$

$\hat{A}_\xi^\pm, \hat{B}_\xi^\pm$  are normalized Jacobi matrixes of the next form:

$$\hat{A}_\xi^\pm = R \left( \frac{1 \pm \text{sign}(\Lambda_\xi)}{2} \right) R^{-1}, \quad \hat{B}_\xi^\pm = T \left( \frac{1 \pm \text{sign}(\Lambda_\eta)}{2} \right) T^{-1} \tag{3.3}$$

$\tilde{E}^m, \tilde{F}^m$  are modified flows on the nodal points  $(i, j)$  consisting of source convective vectors  $(\tilde{E}, \tilde{F})$  and additive high-order accuracy parameters.

In contrast to the high-order accuracy parameters of [18], vectors  $\tilde{E}_{\xi j}, \tilde{D}_{\xi j}$  for positive and negative eigenvalues  $\lambda_{ij}$  are written in the next form:

$$\tilde{E}_{\xi j} = \begin{cases} \frac{\alpha_{2ij} \bar{E}_{\xi i + \frac{1}{2}j}}{\sum_{L=0}^2 \alpha_{Lij}} + \frac{\alpha_{1ij} (\bar{E}_{\xi i + \frac{1}{2}j} + \bar{E}_{\xi i - \frac{1}{2}j})}{2 \sum_{L=0}^2 \alpha_{Lij}} + \frac{\alpha_{0ij} \bar{E}_{\xi i + \frac{1}{2}j}}{\sum_{L=0}^2 \alpha_{Lij}} & \text{if } \lambda_{ij} > 0 \\ \frac{\bar{\alpha}_{2ij} \bar{E}_{\xi i + \frac{1}{2}j}}{\sum_{L=0}^2 \bar{\alpha}_{Lij}} + \frac{\bar{\alpha}_{1ij} (\bar{E}_{\xi i + \frac{1}{2}j} + \bar{E}_{\xi i - \frac{1}{2}j})}{2 \sum_{L=0}^2 \bar{\alpha}_{Lij}} + \frac{\bar{\alpha}_{0ij} \bar{E}_{\xi i + \frac{1}{2}j}}{\sum_{L=0}^2 \bar{\alpha}_{Lij}} & \text{if } \lambda_{ij} < 0 \end{cases} \tag{3.4}$$

$$\tilde{D}_{\xi j} = \begin{cases} \frac{\alpha_{2ij} \Delta_+ \bar{D}_{\xi i + \frac{1}{2}j}}{\sum_{L=0}^2 \alpha_{Lij}} + \frac{\alpha_{1ij} (\Delta \bar{D}_{\xi i + \frac{1}{2}j} + \Delta_+ \bar{D}_{\xi i - \frac{1}{2}j})}{2 \sum_{L=0}^2 \alpha_{Lij}} + \frac{\alpha_{0ij} \Delta \bar{D}_{\xi i - \frac{1}{2}j}}{\sum_{L=0}^2 \alpha_{Lij}} & \text{if } \lambda_{ij} > 0 \\ \frac{\alpha_{2ij} \Delta_+ \bar{D}_{\xi i + \frac{1}{2}j}}{\sum_{L=0}^2 \alpha_{Lij}} + \frac{\alpha_{1ij} (\Delta \bar{D}_{\xi i + \frac{1}{2}j} + \Delta_+ \bar{D}_{\xi i - \frac{1}{2}j})}{2 \sum_{L=0}^2 \alpha_{Lij}} + \frac{\alpha_{0ij} \Delta \bar{D}_{\xi i - \frac{1}{2}j}}{\sum_{L=0}^2 \alpha_{Lij}} & \text{if } \lambda_{ij} < 0 \end{cases}$$

where

$$\begin{aligned} \bar{E}_{\xi i \pm \frac{1}{2} j} &= (R \operatorname{sign}(\Lambda_{\xi}) R^{-1})_{i \pm \frac{1}{2} j} \left[ \frac{I - (\Delta t / \Delta \xi)(R|\Lambda_{\xi}|R^{-1})_{i \pm \frac{1}{2} j}}{2} \right] \Delta_{\pm} \tilde{E}_{ij}, \\ \bar{D}_{\xi i \pm \frac{1}{2} j} &= (R \operatorname{sign}(\Lambda_{\xi}) R^{-1})_{i \pm \frac{1}{2} j} \left[ \frac{\left[ (\Delta t / \Delta \xi)(R|\Lambda_{\xi}|R^{-1})_{i \pm \frac{1}{2} j} \right]^2 - I}{2} \right] \Delta_{\pm} \tilde{E}_{ij}, \quad \widehat{D}_{\xi i \pm \frac{1}{2} j} = \bar{E}_{\xi i \pm \frac{1}{2} j} + \bar{D}_{\xi i \pm \frac{1}{2} j} \end{aligned}$$

Values for weight coefficients  $\alpha_{Lij}, \bar{\alpha}_{Lij} > 0$  ( $L = 0, 1, 2$ ) are obtained in the next form:

$$\alpha_{Lij} = \frac{C_{Lij}}{(\varepsilon + IS_{i+Lj})^3} \text{ и } \bar{\alpha}_{Lij} = \frac{\bar{C}_{Lij}}{(\varepsilon + IS_{i+Lj})^3} \tag{3.5}$$

where

$$C_{0ij} = \frac{1}{12}, C_{1ij} = \frac{1}{2}, C_{2ij} = \frac{1}{4}, \bar{C}_{0ij} = \frac{1}{4}, \bar{C}_{1ij} = \frac{1}{2}, \bar{C}_{2ij} = \frac{1}{12} \tag{19}$$

and  $IS_{ij}$  is an indicator of smoothness of the solution and is found by summing all the root-mean-square

values of the derivatives of the desired vector  $\tilde{U}$ :

$$IS_{ij} = \frac{1}{2} \left[ (\Delta \tilde{U}_{i-2j})^2 + (\Delta \tilde{U}_{i-1j})^2 \right] + \left[ \Delta^2 \tilde{U}_{i-2j} \right]^2 \tag{3.6}$$

where  $\Delta \tilde{U}_{ij} = \tilde{U}_{i+1j} - \tilde{U}_{ij}$  and  $\Delta^2 \tilde{U}_{ij} = \Delta \tilde{U}_{i+1j} - \Delta \tilde{U}_{ij}$ .

vectors: vectors of second derivatives and vectors of dissipative members and flow vectors with mixed derivatives are approximated explicitly with a second order of accuracy [18]. Linearization of convective terms is carried out using the properties of homogeneity.

To avoid uncertainty in the denominator of the weight coefficients  $\alpha_{Lij}$  and  $\bar{\alpha}_{Lij}$  the low coefficient  $10^{-7} < \varepsilon < 10^{-5}$  is added in (3.6). Vectors  $\vec{E}_{\eta ij}$  and  $\vec{D}_{\eta ij}$  are written in the same way. Further in the system of equations (3.2), terms containing second derivatives are represented as a sum of two

After applying factorization to the system (3.2), we have two one-dimensional operators for an implicit solution with respect to the vector of thermodynamic parameters by matrix driving:

1-st step.

$$\left[ I + \Delta t \left[ \left( \hat{A}_{i-\frac{1}{2}j}^+ \Delta_- A_{\xi ij}^n + \hat{A}_{i+\frac{1}{2}j}^- \Delta_+ A_{\xi ij}^n \right) + \Delta \left( \frac{\mu_i \xi_x^2}{\operatorname{Re} J} \right)_{ij} \Delta \left( \frac{1}{U_1^n} \right)_{ij} \right] \right] U_{ij}^* = RHS_{\xi ij}^n + RHS_{\eta ij}^n$$

2-nd step.

$$\left[ I + \Delta t \left[ \left( \widehat{B}_{ij-\frac{1}{2}}^+ \Delta_- B_{\eta ij}^n + \widehat{B}_{ij+\frac{1}{2}}^- \Delta_+ B_{\eta ij}^n \right) + \Delta \left( \frac{\mu_i \eta_z^2}{\text{Re} J} \right)_{ij} \Delta \left( \frac{1}{U_1^n} \right)_{ij} \right] \right] \widetilde{U}_{ij}^{n+1} = U_{ij}^* \quad (3.7)$$

were

$$RHS_{\xi j}^n = \widehat{A}_{i+\frac{1}{2}j}^- \left[ (\bar{E}_{\xi i+1j} + \bar{D}_{\xi i+1j}) - (\bar{E}_{\xi ij} + \bar{D}_{\xi ij}) \right]^n + \widehat{A}_{i-\frac{1}{2}j}^+ \left[ (\bar{E}_{\xi ij} + \bar{D}_{\xi ij}) - (\bar{E}_{\xi i-1j} + \bar{D}_{\xi i-1j}) \right]^n$$

The second addend  $RHS_{\eta j}^n$  is written the same way.

The vector of mass concentrations of the mixture is determined using a scalar sweep. For approximation of the first derivatives in the system (3.7) the differences against the flow with the first order of accuracy are used and for the second derivatives, the central differences with the second order of accuracy are used. The temperature is determined in accordance with the [16].

## Results and analysis

The calculations were carried out on a grid separated by spatial coordinates with the next parameters:

$$2 \leq M_\infty \leq 6, \quad 2 \leq n \leq 15, \quad \text{Re} = 10^6 - 10^7, \quad \text{Pr} = 0.7$$

To test the numerical method, the following experiment was performed: through the slit on the wall of 0.1 cm wide the hydrogen sound jet of  $T_0 = 800K$  and  $n = 10.29$  was injected perpendicular to the main air flow (oxygen and nitrogen) of parameters  $M_\infty = 3.75$ ,  $P_\infty = 11090 Pa$ ,  $T_\infty = 629.43K$ ,  $Pr = 0.7$ ,  $Re = 62.73 \times 10^6$ . The height and width were  $H = 15.2 sm$  and  $L = 45 sm$ , respectively. Specific heat capacities at constant

pressure  $C_{pk}$  of  $k$ -component were calculated using fourth-order polynomial interpolation in temperature:

$$C_{pk} = \sum_{i=1}^5 a_{ki} T^{i-1}, \quad (4.1)$$

where  $\{a_{ki}\}$  is an empirical constant defined for temperature within  $300 < T < 5000K$  [20].

Table 1 presents the sensitivity of the convergence of solutions to the characteristics of the grid by estimating the total  $L_1^p = \frac{1}{N} \sum_{n=1}^N |\varepsilon_M^n - \varepsilon_{\hat{M}}^n|$  and

mean-square  $L_2^p = \frac{1}{N} \sqrt{\sum_{n=1}^N |\varepsilon_M^n - \varepsilon_{\hat{M}}^n|^2}$  deviations of

the norms of density residuals. Here  $\varepsilon_M^n = \max_{(i,j) \in M} |\rho_{i,j}^{n+1} - \rho_{i,j}^n|$ ,  $\varepsilon_{\hat{M}}^n = \max_{(i,j) \in \hat{M}} |\rho_{i,j}^{n+1} - \rho_{i,j}^n|$ ;  $N$  is

the number of iterations. Estimates were built for WENO and ENO schemes by successive refinement of the grids, and the grid  $M$  with nodes  $I \times J$  was taken as the initial one, then the nodes  $M$  and  $L$  of the grid  $\hat{M}$  were varied. As follows from the table, the difference in the deviation of the values of the norms of the density residuals decreases with the grid refinement. The grid  $\hat{M}$  with nodes  $301 \times 281$  has minimal values while the indicator  $L^p$  for the WENO scheme is less than that of the ENO scheme.

**Table 1** – The relationship between the total and standard deviation (the density difference) on the size of the grid for WENO and ENO schemes

The number of nodes		WENO	ENO	WENO	ENO
$M = I \times J$	$\hat{M} = M \times L$	$L_1^p$	$L_1^p$	$L_2^p$	$L_2^p$
$I = 301,$ $J = 261$	$M = I, L = 221$	$6,09 \cdot 10^{-2}$	$8,02 \cdot 10^{-2}$	$1,14 \cdot 10^{-3}$	$1,4 \cdot 10^{-3}$
	$M = I, L = 281$	$3,37 \cdot 10^{-2}$	$3,49 \cdot 10^{-2}$	$6,27 \cdot 10^{-4}$	$7,22 \cdot 10^{-4}$
$I = 321,$ $J = 281$	$M = 301, L = J$	$2,74 \cdot 10^{-2}$	$3,87 \cdot 10^{-2}$	$5,29 \cdot 10^{-4}$	$8,03 \cdot 10^{-4}$
	$M = 341, L = J$	$2,91 \cdot 10^{-2}$	$3,43 \cdot 10^{-2}$	$6,11 \cdot 10^{-4}$	$7,86 \cdot 10^{-4}$

To compare with experimental data, the problem of a flat supersonic air flow ( $M_\infty=2.9$ ,  $P_\infty=0.0663MPa$ ,  $T_\infty=108K$ ) with perpendicular injection of a helium sound jet ( $T_0=217K$ ,  $P_0=1.24MPa$ ) through a slit on the bottom wall of 0.0559 sm width was calculated. The heights and width of the channel were  $H=7,62sm$  and  $L=25$  sm, respectively. In this experiment it is necessary to know the  $C_{pk}$  (J / (Mol.K)) component of  $O_2, N_2, He$

at a temperature below 300K. Here, the experimental data of [21] are used (Table 2) in which the dependences of  $C_{pk}$  on low temperatures are given. The construction of polynomial (4.1) is carried out using the method of least squares. For this purpose a system of linear algebraic equations is constructed for unknown empirical constants  $\{a_{ki}\}$ , which is solved by the LU decomposition method. The values  $\{a_{ki}\}$  found in this way are shown in Table 3.

**Table 2** – Thermo-chemical table (J / (Mol.K))

T, °K	$C_{P1} (O_2)$	$C_{P2} (N_2)$	$C_{P2} (He)$
100	-----	30.04253461	20.9336046
120	29.66933952	----	20.9336046
140	-----	29.38966128	20.9336046
150	29.40808320	----	20.9336046
170	29.33305574	----	20.9336046
180	-----	29.25719093	20.9336046
210	29.27142605	----	20.9336046
220	-----	29.20326494	20.9336046
250	29.29822157	----	20.9336046
260	----	29.17747260	20.9336046
300	29.45497536	29.17161274	20.9336046

**Table 3** – The values of of the empirical constants  $a_{ki}$

$T < 300K$	$O_2$	$N_2$	$He$
$a_{k1}$	0.34843577E+02	0.39755287E+02	0.209336046E+02
$a_{k2}$	-0.90674514E-01	-0.20027529E+00	0.000000000E+00
$a_{k3}$	0.56072001E-03	0.14293081E-02	0.000000000E+00
$a_{k4}$	-0.15761941E-05	-0.45017727E-05	0.000000000E+00
$a_{k5}$	0.17168133E-08	0.52356848E-08	0.000000000E+00

Figure 2 shows the calculated and measured values of the pressure distribution on the wall in front of the slit and behind it. Curves 1, 2 are numerical calculations of WENO and ENO schemes, respectively; ••• is an experiment from [1]. The figure shows good agreement between the numerical and experimental data in front of the slit. However, behind the slit the values were

underestimated. The curve obtained using the WENO scheme is located below the curve corresponding to the experiments and the curve obtained using the ENO scheme, because of the dissipative properties of the WENO scheme. In general, there is satisfactory agreement between the results of calculations and experimental measurements.

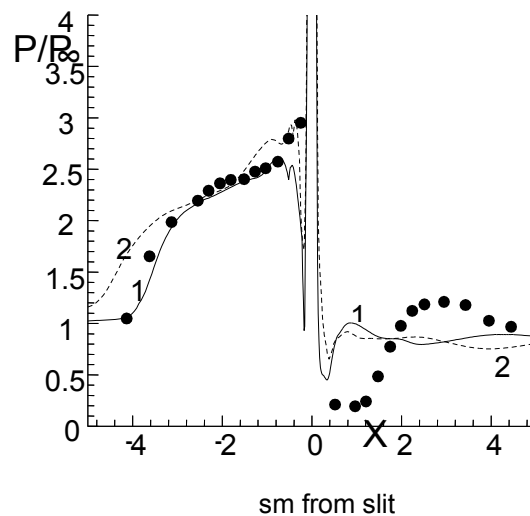


**Figure 2** – The pressure distribution on the wall: “●●●” is the experiment [1], curve 1 is the WENO scheme, curve 2 is the ENO scheme

In Figures 3-6, the results of calculations of the problem of a flat supersonic air flow with transverse injection of a hydrogen sound jet through a slit on the bottom wall are given. The slit sizes of the injection jet are varied with three cases of the physical width of the slit ( $h_1$ ,  $h_2$ ,  $h_3$ ). In the first case, the dimensionless parameters of the computational domain are as follows:  $h = 1$ ,  $L = 125$ ,  $H = 20$ , and, for the second case:  $h = 1$ ,  $L = 100$ ,  $H = 16$ , which corresponds to  $h_2 = 1.33h_1$ , and for the third case:  $L = 75$ ,  $H = 12$ ,  $h_3 = 1.66h_1$ .

The parameters of oncoming flow are:  $M_\infty = 3.75$ ,  $T_\infty = 629.43K$ ,  $Pr = 0.7$ ,  $Re = 10^6$ ; the parameters of the jet are:  $T_0 = 800K$ ,  $n = 15$ . The width of the boundary layer on the input section on walls is  $\delta = 0.38/h_i$ , where  $i=1,2,3$ .

When an underexpanded jet flows into a stream, the pressure in the jet tends to equalize with the ambient pressure as a result of which the jet expands with the formation of a family of rarefaction waves that move to the jet boundaries forming a hanging shock which is closed by the Mach disk. The distribution of the local Mach number ( $M = \sqrt{u^2 + w^2}/c$ , with  $c$  being a local velocity of sound, is shown in Figure 3 (3a- $h_1$ , 3b- $h_2$ , 3c- $h_3$ ). It follows from the graph that for  $h_1$  (Figure 3a) the jet injected at a sonic speed accelerates and goes into a supersonic zone at some distance (the value of the local Mach number

increases to 2.5), then the boundary of the resulting supersonic zone closes, delineating a circle. This circle corresponds to the barrel separating the supersonic zone from the subsonic one. At the top of the barrel the compression waves converge forming a Mach disk. Behind the barrel the flow slows down and becomes subsonic with a Mach number of 0.4. Ultimately, the flow of the jet accelerates and goes into the supersonic zone and the Mach number increases to 3 and above. With an increase in the slit width, a noticeable increase in the size of the circle is observed which can be traced from the comparison of Figures 3a and Figures 3b. However, in Figure 3c, the narrowing of the barrel is clearly observed despite the fact that here the slit size is maximum. The graphs clearly show that the size of the Mach disk varies in an ambiguous manner although it is known that an increase in the size of the slit leads to an expansion of the barrel-like structure in the jet and, consequently, to an increase in the Mach disk. Such an increase in the size of the Mach disk is explained in the case of  $h_3$  a shift of the detachment zone towards the input boundary, the distance between the jet and the upper return area, respectively, becomes minimal (it is a confuser). As a result, the oncoming flow is significantly accelerated, thereby preventing the expansion of the jet.

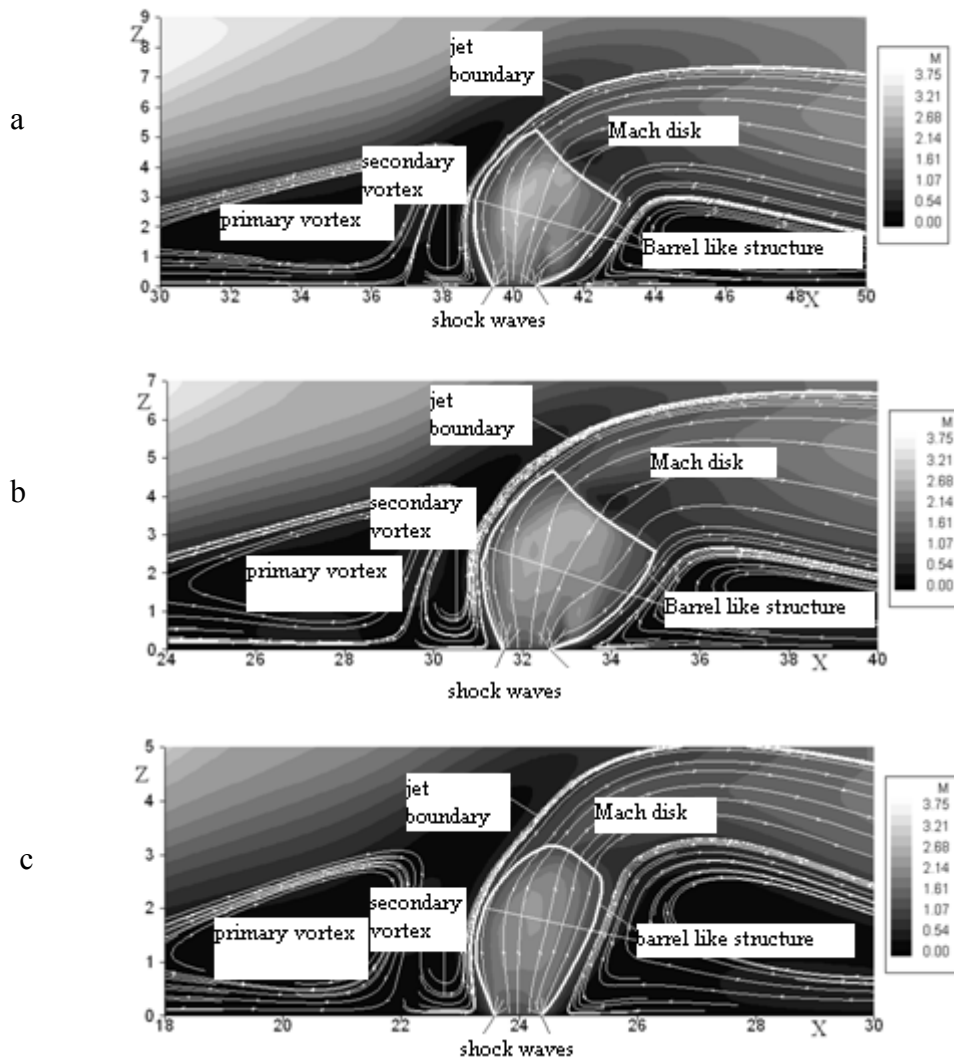


Figure 3 – The distribution of the local Mach number for the slit width:  
 a)  $h_1$ , b)  $h_2$ , c)  $h_3$

The results of numerical experiments for the velocity vector field and streamlines, Figure 4 (4a- $h_1$ , 4b- $h_2$ , 4c- $h_3$ ), show a picture of the vortex structure arising from the interaction of shock waves with both the lower boundary layer and the upper one. The graph shows that in the zone adjoining to the wall, two vortices are formed in front of the jet which formed as a result of the primary and secondary separation of the flow from the wall. The directions of movement in them are opposite due to part of the air flow directly near the wall passing the sections of the oblique shock (2) and closing (3) turns down to the wall and penetrates into the zone of detached flow, then spreads in opposite directions. In this case, the vortex located closer to

the jet moves counterclockwise, and the vortex located at a greater distance from it moves clockwise which is observed in the calculation results. Behind the jet the occurrence of a vortex region is associated with a zone of low pressures. The graphs show the region of separation on the upper wall due to the interaction of the head shock wave (1) with the upper boundary layer. The qualitative pictures of the return zones are similar in all three cases. However, they are quantitatively different since dimensions increase significantly with increasing of the slit width.

In Figure 4a-c in addition to the known ones, there is an additional vortex on the bottom wall at some distance behind the jet which was

formed as a result of the interaction of the shock (6) with the bottom boundary layer. As the size of the slit increases, it shifts towards the jet (comparison of Figure 4a-b). Thus, we can

conclude that an increase in the size of the slit will lead to an increase in the mixing of air and fuel directly behind the injected jet due to the extensive zones of return flows.

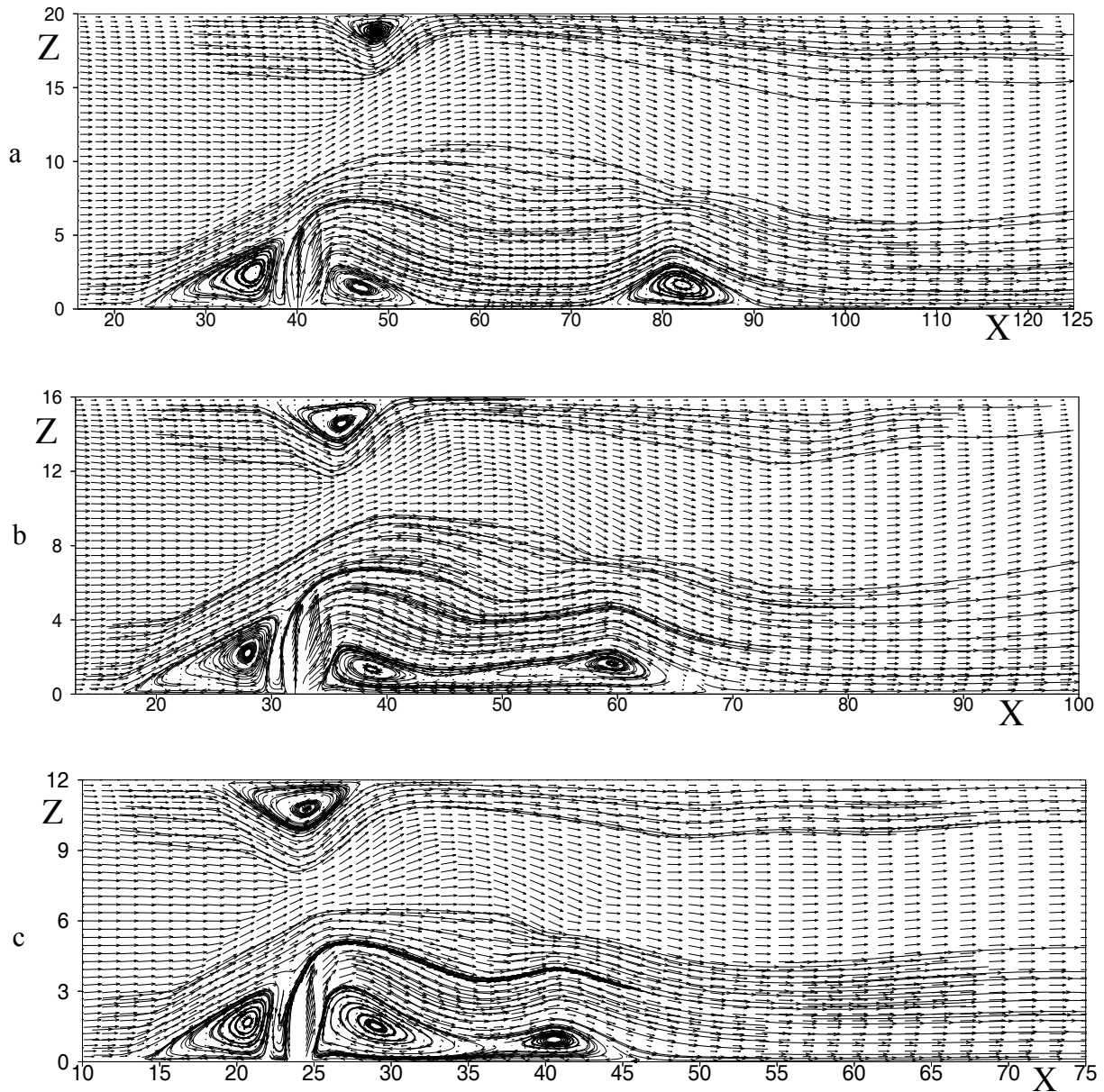


Figure 4 – The velocity vectors and streamlines for the slit width:

a)  $h_1$ , b)  $h_2$ , c)  $h_3$

Figure 5 a-c shows the distribution of the mass concentration of hydrogen for all three considered slits. The contours of a constant concentration of hydrogen show that the maximum concentration value is reached behind the jet. The results show that increasing the size of the slit affects the range of

the injected jet, so with  $h_1$  the line of 1% hydrogen concentration rose to a height of 45% of the total height of the channel (Figure 5a), when with  $h_2$  the same line corresponds to half of the height of the channel, but for  $h_3$  is 47.5% of the height of the channel. In this case, a decrease in the range of the

injected hydrogen also indicates a blockage of the jet.

The pressure distribution on the bottom wall (Figure 6a) shows that the excess pressure in front of the jet increases and at some distance behind the

jet its growth is also observed due to the detachment of the boundary layer. At the same time, it is noticeable from the graph that the curves for large  $h$  are significantly higher. A similar pattern is observed on the upper wall (Figure 6b).

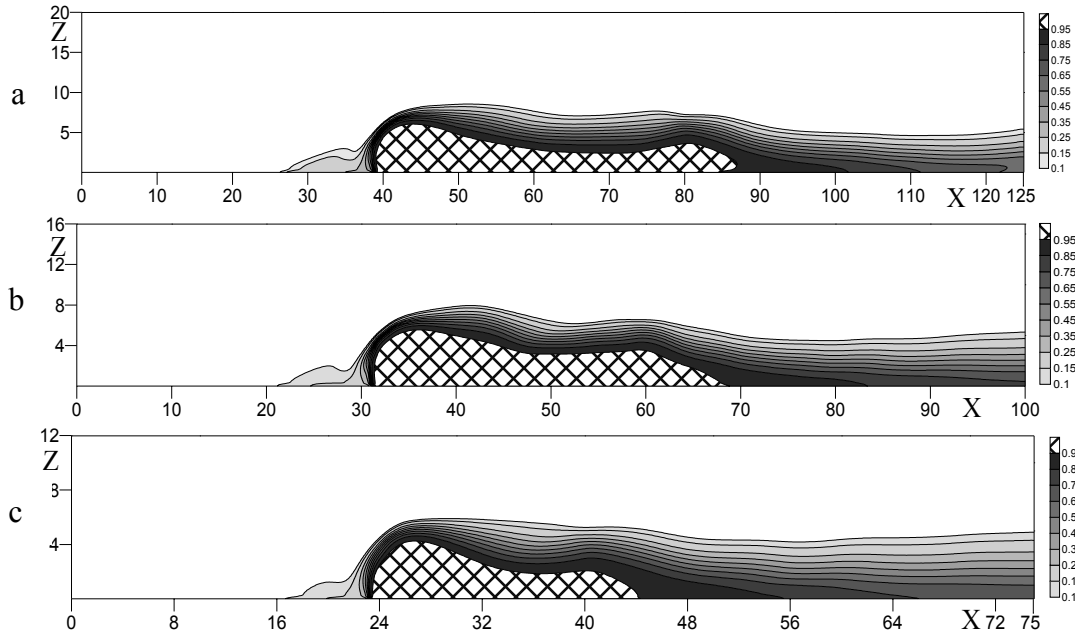


**Figure 5** – The distribution of the mass concentration of hydrogen for the slit width:  
 a)  $h_1$ , b)  $h_2$ , c)  $h_3$

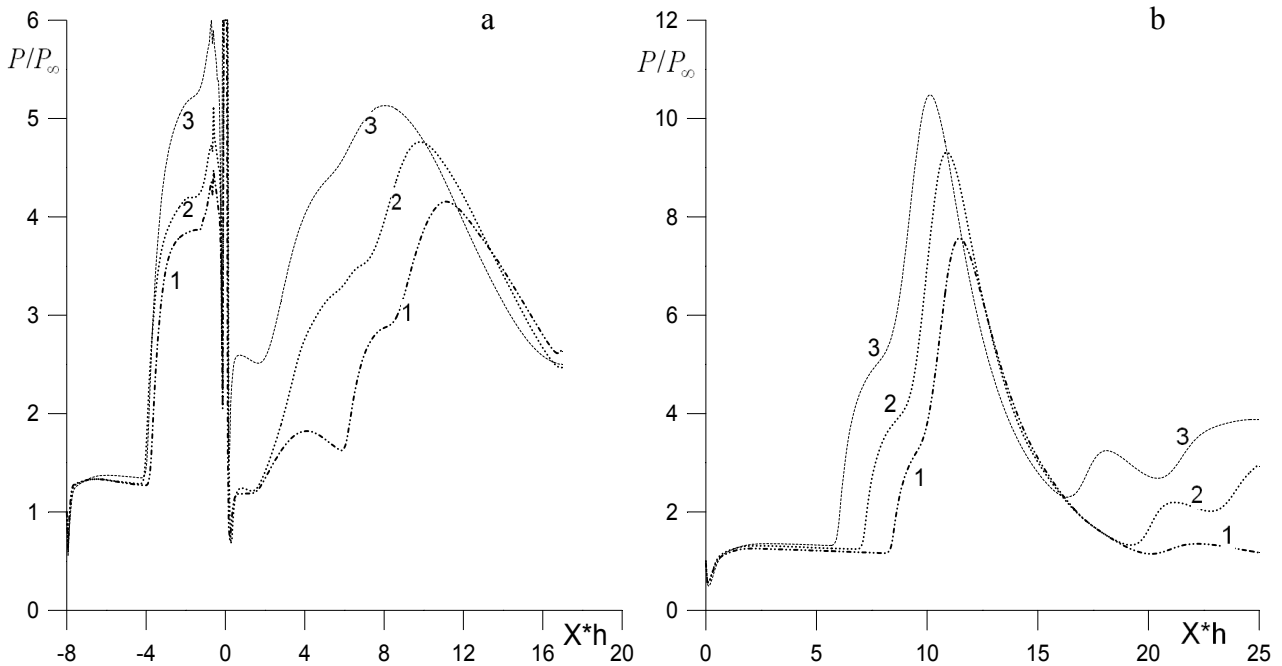


**Figure 6** – The pressure distribution on the bottom and upper walls

## Conclusion

Using a numerical experiment, a shock-wave structure and a detachment region are obtained due to the interaction of shock waves with the boundary layer on both the upper and lower walls of the channel and depending on the size of the injected jet. An ambiguous decrease is shown in the expansion of the jet with an increase in the width of the slit which is a consequence of a confuser between the injected jet and the detachment zone on the upper wall. In addition to the well-known shock-wave pattern an additional structure appeared here due to the interaction of the reflected shock (6) with the boundary layer on the bottom wall at some distance behind the jet which can lead to an increase in air and fuel mixing due to the extensive return flow zones. It is established that, depending on the increase of  $h$ , the range of the jet decreases due to its locking. Excessive pressure on the walls increases with increasing jet size which leads to an increase in the load on the channel walls. Comparison of calculations with experimental data shows satisfactory agreement of results. Thus, the numerical model developed in this paper for calculating turbulent flows based on the WENO scheme allows one to study both the supersonic flow of a multicomponent gas and to simulate combustion processes.

## References

1. Shun J., Sh., Yun S. "Chislenoe issledovanie techenii s khimicheskimi reaktsiyami na osnove LU-faktorizovannoi skhemi, postroennoi metodom simetrichnoi posledovatelnoi verkhnei relaksatsii [Numerical study of flows with chemical reactions based on the LU-factorized scheme, constructed by the method of symmetric sequential upper relaxation]." *Aerospace Engineering* 10 (1990): 102-113.
2. Chenault F.C., Beran P.S. "k  $\epsilon$  and Reynolds Stress Turbulence Model Comparisons for Two-Dimensional Injection Flows." *AIAA Journal* 36, no. 8 (1998): 1401-1412.
3. Aso S., Inoue K., Yamaguchi K., Tani Y. "A study on supersonic mixing de circular nozzle with various injection angles for air breathing engine." *Acta Astronautica* 65 (2009): 687-695.
4. Spade F., Zukoski Y. "Issledovanie vzaimodeistviya gazovoi strui, vitekayushei iz poperechnoi sheli, so sverkhzvukovim potokom [Investigation of the interaction of a gas jet flowing from a transverse slit with a supersonic flow]." *Rocket technology and astronautics* 2 (1968): 16-25.
5. Avduyevskii V.S., Medvedev K.I., Polyanskii M.N. "Vzaimodeistvie sverkhzvukovogo potoka s poperechnoi stuei, vduvaemoi cherez krugloe otverstie v plastine [The interaction of supersonic flow with a transverse jet blown through a round hole in the plate]." *News of the USSR Academy of Sciences. Fluid and gas mechanics* 5 (1970): 193-197.
6. Glagolev A.I., Zubkov A.I., Panov U.A. "Vzaimodeistvie strui gaza, vytekayushei iz otverstiya v plastine, so sverkhzvukovim potokom [The interaction of the gas jet flowing out of the hole in the plate with supersonic flow]." *News of the USSR Academy of Sciences. Fluid and gas mechanics* 2 (1968): 99-102.
7. Shets D., Hoskins P.F., Leman H. "Structura poperechnikh strui, istekayushikh v sverkhzvukovoi potok s bolshoi stepenyu nedorasshireniya [The structure of transverse jets flowing into a supersonic flow with a high degree of under-expansion]." *Rocket technology and astronautics* 5 (1967): 65-69.
8. Huang W., Zhen-guo Wang, Wu J., Shi-bin Li "Numerical prediction on the interaction between the incident shock wave and the transverse slot injection in supersonic flows." *Aerospace Science and Technology* 1.86 (2012): 1-9.
9. Kim J.H., Yoon Y., Jeung I.S., Huh H., Choi J.Y. "Numerical study of mixing enhancement by shock waves in model scramjet engine." *AIAA Journal* 41 (6) (2003): 1074-1080.
10. Liou W.W., Huang G., Shih T.H. "Turbulence model assessment for shock wave/turbulent boundary-layer interaction in transonic and supersonic flows." *Computers & Fluids* no. 29 (2000): 275-299.
11. Knight D., Yan H., Panaras A., Zheltovodov A. "RTO WG 10: CFD validation for shock wave turbulent boundary layer interactions." *AIAA Paper N 2002-0437*.
12. Fyodorova N.N., Fedorchenko I.A. "Raschyot vzaimodeistviya padayushego kosogo skachka uplotneniya s turbulentnim pogranchnim sloem na plastine [Calculation of the interaction of a falling oblique shock wave with a turbulent boundary layer on a plate]." *Applied mechanics and technical physics* 45, no. 3 (2004): 61-71.
13. Harten A., Osher S., Engquist B., Chakravarthy S.R. "Some Results on Uniformly High-Order Accurate Essentially Non-Oscillatory Schemes." *Applied Num. Math.* no. 2 (1986): 347-377.

14. Yershov S.V. "Kvazimonotonnaya ENO skhema povishennoi tochnosti dlya integrirovaniya uravnenii Eulera i Navie-Stoksa [Quasi-monotone ENO-scheme of increased accuracy for integrating the Euler and Navier-Stokes equations]." *Math modeling* 6, no. 11 (1994): 63-75.
15. Yang J.Y. "Third\_Order Non-Oscillatory Schemes for the Euler Equations." *AIAA Journal* 29, no. 10 (1991): 1611-1618.
16. Beketayeva A.O., Naimanova A.Z. "Primenenie ENO (Essentially Non-Oscillatory) skhemi dlya modelirovaniya techeniya mnogokomponentnoi gazovoi smesi [The use the ENO (Essentially Non-Oscillatory) Scheme to Simulate a Multicomponent Gas Mixture]." *Computational Technologies* 12, no. 4 (2007): 17-25.
17. Poinot T.J., Lele S.K. "Boundary Conditions for Direct Simulation of Compressible Viscous Flows." *Journ. of Comput. Phys.* no. 101 (1992): 104-129.
18. Bruel P., Naimanova A.Zh. "Computation of the normal injection of a hydrogen jet into a supersonic air flow." *Thermophysics and Aeromechanics* 17, no. 4 (2010): 531-541.
19. Liu X., Osher S., and Chan T. "Weighted Essentially Non-oscillatory Schemes." *Journal of Computational Physics* 115 (1994): 200-212.
20. Kee R.J., Rupley F.M., Miller J.A. "CHEMKIN-II: a FORTRAN chemical kinetic package for the analysis of gas-phase chemical kinetics." *SANDIA Report SAND89-8009* (1989).
21. Kikoina I. K. "Tablitsi fizicheskikh velichin [Physical Parameters Tables]." Moscow: *Atomizdat* (1976): 1008.

IRSTI 44.39.03

<sup>1,\*</sup>Zh. Baizhuma, <sup>1</sup>S.A. Bolegenova, <sup>1</sup>R.K. Manatbayev,  
<sup>2</sup>K. Baktybekov, <sup>2</sup>A. Syzdykov

<sup>1</sup>Department of Thermal Physics and Technical Physics,  
Al-Farabi Kazakh National University, Almaty, Kazakhstan

<sup>2</sup>Kazakhstan Gharysh Sapary, Astana, Kazakhstan

\*e-mail: baizhuma.zhandos@gmail.com

### **Evaluation of wind power potential in shelek corridor (Kazakhstan) using weibull distribution function**

**Abstract.** Kazakhstan currently has one of the highest, per capita, carbon footprints in the world. There are heavy reliance (approx 85%) on coal for electricity production in Kazakhstan. Coal is a very carbon intensive fuel. A drive to moderate coal's contribution to electricity production provides a driver for wind energy development. Finding a suitable location requires a detailed and often costly analysis of local wind conditions. Wind resource assessment is a crucial first step in gauging the potential of a site to produce energy from wind turbines. In this paper, the wind energy potential of Shelek corridor, located in the Almaty region in Kazakhstan were examined. Local wind speed distributions are represented by Weibull statistics. The results show that the average annual mean wind speed variation for Shelek corridor ranges from 4.0 to 8.0 m/s. The wind power density variation based on the Weibull analysis ranges from 280.0 to 320.0 W/m<sup>2</sup>.

**Key words:** wind power, energy production, renewable energy, MERRA, Weibull distribution.

#### **Introduction**

For nowadays Kazakhstan is among the top 20 countries which produce the highest carbon dioxide emission per capita. There are several reasons of this such as a small population per square kilometer, a strong dependence of the power plant on coal. Coal emits very high amount of carbon dioxide to the atmosphere. It means that wind electric stations will be attractive opportunity for Government and business sector. Investing in such projects is commercially feasible [1].

Kazakhstan's geographical location is very suitable to develop wind energy stations with power up to 760 GW. For instance; Shelek corridor has potential to produce power from wind energy approximately 3200 kW/h/MW [2].

The performance of the wind power conversion system depends on a wide range of criteria including

a lot of aspects [3]. The characteristics of the wind tendency are one of the main and influential parameters that support when determining the suitability of a site for the use of wind energy. Due to the stochastic nature of the wind, several models were developed to analyze the available wind data in order to obtain the characteristics of any wind mode. One of these established models operates on the basis of the Weibull distribution [3]. This article presents the details of the analysis based on the Weibull distribution of wind data, from the NASA's Modern-Era Retrospective Analysis for Research and Applications.

#### **Kazakhstan's wind power market**

The Republic of Kazakhstan has the ninth largest territory in the world. It is about 2.7 million km<sup>2</sup>. However, Kazakhstan is one of the countries

with the least population density in the world (5.5 persons per km<sup>2</sup>). There are three cities with population over 1 million people: Astana, Almaty and Shymkent.

Kazakhstan has huge resources of fossil fuels such as coal, oil, gas and uranium. These resources are being actively exporting. For instance, Kazakhstan produces just less than 100 million tons of coal and approximately 35% of this is exported to the neighboring countries. 1.5 million barrels of oil produced per one day. And 75% of them sold to the China and Russia.

There is no any country in the world, which produces more uranium than Kazakhstan. According to the data in 2009 year, 27.6% of world's uranium production was made by Kazakhstan.

Excess of energy resources is the main factor hindering the development of renewable energy sources in Kazakhstan.

Based on the outcomes of the World Summit on Sustainable Development held at Johannesburg in 2002 Kazakh government accepted Sustainable Development Concept for 2007-2024. That Concept was devoted to sustainable use of renewable

resources and alternative energy in Kazakhstan. Efficient and sustainable use of renewable resources and alternative energy sources will be possible if:

- innovative technologies in use of land, water, forestry, fishery, biological resources and renewable sources of energy will be introduced;
- efficient use of hydropower resources, solar and wind resources and other renewable resources and alternative energy sources will be simulated;
- the Centers for distribution of international experience in the area of energy and resource efficiency and use of renewable sources of power will be established.

Considering all of the above, it is possible to list the main challenges, which are the strong drivers for the development of wind energy in Kazakhstan:

- the old power generation infrastructure;
- high amount of transition and distribution loses;
- The highest carbon footprints in the world.

As a result, since 2012 year the amount of installed capacity by the onshore wind turbines has increased 65 times. It can be shown in the diagram below.

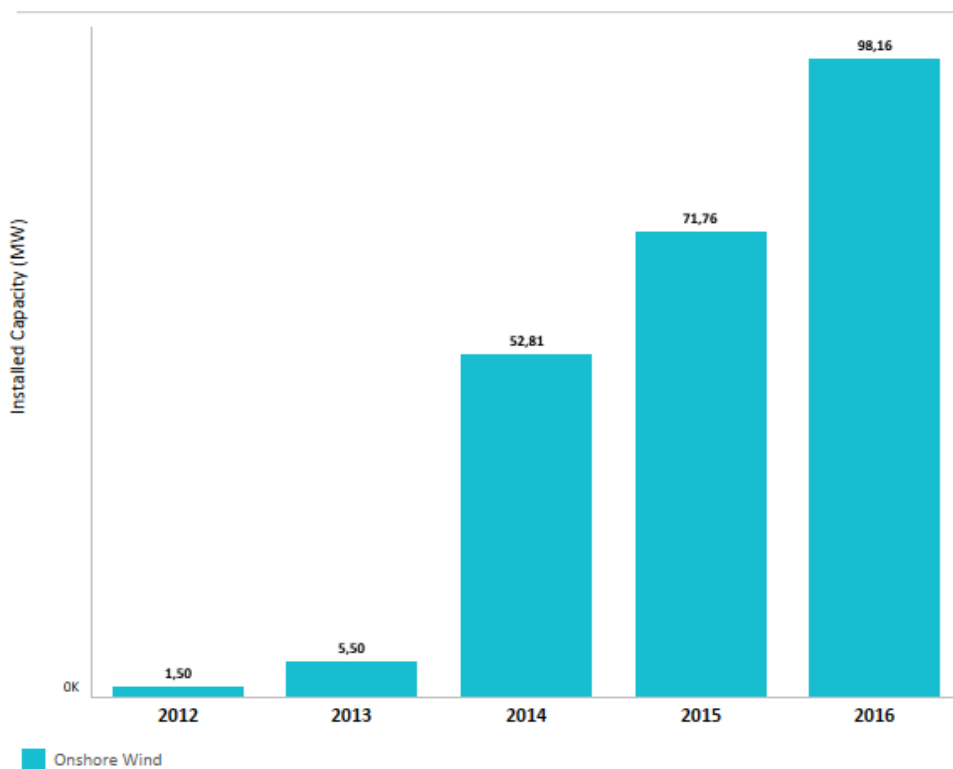


**Figure 1** – Trends in renewable energy (Installed capacity)

In 2012, installed capacity was only 1.5 MW, the first wind power station was installed in Kordai, Zhambyl region. Next year power production increased three times. 2014 year was significant for Kazakhstan wind power market, because the second wind power station was set up in Ereimentau, Akmola region. And it drove to fundamental growth in the installed capacity: from 5.5 MW in 2013 to the 52.81 MW in 2014. In 2015 and 2016, there were still positive trends in the installed capacity. Compared to 2014 year, potential power produced from the wind rose by the 40% each year.

### Methods and materials

There are two ways of obtaining data. First way is analysing of production data. The benefits of using production data are that they are reflecting true fluctuations and do not require any additional calculations. But this approach is applicable to the places where a wind turbine has already been installed. The second way is using data from the weather station. However, that way has several disadvantages: it is not available; data records sometimes not complete. Moreover to that, to calculate a new location, you need to install anemometers. This is not economically profitable [4].

In Kazakhstan there is no free available wind speed data at the moment. Companies should measure wind data themselves. Previously a wind atlas of Kazakhstan was created in the framework of the UNDP / GEF Project and the Government of the Republic of Kazakhstan "Kazakhstan is an initiative to develop the wind energy market". However, at this moment that site is not available.

Ritter et al. [4], recommended an alternative dataset which is providing wind power analysis and reanalysis data, such as Modern-Era Retrospective Analysis for Research and Applications (MERRA) data provided by NASA [5]. MERRA offers wind data all over the world and an hourly temporal resolution since 1979. It consist two components at three different heights (2 m, 10 m and 50 m above ground). A northward and an eastward wind component are helpful to derive the wind speed and wind direction at various turbine heights [6].

In this study the data used from "MERRA-2 inst1\_2d\_asm\_Nx: hourly, instantaneous, Single-Level, Assimilations, Single-Level Diagnostics V5.12.4" during the period from 01.01.2015, until 28.02.2018 for each day. We used the northward and eastward wind speed at the heights of 2 m, 10 m

and 50 m above the ground. To cover all Shelek corridor grid points with a latitude between 44.0 E and 47.50 E and a longitude between 73.50 N and 77.80 N are used.

In recent years, more attention has been paid to the Weibull distribution, as suggested by the nearby approximation of the probabilistic laws of a number of natural phenomena and is expected to ensure a good correspondence to the experimental data [7].

Mathematically, i.e. The Weibull distribution function of the two parameter functions is expressed as:

$$f(v) = \frac{k}{c} \left(\frac{v}{c}\right)^{k-1} e^{-\left(\frac{v}{c}\right)^k} \quad (1)$$

The integral distribution function  $F(x)$  is given by:

$$F(v) = 1 - e^{-\left(\frac{v}{c}\right)^k}, \quad (2)$$

where:

$v$  – wind speed, m/s;

$k$  – shape factor ;

$c$  – scale parameter, m/s.

The shape factor  $k$  is the main factor in determining the uniformity of the wind. The uniformity of the wind changes direction with a change to  $i$ . with increasing  $k$ , the uniformity of the wind increases.

It has been established that almost all parameters, such as wind speed, wind speed probability, must be within a certain range, the energy is available in a certain mode, etc., are necessary to fully appreciate the dignity of the wind regime, depend on the rough calculation of these values of  $k$  and  $c$  [8].

$k$  and  $c$  parameters can be found with the several methods such as the power density method; least square method, Modified likelihood method etc. [9]. The methods are briefly discussed below

#### 1) Standard deviation method

The standard deviation method gives the ratio between the mean ( $v_m$ ) and the standard deviation ( $\sigma_v$ ):

$$\left(\frac{\sigma_v}{v_m}\right)^2 = \frac{\Gamma\left(1+\frac{2}{k}\right)}{\Gamma^2\left(1+\frac{1}{k}\right)} - 1 \quad (3)$$

After  $k$  is determined,  $c$  is determined as:

$$c = \frac{v_m}{\Gamma(1+\frac{1}{k})} \tag{4}$$

$$k = 1 + \frac{3.69}{E_{pf}^2} \tag{7}$$

In a simple methodology, an acceptable approximation for  $k$  and  $c$  can be approximated:

$$c = \frac{\bar{v}}{\Gamma(1+\frac{1}{k})} \tag{8}$$

$$k = \left(\frac{\sigma_v}{v_m}\right)^{-1.090} \tag{5}$$

$$c = \frac{2v_m}{\sqrt{\pi}} \tag{6}$$

**2) Empirical method (EM)**

A special case of the method of moments, the empirical method determines  $k$  &  $c$ , as in equations (4), (5):

$$k = \left(\frac{\sigma}{\bar{v}}\right)^{-1.086}$$

$$c = \frac{\bar{v}}{\Gamma\left(1 + \frac{1}{k}\right)}$$

$$\Gamma(x) = \int_0^\infty t^{x-1} e^{-t} dt$$

**3) Power density method (PDM)**

This is the one of the most important methods of determining  $k$  and  $c$ . First of all, energy pattern factor  $E_{pf}$  is calculated by the division of cubic wind speed to cube of mean wind speed [9-10]. After that  $k$  and  $c$  may be found by formulas (7, 8):

**4) Modified likelihood method (MLM)**

That method was proposed by Stevens and Smulders [10] and describes  $k$  and  $c$  by the following formulas:

$$k = \left[ \frac{\sum_{i=1}^n v_i^k \ln(v_i)}{\sum_{i=1}^n v_i^k} - \frac{\sum_{i=1}^n \ln(v_i)}{n} \right]^{-1}$$

$$c = \left( \frac{1}{n} \sum_{i=1}^n v_i^k \right)^{1/k}$$

**Results and Discussion**

In this study the data used from 01.01.2015, until 28.02.2018 for each day. The northward and eastward wind speed at the heights of 2 m, 10 m and 50 m above the ground were horizontally interpolated by the formula [4]:

$$v_m = \sqrt{u_h^2 + v_h^2} \tag{9}$$

Monthly mean values of wind speed are shown in the tables 1-3. The frequency distribution of the data is shown in Table 4.

**Table 1** – Monthly mean velocities at height of 2 m

Month	Mean velocity m/s			
	2015	2016	2017	2018
January	2.7242	3.3995	2.9572	5.9183
February	3.4051	3.6068	2.8878	3.0978
March	2.2784	2.8207	3.4395	-
April	2.0906	2.2409	1.6123	-
May	1.5377	2.8716	2.6959	-
June	2.4187	1.0863	0.8440	-
July	2.4385	1.3534	2.4462	-
August	1.9352	5.6995	4.1758	-
September	2.5953	5.6995	2.6755	-
October	2.0809	2.5965	2.1037	-
November	2.2991	2.3995	2.5797	-
December	2.9105	2.5473	3.1505	-

**Table 2** – Monthly mean velocities at height of 10 m

Month	Mean velocity m/s			
	2015	2016	2017	2018
January	3.3320	3.6725	3.3897	6.4588
February	3.8281	4.0027	3.4253	3.6344
March	2.9956	3.2741	4.0367	-
April	2.3681	2.6763	2.0381	-
May	1.8185	3.0655	2.9150	-
June	2.8588	1.2251	0.9799	-
July	3.0926	1.4276	2.9774	-
August	2.4606	6.4904	4.7401	-
September	3.0329	6.4904	3.3571	-
October	2.4876	3.0643	2.6479	-
November	2.7427	3.0442	2.9889	-
December	3.4514	2.9444	3.7378	-

**Table 3** – Monthly mean velocities at height of 50 m

Month	Mean velocity m/s			
	2015	2016	2017	2018
January	5.4955	5.8329	5.8604	9.8087
February	5.8815	6.2380	5.3924	5.6900
March	4.3439	6.3175	6.0201	-
April	3.7365	4.8102	3.1457	-
May	2.4771	4.1304	4.5861	-
June	4.7340	4.1634	1.7987	-
July	4.9166	1.6786	4.7932	-
August	4.0327	2.2848	7.8409	-
September	4.7945	9.3863	5.1376	-
October	3.8964	9.3863	4.1561	-
November	4.6451	5.0147	4.9872	-
December	5.4955	4.5663	6.0211	-

According to these table the highest speed was detected in January, 2018 and reached almost 6m/s in between 2015 and 2017, and over 9 m/s in 2018. Respectively in the beginning of summer there always was low wind speed. The least meaning of wind speed for summer is 0.9 m/s.

Collected speed data was also divided to the intervals to find more common velocity. It was observed that the most frequent velocity at height 2 m is 2÷3 m/s (0.58). As for 10 m height 3÷4 m/s repeated with almost 40% frequency. The wind

speed of 4-6 m/s at the height of 50 m was repeated at a frequency of 0.6.

As we can see from the table, when the height is increasing the value of velocity is also increases. Thus, wind speed data at these three heights could be vertically extrapolated to the turbine height [11].

From the above formulas and wind data, the results for shape and scale parameters are calculated using various methods described above is indicated in Table 4.

**Table 5** – Wind velocity distribution

Methods	Frequency					
	2 m		10 m		50 m	
	k	c	k	c	k	c
SDM	2.74	3.14	2.93	3.66	3.10	5.74
EM	2.53	3.13	2.70	3.65	2.86	5.72
PDM	2.73	3.12	2.92	3.63	3.09	5.70
MLM	2.62	3.13	2.76	3.63	2.93	5.70

Accuracy of calculations was checked by the following three methods: RMSE,  $R^2$  and *Chi – Square* tests:

$$RSME = \left[ \frac{1}{N} \sum_{i=1}^N (y_i - x_i)^2 \right]^{1/2}$$

$$\chi^2 = \frac{\sum_{i=1}^N (y_i - x_i)^2}{N - n}$$

$$R^2 = \frac{\sum_{i=1}^N (y_i - z_i)^2 - \sum_{i=1}^N (y_i - x_i)^2}{\sum_{i=1}^N (y_i - z_i)^2}$$

Where  $y_i$  is observed frequency and  $x_i$  Weibull’s frequency,  $N$  is a number of observations,  $n$  is a number of used constants. The results are shown in a table below

**Table 6** – Wind velocity distribution

Tests	SDM	EM	PDM	MLM
RSME	0.675	0.0678	0.0692	0.0673
Chi-square	0.063	0.0063	0.0067	0.0061
$R^2$	0.9485	0.9469	0.9472	0.9466

As shown in Figures 1-6, all the methods discussed show more or less similar results, even if the maximal likelihood method and the energy properties are a little more accurate and, therefore, can be considered as the most appropriate.

As we can see from the graph, the most probable wind speed at this height is under 3 m/s. And our calculations have shown the mean value of the velocity is 2.78 m/s.

According to the Fig.4 we can see that the most probable wind speed occurs at speed 5 m/s with a probability of 22.5%. This means that at Shelek corridor the wind speed that often arises at 5 m/s.

Usually, 4-5 m/s is an ideal wind speed for wind turbines. However, the use of wind energy is commercially installed only for high (8-9 m/s) and medium (6-7 m/s) wind conditions. If wind energy

is available in low wind conditions, it is possible to develop turbines specifically for these regions, which will help to reduce dependence on fossil fuels.

To analyze the wind energy potential there is also mean power density based on Weibull distribution must be calculated [13].

$$P_{WD} = \frac{1}{2} \rho c^3 \Gamma\left(1 + \frac{3}{k}\right) \tag{10}$$

Where  $c$  shape factors which were calculated by the four methods described below.  $\rho$  is air density related to the pressure, temperature and humidity. However, air density has not significant effect on wind resource calculations, thus it can be taken as a constant value 1.225 g/cm<sup>3</sup>.

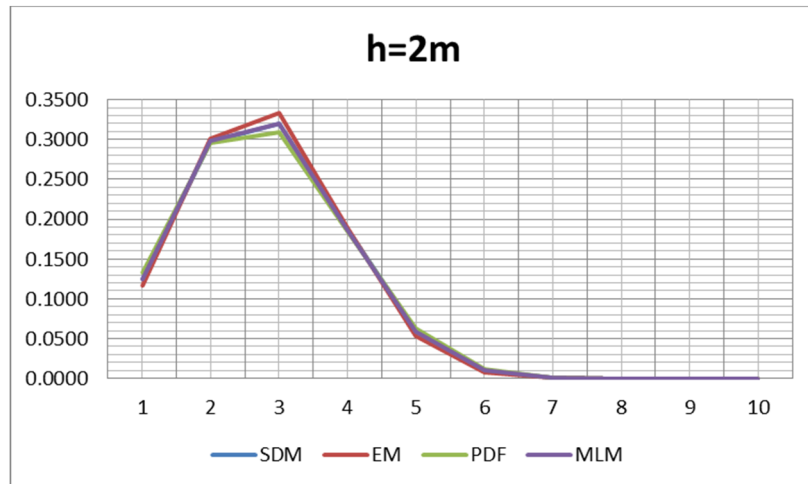


Figure 2 – Weibull distribution at the height of 2 m

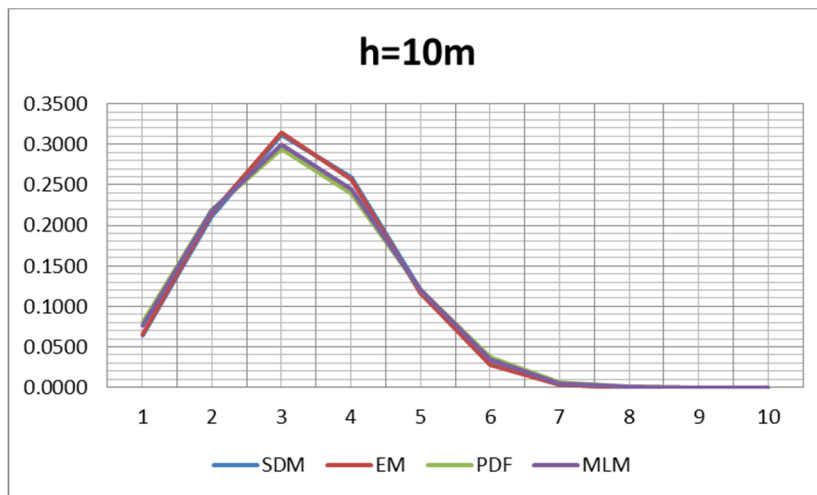


Figure 3 – Weibull distribution at the height of 10 m

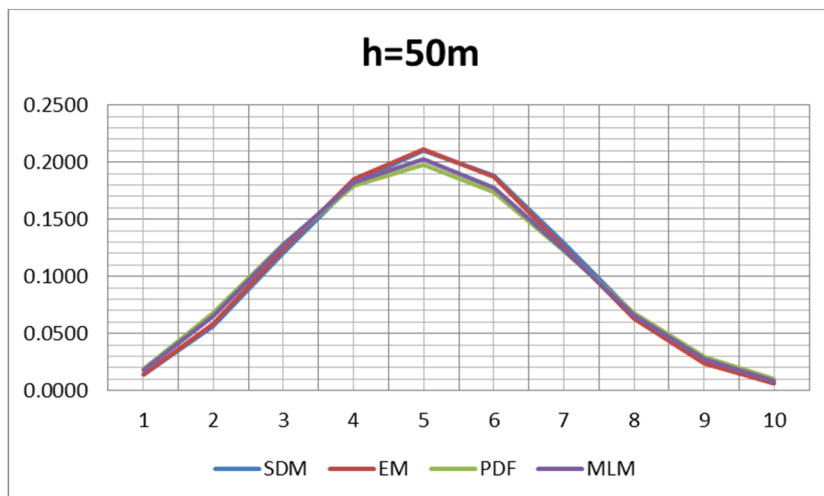


Figure 4 – Weibull distribution at the height of 50 m

On the other hand, mean power density can be calculated by the formula:

$$P_{REF} = \frac{1}{2} \rho \bar{v}^3 \quad (11)$$

## Conclusion

The potential of wind energy in Shelek corridor have been studied in this analysis using widely used Weibull distribution technique. The Weibull parameters such as shape factor and scale factor have been calculated by four different methods such as least squares method, power density method, empirical method and modified likelihood method. Relative percentage of error and chi-square error has been analyzed for each method and also calculated the efficiency of these methods. The wind data was obtained from NASA Modern-Era Retrospective Analysis for Research and Applications “MERRA-2 inst1\_2d\_asm\_Nx: hourly, instantaneous, Single-Level, Assimilations, Single-Level Diagnostics V5.12.4” during the period from 01.01.2015, until 28.02.2018 for each day.

The results found that Shelek complex is prospective site to set up vertical axed wind turbine. The results have been verified by Weibull distribution technique where Weibull shape factor and scale factor were calculated using four different approaches. The statistical analysis also found the modified likelihood method is more efficient method with minimum error in the wind data analysis. The study presented the potential of Shelek corridor to produce pure energy using wind power.

## References

1. Lessons learnt from the UNDP-GEF project “Kazakhstan – Wind Power Market Development Initiative”, Final report, 2011
2. M. Karataev, Michele L. Clarke, Current energy resources in Kazakhstan and the future potential of renewables: A review, European Geosciences Union General Assembly, (2014)
3. M. Shoaib, I. Siddiqui, Y.M. Amir, S.Ur Rehman, Evaluation of wind power potential in Baburband (Pakistan) using Weibull distribution function, Renewable and Sustainable Energy Reviews 70, 1343–1351 (2017)
4. M. Ritter, Z. Shen, B.L. Cabrera, M. Odening, Designing an index for assessing wind energy potential, Renewable Energy, 83, 416-424 (2015)
5. M.M. Rienecker et al, MERRA: NASA’s Modern-Era Retrospective Analysis for Research and Applications, Journal of climate, 24, 3624 (2011)
6. K.J. Thuryan, D. Strickland, D.E. Berg, Power of wind turbines with a vertical axis of rotation, Aerocomic technics, 1988
7. M. Ritter, Z. Shen, B.L. Cabrera, M. Odening, L. Deckert, A new approach to assess wind energy potential, Energy Procedia 75, 671 – 676 ( 2015 )
8. N. Nawri et al., The wind energy potential of Iceland, Renewable energy, 69, 290-299 (2014)
9. A.K. Azad, M.G. Rasull, Rubayat Islam, Imrul R. Shishir, Analysis of wind energy prospect for power generation by three Weibull distribution methods, Energy Procedia 75, 722 – 727 ( 2015 )
10. S.H. Pishgar-Komleh, A. Akram, Evaluation of wind energy potential for different turbine models based on the wind speed data of Zabol region, Iran, Sustainable Energy Technologies and Assessments 22, 34-40 (2017)
11. M. Ritter, L. Deckert, Site assessment, turbine selection, and local feed-in tariffs through the wind energy index, Applied Energy, 185, 1087-1089 (2017)
12. A. Sarkar, G. Gugliani, S. Deep, Weibull model for wind speed data analysis of different locations of India, KSCE Journal of Civil engineering, 21, 2764-2776, 2017
13. P. Wais, A review of Weibull functions in wind sector, Renewable and Sustainable Energy Reviews, 70, 1099-1107, 2017

IRSTI 29.27.47; 29.27.17

<sup>1</sup>K.N. Dzhumagulova, <sup>1</sup>T.S. Ramazanov, <sup>1</sup>R.U. Masheyeva, <sup>2</sup>Z. Donkó<sup>1</sup>Al-Farabi Kazakh National University, Almaty, Kazakhstan<sup>2</sup>Institute for Solid State Physics and Optics, Wigner Research Centre  
of the Hungarian Academy of Sciences, Budapest, Hungary

\*e-mail: masheyeva.ranna@gmail.com

### **Influence of background gas and external magnetic field on the localization of particles in two dimensional yukawa systems**

**Abstract.** We investigate the simultaneous effect of a static homogeneous external magnetic field and a background gas medium on the quasi-localization of the dust particles – characterized quantitatively by cage correlation functions – in strongly coupled two-dimensional Yukawa systems. We apply the Langevin dynamics computer simulation method in which the frictional and Lorentz forces are taken into account. Both the presence of the magnetic field and the friction originating from the background gas, when acting alone, increase the caging time. When present simultaneously, however, we find that their effects combine in a non-trivial manner and act against each other within a window of the parameter values. For a fixed magnetic field, the increasing friction was found to first decrease the caging time and then to increase it beyond a certain value of the friction coefficient that depends on the magnetic field strength. A qualitative explanation was given for these observations based on the analysis of the peculiarities of the trajectories of individual particles.

**Key words:** cage correlation, dusty plasma, Langevin dynamics simulation.

#### **Introduction**

Strongly coupled plasmas are characterized by a pair-interaction potential energy that dominates the average kinetic energy of the particles [1]. Systems with this property can be described by the “one-component plasma” (OCP) model, which considers explicitly only a single type of charged species and assumes an inter-particle potential that accounts for the presence and effects of the other type(s) of species. The polarizable form of the interaction potential is the Yukawa type, while the non-polarizable form is the Coulomb type; the corresponding systems are, respectively, quoted as Coulomb-OCP and Yukawa-OCP (YOCP). This latter type represents an important model system for dusty plasmas, for example, refs. [2–5]. In the simulations of these systems, the background plasma environment is accounted for by the screening of the Coulomb potential. The presence of

the gaseous environment may be taken into account by using the Langevin simulation approach [6–9], where two additional terms are incorporated into the equation of motion. One of the terms represents a friction by a homogeneous background, while the other term adds momentum to the particles in form of random kicks that change the direction of the motion. The action of these two terms can be balanced to reach a desired system temperature.

The possibility of the presence of an external magnetic field has opened a new area of dusty plasma research. Interesting new effects have been observed in the experiments [10–12], which, however, are closely related to the influence of the magnetic field on the discharge plasma that embeds the dust suspension itself. The reason for this is that due to the specific charge-to-mass ratios, the electrons and ions become very strongly magnetized before any effect on the dust particles sets on. Understanding the effects observed experimentally

is difficult because of the very demanding computational needs—simulation of dusty plasma experiments with strong magnetic fields is certainly an emerging area [13]. To overcome the problem of the magnetization of the discharge plasma, another approach, based on the equivalence of the (magnetic) Lorentz force and the Coriolis force experienced in a rotating frame of reference, was advised in Refs. [14, 15]. Implementation of this method and a successful identification of magnetoplasmons in a “quasi-magnetized” rotating dusty plasma were reported by Hartmann et al. [16].

Most of the computational studies have, meanwhile, concentrated on idealized systems, where the dust particles experience the effect of the magnetic field, whereas the surrounding medium is left unperturbed by this field. Many of the properties of such idealized systems have been studied by many-body (typically Molecular Dynamics) simulations. Collective excitations have been explored in Refs. [17, 18]; the effect of the magnetic field on the diffusion was analysed in Refs. [19, 20], while heat transport was addressed by Ott et al. [21].

Many of the properties of the strongly coupled complex plasmas are strongly related to one of its outstanding features, the quasi-localization of the particles in these systems [22]. A mathematical framework based on tracking the surroundings of individual particles has been developed by Rabani et al. [23]. The duration of the localization can be quantified by means of the so-called “cage correlation functions”. The effect of a static uniform external magnetic field on the cage correlation functions in frictionless two-dimensional Yukawa systems has been investigated by Dzhumagulova et al., [24] while the effect of the friction force, induced by the presence of the buffer gas, has been addressed by Dzhumagulova et al. [25] Here, our aim is to study the simultaneous effect of the magnetic field and the friction on the cage correlation functions. The interplay of these two effects is an open question that can only be answered by a systematic parametric study due to the inherent non-linearity of the system under investigation. Our studies are based on Langevin dynamics (LD) simulation into which a proper description of the movement of the particles under the influence of an external magnetic field is incorporated [26–28].

Our numerical integration scheme of the particles’ equations of motion follows the approach of Ref. [29], which takes into account the external magnetic field in the expansion of positions and

velocities in the Taylor series. In Ref. [30], we introduced the friction force into the Velocity Verlet scheme, which is used in the present simulations. The scheme has been verified via comparisons of the cage correlation functions obtained in the limiting cases, when the friction force or the Lorentz force tends to be zero.

The model and the computational methods are described in Section 2, while the results are presented in Section 3. A brief summary is given in Section 4.

## Model and Method

We apply the following form for the interaction potential of the particles, which had a screening property of the surrounding plasma environment:

$$\phi(r) = \frac{Q}{4\pi\epsilon_0} \frac{\exp(-r/\lambda_D)}{r}, \quad (1)$$

where  $Q$  is the charge of the particles and  $\lambda_D$  is the screening (Debye) length.

We study a two-dimensional (2D) system; the particles move in the  $(x, y)$  plane, and the magnetic field is assumed to be homogeneous and directed perpendicularly to the layer of the particles, that is  $\mathbf{B} = (0, 0, \mathbf{B})$ . The equation of motion of the particles (given here for particle  $i$ ) is:

$$m\ddot{\mathbf{x}}_i(t) = \sum_{i \neq j} \mathbf{F}_{ij}(r_{ij}) + Q[\mathbf{v}_i \times \mathbf{B}] - \nu m \mathbf{v}_i(t) + \mathbf{F}_{Br}, \quad (2)$$

where the first term on the right side gives the sum of inter-particle interaction forces (to be computed for  $(i, j)$  particle pairs that are separated by a distance  $r_{ij}$ ), the second is the Lorentz force, and the third term represents the friction force (proportional to the particle velocity,  $\nu$  is the friction coefficient of the dust particles in the background gaseous environment), while the fourth term represents an additional randomly fluctuating “Brownian” force.

The ratio of the inter-particle potential energy to the thermal energy is expressed by the coupling parameter

$$\Gamma = \frac{Q^2}{4\pi\epsilon_0 a k_B T}, \quad (3)$$

where  $T$  is temperature, and  $a = (1/\pi n)^{-1/2}$  is the 2D Wigner–Seitz radius, with  $n$  being the areal number density of the particles. We introduce the screening parameter  $\kappa = a/\lambda_D$ . The strength of the magnetic field is expressed in terms of

$$\beta = \frac{\Omega}{\omega_p}, \quad (4)$$

where  $\omega_p = \sqrt{nQ^2/2\varepsilon_0 m a}$  is the nominal 2D plasma frequency, and  $\Omega = QB/m$  is the cyclotron frequency. The strength of the friction is defined by the dimensionless parameter

$$\theta = \frac{\nu}{\omega_p}. \quad (5)$$

So, the system is fully characterized by four parameters:  $\Gamma, \kappa, \beta$  and  $\theta$ .

We apply Langevin Dynamics (LD) simulation method to describe the motion of the particles governed by the equation of motion (2). To integrate this equation, a new numerical scheme based on the Taylor expansion of the particle acceleration and velocity, followed by the correct choice of all the terms that are not higher than  $O((\Delta t)^2)$  is used. The scheme was obtained by applying the technique developed by Spreiter and Walter, [29] but takes into account the friction force [30].

We use the localization of the particles characterized by the cage correlation function by using the method of Ref. [23], which allows the tracking of the changes in the surroundings of individual particles. We use a generalized neighbor list  $l_i$  for particle  $i$ ,  $l_i = \{f(r_{i,1}), f(r_{i,2}) \dots f(r_{i,N})\}$  ( $f_{i,i}$  is excluded from the neighbour list, i.e. only “real” neighbours are taken into account). Due to the underlying sixfold symmetry of the system, we always search for the six closest neighbours of the particles, and the  $f-s$  corresponding to these particles are set to a value 1, while all other  $f-s$  are set to 0. The similarity between the surroundings of the particles  $t=0$  and  $t>0$  is measured by the list correlation function (defined as the normalized scalar product of the list correlation functions at time stand 0):

$$C_i(t) = \frac{\langle l_i(t)l_i(0) \rangle}{\langle l_i(0)^2 \rangle}, \quad (6)$$

where  $\langle \dots \rangle$  denotes averaging over particles and initial times. Obviously,  $C_i(t=0) = 1$ , and  $C_i(t)$  is a monotonically decaying function.

The number of particles that have left the original cage of particle  $i$  at time  $t$  can be determined as

$$N_i^{out}(t) = |l_i(0)^2| - l_i(0) \cdot l_i(t), \quad (7)$$

here, the first term gives the number of particles around particle  $i$  at  $t=0$ , which equals to six in our case. The second term gives the number of “original” particles that remained in the surrounding after time  $t$ . The cage correlation function  $C_{cage}$  is obtained by averaging the function  $\Theta(c - n_i^{out})$  over particles and initial times, that is,

$$C_{cage}^c(t) = \left\langle \Theta \left[ c - n_i^{out}(0, t) \right] \right\rangle. \quad (8)$$

where  $\Theta$  is the Heaviside function. We compute the cage correlation functions for,  $c=3$  and take the definition of the “caging time” introduced by Donkó et al., [31] according to which  $t_{cage}$  is defined as the time when  $C_{cage}^3(t)$  decays to a value 0.1.

The number of simulated particles is fixed at  $N=1000$  that move within a quadratic simulation box. The positions of the particles are chosen randomly at the initialization of the simulations, and their velocities are sampled from a Maxwell distribution with a temperature that corresponds to the value of specified  $\Gamma$ . During the initial phase of the simulations, the system is thermalized, but thermostation is stopped before the data collection phase starts.

## Results

Below we present the results of our simulations obtained for the cage correlation functions under the conditions of the simultaneous presence of the external magnetic field and the friction. In order to use the same numerical scheme throughout our

work, we had to use finite values of the magnetic field and the friction coefficient. The field-free and/or frictionless cases are approximated by using very small values of these coefficients ( $10^{-6} - 10^{-5}$ ) in the simulations. The results obtained this way approximate the “true”  $\beta = 0$  and/or  $\theta = 0$  results well within the statistical noise of the results. Nonetheless, at the presentation of the results, we give the precise (low) values of these coefficients used in the respective simulations.

Figure 1a shows the  $C_{cage}^3(t)$  functions obtained at fixed system parameters  $k = 2$  and  $\Gamma = 20$  at a magnetic field  $\beta = 0.5$ , with the friction coefficient  $\theta$  scanned over the domain between  $10^{-5}$  (representing a case with vanishing friction) and  $0.5$  (representing a case with high friction). In panel (b) of the same figure, another set of data is presented for a stronger magnetic field of  $\beta = 1.0$ . One plasma oscillation period, disregarding the effect of the magnetic field, corresponds to  $\omega_E T \sim 2\pi$ , where  $\omega_E$  is the Einstein frequency [32] that reflects the slowing down of the dynamics due to the effect of the screening. At the given value of the screening parameter  $k = 2$  we find

$\omega_E / \omega_p \cong 0.49$  [32], resulting in  $\omega_p T \approx 4\pi \approx 12.6$ . As a general observation, we can note that the cage correlation functions decay to the 0.1 value – specified to correspond to the caging time – on the time scale of 2 – 5 plasma oscillations for the conditions of Figure 1. Such a long decay is characteristic for strong-coupled plasmas where the time scale for the diffusion of the particles is slower compared to the plasma oscillations, i.e. the particles are “quasi-localized” on the potential surface [22].

We can also observe, by comparing panels (a) and (b) of Figure 1, that the increasing friction has a more significant effect on the correlation function in the lower  $\beta$  case. At  $\beta = 0.5$ , the correlation function increases monotonically with increasing  $\theta$ , however, for  $\beta = 1.0$  a closer observation of the behavior (see the inset in Figure 1 b)) reveals a non-monotonic behavior. The increasing  $\theta$  shifts the crossing of the correlation functions with the  $C_{cage} = 0.1$  line towards lower times first, and beyond  $\theta \approx 0.1$  this trend reverses and remains the same for higher friction values.

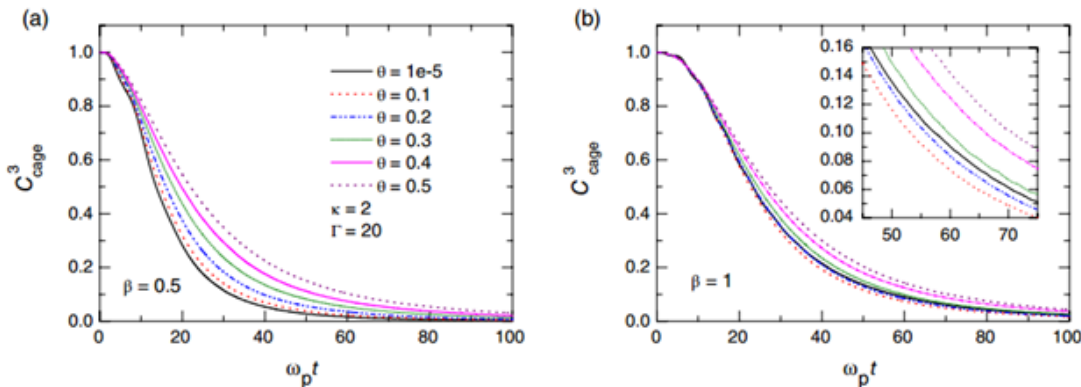


**Figure 1** – Cage correlation functions for  $\Gamma = 20$  and  $k = 2$  for (a)  $\beta = 0,5$  and (b)  $\beta = 1,0$  for a wide range of the friction coefficient  $\theta$ . The legend shown in (a) also holds for panel (b). The inset in (b) zooms at the region when the correlation functions cross the  $C_{cage} = 0.1$  line (at times that correspond to the caging time)

The effect of a changing strength of magnetic field on the cage correlation functions is presented in Figure 2 for  $\Gamma = 20$  and  $\kappa = 2$ , for the  $\theta = 0.1$  (panel (a)) and  $\theta = 0.5$  values of the friction coefficient. The correlation functions increase monotonically with increasing  $\beta$  in both cases, a stronger influence is found at the lower value of friction (panel (a)).

The non-monotonic dependence of the caging time on the friction coefficient is further analysed in Figure 3. At small values of the magnetic field, the caging time increases monotonically with increasing friction. At  $\beta > 0,5$ , however, as already indicated in Figure 1b, this dependence is non-monotonic. The effect – that the caging time first decreases as a function of  $\theta$  – becomes more pronounced at higher

magnetic fields. The value of  $\theta$  where the minimum of  $T_{cage}$  occurs ( $\theta_{min}$ ), as well as the  $\theta$  value ( $\theta_{cross}$ ) where the effect of magnetic field and friction

“compensate each other”, that is, when  $T_{cage}$  becomes the same again as at  $\beta = 0$ , both increase with increasing magnetic field.

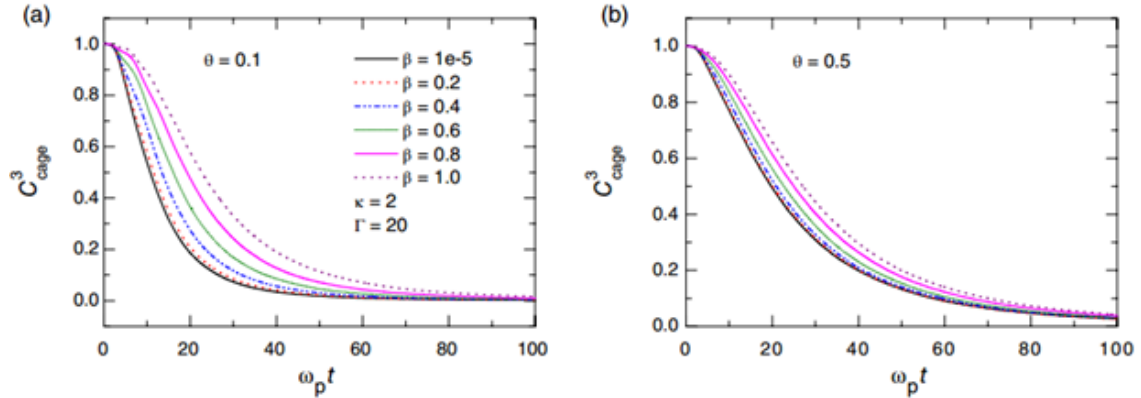


Figure 2 – Cage correlation functions for  $\Gamma = 20$  and  $k = 2$  for (a)  $\theta = 0.5$  and (b)  $\theta = 1.0$  for a wide range of the reduced magnetic field  $\beta$

The interplay of the magnetic field and the friction is non-trivial. Both mechanisms, when acting alone, are known to increase the caging time. The magnetic field results in this by forcing the particles to move on circular trajectories. When the Larmor radius is smaller than the interparticle separation, diffusive motion across the field lines is significantly hindered, and the caging time is enlarged [24]. The effect of friction on the caging time is similar [25] but results from a different physical mechanism. As explained

earlier, the presence of the gaseous environment is modelled via a damping mechanism by the background (as a continuum) and by a random (“Brownian”) force that emulates random kicks by gas particles. The first of these slows down the particle motion, while the second increases the energy of the particle but randomizes its direction of velocity. The inverse of the frequency (related to the friction coefficient as  $\theta = \nu / \omega_p$ ) can be viewed as the timescale for the change of the direction of velocity.

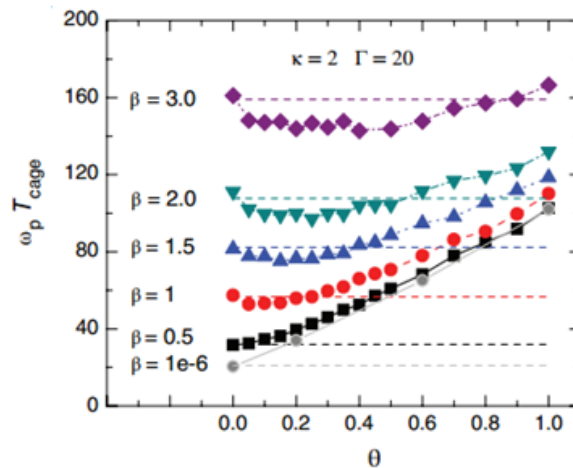


Figure 3 – Dependence of the caging time on the friction parameter  $\theta$  at given values of  $\beta$  in the highly magnetized domain. Note the non-monotonic dependence of  $T_{cage}$  on  $\theta$  for the  $\beta > 0$  cases. The dashed horizontal lines correspond to  $T_{cage}$  at  $\theta = 0$

## Conclusion

In this paper, we have investigated the simultaneous effect of friction induced by the gas environment, as well as a homogeneous external magnetic field, on the quasi-localization of dust particles in a 2D layer. The system has been described by LD simulation. We have found that, when acting alone, both an increasing friction coefficient and an increasing strength of the magnetic field enhance the caging of the particles, as quantified by the cage correlation functions. When present simultaneously, however, a non-trivial interplay of the two effects was observed. For a fixed magnetic field ( $\beta > 0$ ), the increasing friction was found to first decrease the caging time and then to increase it beyond a certain value of the friction coefficient that depends on the magnetic field strength. A qualitative explanation was given for these observations based on the analysis of the peculiarities of the trajectories of individual particles; however, a more detailed, quantitative understanding of the effect calls for further studies that include the analysis of the velocity autocorrelation function of the particles.

## Acknowledgment

The authors acknowledge support within the Grant **AP05132665** of the Ministry of Education and Science of the Republic of Kazakhstan.

1. Books (Edited Volume or Chapter Within an Edited Volume): Editor's Last name, First name, ed. *Title*. City: Publisher, Year.

## References

1. Kalman G. J., Blagoev K., Rommel M. E., ed. *Strongly Coupled Coulomb Systems*. City: New York, Plenum Press, 1998.
2. Mendis D. A., Rosenberg M. "Cosmic Dusty Plasma." *Annu. Rev. Astron. Astrophys.* 32. (1994): 419-463.
3. Bonitz M., Henning C., Block D. "Complex plasmas: a laboratory for strong correlations." *Rep. Prog. Phys.* 73. (2010): 066501.
4. Thomas H., Morfill G. E., Demmel V., Goree J., Feuerbacher B., Möhlmann D. "Plasma Crystal: Coulomb Crystallization in a Dusty Plasma." *Phys. Rev. Lett.* 73. (1994): 652.
5. Chu J. H., I. Lin. "Direct observation of Coulomb crystals and liquids in strongly coupled rf dusty plasmas." *Phys. Rev. Lett.* 72. (1994): 724009.
6. Ramazanov T. S., Dzhumagulova K. N. "Shear viscosity of dusty plasma obtained on the basis of the Langevin dynamics." *Contrib. Plasma Phys.* 48. (2008): 357.
7. Vaulina O. S., Adamovich X. G., Petrov O. F., Fortov V. E. "Evolution of the mass-transfer processes in nonideal dissipative systems. I. Numerical simulation." *Phys. Rev. E.* 77. (2008): 066403.
8. Liu B., Goree J. "Simulation of Three-Dimensional Dusty Plasmas." *IEEE Trans. Plasma Sci.* 42. (2014): 2686.
9. Arp O., Caliebe D., Piel A. "Cavity dynamics and particle alignment in the wake of a supersonic projectile penetrating a dusty plasma." *Phys. Rev. E.* 83. (2011): 066404.
10. Samsonov D., Zhdanov S., Morfill G., Steinberg V. "Levitation and agglomeration of magnetic grains in a complex (dusty) plasma with magnetic field." *New J. Phys.* 5. (2003): 24.
11. Reichstein T., Wilms J., Greiner F., Piel A., Melzer A. "Experiments and Simulations of Particle Flows in a Magnetized Dust Torus." *Contrib. Plasma Phys.* 52. (2012): 813.
12. Thomas Jr. E., Lynch B., Konopka U., Merlino R. L., Rosenberg M. "Quasi-discrete particle motion in an externally imposed, ordered structure in a dusty plasma at high magnetic field." *Phys. Plasmas.* 22. (2015): 030701.
13. Hartmann P. "Imposed ordered structure in magnetized discharge." 70 th Annual Gaseous Electronics Conf., Pittsburgh, PA, 2017.
14. Kählert H., Carstensen J., Bonitz M., Löwen H., Greiner F., Piel A. "Magnetizing a Complex Plasma without a Magnetic Field." *Phys. Rev. Lett.* 109. (2012): 155003.
15. Bonitz M., Kählert H., Ott T., Löwen H. "Magnetized strongly coupled plasmas and how to realize them in a dusty plasma setup." *Plasma Sources Sci. Technol.* 22. (2013): 015007.
16. Hartmann P., Donkó Z., Ott T., Kählert H., Bonitz M. "Magnetoplasmons in Rotating Dusty Plasmas." *Phys. Rev. Lett.* 111. (2013): 155002.
17. Bonitz M., Donkó Z., Ott T., Kählert H., Hartmann P. "Nonlinear magnetoplasmons in strongly coupled Yukawa plasmas." *Phys. Rev. Lett.* 105. (2010): 55002.

18. Hou L.J., Shukla P. K., Piel A., Mišković Z. L. "Wave spectra of two-dimensional Yukawa solids and liquids in the presence of a magnetic field." *Phys. Plasmas*. 16. (2009): 073704.
19. Feng Y., Goree J., Liu B., Intrator T. P., Murillo M. S. "Superdiffusion of two-dimensional Yukawa liquids due to a perpendicular magnetic field." *Phys. Rev. E*. 90. (2014): 013105.
20. Ott T., Bonitz M. "Diffusion in a Strongly Coupled Magnetized Plasma." *Phys. Rev. Lett.* 107. (2011): 135003.
21. Ott T., Bonitz M., Donkó Z. "Effect of correlations on heat transport in a magnetized strongly coupled plasma." *Phys. Rev. E*. 92. (2015): 063105.
22. Golden K. I., Kalman G. J. "Quasilocalized charge approximation in strongly coupled plasma physics." *Phys. Plasmas*. 7. (2000): 14-32.
23. Rabani E., Gezelter J. D., Berne B. J. "Calculating the hopping rate for self-diffusion on rough potential energy surfaces: Cage correlations." *J. Chem. Phys.* 107. (1997): 6867-6876.
24. Dzhumagulova K. N., Masheeva R. U., Ramazanov T. S., Donkó Z., Dzhumagulova K. N., Masheeva R. U., Ramazanov T. S., Donkó Z. "Simultaneous effect of an external magnetic field and gas-induced friction on the caging of particles in two-dimensional Yukawa systems." *Phys. Rev. E*. 89. (2014): 033104.
25. Dzhumagulova K. N., Masheyeva R. U., Ramazanov T. S., Donkó Z. "Effect of Buffer Gas Induced Friction on the Caging of Particles in a Dusty Plasma." *Contrib. Plasma Phys.* 562. (2016): 215-220.

IRSTI 29.19.21

<sup>1</sup>P. Safarik, <sup>2,\*</sup>A.O. Nugymanova

<sup>1</sup>Department of Fluid Dynamics and Thermodynamics,  
Czech Technical University in Prague, Prague, Czech Republic

<sup>2</sup>Department of Thermal Physics and Technical Physics,  
Al-Farabi Kazakh National University, Almaty, Kazakhstan

\*e-mail: aijoka01@gmail.com

### **Application of electron-beam technology to reduce anthropogenic load of thermal power plants**

**Abstract.** This article evaluated the level of air pollution during the combustion of Karaganda coal in thermal power plants. The technical analysis of coal is lead and parameters of quality of coal are defined. With the use of the “Era-Air” software complex designed for solving a wide range of tasks in the area of atmospheric air protection, the complex indicators of average annual pollution in the atmosphere of the city Shakhtinsk were calculated, maximally different emissions of ash, sulfur oxides, carbon, nitrogen, resulting from the burning of Karaganda coal at thermal power plants. It is established that a complex index of pollution of atmospheric air of the city Shahtinsk more than two times higher than index of pollution, calculated for five types of pollutants. Currently available methods of reducing greenhouse gases into the atmosphere from coal combustion based on electron beam technology. Electron-beam technologies are aimed at changing the physicochemical properties of the combusted fuel with objective of increase of efficiency and completeness of coal combustion. Preliminary electron beam processing of coal leads to decrease in emissions into the atmosphere, reduces the amount of ash and slag, and reduces the maximum single-time emissions.

**Key words:** thermal power plants, high ash coal, maximum one-time emissions, surface concentrations, electron-beam processing.

#### **Introduction**

Air pollution – a serious environmental problem of Kazakhstan, especially in the industrial areas become by the centers of accommodation of the industrial enterprises and located in industrial areas. The basic volume of emissions of a dust, sulfur dioxide and nitrous oxide are accounted for by three main sectors of Kazakhstan: electric power industry with use of the mineral fuel, processing and mining branches and transport [1].

The greatest emissions of dust, sulphur dioxide and nitrogen oxide generates electric power industry, as well as heating plants, i.e. combustion sources natural fuel [2]. They make the most significant contribution to total emissions of

pollutants into the atmosphere – 40% of total emissions, including 50% of particulate emissions, 47% of sulfur dioxide emissions and 60% of nitrogen oxide emissions [3]. A significant part of emissions is due to the use of poor quality coal and absence of the effective equipment for the control of pollution in power plants and district heating plants.

In recent years, Kazakhstan has seen a significant increase in air pollution. The substances polluting air increase the frequency of diseases and thereof lead to drawing of direct and indirect damage to national economy in the form of expenses for services of healthcare and decline of productivity of work. The republic's emission standards are much higher than European [4]. Therefore, to improve air quality in Kazakhstan

should consider establishing more stringent standards on emissions of dust, sulphur dioxide and nitrogen oxide.

Currently, various methods of utilization of greenhouse gases contained in the emissions of enterprises are widely applied. However, it may be appropriate decrease in emissions due to improvement of quality of combusted fuel, increasing the efficiency of its combustion process.

Thus, the purpose of this article is to quantify maximum one-time emissions and surface concentrations of pollutants from a thermal power plant when burning irradiated and non-irradiated Karaganda coal.

### Materials and Methods

As object of research was selected Karaganda coal, burned in the combustion chamber of the boiler BKZ-75, established at Shakhtinskaya CHP (Kazakhstan) [5].

To modify the quality of the Karaganda coal, experiments on the radiation treatment of coal were carried out, carried out on the electronic accelerator ILU-6. The accelerator generated electrons with energy of 1.3 MeV, the dose rate varied from 0.19 to 0.33 Mrad / s, the total absorbed dose varied from 10 to 200 Mrad. The temperature of the coal layer thickness 7 mm was controlled using thermocouples and supported between 60-70 and 250-260°C. Gaseous products released during radiolysis were collected in a gasometer and analyzed on a chromatograph. The composition of coal after

radiation exposure was studied by chemical elemental analysis and OS spectroscopy [6]. The general view of accelerator ILU-6 is shown in the Figure 1. The main characteristics of the burned Karaganda coal and coal that has passed the electron-beam processing are shown in Table 1.

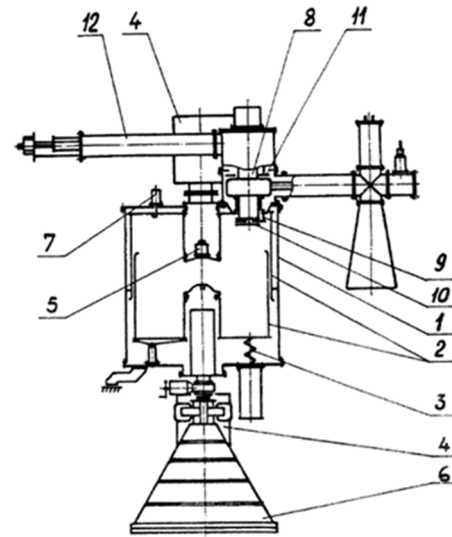


**Figure 1** – The general view of the ILU-6 accelerator.

- 1 – vacuum volume, 2 – the resonator, 3 – choke of the lower half of the resonator, 4 – magnetic discharge pumps, 5 – electron injector, 6 – the venting device, 7 – measuring loop, 8 – lamp of the generator, 9 – pillar of a loop of communication, 10 – vacuum loop coupling capacitor, 11 – moving plate of feedback capacitor, 12 – cathode loop

**Table 1** – The main characteristics of the burned Karaganda coal and coal that has passed the electron-beam processing

Fuel	W %	V <sub>daf</sub> %	S <sub>d</sub> %	A <sub>d</sub> %	C <sub>daf</sub> %	H <sub>daf</sub> %	N <sub>daf</sub> %	O <sub>dafd</sub> %	Q MJ/kg
non-irradiated	10.6	22	1.04	35.1	43.21	3.6	1.21	5.24	18.56
radiated	8.4	16	1.02	31	45	4.06	1.20	6.37	18.2

In this paper are carried out researches on influence of electron beam processing of coal on increasing the efficiency of its combustion and reducing emissions of harmful substances into the atmosphere. The calculation of the maximum values of surface concentrations of harmful substances in the atmospheric air was performed in the “Era-Air” software package [7]. The “Era-Air” software package is intended for the decision of a wide class of problems in the field of air protection connected with calculations of atmospheric contamination.

For the calculation the analytical method was used using the accepted data analysis technique [8]. For calculation of total emissions of solid particles, the values of the required values for each fuel are selected in accordance with international standards and reference data of the standard method for calculating boilers in accordance with the calorific value, capacity of boilers:

$$M_S = B \frac{A^r}{100 - G_{entr}} \alpha_{entr} (1 - \eta_3), (g/s) \quad (1)$$

here  $B$  is the consumption of natural fuel, t/year (g/s);

$A^r$  – ash content of fuel on the working mass, %;

$\alpha_{entr}$  – the proportion of ash carried away by gases from the boiler;

$\eta_3$  – fraction of solid particles trapped in ash collectors;

$G_{entr}$  – the content of combustible in the entrainment, %.

Calculation of emissions of nitrogen oxides: when burning solid fuel combustion [9]:

$$M_{NO_x} = B_p Q_i^r K_{NO_x}^G \beta_r k_p, \text{ (g/s) } , \quad (2)$$

where  $B_p$  – estimated fuel consumption, t/year;

$Q_i^r$  – lower heat of combustion of fuel, MJ/kg;

$K_{NO_x}^G$  – specific emission of oxides depending on the type of fuel burned;

$\beta_k$  – dimensionless coefficient, taking into account the principal design of the burners;

$\beta_t$  – dimensionless coefficient, taking into account the temperature of the air supplied for combustion;

$\beta_k$  – dimensionless coefficient that takes into account the effect of excess air on the formation of oxide substances;

$\beta_r$  – is a dimensionless coefficient that takes into account the stepwise introduction of air into the combustion chamber;

$k_p$  – conversion factor (when determining emissions in grams per second is 1, in determining emissions in tons per year is  $10^{-3}$ ).

Calculation of sulfur oxide emissions [10]:

$$M_{SO_2} = 0.02BS^r(1 - \eta'_{SO_2})(1 - \eta''_{SO_2}), \text{ (g/s) } (3)$$

where  $B$  is the natural fuel consumption, t/year (g/s);

$S^r$  – sulfur content in fuel for the working mass, %;

$\eta'_{SO_2}$  – the proportion of sulfur oxides bound by fly ash in the boiler;

$\eta''_{SO_2}$  – the proportion of sulfur oxides trapped in a wet ash trap along with the trapping of solid particles.

Calculation of carbon monoxide emissions [11]:

$$M_{CO} = 10^{-3}BC_{CO} \left(1 - \frac{q_4}{100}\right), \text{ (g/s) } \quad (4)$$

where  $C_{CO}$  is the yield of carbon monoxide during fuel combustion, g/kg;

$q_4$  – heat loss due to mechanical incompleteness of fuel combustion, %.

Specific emissions of pollutants are calculated on the basis of the known amount of emissions per unit time and the corresponding fuel consumption spikes [12-13]. The specific release of the  $i$  – th substance can be determined by the unit of heat introduced into the furnace (g/MJ) or expressed as the concentration of this substance in  $1 \text{ m}^3$  of flue gases, taken under normal conditions, and the excess air factor  $\alpha = 1.4$ .

## Results and Discussion

In the given work total emissions of harmful substances according to characteristics of a boiler have been calculated. Steam boiler factory brand BKZ-75 – performance 75 t/h (51.45 Gcal/h), the temperature of superheated steam 440 C and the pressure of superheated steam 39 kgf/cm.

The results of the calculation of gross emissions (t/year) and specific emission (g/s) of pollutants are given in the Table 2. When burning fossil fuels in an atmosphere are thrown out carbon oxides, nitrogen and sulfur dioxide. According to the hygienic requirements set maximum-permissible concentration (maximum concentration limit,  $\text{mg}/\text{m}^3$ ) of harmful substances polluting the atmospheric air are established. Maximum permissible concentration are accepted according to [14] and resulted in Table 3.

It has been established that when burning Karaganda coal, a large amount of pollutants are emitted into the atmosphere, the concentration of which exceeds the maximum one-time and daily average concentrations of impurities.

Our calculations show that average daily concentrations of pollutants exceed maximum permissible concentrations (concentration not having adverse effects on human health). From this we can conclude that will worsen human health (environmental condition). Therefore, it is necessary to reduce the anthropogenic load on the ecosystem.

**Table 2** – Calculation of gross emissions (tons/year), specific emissions (g/s) of pollutants and average daily surface concentrations (mg/m<sup>3</sup>)

Fuel	Harmful substances		
	<i>CO</i>	<i>NO<sub>2</sub></i>	<i>SO<sub>2</sub></i>
	Gross emissions, t/year		
Karaganda coal (non-irradiated)	120.3	7.4	12.72
Karaganda coal (irradiated)	100.4	7.6	10.56
	Specific emissions, g/s		
Karaganda coal (non-irradiated)	3.8	0.23	0.40
Karaganda coal (irradiated)	3.18	0.24	0.33
	Average daily surface concentrations, mg/m <sup>3</sup>		
Karaganda coal (non-irradiated)	9.1	0.1	0.24
Karaganda coal (irradiated)	8.3	0.7	0.20

**Table 3** – Maximum permissible concentration (maximum concentration limit) of polluting substances in atmospheric air of localities

№ code	The name of substance	The formula	The value of maximum concentration limit (mg/m <sup>3</sup> )		Hazard class
			maximum one-time	average daily	
1	Carbon oxide	<i>CO</i>	0.05	0.15	4
2	Nitrogen (II) oxide	<i>NO<sub>2</sub></i>	0.04	0.85	2
3	Sulfur (II) oxide	<i>SO<sub>2</sub></i>	0.03	0.005	3

## Conclusion

The following conclusions can be made from the research:

– Preliminary electron beam processing of coal leads to decrease in emissions in an atmosphere, decrease in emissions in an atmosphere, and reduces maximum-one-time emissions (see Tables 1, 2) at least from 0.6% up to 9% for different greenhouse gases.

– Electron beam processing is an environmentally friendly non-reagent way to control the quality of the burned fuel. To obtain a significant technological effect, treatment with doses up to 50 Mrad is necessary. The given doses can be recruited for 4-5 seconds. The environmental purity of electron-beam processing is due to the fact that the irradiated coal does not have induced radioactivity, because the energy of accelerated electrons are ten times less energy electrons provoking the occurrence of nuclear chemical transformation in the irradiated material. When exposed to electrons of this energy, there are

processes associated with the excitation of valence electrons, and unusual valence states can occur, chemically active particles, ions, and other.

– Thus, the electron beam method allows you to change the processes of burning coal that have undergone preliminary electron beam processing. Given the high performance of modern electron accelerators, preliminary calculations show the economic integrity of using electron-beam processing of coal in practice.

## Acknowledgments

This work was supported by Ministry of Education and Science of the Republic of Kazakhstan (grant No. AP05133590 “Creation of new computer technologies for 3D modeling of heat and mass transfer processes in high-temperature physic chemically reactive media”, 2018-2020).

The last author, P. Safarik, expresses acknowledgements for support by the Project No. CZ.216/3.1.00/21569 Centre 3D Volumetric Anemometry.

## References

1. Serikov E.A. *Heat energy systems and energy use in industrial heat technology production*. Tutorial. Almaty: AIES, 2006.
2. Askarova A.S., Mazhrenova N.R. *Environmental problems of the fuel and energy industry of Kazakhstan and non-traditional solutions to them*. Almaty: Kazakh University, 1997.
3. BP Statistical Review of World Energy 2016. 46 p. <http://bp.com/statisticalreview>.
4. World Bank Group. *Kazakhstan Partnership Programme Snapshot* (<http://www.worldbank.org/content/dam/Worldbank/document/Kazakhstan-Snapshot.pdf>); 2014
5. Askarova, A.S., Bolegenova, S.A., Maksimov, V.Yu., et.al.: Numerical research of aerodynamic characteristics of combustion chamber BKZ-75 mining thermal power station. Proceeding of the 20th International Congress of Chemical and Process Engineering, CHISA. Volume 42, 2012:1250-1259.
6. Mazhrenova H.P., Rudenko H.B., Medeuov Ch.K., Kozhakhmetov S.M. *Basics of complex processing of mineral raw materials using radiation processes*. Almaty: KazSU, 1995
7. <https://www.era-environmental.com> / solutions / environmental-management-system
8. Collection of methods for calculating emissions of harmful substances into the atmosphere by various industries. Almaty, 1996.
9. Li S., Xu T., Sun P., Zhou Q., Tan H., Hui, S. "NO<sub>x</sub> and SO<sub>x</sub> emissions of a high sulfur self-retention coal during air-staged combustion". *Journal Fuel*. Volume 87, 2017:723-731.
10. Su F.Q., Itakura K.I., Deguchi G., Ohga K. "Monitoring of coal fracturing in underground coal gasification by acoustic emission techniques". *Journal Applied Energy*. Volume 189, 2017:142-156.
11. Aijun L., Zhang A., Zhou Y., Yao X. "Decomposition analysis of factors affecting carbon dioxide emissions across provinces in China". *Journal Cleaner Production*. Volume 141, 2017:1428-1444
12. Staron A., Banach M., Kowalski Z., Staron P. "Impact of waste soot on properties of coal-water suspensions". *Journal Cleaner Production*. Volume 135, 2016:457-467
13. Dmitrienko M.A., Nyashina G.S., Strizhak P.A. "Environmental indicators of the combustion of prospective coal waterslurry containing petrochemicals". *Journal Hazard Materials*. Volume 338, 2017:148-159.
14. Hygienic standard. *Maximum allowable concentrations (MACs) of pollutants in the airresidential areas*. Almaty, 1999

IRSTI 29.19.24

A.K. Shokanov, M.K. Kulbek, Sh.I. Hamraev, \*Y.A. Smikhan

Abai Kazakh National Pedagogical University, Almaty, Kazakhstan

\*e-mail: erkebulan1@mail.ru

### Mössbauer research in zoloceramic materials

**Abstract.** The work is devoted to Mössbauer studies of new building materials derived from wastes from coal-fired power plants. Measurements of Mössbauer spectrometers were carried out on the MC1104EM unit in the regime of constant acceleration with a source of  $^{57}\text{Co}$  (Cr). The elemental composition of each sample was determined by means of X-ray fluorescence analysis (XRF) on the RLP-21 installation. According to the results of studies of volume-surface concentric-zonal color effects in zoloceramic materials, the phase composition of iron compounds and their ratios is established by the Mössbauer method, and their elemental composition with 32 components is determined with high accuracy by means of XRF. The technology of obtaining gold-ceramic materials with volumetric-surface color effects is described.

**Key words:** MOSSBAUER spectroscopy, X-ray fluorescence analysis, NGR spectrum, aluminasilicate compositions.

The paper describes the results of a study of volume-surface concentric zonal color effects in gyro ceramic materials. The dependence of zonal flowers on the phase composition is established by the Mossbauer effects method.

In the production of the ceramic materials, used both in construction and in everyday life, one of the fundamental factors that predetermine the aesthetic-consumer properties is their whiteness and color, which makes it possible to create a wide variety of color compositions [1-3].

Intensive staining of ceramics in the presence of non-silicate iron in clays is due to condensed iron-containing phases, such as hematite  $\alpha\text{-Fe}_2\text{O}_3$  (reddish-pink, red-brown and brown), magnetite  $\text{Fe}_3\text{O}_4$  (brown to black) and various ferrites [4-7].

The objects of the research were new gyro ceramic examples – tiles based on ash TPP and monothermical clay.

To obtain a raw mixture of polycrystalline ashceramic tiles, consisting of 70% (mass) of ash from TESs with a residual fuel content of 8-9% and 30% of moderate plastic thin ground monothermical clay as a dry powder, mixed carefully in a mixer. The beam was formed on a strip press in such form of a cylinder with size  $d = 50$  mm,  $h = 250 \div 350$  mm,

after which the samples were dried at 100-110 °C, and then fired in an oxidizing medium by forced high-speed conditions: rising of temperature 950 °C with a speed of 20 °C / min; hold at this maximum temperature for 60 min. The total duration of the firing cycle was 107 minutes.

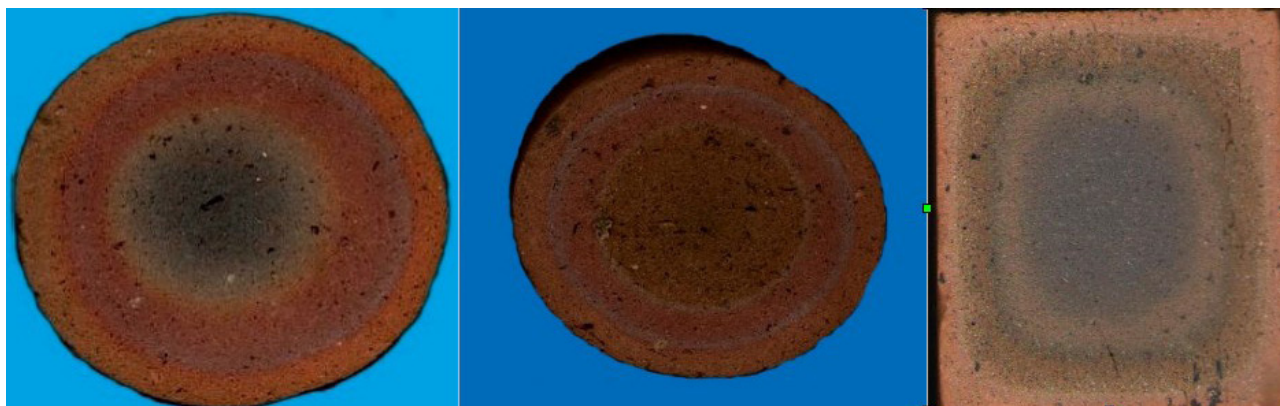
The baked beam was cut by abrasive circles across, accordingly the required thickness of the tiles (10-15 mm). The chemical composition of the using ash is shown in Table 1.

The surface of the obtained tiles along the entire depth of the volume has a polycrystalline zonal color, which is formed in association with the creation at roasting on the proposed mode in the different layers of the beam – sample of the necessary temperature and gas modes, providing different degrees of combustion of residual carbon of ash and oxidation of iron.

The colored concentric zones on the surface of the tiles in cross section are situated as follows: in the middle part a gray circle with a diameter of 33 mm, which is surrounded by a thin strip yellow color (2.5 mm), around it is a strip (3 mm) of violet-red color, outside of the surface of the tile is painted in a light brown (cream) color, the width of which is 3 mm (Fig. 1).

**Table 1**

Ashes (coal)	SiO <sub>2</sub>	Al <sub>2</sub> O <sub>3</sub>	Fe <sub>2</sub> O <sub>3</sub>	FeO	TiO <sub>2</sub>	CaO	MgO	SO <sub>3</sub>	K <sub>2</sub> O	Na <sub>2</sub> O
Ash of Almaty TPP (Coal of Karaganda pool)	56,52	25,58	2,39	2,39	0,93	2,17	0,45	0,48	0,20	-

**Figure 1** – Painting of colored concentric zones on the surface of tiles in a cross-section

From the corresponding zones of different colors samples were cut, the samples were exposed to nuclear gamma resonance spectroscopy (NGRS) and atomic force microscopy.

As is known, iron in the samples can contain both Fe<sup>3+</sup> and Fe<sup>2+</sup> [9]. In the spectra of samples of compounds iron can appear as the magnetite (Fe<sub>3</sub>O<sub>4</sub>), mullite (3Al<sub>2</sub>O<sub>3</sub> • 2SiO<sub>2</sub>), ε-wollastonite (β-Ca<sub>3</sub>Si<sub>3</sub>O<sub>9</sub>), anorthite (CaO • Al<sub>2</sub>O<sub>3</sub> • 2SiO<sub>2</sub>), fayalite (Fe<sub>2</sub>SiO<sub>4</sub>), hematite (Fe<sub>2</sub>O<sub>3</sub>), solid aqueous of a different phase, also as the ferrites [6-9].

The Mossbauer's investigations were carried out on device MC1104EM in mode with a constant acceleration for absorption. The source was <sup>57</sup>Co in the matrix of chromium. The spectra were taken at room temperature. The isomeric shifts of the Mossbauer spectra were determined with relation to α-iron.

Mossbauer research of samples on the nucleus of <sup>57</sup>Fe have shown that the spectra have a complex form. They consist of a superposition of several doublets and sextets having different parameters. We have used special computer programs for their decoding. In addition, these spectra were compared for identification with the control spectra of the known components.

The spectrum of Mossbauer of the central part of the sample has a broadened asymmetric quadrupole

doublet. Computer processing made it possible to determine that it decomposes into four quadrupole doublets (Fig. 2).

Table 2 shows the hyperfine structure of the Mossbauer spectrum.

It can be seen from Table 2 that the Mössbauer spectrum of the sample does not have a magnetic structure. It consists of four diamagnetic components having different phase states. Each of them is characterized by a separate hyperfine structure (Table 2). These components, possibly, characterize oxides (SiO<sub>2</sub>, Al<sub>2</sub>O<sub>3</sub>, CaO and SO<sub>3</sub>) containing in the composition of ferric and ferrous iron in different concentrations [9]. The superposition of these components probably colored of the central part of the circular sample to a yellowish-brown (gray) color.

The second layer of the sample has a complex hyperfine structure. The parameters of the Mossbauer spectra of the sample have substantially changed. The spectrum of this layer differs greatly from the spectrum of the central layer, computer processing has shown that it consists of three quadrupole doublets and two sextets (Fig. 3). Quadrupole doublets have a different parameters.

The Mossbauer parameters of the hyperfine structure are shown in Table 3.

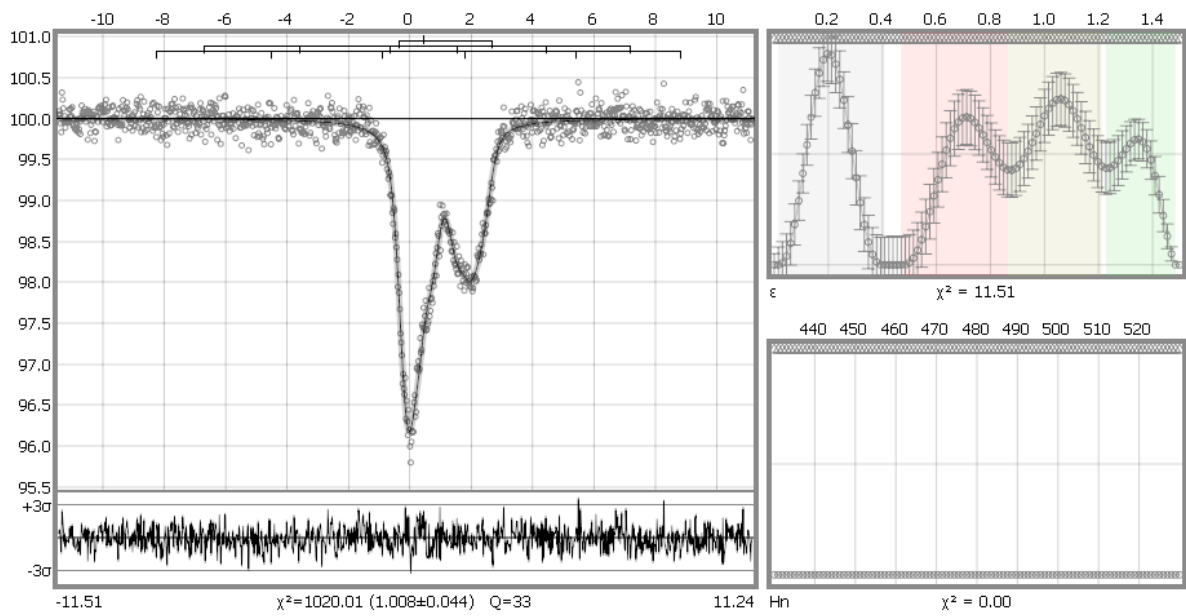


Figure 2 – Spectrum of Mossbauer of the central part of the sample

Table 2

№	Isomeric shift, $\sigma$ , mm/s.	Quadrupole splitting, $\epsilon$ , mm/s.	Magnetic splitting $H_{\text{eff}}$ , kE	The half-width of the line, $\Gamma$ , mm/s	The share of Fe, % in spectrum	Formula of oxides
1.	$0,532 \pm 0,016$	$0,230 \pm 0,018$	-	$0,638 \pm 0,031$	$22,7 \pm 4,0$	$\text{SiO}_2$
2.	$0,786 \pm 0,050$	$0,778 \pm 0,60$	-	$0,638 \pm 0,031$	$36,5 \pm 5,0$	$\text{Al}_2\text{O}_3$
3.	$0,953 \pm 0,040$	1,117	-	$0,638 \pm 0,031$	$27,0 \pm 4,0$	$\text{CaO}$
4.	$1,272 \pm 0,170$	$1,263 \pm 0,160$	-	$0,638 \pm 0,031$	$13,9 \pm 4,0$	$\text{SO}_3$

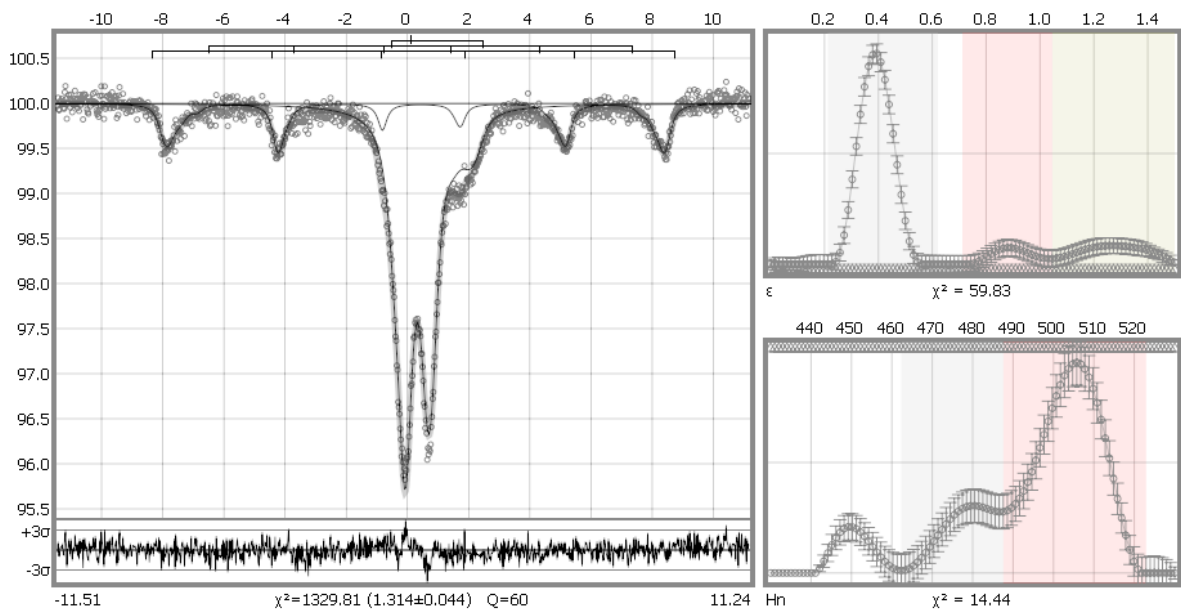


Figure 3 – Mossbauer spectrum of the second layer of the sample

Table 3

№ π/π	Isomeric shift, $\delta$ , mm/s.	Quadrupole splitting, $\epsilon$ , mm/s.	Magnetic splitting $H_{\text{eff}}$ , kE	The half-width of the line, $\Gamma$ , mm/s	The share of Fe, %
1.	0,3221±0,023	0,390±0,004	-	0.541±0,009	61,5±1,3
2.	0,621±0,022	0,902±0,040	-	0.541±0,009	5,5±1,0
3.	0,835±0,014	1,271±0,017	-	0,541±0,009	11,1±0,8
4.	0,366±0,007,	-0,076±0,008	494,20±0,70	0.351±0,040	22,0±0,7
5.	0,366±0,007	-0,096±0,006	503,79±0,50	0.351±0,040	15,9±0,9

A comparison of this spectrum with the  $\beta$ -wollastonite ( $\text{CaSiO}_3$ ) spectrum containing 1% trivalent iron of the oxide showed their strong similarity. It is known [7-9], in the structure of high calcium ceramics containing a significant amount of glass phase, on a level with anorthite ( $\text{CaO} \cdot \text{Al}_2\text{O}_3 \cdot 2\text{SiO}_2$ ) can crystallize  $\beta$ -wollastonite ( $\text{CaSiO}_3$ ) and aluminosilicate, also calcium-containing solid solutions.

As we see, in the structure of a solid solution of  $\beta$ -wollastonite with  $\text{Fe}_2\text{O}_3$  content, 3 components of the NGR spectrum are fixed in the form of doublets corresponding to  $\text{Fe}^{2+}$  ions in three crystallographic positions (Table 3). In addition,

along with doublets, two more sextets appear in the spectra, which is due to the presence of trivalent iron oxide. The doublets, quadrupole splitting ( $\epsilon = 0.902 \pm 0.040$  mm/s,  $\epsilon = 1.271 \pm 0.017$  mm/s) correspond to the compounds of bivalent iron, and ( $\epsilon = 0.390 \pm 0.004$  mm / s.) to the compounds of trivalent iron. We assume that metakaolinite is formed on the level with  $\beta$ -wollastonite in the test sample.

The solubility of  $\text{Fe}_2\text{O}_3$  in metakaolinite ( $\text{Al}_2\text{O}_3 \cdot 2\text{SiO}_2$ ) is insignificant and amounts to only 5.44% of the total additive  $\text{Fe}_2\text{O}_3$ . The remaining amount of  $\text{Fe}_2\text{O}_3$  remains in the free state in the form of hematite ( $\alpha\text{-Fe}_2\text{O}_3$ ) (Fig. 4).

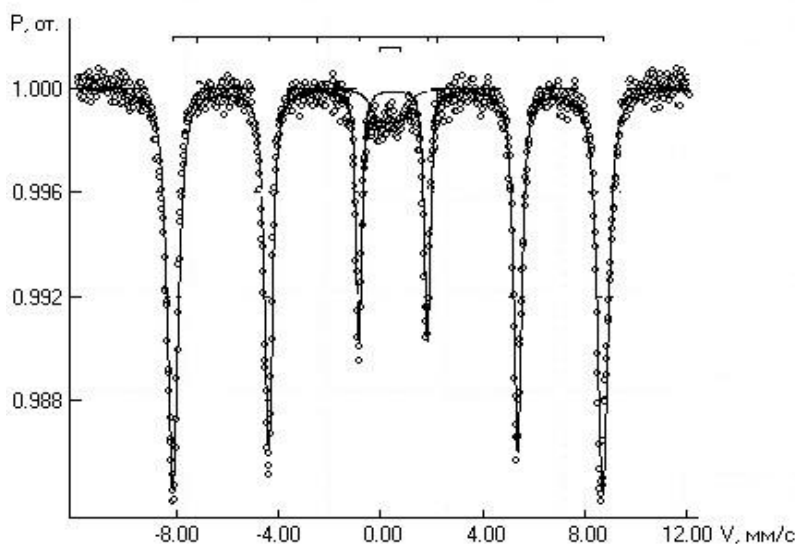


Figure 4 – NGR – metakaolinite spectrum ( $\text{Al}_2\text{O}_3 \cdot 2\text{SiO}_2$ ) with  $\text{Fe}_2\text{O}_3$  content of 1.5% [2]

NGR – the spectrum of meta kaolinite ( $\text{Al}_2\text{O}_3 \cdot 2\text{SiO}_2$ ) with an  $\text{Fe}_2\text{O}_3$  content of 1.5% is represented by a sextet and a doublet of  $\text{Fe}_3^+$  ions. The sextet has the following parameters:  $\delta = 0,382$ mm/s.,  $\epsilon = -0,209$

mm/s.  $H_{\text{eff}} = 523.5$  kE,  $G = 0.511$  mm/s. As can be seen, the parameters of the sextet correspond to the presence of  $\text{Fe}_3^+$  in hematite  $\alpha\text{-Fe}_2\text{O}_3$  in the amount of 94.56% of its content, and 5.44% of  $\text{Fe}_3^+$  in the

form  $[\text{Fe}_3+\text{O}_6]_{9-}$  enters the structure of metakaolinite, replacing  $\text{Al}_{3+}$  in it according to the scheme:  $[\text{Al}_3+\text{O}_6]_{9-} - [\text{Fe}_3+\text{O}_6]_{9-}$

The doublet in the spectrum ( $\delta = 0.341$  mm/s,  $\varepsilon = -0.794$  mm/s,  $\Gamma = 0.775$  mm/s.), possibly, corresponds to a solid solution  $(\text{Al}_{2-x}\text{Fe}_x\text{O}_3) \cdot 2\text{SiO}_2$ . These isovalent substitutions in crystallochemical close ions do not cause electronic and crystallographic changes in the structure of the crystalline lattice of mullite ( $3\text{Al}_2\text{O}_3 \cdot 2\text{SiO}_2$ ), which does not lead to a significant decrease in light absorption and, consequently, to a sharp decrease in the reflection coefficient.

In our case, the appearance of the doublet ( $\delta = 0.3221$  mm/s,  $\varepsilon = -0.390$  mm/s) is possibly due to the state of ferric iron, which is surrounded by a solid solution of metakaolinite. The combination of these constituents in the sample probably causes the appearance of a yellow color.

In the third layer of the sample in the spectrum, we observe one quadrupole doublet and two sextets (Fig. 5).

Table 4 shows the values of the Mossbauer hyperfine spectral parameters.

The intensity of the doublet in this spectrum is less than the intensity of the lines of the first doublet on the second layer. Their hyperfine parameters are close to each other. It can be asserted that these doublets are connected, with states of iron atoms, located in the same positions, corresponding to ions of bivalent iron. On the level with the doublet, we observe two sextets with similar isomeric shifts, which differ in the values of quadrupole doublets  $\varepsilon$  and effective magnetic fields  $H_{\text{eff}}$  on the  $^{57}\text{Fe}$  nuclei.

Comparison of this spectrum with the spectrum of mullite ( $3\text{Al}_2\text{O}_3 \cdot 2\text{SiO}_2$ ) showed their strong external similarity.

Studies of MOSSBAUER spectroscopy data obtained crystal-chemical state of the ions  $\text{Fe}^{3+}$  and  $\text{Fe}^{2+}$  in the mullite synthesized by sintering at  $1350^\circ\text{C}$  with the addition of 1.5%  $\text{Fe}_2\text{O}_3$ , the spectra of which is shown in Fig. [6].

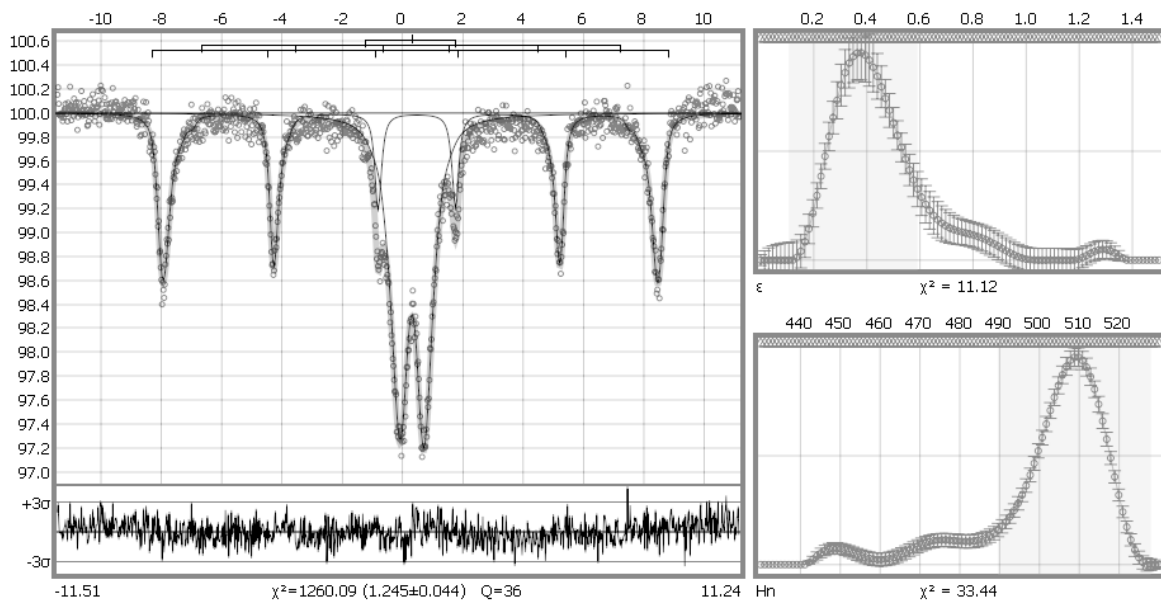
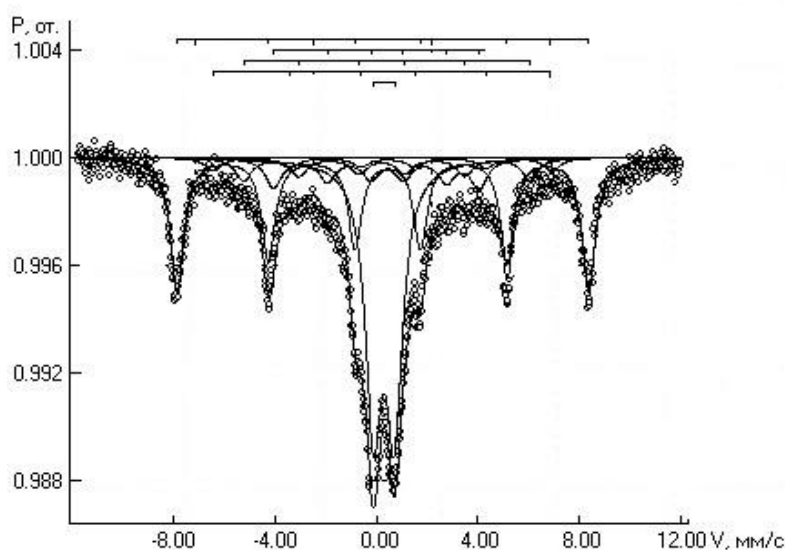


Figure 5 – Mossbauer spectrum of the third layer of the sample

Table 4

No	Isomeric shift, $\delta$ , mm/s.	Quadrupole splitting, $\varepsilon$ , mm/s.	Magnetic splitting $H_{\text{eff}}$ , kE	The half-width of the line, $\Gamma$ , mm/s	The share of Fe, %	Phase state Fe
1.	$0,311 \pm 0,0025$	$0,3890 \pm 0,0006$		$0,469 \pm 0,070$	$46,2 \pm 2,5$	$(3\text{Al}_{2-x} \cdot \text{Fe}_{x3+}) \text{O}_3 \cdot 2\text{SiO}_2$
2.	$0,370 \pm 0,0021$	$-0,370 \pm 0,0021$	430,00	$0,240 \pm 0,016$	$16,0 \pm 0,5$	$\text{Fe}_2\text{SiO}_4$
3.	$0,3684 \pm 0,0022$	$-0,1040 \pm 0,0022$	489,60	$0,240 \pm 0,016$	$38,0 \pm 0,7$	$\text{Fe}_2\text{O}_3$



**Figure 6** – MRI spectrum of the mullite ( $3\text{Al}_2\text{O}_3 \cdot 2\text{SiO}_2$ ) with a content of 1.5%  $\text{Fe}_2\text{O}_3$

In the spectrum of mullite ( $3\text{Al}_2\text{O}_3 \cdot 2\text{SiO}_2 + 1,5\% \text{Fe}_2\text{O}_3$ ), there are four sextets and one doublet.

Their hyperfine parameters are given in Table 5.

As can be seen from table 5 39,3% of Fe is in the trivalent state in the form of  $\alpha\text{-Fe}_2\text{O}_3$ , 10,75% of Fe in the composition of magnetite  $\text{Fe}_3\text{O}_4$  and 36,99% of Fe in the solid solution of mullite, as the firing was carried out in an oxidizing environment. In the formation of solid solution of mullite ( $3\text{Al}_2\text{O}_3 \cdot 2\text{SiO}_2 \cdot \text{Fe}$ ) most likely isovalent substitution of  $\text{Al}^{3+}$  ions for  $\text{Fe}^{3+}$  in its structure in the form of tetrahedra and octahedra according to the schemes:  $[\text{AlO}_4]_5 \rightarrow [\text{FeO}_4]_5$  и  $[\text{AlO}_6]_9 \rightarrow [\text{FeO}_6]_9$ .

This character of isomorphism and formation of the solid solution does not lead to deformation of the crystal lattice and electronic defect structure of mullite ( $3\text{Al}_2\text{O}_3 \cdot 2\text{SiO}_2$ ) and does not cause a sharp light absorption and the reduction of the reflection coefficient.

However, of 21.12% of iron is in the divalent state in the composition of magnetite  $\text{Fe}_2\text{O}_4$  – 8.70% and

in the composition of the fayalite  $\text{Fe}_2\text{SiO}_4$  -12,42%. The formation of  $\text{Fe}_2+$  in FeO is due to the thermal dissociation of  $\text{Fe}_2\text{O}_3$ .

$\text{Fe}_2+$  ions formed as a result of thermal dissociation at  $t > 800^\circ\text{C}$ , react with  $\text{Fe}_2\text{O}_3$ , forming magnetite  $\text{Fe}_3\text{O}_4$ :

Moreover, when interacting with  $[\text{SiO}_4]_4 - \text{FeO}$  forms fayalite ( $\text{Fe}_2\text{SiO}_4$ ), which is confirmed by MOSSBAUER spectroscopy [7-10].

Therefore, in the synthesis of mullite ( $3\text{Al}_2\text{O}_3 \cdot 2\text{SiO}_2$ ) in the solid phase processes, the presence of unreacted hematite  $\alpha\text{-Fe}_2\text{O}_3$  containing of purple-brown color and the formation of magnetite  $\text{Fe}_3\text{O}_4$  with black color, and fayalite lead to strong light absorption and thereby reduction of the reflectance and whiteness of mullite.

The results of x-ray phase analysis confirmed the validity of the proposed mechanism of the effect of  $\text{Fe}_2\text{O}_3$  on the structure of mullite ( $3\text{Al}_2\text{O}_3 \cdot 2\text{SiO}_2$ ) solid-phase sintering [6].

**Table 5**

Type of the spectrum	$\delta$ , mm/s.	$\varepsilon$ , mm/s.	$\Gamma$ , mm/s	$H_{\text{eff}}$ , kE	Crystal graphics position Fe	The share of Fe, %	Phase state Fe
sextet 1	0,362	-0,187	0,647	504,5	$[\text{Fe}_3+\text{O}_6]_9$	39,30	$\alpha\text{-Fe}_2\text{O}_3$
sextet 2	0,211	-0,429	0,776	251,8	$\text{Fe}_{3+}$	10,75	$\text{Fe}_3\text{O}_4$
sextet 3	0,319	0,200	0,776	351,3	$\text{Fe}_{2+}$	8,70	$\text{Fe}_3\text{O}_4$
sextet 4	0,350	-0,200	0,776	415,0	$[\text{Fe}_2+\text{O}_6]_{10}$	12,42	$\text{Fe}_2\text{SiO}_4$
Doublet 1	0,303	0,828	0,776	-	$[\text{Fe}_3+\text{O}_6]_9$	36,99	$(3\text{Al}_{2-x}\cdot\text{Fe}_{x^{3+}})\text{O}_3 \cdot 2\text{SiO}_2$

Received our mossbauer studies confirm these data. A very important are such studies for the aluminosilicatecalcium–anortite( $\text{CaO}\cdot\text{Al}_2\text{O}_3\cdot 2\text{SiO}_2$ ), one of the main crystalline phases in the structure of various ceramic materials and products, including rough wall ceramics based on clays with a high content of impurities or specifically the additives  $\text{CaCO}_3$  to provide the required exploitation properties.

It is known [7-9], the basis of the feldspar structure, including the anortite, is a framework of interconnected layers of tetrahedrons  $[\text{SiO}_4]_4$ -and  $[\text{AlO}_4]_5$  through the summit.

Study by mossbauer spectroscopy of the effect of oxides of  $\text{Fe}_2\text{O}_3$  on the phase and crystal-chemical state  $\text{Fe}^{3+}$  ions taking into account the particular

structure of anortite confirmed the above views about the mechanism of formation of iron solid solution (figure 7).

Analysis of the Mossbauer spectra (Fig.7) and their parameters confirm the presence in samples of anortite ( $\text{CaO}\cdot\text{Al}_2\text{O}_3\cdot 2\text{SiO}_2$ ), both of 0.5% and 3.0%  $\text{Fe}_2\text{O}_3$  4 non-equivalent  $\text{Fe}^{3+}$  component ions in their structure (table 6). This is sextet with parameters AGRS, including the magnetic field tensions,  $H_{\text{eff}}=510,8; 512,0 \text{ k}\mathcal{E}$  indicating the presence and magneto-ordered phase of  $\alpha\text{-Fe}_2\text{O}_3$ . This proves that even when the content of  $\text{Fe}_2\text{O}_3 = 0.5\%$  iron ions  $\text{Fe}^{3+}$  is not completely included in the structure of anortite ( $\text{CaO}\cdot\text{Al}_2\text{O}_3\cdot 2\text{SiO}_2$ ), and the solubility of the  $\text{Fe}_2\text{O}_3$  in the anortite is 0.75 – 0.78 % by weight.

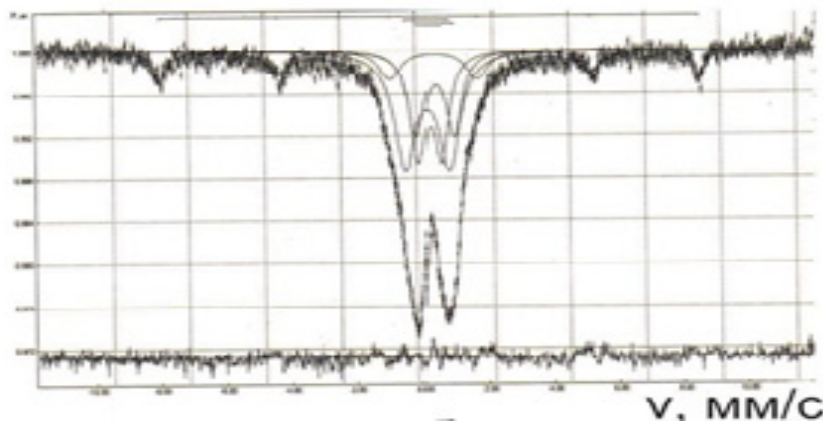


Figure 7 – MOSSBAUER spectra of anortite ( $\text{CaO}\cdot\text{Al}_2\text{O}_3\cdot 2\text{SiO}_2$ ) containing  $\text{Fe}_2\text{O}_3$ , % by mass: 3.0

Table 6

The amount of $\text{Fe}_2\text{O}_3$ , %	Type of the spectrum	$\delta$ , mm/s.	$\epsilon$ , mm/s.	$\Gamma$ , mm/s	$H_{\text{eff}}$ , kE	Crystal graphics position Fe	The share of Fe,%	Phase state Fe
0,3	Sextet	0,33	-0,13	0,52	512,0	$[\text{FeO}_6]_9$ .	21,79	$\text{Fe}_2\text{O}_3$
0,3	Doublet 1	0,18	1,28	0,77	-	$[\text{AlO}_4]_5$ .	36,44	$\text{CS}_2\text{A}_2\text{O}_8\cdot\text{F}$
0,3	Doublet 2	0,42	1,11	0,57	-	$[\text{Si O}_4]_4$ .	19,73	$\text{CS}_2\text{A}_2\text{O}_8\cdot\text{F}$
0,3	Doublet 3	0,26	0,66	00,53	-	$[\text{CaO}_{10}]_{18}$ .	22,04	$\text{CS}_2\text{A}_2\text{O}_8\cdot\text{F}$

Moreover, the parameters of the AGRS spectra (table 6) identified 3 non-equivalent positions of the  $\text{Fe}^{3+}$  ions are represented by doublets 1,2, and 3, is isomorphic – having replaced in the crystal lattice of anortite ions  $\text{Ca}^{2+}$ ,  $\text{Si}_4$ ,  $\text{Al}^{3+}$  to form solid iron-containing solution of the composition:  $[\text{Ca}_{1-x}\text{Fe}_x\cdot\text{Al}_2\text{-yFe}_y\cdot\text{Si}_2\text{-z}\cdot\text{Fe}_z]_8\text{O}_8$ . In the technology of thin, construction and artly-decorative ceramics a significant role play a vitreous phase aluminasilicate

compositions in ensuring the white, color and physico-technical properties. As can be seen from the informations shown in table 6, when the content of  $\text{Fe}_2\text{O}_3$  from 0 to 1%, the reflection coefficient of the glass phase fused from pure oxides at a temperature  $1400^\circ\text{C}$ , reduced slightly from 86,1 to 70.9%.

This is because in the oxidative conditions of firing and cooling  $\text{Fe}^{3+}$  ions substitute for isovalent ions  $\text{Al}^{3+}$  in the tetrahedral  $[\text{AlO}_4]_5$  according to

the scheme:  $[\text{AlO}_4]_5 \rightarrow [\text{FeO}_4]_5$  that does not cause strong light absorption and reduce reflectance. When the content of  $\text{Fe}_2\text{O}_3$  equal to 3% the reflection coefficient of the glass phase is significantly reduced and is 48.3%. Effect of glass phase on the whiteness of the product depending on the content  $\text{Fe}_2\text{O}_3$  largely depends on the quantity, viscosity-forming melt and the firing temperature.

These phase and crystal-chemical features of dyeing aluminate and aluminosilicate crystalline and glassy phases are very important in the development of effective methods for producing materials isdelii as high whiteness (porcelain, faience), and intensely vivid colors, light and dark spectra in construction ceramics.

The formation of iron solid solutions in the crystal phases with a complex structure results in a significant reduction of the reflection coefficient of metakaolinite  $\text{Al}_2\text{O}_3 \cdot 2\text{SiO}_2$ , and wollastonite ( $\text{CaOSiO}_2$ ) and anortite ( $\text{CaO} \cdot \text{Al}_2\text{O}_3 \cdot \text{SiO}_2$ ) even ( $\text{CaO} \cdot \text{Al}_2\text{O}_3 \cdot 2\text{SiO}_2$ ), with the content of 0.5%  $\text{Fe}_2\text{O}_3$  and can be explained by the isomorphism and crystal-chemical state of the

ions  $\text{Fe}^{3+}$ , given the structures of these phases. Higher susceptibility to staining of wollastonite and anortite oxide  $\text{Fe}_2\text{O}_3$  due to the formation of iron containing clusters in a nano-complex of the crystal lattice due to isomorphous substitutions in the tetrahedral  $[\text{SiO}_4]_4$ - and  $[\text{AlO}_4]_5$ ,  $\text{Si}_4$  and  $\text{Al}^{3+}$  ions and  $\text{Ca}^{2+}$  ions in the voids of the lattice  $\text{Fe}^{3+}$  and the presence of free  $\alpha - \text{Fe}_2\text{O}_3$ , not included in the structure of the solid solution and the low solubility limit of  $\text{Fe}_2\text{O}_3$  in the structure of wollastonite ( $\text{CaSiO}_3$ ) and anortite ( $\text{CaO} \cdot \text{Al}_2\text{O}_3 \cdot 2\text{SiO}_2$ ), which is 0.68 to 0.69 and 0.75 – 0.78 percent by weight, respectively. When the exaggeration of the number of  $\text{Fe}_2\text{O}_3$  to 1.0%, TO of aluminosilicate phases mullite ( $3\text{Al}_2\text{O}_3 \cdot 2\text{SiO}_2$ ) and glass phase decreases relatively not very high, respectively, 17.6 and 15.2% in comparison with the sample without  $\text{Fe}_2\text{O}_3$ . Isovalent substitution in crystal-close ions do not cause electronic and crystallographic changes in the structure of the crystal lattice of the mullite that does not lead to a significant reduction in light absorption and consequently, to a sharp decrease of the reflection coefficient.

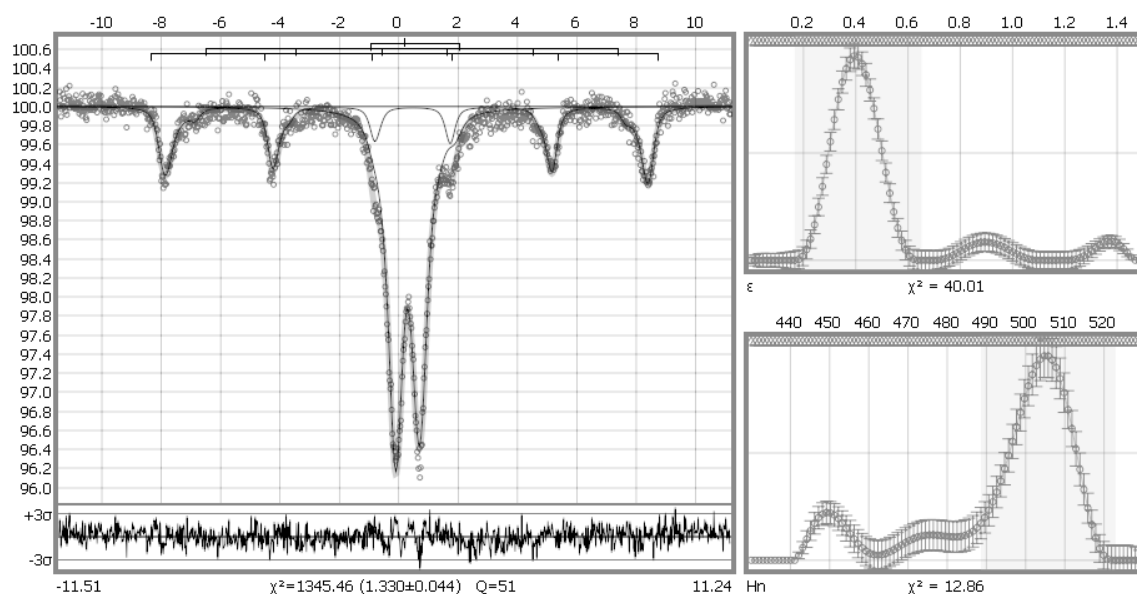


Figure 8 – a Mossbauer spectrum of the fourth layer of sample

Table 7

№	Isomeric shift, $\delta$ , mm/s.	Quadrupole splitting, $\epsilon$ , mm/s.	Magnetic splitting $H_{\text{eff}}$ , kE	The half-width of the line, $\Gamma$ , mm/s	The share of Fe, %
1.	0,300±0,0018	0,399± 005		0,524±0,012	69,6±0,8
2.	0,381±0,006	-0,092±006	494,86 ±0,60	0,375±0,027	14,4±0,8
3.	0,366±0,004	-0,098± 004	504,32 ±1,30	0,375±0,027	16,5±1,3

Substitutions like this take place in the structure of the glass phase. Therefore, from the perspective of lightening the coloring of ceramics, i.e., increase its reflectivity, the formation of iron containing solid solutions of wollastonite and anortite on the one hand is positive, because the reflection coefficient with  $\text{Fe}_2\text{O}_3$  contents up to 1% significantly higher reflectance of the hematite with content 6.5%. This is to some extent neutralizes their color with oxide  $\text{Fe}_2\text{O}_3$ . However, when increased amounts of  $\text{Fe}_2\text{O}_3$ , in particular the masses on the basis of iron-bearing clays in the production of building ceramics, the efficiency of neutralization of its coloration is significantly reduced with the presence of free  $\alpha\text{-Fe}_2\text{O}_3$  with a limited solubility limit in the structures

of wollastonite ( $\text{CaSiO}_3$ ) and anortite ( $\text{CaO-Al}_2\text{O}_3\text{-SiO}_2$ ), and also due to the heterogeneous nature of the formation of the solid solutions with  $\text{Fe}^{3+}$  and their clusters, probably in the third word is formed purple-red color.

In the fourth layer of the sample in the spectrum, there is one doublet and two sextet (Fig.8).

Hyperfine parameters of mossbauer spectra are shown in table 7.

There is an increase in the intensity as a doublet, and the second sextet, which indicates the increase in the number of iron ions in these states. The intensity of the first sextet is smaller than in the previous case. All these changes in the spectra of mossbauer is strongly reflected in the dawn samples.

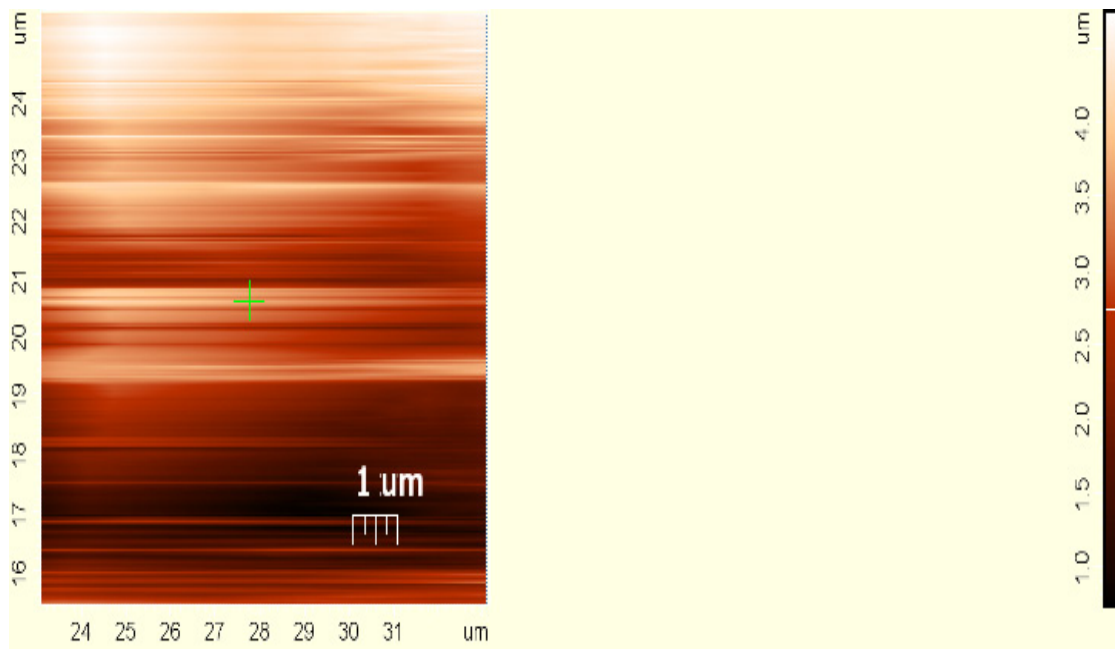


Figure 9 – Topography of the sample surface(7x7) mkm, obtained using atomic force microscope

Effect of coloring impurities of Fe on the color silicate phases, the most common of which in the structure of low-temperature ceramics containing carbonate materials are  $\beta$ -wollastonite ( $\text{CaSiO}_3$ ) and aluminosilicate Ca – anortite ( $\text{CaO-Al}_2\text{O}_3\text{-SiO}_2$ ), calcium containing solid solutions. These structures are characterized by often laminated or framed structure with complex relationships of silicate and aluminosilicate polyhedra of various degree of their association. This causes in some of the aluminosilicates the formation in nanoobject of their structures of Fe-containing clusters that cause strong absorption and a sharp decrease in the reflection coefficient. Because these phases are common to the

products of construction and other types of ceramics, it is extremely important the study of whiteness and staining in the presence in their composition of  $\text{Fe}_2\text{O}_3$ . Staining of 4-th layer of light – brown color, probably due to the formation of  $\beta$ -wollastonite ( $\text{CaSiO}_3$ ) and aluminosilicate Ca – anortite ( $\text{CaO-Al}_2\text{O}_3\text{-SiO}_2$ ), calcium containing solid solution.

As can be seen from the above data, the ability to stain various phases of the oxide  $\text{Fe}_2\text{O}_3$  is very different depending on the structure of the phases and their crystal chemistry and phase state of Fe.

The results of the research of the micro-nanostructure of the surface layer of different zones of the samples is shown in Fig.9. It was found that

significant differences in the studied layers of samples are not observed.

### References

1. Belenky E.F. *Chemistry and technology of pigments* / E.F. Belenky, I.V. Riskin. – L.: Chemistry, 1974 – 656 p.
2. Zubehin A.P., Yatsenko N.D., Bolyak V.I., Verevkin K. A., Filatova E.V. “The influence of chemical and phase composition on the color of ceramic bricks”. *Building materials*. №4. 2008.
3. Mukhopadhyay T.K., Prasad S.D., Dan T.K. “Study on Improvement of Thermomechanical Properties of Red Clay Wares with Addition of Wollastonite”. *Research and Industry*. Vol. 40, №4 (1995): 306-310.
4. Yatsenko N.D., Madoyan A.A., Zubekhin A.P., Ratkova V.P., Golovanova S.P. “Influence of Calcium Containing Waste on Sintering of Faience Masses”. *Technology: Ser. Constructions from composite materials: interdigit. scientific – technical. Sat. – M.* №3-4 (1998): 11-13.
5. Vil’bitskaya N.A. *Features of the formation of crystalline phases in high-calcium ceramics* / Vil’bitskaya N.A., Golovanova S.P.
6. Yatsenko N.D. Scientific foundations of resource-saving technologies of wall and facing ceramics and management of its properties. The dissertation author’s abstract on the competition of a scientific degree of Doctor of Technical Sciences. Novochoerkassk, 2015.
7. Vereshchak M.F., Goldmann M.M., Zhetbaev A.K., Solenko T.S. “Studies of the Fe<sub>2</sub>O<sub>3</sub>-Na<sub>2</sub>O-SiO<sub>2</sub> system using the Mossbauer effect”. *FTT*. Vol. 16, №1231 (1974).
8. Neither L.P., Zhetbaev A.K., Goldmann M.M., Vereschak M.F. “The use of Mössbauer spectroscopy for the investigation of iron-containing compounds in clay production”. *Bulletin of the Academy of Sciences of the Kazakh SSR* № 7 (1974): 26.
9. Gol’danskii V.I. Krizhanskii LM, Khrapov V.V. *Chemical applications of Mossbauer spectroscopy*. Moscow: Moscow State University; 1970-206p.

IRSTI 27.35.55

S. Subhaschandra Singh

Department of Physics, Imphal College, Imphal-795001, Manipur, India.  
e-mail: subhasic@yahoo.co.in

**Soliton solutions  
of a generalized Klein–Gordon equation  
with power-law nonlinearity via the first integral method**

**Abstract.** This paper studies solitary wave solutions of a generalized nonlinear Klein-Gordon (KG) equation with power-law nonlinearity via the so-called first integral method. Using the method, some soliton solutions of the equation are obtained. The method is hereby shown to be an efficient and reliable mathematical tool for solving many nonlinear evolution equations arising in a number of problems in science and engineering.

**Key words:** Soliton, power-law nonlinearity, quantum field theory (QFT).

### Introduction

The Klein-Gordon (KG) equation is an important equation in theoretical physics especially in quantum field theory (QFT) and relativistic quantum mechanics. It also appears in nonlinear optics and plasma physics. The Klein-Gordon equation often arises in physics in linear as well as nonlinear forms. In the past, the equation had been extensively studied by many physicists and applied mathematicians with the help of a variety of methods. This paper deals with solving a particular form of the generalized Klein-Gordon (GKG) equation with full nonlinearity via the first integral method [1 – 7].

The generalized Klein-Gordon equation [8 – 10] that is to be studied in this paper is written in the form

$$q_{tt} - \mu^2 q_{xx} + \alpha q - \beta q^n + \gamma q^{2n-1} = 0, \quad (1)$$

where the dependent variable  $q(x, t)$  represents a wave profile,  $x$  and  $t$  are spatial and temporal variables,  $\mu, \alpha, \beta, \gamma$  are real-valued constants and  $n = 2, 3, 4, \dots$

### Reduction to Nonlinear Ordinary Differential Equation (NLODE)

To reduce Eq.(1) to a nonlinear ordinary differential equation (NLODE), we put

$$q(x, t) = u(\xi), \xi = x - vt \quad (2)$$

where  $v$  is a constant, generally the constant speed of wave propagation.

Now, from eq.(2), we have

$$q_{tt} = v^2 \frac{d^2u}{d\xi^2}, q_{xx} = \frac{d^2u}{d\xi^2}.$$

Substituting these derivatives in Eq.(1), we obtain

$$(v^2 - \mu^2) \frac{d^2u}{d\xi^2} + \alpha u - \beta u^n + \gamma u^{2n-1} = 0. \quad (3)$$

Thus, Eq.(1) is reduced to a NLODE.

Let us further simplify the reduced NLODE by putting

$$u(\xi) = [U(\xi)]^{\frac{1}{n-1}}. \quad (4)$$

Then, we have

$$\frac{du}{d\xi} = \frac{1}{n-1} U^{\frac{2-n}{n-1}} \frac{dU}{d\xi} \quad (5)$$

and

$$\frac{d^2u}{d\xi^2} = \frac{2-n}{(n-1)^2} U^{\frac{3-2n}{n-1}} \left(\frac{dU}{d\xi}\right)^2 + \frac{1}{n-1} U^{\frac{2-n}{n-1}} \frac{d^2U}{d\xi^2}. \quad (6)$$

Substituting Eqs.(4) to (6) in Eq. (3), we obtain

$$\begin{aligned} & (n-1)(v^2 - \mu^2)U \frac{d^2U}{d\xi^2} - \\ & - (n-2)(v^2 - \mu^2) \left(\frac{dU}{d\xi}\right)^2 + \\ & + (n-1)^2 \alpha U^2 - (n-1)^2 \beta U^3 + \\ & + (n-1)^2 \gamma U^4 = 0. \end{aligned} \quad (7)$$

Solving Eq. (7) and using Eqs. (2) and (4), we can obtain the solution  $q(x, t)$  of Eq. (1).

In this paper, solutions of Eqs. (7) are to be obtained via a method known as the first integral method.

#### Algorithm of the First Integral method

Before applying the first integral method in finding the solutions of Eq. (7), we introduce an algorithm of the method as in the following.

Let us consider a general NLPDE in the form

$$F(u, u_x, u_t, u_{xx}, u_{xt}, u_{tt}, u_{xxx}, \dots) = 0, \quad (8)$$

where  $u = u(x, t)$  is its solution,  $x$  and  $t$  represent the spatial and the temporal variables and  $F$  represents a polynomial in  $u$  and its partial derivatives. Here, the subscripts denote differentiations with respect to them.

Let us introduce the transformations,

$$u = u(x, t) = U(\xi), \xi = x - vt, \quad (9)$$

where  $v$  is a constant to be determined latter.

Now, we have,

$$\begin{aligned} u_x &= \frac{\partial u}{\partial x} = \frac{dU}{d\xi}, u_t = \frac{\partial u}{\partial t} = -v \frac{dU}{d\xi}, \\ u_{xx} &= \frac{\partial^2 u}{\partial x^2} = \frac{d^2U}{d\xi^2}, u_{xt} = \frac{\partial^2 u}{\partial x \partial t} = -v \frac{d^2U}{d\xi^2}, \\ u_{tt} &= \frac{\partial^2 u}{\partial t^2} = v^2 \frac{d^2U}{d\xi^2}, etc. \end{aligned} \quad (10)$$

Using Eqs. (9) and (10), we can reduce Eq. (8) to a nonlinear ordinary differential equation (NLODE) of the form

$$G(U, U', U'', U''', \dots) = 0 \quad (11)$$

where the primes denote derivatives with respect to the same variable ( $\xi$ ) such that

$U' = \frac{dU}{d\xi}, U'' = \frac{d^2U}{d\xi^2}, etc.$  and  $G(U, U', U'', \dots)$  denotes another polynomial in  $U$  and its derivatives with respect to  $\xi$ .

This is exactly the way by which Eq. (1) was reduced to Eq. (7).

Now, Let us suppose that the solution of the Non Linear Ordinary Differential Equation (NLODE) (11) can be expressed as

$$U(\xi) = f(\xi). \quad (12)$$

We further introduce the following new variables

$$\begin{aligned} X(\xi) &= f(\xi), Y(\xi) = f'(\xi) = \\ &= X'(\xi) = \frac{df}{d\xi} = \frac{dX}{d\xi} \end{aligned} \quad (13)$$

leading to the plane autonomous system

$$Y(\xi) = X'(\xi), Y'(\xi) = H(X(\xi), Y(\xi)), \quad (14)$$

where  $H$  is a polynomial in  $X$  and  $Y$ .

If we can find two first integrals to the system of equations in (14) under the same conditions, then the analytic solutions of equations (14) can be obtained directly. However, in general, it is really difficult for us to realize this even for one first integral, because for a given plane autonomous system, there exists neither a systematic theory that can tell us how to find its first integrals nor a logical way for telling us what these first integrals are. We will apply the Division Theorem to obtain a first integral to the system of equations (14) which reduces eqn. (11) to a first order integrable ODE. An exact solution of eqn. (8) is then obtained by solving this ODE. For convenience, let us recall the division theorem for two variables in the complex domain  $C[w, z]$ .

**Division Theorem:** For two polynomials  $P(w, z)$  and  $Q(w, z)$  in a complex domain  $C[w, z]$ , if  $P(w, z)$  is irreducible in  $C[w, z]$  and if  $Q(w, z)$  vanishes at all zero points of  $P(w, z)$ , then there exists another polynomial  $G(w, z)$  in  $C[w, z]$  such that  $Q(w, z) = P(w, z) G(w, z)$ . The division theorem follows immediately from Hilbert – Nullstellensatz theorem of commutative algebra.

**Application of the First Integral method in solving the Generalized Klein–Gordon equation**

In this section, the first integral method is applied in finding soliton solutions of Eq. (7) and hence of Eq. (1).

In Eq. (7), let us put

$$X(\xi) = U(\xi), Y(\xi) = X'(\xi) = \frac{dX}{d\xi}, \quad (15a)$$

$$\begin{aligned} Y'(\xi) &= \frac{dY}{d\xi} = \frac{(n-2)}{(n-1)} \frac{(U')^2}{U} + \\ &+ \frac{(n-1)}{(\mu^2 - \nu^2)} [\alpha U - \beta U^2 + \gamma U^3] = \\ &= \frac{(n-2)}{(n-1)} \frac{1}{X} Y^2 + \\ &+ \frac{(n-1)}{(\mu^2 - \nu^2)} [\alpha X - \beta X^2 + \gamma X^3]. \end{aligned} \quad (15b)$$

Further, let us introduce another new variable  $\eta$  such that

$$d\xi = X d\eta.$$

Then, Eqs.(15) yield

$$\begin{aligned} \frac{dX}{d\eta} &= XY, \frac{dY}{d\eta} = \frac{n-2}{n-1} Y^2 + \\ &+ \frac{n-1}{\mu^2 - \nu^2} [\alpha X^2 - \beta X^3 + \gamma X^4]. \end{aligned} \quad (16)$$

We suppose that  $X(\eta)$  and  $Y(\eta)$  are nontrivial solutions of Eq. (16) and  $q(X(\eta), Y(\eta)) = \sum_{j=0}^m a_j(X) Y^j(X)$  is an irreducible polynomial in the complex domain  $C[X, Y]$  such that

$$q(X(\eta), Y(\eta)) = \sum_{j=0}^m a_j(X) Y^j(X) = 0, \quad (17)$$

where  $a_j(X)$  ( $j = 0, 1, 2, 3, \dots, m-1, m$ ) are polynomials in  $X$  and  $a_m \neq 0$ .

Here, Eq.(17) is called the first integral to the system of Eqs.(16).

By division theorem, there exists a polynomial  $g(X) + h(X)Y$  in the complex domain  $C[X, Y]$  such that

$$\frac{dq}{d\eta} = \frac{dq}{dX} \frac{dX}{d\eta} + \frac{dq}{dY} \frac{dY}{d\eta} =$$

$$= \{g(X) + h(X)Y\} \sum_{j=0}^m a_j(X) Y^j(X). \quad (18)$$

Now, using Eqs.(16), (17) and (18) we write

$$\begin{aligned} &\sum_{j=0}^m a'_j(X) X Y^{j+1} + \\ &+ \sum_{j=0}^m j a_j(X) Y^{j-1} \left\{ \frac{n-2}{n-1} Y^2 + \frac{n-1}{\mu^2 - \nu^2} [\alpha X^2 - \beta X^3 + \gamma X^4] \right\} = \\ &= \sum_{j=0}^m g(X) a_j(X) Y^j + \sum_{j=0}^m h(X) a_j(X) Y^{j+1}. \end{aligned}$$

From the above equation, equating the coefficients of  $Y^j$  ( $j = m+1, m, \dots, 3, 2, 1, 0$ ) from both sides, we obtain

$$X a'_m(X) = h(X) a_m(X) - m \frac{(n-2)}{(n-1)} a_m(X), \quad (19a)$$

$$\begin{aligned} X a'_{m-1}(X) &= g(X) a_m(X) + h(X) a_{m-1}(X) - \\ &- \frac{(m-1)(n-2)}{n-1} a_{m-1}(X), \end{aligned} \quad (19b)$$

$$\begin{aligned} X a'_2(X) &= g(X) a_3(X) + h(X) a_2(X) - \\ &- \frac{2(n-2)}{n-1} a_2(X) - \\ &- \frac{4(n-1)}{\mu^2 - \nu^2} a_4(X) [\alpha X^2 - \beta X^3 + \gamma X^4], \end{aligned} \quad (19c)$$

$$\begin{aligned} X a'_1(X) &= g(X) a_2(X) + h(X) a_1(X) - \\ &- \frac{n-2}{n-1} a_1(X) - \\ &- \frac{3(n-1)}{\mu^2 - \nu^2} a_3(X) [\alpha X^2 - \beta X^3 + \gamma X^4], \end{aligned} \quad (19d)$$

$$\begin{aligned} X a'_0(X) &= g(X) a_1(X) + h(X) a_0(X) - \\ &- \frac{2(n-1)}{\mu^2 - \nu^2} a_2(X) [\alpha X^2 - \beta X^3 + \gamma X^4], \end{aligned} \quad (19e)$$

$$a_1(X) \frac{n-1}{\mu^2 - v^2} [\alpha X^2 - \beta X^3 + \gamma X^4] = \\ = g(X) a_0(X). \quad (19f)$$

Since  $a_m(X)$  is a polynomial in  $X$ , we deduce from Eq.(19a) that  $h(X) = \frac{m(n-2)}{n-1}$ .

For simplicity, we take  $a_m(X) = 1$ . We can find the degrees of  $g(X)$ ,  $a_0(X)$ ,  $a_1(X)$ , etc. by balancing of degrees in Eqs.(19). Then, we express these functions as polynomials of appropriate degrees in  $X$  with undetermined coefficients. Substituting such polynomials in appropriate equations in (19) and equating coefficients of like powers of  $X$  from both sides of the resulting equation, we can find the undetermined coefficients. Thus, we can know the exact expressions of  $a_0(X)$ ,  $a_1(X)$ ,  $a_2(X)$ , etc. Substitution of these expressions in Eq.(17) can yield the expression(s) for  $Y$ . Recalling that  $Y = \frac{dX}{d\xi}$ , we can find  $X(\xi)$  or  $U(\xi)$  on integration.

Then using Eqs. (2) and (4), we can arrive at  $u(\xi)$  and hence at  $q(x, t)$ .

In a particular case, let us take  $m = 1$ . Then, Eqs.(19) yield

$$X a_1'(X) = \left\{ h(X) - \frac{n-2}{n-1} \right\} a_1(X), \quad (20a)$$

$$X a_0'(X) = g(X) a_1(X) + h(X) a_0(X), \quad (20b)$$

$$a_1(X) \frac{n-1}{\mu^2 - v^2} [\alpha X^2 - \beta X^3 + \gamma X^4] = \\ = g(X) a_0(X). \quad (20c)$$

Since  $a_j(X)$  are polynomials in  $X$ , we deduce from Eq. (20a) that  $a_1(X)$  is a constant and  $h(X) = \frac{n-2}{n-1}$ . For simplicity, we take  $a_1(X) = 1$ . From balancing of degrees in Eqs. (20), we conclude that  $\deg[g(X)] = \deg[a_0(X)] = 2$ .

We suppose that

$$a_0(X) = A_0 + A_1 X + A_2 X^2 \quad (21)$$

where  $A_0, A_1, A_2$  ( $A_2 \neq 0$ ) are arbitrary constants to be determined.

Substituting the expressions for  $a_0(X)$  and its derivative  $a_0'(X)$  and also the values of  $a_1(X)$  and  $h(X)$  in Eq. (20b), we have

$$A_1 X + 2A_2 X^2 = g(X) + \\ + \frac{n-2}{n-1} [A_0 + A_1 X + A_2 X^2] \text{ Or, } g(X) = \\ = -\frac{n-2}{n-1} A_0 + \frac{1}{n-1} A_1 X + \frac{n}{n-1} A_2 X^2. \quad (22)$$

Substituting the expressions for  $a_0(X)$ ,  $a_1(X)$ ,  $g(X)$  in Eq. (20c), we obtain

$$\frac{n-1}{\mu^2 - v^2} [\alpha X^2 - \beta X^3 + \gamma X^4] = \left( -\frac{n-2}{n-1} A_0 + \frac{1}{n-1} A_1 X + \frac{n}{n-1} A_2 X^2 \right) (A_0 + A_1 X + A_2 X^2).$$

Equating coefficients of like powers of  $X$  from both sides of the above equation, we obtain

$$\frac{n-2}{n-1} A_0^2 = 0, \quad (23)$$

$$\frac{3-n}{n-1} A_0 A_1 = 0, \quad (24)$$

$$\frac{2}{n-1} A_0 A_2 + \frac{1}{n-1} A_1^2 - \frac{\alpha(n-1)}{\mu^2 - v^2} = 0, \quad (25)$$

$$\frac{n+1}{n-1} A_1 A_2 + \frac{\beta(n-1)}{\mu^2 - v^2} = 0, \quad (26)$$

$$\frac{n}{n-1} A_2^2 - \frac{\gamma(n-1)}{\mu^2 - v^2} = 0. \quad (27)$$

From Eq.(23), we obtain  $A_0 = 0$  and then Eq.(25) yields

$$A_1 = \mp (n-1) \sqrt{\frac{\alpha}{\mu^2 - v^2}}. \quad (28)$$

Further, from Eq. (27), we have

$$A_2 = \pm (n-1) \sqrt{\frac{\gamma}{n(\mu^2 - v^2)}}. \quad (29)$$

Using these values of  $A_1$  and  $A_2$ , Eq. (26) yields the constraint condition

$$\gamma = \frac{n\beta^2}{\alpha(n+1)^2}. \quad (30)$$

Hence, we write

$$A_2 = \pm \frac{\beta(n-1)}{\alpha(n+1)} \sqrt{\frac{\alpha}{\mu^2 - v^2}}. \quad (31)$$

Substituting the values of  $A_0, A_1$  and  $A_2$  in Eq. (21), we have

$$a_0(X) = \mp (n - 1) \sqrt{\frac{\alpha}{\mu^2 - v^2}} X \pm \pm \frac{\beta(n - 1)}{\alpha(n + 1)} \sqrt{\frac{\alpha}{\mu^2 - v^2}} X^2. \tag{32}$$

As  $m = 1$  and  $a_1(X) = 1$  in the present case, Eq. (17) yields

$$a_0(X) + Y = 0$$

$$Or, Y = \frac{dX}{d\xi} = -a_0(X) =$$

$$= \pm (n - 1) \sqrt{\frac{\alpha}{\mu^2 - v^2}} X \mp \mp \frac{\beta(n-1)}{\alpha(n+1)} \sqrt{\frac{\alpha}{\mu^2-v^2}} X^2. \tag{33}$$

Integrating Eq. (33), we obtain the solutions

$$U(\xi) = X(\xi) = \pm \frac{(n + 1)\alpha}{2\beta} \times \times \left\{ 1 \pm \tanh \left[ \frac{(n-1)}{2} \sqrt{\frac{\alpha}{\mu^2-v^2}} (\xi - \xi_0) \right] \right\} \tag{34}$$

and

$$U(\xi) = X(\xi) = \pm \frac{(n + 1)\alpha}{2\beta} \times \times \left\{ 1 \pm \coth \left[ \frac{(n-1)}{2} \sqrt{\frac{\alpha}{\mu^2-v^2}} (\xi - \xi_0) \right] \right\} \tag{35}$$

where  $\xi_0$  is an integration constant.

Choosing  $\xi_0 = 0$  and recalling that  $q(x, t) = u(\xi) = [U(\xi)]^{\frac{1}{n-1}}$  with  $\xi = x - vt$ , we obtain kink and anti-kink soliton solutions of Eq. (1) as

$$q(x, t) = \left[ \pm \frac{(n+1)\alpha}{2\beta} \left\{ 1 \pm \tanh \left[ \frac{(n-1)}{2} \sqrt{\frac{\alpha}{\mu^2-v^2}} (x - vt) \right] \right\} \right]^{\frac{1}{n-1}} \tag{36}$$

and

$$(x, t) = \left[ \pm \frac{(n+1)\alpha}{2\beta} \left\{ 1 \pm \coth \left[ \frac{(n-1)}{2} \sqrt{\frac{\alpha}{\mu^2-v^2}} (x - vt) \right] \right\} \right]^{\frac{1}{n-1}}. \tag{37}$$

These solutions are those obtained by *Wazwaz* [11].

One can try for solutions with  $m = 2, 3, 4$  which will become complicated. Attempts for solutions with  $m \geq 5$  must be dropped out as algebraic equations with degrees greater than or equal to 5 are generally not solvable.

**Conclusion**

In this paper, the first integral method is successfully applied in finding exact solutions of generalized Klein-Gordon equation. The performance of this method is found to be effective and reliable. The method can be applied in finding exact solutions of many nonlinear evolution

equations arising in the studies of social dynamics, science and engineering. One advantage of the method is that it is applicable to both integrable as well as non-integrable systems.

**References**

1. Feng, Z.S., The first integral method to study the Burgers Korteweg-de Vries equation// J. Phys. A., 2002, Vol. 35 No. 2, 343–349.
2. Feng, Z. S., On explicit exact solutions to the compound Burg ers- Korteweg-de Vries equation // Phys. Lett. A., 2002, Vol.293, 57 – 66.
3. Feng, Z. S., Travelling wave behavior for a generalized Fisher equation// Chaos, Soliton.Fract., 2008, Vol. 38, 481 – 488

4. Feng, Z. S., Exact solution to an approximate sine-Gordon equation in  $(n + 1)$  – dimensional space//Phys. Lett. A, 2002, Vol.302, 64 – 76 .

5. Feng, Z. S. and Wang, X. H., The first integral method to the two-dimensional Burgers- KdV equation//Phys. Lett. A., 2002, Vol. 308, 173 – 178 .

6. Feng, Z. S. and Knobel, R., Travelling waves to a Burgers- Korteweg – de Vries equation with higher order nonlinearities//J. Math. Anal. Appl., 2007, Vol.328, No. 2, 1435 – 1450 .

1.7 S. Subhaschandra Singh, Solutions of Kudryashov–Sinelshchikov equation and generalized Radhakrishnan–Kundu–Lakshmanan equation by the first integral method//Int. J. Phys. Res. , 2016, Vol. 4, No. 2, 37–42.

7. M. Mirzazadeh, M. Eslami, A. Biswas, Soliton solutions of the generalized Klein–Gordon equation

by using  $(G'/G)$ -expansion method//Comp. Appl. Math., 2013, Vol. 12 Nov.

8. A. Biswas, A. Yildirim, O.M. Aldossary, R.Sassaman, Soliton perturbation theory for the generalized Klein-Gordon equation with full nonlinearity// P. Romanian Acad. A, 2012, Vol. 13, NO. 1, 32-41.

9. R. Sassaman, A. Biswas, Topological and non-topological solitons of the generalized Klein–Gordon equations//Appl. Math. Comput.,2009, Vol. 215, 212–220.

10. A. M. Wazwaz, Compactons, solitons and periodic solutions for some forms of nonlinear Klein–Gordon equations//Chaos Solitons Fractals, 2006, Vol. 28, 1005-1013.

## Contents

Editorial.....	3
<i>B. Mukanova, T. Mirgalikyzy, M. Turarova</i>	
Numerical aspects of the adaptive computational grid in solving the problems of electrical prospecting with direct current .....	4
<i>S. Aisagaliev, Zh. Zhunussova, H. Akca</i>	
Immersion principle for a variation calculus problem with boundary conditions .....	13
<i>A. Bountis</i>	
Complex Dynamics and Statistics in Hamiltonian 1-Dimensional Lattices.....	21
<i>M. Borikhanov, B.T. Torebek</i>	
Critical exponents of Fujita type for certain time-fractional diffusion equations.....	43
<i>B. Bekbolat, N. Tokmagambetov</i>	
On a boundedness result of non-toroidal pseudo-differential operators.....	50
<i>D.B. Zhakebayev, K.K. Karzhaubayev, E.S. Moiseyeva, N.V. Tsoy</i>	
Simulation of thermal flows by lattice Boltzmann method on the CUDA computational platform.....	56
<i>S.D. Maussumbekova, K. Khan</i>	
Computational study of temperature stratification effect on harmful gases expansion in the atmosphere.....	63
<i>A. Beketayeva, A.Zadauly</i>	
Influence of slit sizes on the interaction structure of supersonic turbulent air flow with a multi-component injection jet in a channel .....	72
<i>Zh. Baizhuma, S.A. Bolegenova, R.K. Manatbayev, K. Baktybekov, A. Syzdykov</i>	
Evaluation of wind power potential in shelek corridor (Kazakhstan) using weibull distribution function .....	86
<i>K.N. Dzhumagulova, T.S. Ramazanov, R.U. Masheyeva, Z. Donkó</i>	
Influence of background gas and external magnetic field on the localization of particles in two dimensional yukawa systems .....	94
<i>P. Safarik, A.O. Nugymanova</i>	
Application of electron-beam technology to reduce anthropogenic load of thermal power plants .....	101
<i>A.K. Shokanov, M.K. Kulbek, Sh.I. Hamraev, Y.A. Smikhan</i>	
Mössbauer research in zoloceramic materials .....	106
<i>S. Subhaschandra Singh</i>	
Soliton solutions of a generalized Klein–Gordon equation with power-law nonlinearity via the first integral method .....	116